Calibration System of the Photosensors for the **XENON1T** Dark Matter Search Experiment, and Response of Liquid Xenon to Low-energy Neutron Interactions

Dissertation
zur
Erlangung der naturwissenschaftlichen Doktorwürde
(Dr. sc. nat.)

vorgelegt der
Mathematisch- naturwissenschaftlichen Fakultät
der UNIVERSITÄT ZÜRICH

von
Payam Pakarha,
aus dem Iran

Promotionskommission:
Prof. Dr. L. Baudis (vorsitz),
Prof. Dr. U. Straumann,
Dr. A. Kish

Zürich, 2017

Abstract

The presence of neutral and non-relativistic dark matter has been indicated by several cosmological observation techniques, such as studies of the rotational velocities of spiral galaxies, gravitational lensing, cosmic microwave background, and galactic cluster collisions. Weakly Interacting Massive Particles (WIMPs) are one of the most promising candidates for dark matter and are strongly motivated by theories of supersymmetry and extra dimensions. WIMPs are expected to have very weak couplings to ordinary matter.

The XENON1T detector was constructed at the the underground laboratory of LNGS, in Italy, in order to search for galactic WIMPs via scattering off xenon nuclei, and aims to reach higher sensitivity of $1.6 \times 10^{-47} \, \mathrm{cm}^2$ for WIMP mass of $50 \, \mathrm{GeV}$ after two years of data and using $1 \, \mathrm{ton}$ of xenon in the active volume. The detector is currently acquiring data after all subsystems have been successfully commissioned and a calibration campaign has been pursued. The full description of the detector, and its individual subsystems are presented in chapter 2.

Various types of calibrations are needed to characterize the detector response. In particular, the gains of the 248 photomultiplier tubes (PMTs), used for the signal readout, are required to be calibrated, and monitored regularly, for the entire lifetime of the detector. A major topic of this PhD work included the design, hardware installation, tests, characterization, and commissioning of the PMT calibration system of the XENON1T detector, as described in chapter 3. In addition, an analysis software package was developed, to process the data from PMT calibrations into results of the PMT response, as also explained in chapter 3.

The WIMP interactions with xenon nuclei are expected to occur at energies at energies below $50 \, \mathrm{keV}$. For a given mass and WIMP-nucleon cross-section, the interaction rate is expected to drop dramatically with increase of the recoil energy. At the same time, the response of liquid xenon to low energy nuclear recoils has been studied by several experiments. However, below $5 \, \mathrm{keV}$, there exists only a very few measurements of the response parameters, e.g. relative scintillation efficiency (L_{eff}), and the absolute ionization efficiency (Q_y), which contain large uncertainties.

The Xürich I detector, small time-projection chamber (TPC), was built and successfully used for studying the response of liquid xenon to electronic recoils down to $1.5 \, \mathrm{keV}$. The detector was later upgraded, and aims to measure the response to neutron interactions down to 1-3 keV nuclear recoil energy range. Another major topic of this PhD work was the commissioning of the Xurich II detector, and the characterization studies of the experimental setup. The detector design and detailed description of the commissioning steps are given in chapter 4. The development of the raw data processing software for the experiment is also explained. In addition, the analysis of the calibration data is described, with focus on the study of the nuclear and electronic discrimination power of the xenon target at various applied electric fields, using data from a ^{137}Cs source (for electronic recoils) and from a neutron generator (for nuclear recoils).

Zusammenfassung

Die Existenz kalter, neutraler und nicht-relativistischer dunkler Materie verdeutlicht sich durch verschiedene kosmologische Beobachtungstechniken, unter anderem durch Geschwindigkeitskurven von rotierenden Galaxien, Gravitationslinseneffekte, die kosmische Hintergrundstrahlung und Kollisionen von Galaxiehaufen. WIMPs (engl: Weakly Interactive Massive Particles) sind eine der vielversprechendsten Kandidaten für dunkle Materie begünstigt durch Supersymmetrie und Extra-Dimensions Theorien. Es wird davon ausgegangen, dass WIMPs nur sehr schwache Bindung zu bekannter Materie aufweisen.

Der XENON1T-Detektor wurde am "Laboratori Nazionali del Gran Sasso" (LNGS), Italien, gebaut, um nach galaktischen WIMPs über Streuung an Xenonkernen zu suchen und zielt darauf ab eine wesentlich bessere Empfindlichkeit als bisherige Experimente zu erreichen. Der Detektor folgt momentan der Kalibrierungskampagne, nachdem alle Subsysteme erfolgreich in Betrieb genommen wurden. Die vollständige Beschreibung des Detektors und all seiner einzelnen Subsysteme sind im Kapitel 2 beschrieben.

Zur Charakterisierung der Detektorantwort sind verschiedene Arten von Kalibrierungen erforderlich. Insbesondere müssen die Verstärkungen der 248 Photomultiplier-Röhren (PMTs), die für die Signalauslesung verwendet werden, während der Lebensdauer des Detektors regelmäßig kalibriert und überwacht werden. Ein Hauptthema dieser Doktorarbeit war das Design, die Hardwareinstallation, die Tests und die Charakterisierung sowie die Inbetriebnahme dieses Systems, wie im Abschnitt 3 beschrieben. Darüber hinaus wurde ein Analyse-Softwarepaket entwickelt, um die Daten aus PMT-Kalibrierungen in Ergebnisse der PMT-Antwort zu verarbeiten, wie auch im Abschnitt 3 erläutert.

Es wird erwartet, dass die WIMP-Wechselwirkungen mit Xenonkernen bei Energien im Bereich von 1-100 keV auftreten. Für einen gegebenen Massen und WIMP-Nukleonquerschnitt wird erwartet, daßdie Wechselwirkungsrate dramatisch abfällt, und zwar durch Erhöhung der Rückstoßenergie. Während die Reaktion von flüssigem Xenon auf niederenergetische nukleare Rückstöße durch mehrere Experimente untersucht worden ist. Bei niedrigen Energiebereichen unter 5 keV enthalten die Schätzwerte der Parameter (die relative Szintillationseffizienz (L_{eff}) und die absolute Ionisationseffizienz (Q_y)) große Unsicherheiten.

Der Xürich-Detektor, eine kleine Zeitprojektionskammer (TPC), wurde gebaut und erfolgreich im Zusammenspiel mit flüssigem Xenon auf elektronische Rückstöße bis hinunter zu 1.5 keV untersucht. Der Detektor wurde später aufgerüstet und zielt darauf ab die Reaktionen auf die nuklearen Rückstöße bis hinunter in den 1-3 keV Bereich zu messen. Ein weiteres Schwerpunktsthema dieser Doktorarbeit war die Inbetriebnahme des Xurich(II)-Detektors und die Charakterisierungsstudien, die für die späteren Messungen benötigt werden. In Kapitel 4 wird das Detektordesign, Inbetriebsnahme der Hardware und die Software detailliert beschrieben. Zusätzlich wird die Analyse der Kalibrationsdaten beschrieben. Insbesondere die Untersuchungen der nuklearen und elektronischen Unterscheidungskraft des Xenon Zielobjekts für verschiedene angelegte elektrische Felder mit

$^{(137)}$Cs (für elektronische Rückstösse) und für Daten mit einem Neutronengenerator (für nukleare Rückstösse) werden erklärt.

Contents

List of Figures

List of Tables

Chapter 1

Introduction

1.1 Dark matter

The Newton's law of gravitation had been successful in explaining the cosmological observations. In particular, with a simple equation formulating the force, F, exerted between two objects of mass m_1 and m_2 separated by a distance r as:

$$F = \frac{Gm_1m_2}{r^2},$$ (1.1)

with a constant of proportionality G, known as the Newton's gravitational constant, the motion of planets, moons and comets could be explained.

Einstein revolutionized our understanding of gravity as a geometrical effect, resulting from the curvature of space-time. This curvature is quantified by the metric tensor $g_{\mu\nu}$, that defines a rule for calculating the distance ds between points on our space-time manifold by the relation $ds^2 = g_{\mu\nu}dx^\mu dx^\nu$.

With the assumptions of a homogeneity and isotropy on large scales ($>100\,\mathrm{Mpc}$), the distance between the objects in spherical coordinates (of space-time) can be expressed as:

$$ds^2 = -c^2 dt^2 + a^2(t)[r^2 d\Omega^2 + \frac{dr^2}{1 - kr^2}],$$ (1.2)

with $a(t)$ denoting the scale factor, c being the speed of light in vacuum, Ω being the solid angle, and k, describing the spatial curvature, can take the values of -1, 0, $+1$ for open, flat, and closed universes, respectively.

In addition, the Hubble equation provides an expectation for the expansion rate of the universe at the time t:

$$H(t) = \frac{\dot{a}(t)}{a(t)},$$ (1.3)

while the dot denotes the derivative with respect to time.

Therefore, the so called Friedmann equation can be derived by taking the derivative of both sides of equation 1.2 with respect to time:

$$H^2(t) + \frac{k}{a^2(t)} = \frac{8\pi G}{3}\rho_{tot},$$ (1.4)

where ρ_{tot} is the total energy density of the Universe. The critical density ρ_c is defined to obtain the ideally flat universe (k= 0):

$$\rho_c = \frac{3H^2(t)}{8\pi G}.$$ (1.5)

With this definition, we can then express the content of the universe in terms of their densities relative to ρ_c, by:

$$\Omega = \frac{\rho}{\rho_c}.$$ (1.6)

A standard model of the Universe is developed based on measurements of astrophysical systems at large sizes ranging from galactic to universal scales. The so-called ΛCDM model represents an expanding Universe emerging from a singularity state, called Big Bang. The universe in this model contains a cosmological constant, denoted by Λ (Lambda), associated with dark energy, and cold dark matter (abbreviated CDM) [1].

The majority ($\sim 70\%$) of the content of the universe appears to be in the form of vacuum energy, while the remaining is mostly in a form of invisible matter, called dark matter. In this chapter, the evidences for the existences of dark matter are discussed as well as several candidates and observation strategies.

1.1.1   Observational evidence

Historically, the first observational evidence for the existence of "dark matter" was found by Jacobus Kapteyn, a Dutch astronomer, in his publication "First attempt at a theory of the arrangement and motion of the sidereal system" [2]. In this article, in order to explain the dynamics of stars in our Galaxy, he introduced the so-called "Kapteyn Universe", a lens-shaped island universe of which the matter density decreased away from the center. Kapteyn uses the term dark matter to denote the invisible matter, the existence of which is suggested by its gravity only.

A decade later, a Swiss astronomer, Fritz Zwicky, used this term in a scientific publication for a second time [3]. His intention was to explain the measurement of an unexpectedly high velocities of nebulae in the Coma galaxy cluster through existence of a large amount of non-luminous matter, and hence the term "dark matter" (originally "dunkle Materie" in German language) was mentioned. Zwicky had suggested the existence of another form of matter, which does not emit or absorb light.

Even though Zwicky had a decent prediction of an interesting subject of study for physicists, it was only after 1978, when the contradicting dependency of the rotation speed of stars around galaxies, on their distance to the center of galaxy was first observed by Vera Rubin et. al. [4]. The apparent need for dark matter was widely recognized as a major unsolved problem in astronomy. For instance, in 1939, Horace W. Babcock determined the rotation curve for the Andromeda nebula, which suggested that the mass-to-luminosity ratio increases radially [5]. However, he interpreted his observation by attributing it to either light absorption within the galaxy, or modified dynamics in the outer portions of the spiral, and not to missing matter.

Starting from 1980s, several independent cosmological observations of larger scale objects provided strong evidences for the existence of dark matter. Later, several groups of scientists began to search for different dark matter candidates using different techniques and strategies. Dark matter is still one of the unknown mysteries of universe, and physicists are trying to understand its composition.

- **Galaxy rotation curves:**

  Following Newtonian dynamics, when being far from the visible mass distribution of any object, the speed of a rotating object is expected to drop with increasing the distance from the center of mass as $v \propto 1/\sqrt{r}$. However, observations of rotation curves from several galaxies and galaxy clusters show that the speed stays constant with increasing distance up to 5-10 times larger the visible size of the galaxy. This effect was studied in detail for several galaxies [6, 7] including our own galaxy (the Milky Way) [8], through comparison of the observed curve with simulations using different dark matter distribution patterns around the galaxy. These studies indicate that the dark matter is most probably distributed in a halo structure around galaxies (see figure 1.1).
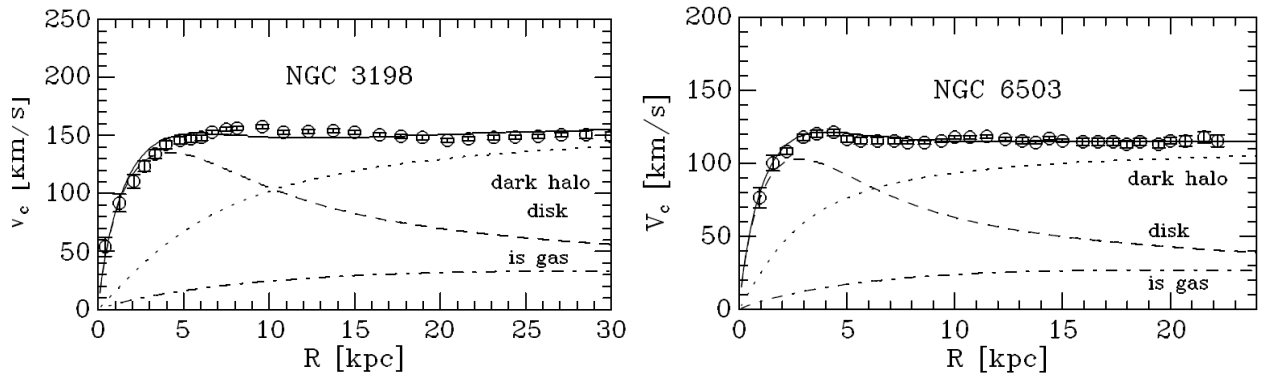
Figure 1.1: The rotation curves for the NGC3198 (left) and NGC6503 (right) galaxies [9]. The circles note the velocity and distances of the measured objects. The solid line illustrates the best fit to the data, and the dashed lines represent the predicted behavior from luminous matter, and the dark matter, distributed in a halo structure.

- **Gravitational lensing:**

  Light rays from a cosmological object can get deflected due to the gravitational field from another large object on their path. This effect allows estimation of the mass and mass distribution of the in-between object, through analyzing the resulting multiple images (strong lensing), or deformation of the observed image (weak lensing). This effect was initially predicted by Albert Einstein [10] in 1936 and later by Zwicky [11].

  Comparing the mass distribution patterns provided by the gravitational lensing methods with that derived from detected luminescence leads to very large mass to light ratio (from a few to hundreds). Moreover, there are large deviations of the baryonic mass distributions from that of the total mass observed through gravitational lensing [12, 13, 14, 15]. The fact that the observed distribution of detected X-rays are consitent with baryonic matter distributions, hints toward a weak self-interacting dark matter [16]. The Bullet Cluster, shown in figure 1.2, is an example of such deviations.

- **Velocity dispersion:**

  By measuring the radial velocity of the objects within a galaxy, or a cluster of galaxies, the statistical velocity dispersion of the objects, around the mean value, can be used to estimate its mass using the Virial theorem [18, 19]. Such calculations were carried out for several

Figure 1.2: Images of the bullet [17] (left) and the MACS J0025.4-1222 [13] (right) galaxy clusters. In both figures, the total projected mass distribution reconstructed from weak gravitational lensing are shown in blue, while the X-ray emitting hot gas observed with Chandra are shown in red. The displacement of one from the other can only be consistently explained by dark matter.

clusters, with a wide range of measured dark matter to visible matter mass ratios, ranging from almost unity [20] for some clusters, up to nearly 1000 for other cases [21].

- **Cosmic Microwave Background (CMB):**

  Recent measurements of the fluctuations within the power spectrum of CMB can probe the Universe back in time when it was 400 000 years old [22, 23]. Information about the baryonic, dark matter and dark energy content of the Universe can be extracted from the power spectrum of these fluctuations. Present estimates provide the values of $\Omega_b = 0.049$, $\Omega_{DM} = 0.265$, and $\Omega_\Lambda = 0.686$ for the abundances of baryonic matter, dark matter, and dark energy respectively [22].

- **Structure formation:**

  Later in time after Big Bang, small anisotropies gradually grew, and stars, galaxies, and larger structures began to appear. Several computer simulations have been performed, attempting to achieve the Universe in the shape it is currently observed, starting from our knowledge of Big Bang nucleosynthesis, and including the dynamics derived from the observations of the currently formed objects [24, 25]. Including dark matter into these computer simulations closes gaps in models of large-scale structures. Besides, neglecting the presence of dark matter at the early Universe, the current content of the Universe as observed by CMB measurements has never been reached. Simulations confirm that the structure formation models with "cold" dark matter are consistent with the structures observed through galaxy surveys. Most simulations find the best fitting solution to the observations through models of dark matter in a halo structure around galaxy clusters, with higher density gathered around the center of the galaxies [25].

1.1.2   Nature of dark matter

Due to the lack of any validated discovery claim of dark matter particles or dark matter interactions with visible matter, our knowledge about the nature of dark matter has been limited to cosmological and astronomical constraints, which are further narrowed by the improved limits from observations. Several theories have provided candidates for dark matter. While some of the candidates are currently ruled out through observational constraints, others remain as a challenge for experimental scientists to detect. In the following, several dark matter candidates are briefly described.

- **Massive astrophysical compact halo objects (MACHOs):**

  MACHOs, such as neutron stars, black holes, brown dwarfs or unassociated planets that would emit very little to no radiation ("dark") can represent a possible candidate for the observed missing mass in large astrophysical objects, like galaxies. Even though such hypothesis is disfavored by the studies of the Big Bang Nucleosynthesis (BBN), several studies in the search for such objects, using gravitational microlensing, have been carried out [26].

  In particular, the MACHO collaboration has reported the results from 5.7 years of observations. An exlusion limit is obtained, with 95 % confidence level, that the objects with masses ranging from 0.3 to 30 times solar mass, cannot contribute to the whole content of the dark matter halo [27]. Due to existence of a background source, which could not be resolved from their expected signal, these observations are not sensitive to objects with larger masses and hence the possibility of massive objects contributing to the whole content of the dark halo is not yet fully excluded.

- **Neutrinos**

  The Standard Model of particle physics does not contain any particle that meets all the requirements for being attributed to a viable dark matter candidate. Although neutrinos exist, we know from direct experiments and cosmological observations that they are very light (below $\sim 1\,\mathrm{eV}$) and their velocity would be large enough to affect structure formation [28]. Furthermore, due to the fermionic character of neutrinos, their energy state occupation number is constrained by the Fermi-Boltzmann distribution. Thus, they can not account for the observed dark-matter density in halos [29, 30]. Neutrinos would represent an example for hot (relativistic) dark matter, a scenario in which superclusters would form first, and later fragment to galaxies, in contrast to observations [31].

- **Sterile neutrinos**

  As a solution to the smallness of neutrino masses, sterile neutrinos are hypothetically defined particles, which depending on their production mechanism can provide both warm or cold dark matter candidates [32, 33, 34]. Ignoring the possibility that the right-handed neutrinos might also exist and exhibit different features, such as mass, compared to the observed left-handed neutrinos , due to their small theoretically expected masses, the current and previous dark matter detection experiments cannot set constraints on their existence, as their rare interactions with matter would occur at energies which fall below the sensitive threshold of most experiments.

- **Axions and Axion-like particles (ALPs)**

Axions are particles introduced first by Weinberg in 1978 [35]. They are neutral pseudoscalar bosons (or more precisely, Nambu–Goldstone bosons) naturally associated with the spontaneously broken U(1) symmetry, originating from an earlier proposed idea by Peccei and Quinn, as a solution to the strong charge-parity (CP) violation problem in quantum chromodynamics (QCD) [36].

Theoretically, axions can have masses within an enormous range, from 10^{-12} eV to 1 MeV [37], due the wide range of possible energies at which the symmetry breaking can occur. However, there are bounds, provided by astrophysical results on possible axion mass ranges [38]. In addition, the original associated electroweak scale for the symmetry breaking, that results into a proposed mass range and coupling constant for axion coupling to ordinary matter, is already ruled out by experimental observations [39]. Several axion models are proposed, all of which provide solutions to the CP problem, with symmetry breaking scales at orders of magnitude higher energies than originally assumed. Such axions would evade the experimental and astrophysical bounds [40, 41, 42]. Although current viable range of allowed mass for axions is very small (roughly 10^{-6} to 10^{-3} eV), due to their bosonic origin and tiny coupling constants, they can be considered as possible cold dark matter candidates, as they were produced non-thermally in the early universe.

Although there is a strong physics motivation for the existence of axions, they are just a first representative of a new particle family of so called Weakly Interacting Slim Particles (WISPs). Such WISPs are motivated for example by string-theory inspired extensions of the Standard Model, which predict, among others, also the existence of axion-like particles (ALPs) [43, 44]. While entirely unrelated to the Strong-CP problem, ALPs may also be viable dark matter candidates [45, 46]. The properties of the ALPs are similar to that of axions, but in general their mass and coupling to photons are not related, making the corresponding mass and cross-section parameter space larger [47].

- **Heavy photons (dark photons)**

  In 2008, a physics publication by Lotty Ackerman et al. brought a new view into dark matter physics by introducing a new U(1) gauge field that couples only to dark matter [48]. The associated mediator, which is named dark photon, couples the physics of dark sector to ordinary matter. The model was introduced initially considering all the current experimental constraints on possible observable signs of the theory. However, several experiments have tried to set further limits to the theory by searching for detectable interactions predicted by this model, mostly in collider search experiments [49, 50]. For instance, the BABAR collaboration has successfully excluded, with 90 % confidence level, the dark photon mass in ranges between 0.02 to 10.2 GeV, and the mixing strength between dark and light photons between 10^{-3} to 10^{-4} [51]. However, the dark photon is still considered a viable candidate for dark matter with masses in $\sim$10 MeV-10 GeV range, which is consistent with the expectations from BBN and structure formation observations.

- **Super heavy dark matter** At energies close to 10^{22} eV and above, cosmic protons can interact with the CMB and, hence their mean free path is reduced resulting in a suppressed measured flux [52]. However, there are observations of excess of events above this limit, motivating the presence of very heavy particles ($10^{1}2$-10^{16} GeV) which decay into protons at this energy range [53]. Such particles, besides explaining the origin of the observations, are possible dark matter candidates. These particles have extremely low interaction rates,

and are assumed be stable on cosmological timescales, but may annihilate or decay to SM particles which could be detected [54, 55, 56].

- **Weakly interacting massive particles (WIMPs)**

Various theories are proposed to address the existing problems of the Standard Model, some of which contain viable candidates for dark matter. For example, supersymmetic models are postulated to solve the hierarchy problem, as well as to unify the origin of the weak, strong and electromagnetic interactions [57]. Other examples are the "universal extra dimensions" (UED) and the "Little Higgs" models.

In supersymmetry, for each particle in the Standard Model, there is an associated supersymmetric partner, whose spin differs from its partner by 1/2. Bosons and fermions are related in supersymmetry through a conserved symmetry, named R-parity [58]. These models include interactions at which the baryon and lepton numbers are not conserved. Since the experimental observations confirm the conservation of the lepton and baryon numbers with high precisions, such interactions require to have tiny couplings, in order to prevent conflicts with the existing experimental data. In addition, in an ideally preserved "supersymmetry", each pair of superpartners would share the same mass and internal quantum numbers besides spin. This would have made most supersymmetric partners of the Standard Model particles easily detectable, using the current experimental data in hand. As no such observations are reported, the theory necessarily requires a spontaneously broken symmetry [59]. Minimal Supersymmetric Standard Model (MSSM) was the first extended version of the Standard Model that contained supersymmetry [60]. The lightest supersymmetric particle (LSP), which is, in most theories, the superpartner of Higgs, named neutralino [61], presents an ideal cold dark matter particle with mass and interaction cross-sections in a range not yet fully ruled out by experiments, hence it is a viable dark matter candidate.

The UED models suggest to include one or more spatial dimensions beyond the three spatial and one temporal dimensions that are observed [62]. Among the new features that these models present, the lightest of the new particles in UED, which is so-called the lightest Kaluza-Klein particle (LKP), can be considered a dark matter candidate [63, 64].

Little Higgs models are based on the idea that the Higgs is a pseudo-Goldstone boson, arising from some global symmetry breaking at a TeV energy scale [65]. A new symmetry, denoted T-parity, is introduced in Little Higgs models under which all heavy gauge bosons and scalar triplets are odd. Similar to supersymmetry particles, among the T-odd particles, the lightest T-odd particle (LTP) is known to be stable and can serve as a dark matter candidate [66].

Therefore, WIMPs are well motivated candidates for dark matter from both theoretical and experimental aspects. WIMPs are relevant for the topic of this PhD work and hence, their detection principles and the current status of the experimental efforts for WIMP dark matter searches are explained in detail in section 1.2.

1.2   Detection of dark matter in the form of WIMPs

A large variety of strategies and methods are proposed and used to design and construct experiments aiming for dark matter detection in the form of WIMPs. These are classified into 3 major methodologies: direct, indirect and collider searches. While indirect and collider searches

are described very briefly in sections 1.2.1, and 1.2.2, the direct searches are relevant to the topic of this work and are hence described in detail in section 1.2.3.

The different search methods are not competitive but mostly complementary to one another as their physics reach and sensitivities differ in several aspects due to the practical and technical challenges that each method faces, e.g. effective thresholds, background and signal rates, etc. [67]. As an example, in figure 1.3, the sensitivites of various search methods are compared in a parameter phase-space which is relevant for a simplified MSSM model named phenomenological MSSM (pMSSM) [68].
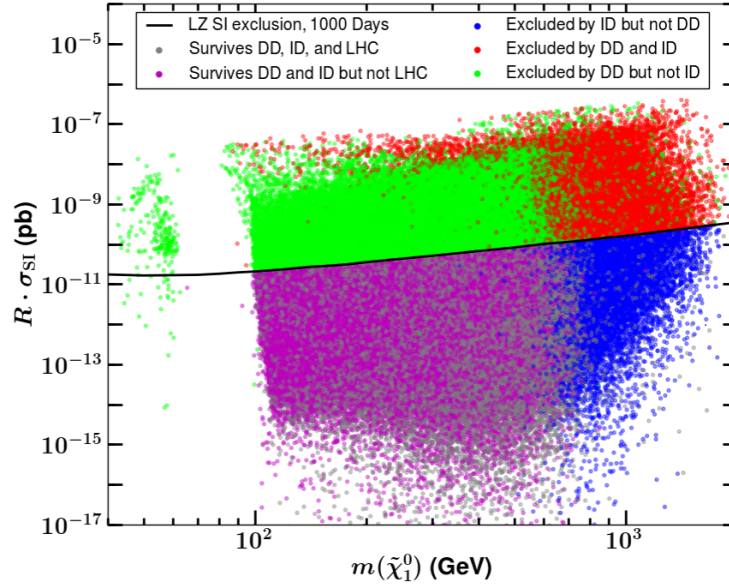
Figure 1.3: Comparison of the sensitivities of various dark matter search methods, color-coded as indicated, in the LSP mass versus scaled SI cross section plane for the pMSSM model [68]. The models are divided into categories, depending on whether dark matter can be discovered in the future direct detection experiments (green points), indirect detection experiments (blue points) or both (red points). The gray points represent models that may be discovered at the upgraded LHC (considering 14 TeV limit for collision energy), but escape detection in the future direct or indirect detection experiments. The projected LZ exclusion limit is however does not represent the ultimate goal of direct detection experiments and can be improved by larger detectors such as DARWIN.

1.2.1   Indirect searches

Even though after freeze-out dark matter pair annihilation will become largely suppressed, the self-annihilation process, that was relevant in the early Universe, can give rise to the Standard Model particles, that might be observed above the astrophysical cosmic ray background. WIMPs are expected to annihilate into primary Standard Model particles, such as W^+W^-, $\mu^+\mu^-$, t^+t^-, etc., which then decay and give rise to energetic cosmic rays, such as ν, γ, e^+, e^- [28].

Indirect detection of dark matter expects observation of the products of dark matter annihilation, from regions in the surrounding universe with a high dark matter density like the galactic

center, dwarf spheroidal galaxies, or galaxy clusters. Knowing the halo density distribution, for instance by using numerical simulations [69], one can also estimate the annihilation probability [70].

There are several physical constraints, set by the world's leading indirect search experiments, for which some examples are briefly described below. However, according to most interpretations, in all these cases, the observed signal contains large systematic uncertainties, mostly due to the dependency of the results on the background prediction models.

For instance, data from the PAMELA experiment shows that the positron fraction increases sharply over much of the sensitive range (1.5 - 100 GeV), appearing to be completely inconsistent with predictions from other sources, and can hence be atrributed to dark matter annihilation [71].

Independently, an interpretation of the Fermi Large Area Telescope data claims signals that hint to dark matter annihilation in the region around the galactic center from b quark and $\tau^+\tau^-$ channels with expected dark matter masses of 39.4 GeV and 9.4 GeV, respectively [72]. Another example is the AMS-02 cosmic ray antiproton flux data that also leads towards predictions for annihilation of 30-70 GeV dark matter [73]. Furthermore, XMM-Newton telescope has observed an identified weak line at 3.5 keV energy in the X-ray spectra of the Andromeda galaxy, and the Perseus galaxy cluster, which is in agreement with physical expectations from dark matter annihilation [74] while there exists some astrophysical explanations for this signal.

None of the observational claims for dark matter detection have been successful to provide a clear signature that can be only attributed to dark matter, and no other background sources, that are possibly ignored or underestimated. Finally, with the few exceptions mentioned above, most experiments either observe no excess among the predicted spectra, or find explanations for the observed anomalies from other baryonic sources, which are not considered initially. In this case, bounds on the WIMP annihilation cross section can be set. Figure 1.4 shows the summary of the current limits on dark matter annihilation cross-section from various indirect search experiments, displayed as a function of dark matter mass [75]. At higher masses, the strongest bounds are from a H.E.S.S. analysis of the Galactic Center halo [76].
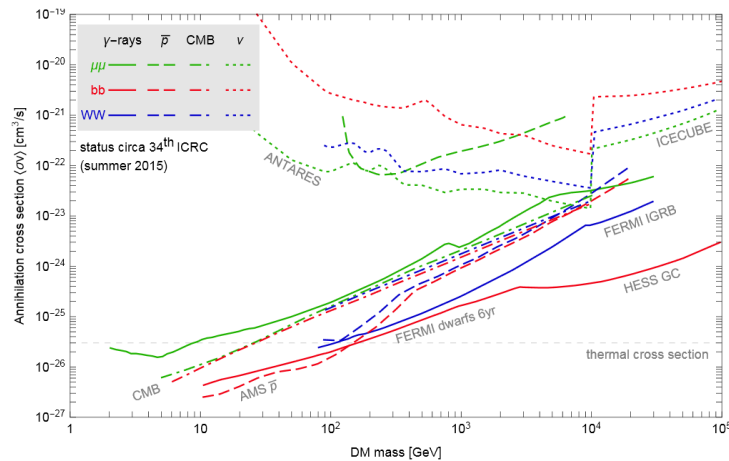
Figure 1.4: Summary chart of the current most stringent bounds on DM annihilation cross-section, in different channels and from different searches [75].

1.2.2   Collider searches

Another dark matter search scenario is through collider experiments. In particular, at the large Hadron Collider (LHC), one can probe the production of dark matter particles in p-p collisions (i.e. $pp \longrightarrow \chi\bar{\chi}$). Using an effective field theory (EFT) approach, the possible dark matter interaction cross-sectons with hadrons can be calculated[77] for different assumptions on the dark matter couplings and processes.

Common to all collider dark matter searches is the signature of missing transverse momentum (missing transverse energy, E_T), an expected trace left behind by the WIMPs escaping the detector. These events can be produced in association with Standard Model particles, most notably photons, or jets (either from quarks or gluons), but also W ,Z, or even Higgs bosons and heavy quarks. Such particles, produced in association with the WIMP pair, will recoil against the invisible particles. The common signature is therefore a large value of E_T and a back-to-back topology between E_T and the Standard Model particle used for tagging[78].

Both ATLAS and CMS collaborations have analyzed their data for signatures of dark matter interactions, such as mono-jets, mono-photon, or mono-W/Z [79, 80, 81, 82], with no evidence for such observations. In figure 1.5, several of the current limits on the WIMP mass and cross-sections are plotted at 90 % confidence level [78].
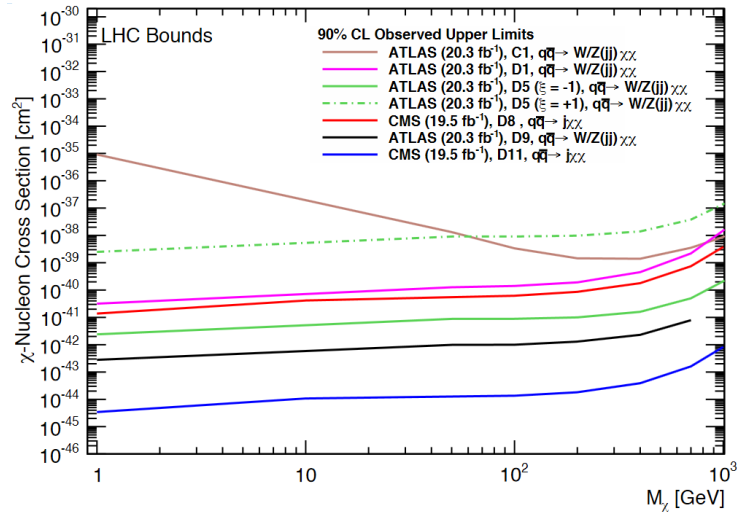
Figure 1.5: The current upper limits on WIMP-nucleon cross section from collider searches, associated to different possible final states [78].

1.2.3   Direct searches

Direct detection experiments generally look for detecting WIMP scattering off the atomic nucleus, depositing a small energy in the form of a nuclear recoil (NR) with energies below few tens of keV [28]. The deposited energy can be observed through three different signals, depending on the detector technology in use. These can be the production of heat (phonons in a crystal), an excitation of the target nucleus which de-excites releasing scintillation photons or by the direct ionization of the target atoms. Different experiments use various detection strategies, focused either on one

of the three, or on the combination of two of these signals. Although, in principle, all three signals could be recorded, such an experiment does not exist to date [29].

While to measure the ionization signal either germanium detectors or gases (low pressure, for directional searches) are employed, scintillation signal can be recorded for crystals as well as for noble gases (also in liquid form). To detect heat, the phonons produced in crystals are collected using cryogenic bolometers at very low temperatures (in mK range). In addition, The heat signal can be observed through nucleation processes in experiments using superheated fluids.

Direct WIMP searches using ultra-low background liquid xenon dual-phase time projection chambers (TPCs) have been leading on setting the best limits for the spin-independent WIMP-nucleus interaction cross sections in the past decade [28, 29, 83]. In section 1.3, the detection of dark matter using a xenon target is discussed.

Currently, XENON100 [84, 85], LUX [86], and PandaX [87] experiments have constrained the cross-section down to an order of 10^{-45}-10^{-46} cm^2 (for particular WIMP masses, in the range of 20-60 GeV/c^2). The future larger scale experiments such as XENON1T [88], LZ [89] and DARWIN [90] will be able to probe this parameter down to 3 orders of magnitude lower than the current limits [91] (see figure 2.19). Among these experiments, XENON1T is currently running experiment, and includes one of the main subjects of this PhD work. This experiment is described in detail in section 2.

Among the detectors not using xenon as the target, the DarkSide-50 experiment has been successful to reach a comparable sensitivity with xenon detectors. While the detector is still acquiring data, its current results give a limit as low as 2×10^{-44} cm^2 for 100 GeV/c^2 WIMP mass, the best result achieved to date with argon in the target [92]. The next generation of the experiment, DarkSide-20k aims to use a 20 ton low-radioactivity argon target, and is expected to start data taking in 2021 [93]. This will provide a projected best sensitivity of $\sim 1 \times 10^{-47}$ cm^2 [93].

For lighter WIMP, in the mass region between 500 MeV/c^2 and 1.8 GeV/c^2 the CRESST II experiment has the best sensitivity. In this detector Dark matter particles are detected by looking for elastic scattering processes of dark matter with nuclei of CaWO$_4$ crystals. The experiment is operated at a temperature of about 15 mK. The CRESST collaboration recently started an upgrade program to further improve the sensitivity in this mass region by several orders of magnitudes [94].

Another example is the SuperCDMS collaboration which uses cryogenic germanium detectors in CDMSlite experiment, operated at a relatively high bias voltage to amplify the phonon signal from WIMP interactions. Although their limits are weaker than the xenon and argon TPC experiments by orders of magnitude for large WIMP masses (>10 GeV/c^2), their very low energy threshold of 56 eV for electronic recoils allows for probing the interactions of very low-mass WIMPs (1-10 GeV/c^2) [95]. SuperCDMS SNOLAB will be the next-generation experiment aimed at detecting low-mass WIMPs using cryogenic detectors of two target materials (germanium and silicon). The experiment is being designed with a projected sensitivity to cross sections of $\sim 1 \times 10^{-43}$ cm^2 for a dark matter particle mass of 1 GeV [96].

The differential rate for WIMP elastic scattering follows [97] :

$$\frac{dR}{dE_R} = N \frac{\rho_0}{m_W} \int_{v_{min}}^{v_{esc}} d\vec{v} f(\vec{v}) v \frac{d\sigma}{dE_R}, \tag{1.7}$$

where N is the number of nuclei, ρ_0 the local dark matter density in the galactic halo, m_W the WIMP mass, $\vec{v}$ the WIMP velocity , $f(\vec{v})$ the WIMP velocity distribution, and $\frac{d\sigma}{dE_R}$ is the WIMP–nucleon differential cross section [98]. v_{min} denotes the minimum velocity that is required for the WIMP to produce a recoil, and is calculated using the equation:

$$v_{min} = \sqrt{\frac{m_N E_{th}}{2m_r}},\tag{1.8}$$

where E_{th} is the energy threshold of the detector, with m_N and m_r denoting the target nucleus and reduced mass, respectively; v_{esc} denotes the galactic escape velocity of WIMPs in the Earth frame, $v_{esc} \simeq 544\,\text{km/s}$ [99].

In the case of a spin-1/2 or spin-1 WIMP field, the differential WIMP-nucleus cross section can be expressed as the sum of the spin-independent (SI) and spin-dependent (SD) terms:

$$\frac{d\sigma}{dE_R} = \frac{m_N}{2m_r^2 v^2}[\sigma_{SI}]F_{SI}^2(E_R) + \sigma_{SD}F_{SD}^2(E_R)]\tag{1.9}$$

where σ_{SI} and σ_{SD} are the cross sections in the zero momentum transfer limits, and F_{SI} and F_{SD} are the nuclear form factors.

For the theories which assume axial-vector coupling of WIMPs to matter, the expected signals are due to WIMP couplings to the nuclear spin and the corresponding cross-section is of the form:

$$\sigma_{SD} = \frac{32}{\pi \hbar^4}\mu^2 G_F^2 \frac{J+1}{J}[a_p S_p + a_n S_n]^2,\tag{1.10}$$

where G_F is the Fermi constant, μ is the reduced mass, J is the spin of the nucleus, a_p and a_n are the spin-dependent couplings of WIMPs to protons and neutrons, respectively, and $S_{n(p)}$ denotes the spin content of the neutrons (protons) within the nucleus. For such interactions, the nuclei with non-zero angular momentum are preferred as targets, considering the corrections due to spin structure functions.

Whereas for theories of scalar, vector, or tensor coupling of WIMPs, the predicted couplings to matter are only through its mass. Similarly, the cross-section for the spin-independent WIMP-nucleon interactions can be expressed as:

$$\sigma_{SI} = \frac{4\mu^2}{\pi}[Zf_p + (A-Z)f_n]^2,\tag{1.11}$$

where m_W is the WIMP mass, and the $f_{n(p)}$ is the 4-fermion coupling to neutrons (protons), and A and Z denote the mass number and atomic number, respectively. For such interactions, nuclei with large A are favored as targets, considering the nuclear form factor corrections.

1.3   Direct dark matter detection using xenon dual-phase time projection chambers (TPCs)

Among the possible detection media that are used for direct WIMP search experiments, xenon has several advantages. First, xenon experiments can take advantage of measuring scintillation and ionization charge simultaneously [100].

Furthermore, as it can be seen in equation 1.11, the cross section for spin-independent interaction of WIMP with matter is approximately proportional to A^2, where A is the atomic mass of the target nucleus. Therefore, xenon detectors can take advantage of higher expected interaction rates for a given WIMP mass and cross-section, compared to other noble gases (see figure 1.8).

Also, due to its high atomic number (Z) and high density in liquid state (almost $3\,\text{g/cm}^3$), LXe is an efficient gamma absorber. This means that the amount of background interacting with the
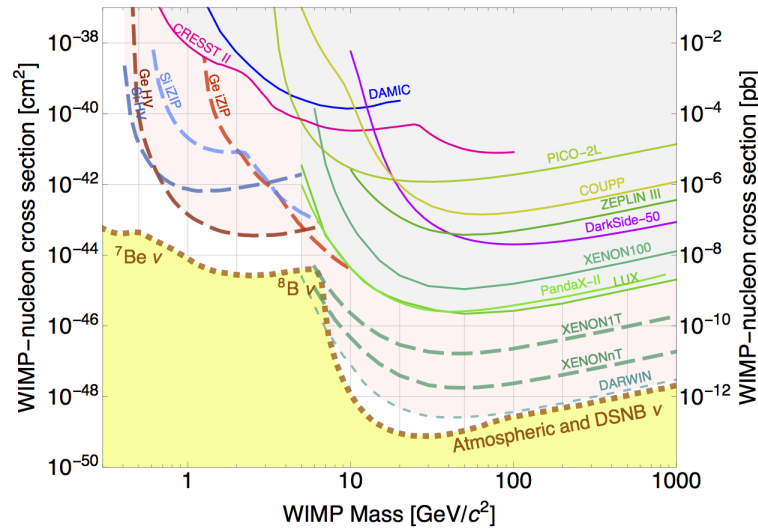
Figure 1.6: The current limits (solid curves) and the projected future sensitivities (dashed curves) to spin-independent WIMP-nucleon cross section as a function of the WIMP mass for several present, and future detectors (figure from Prof. Laura Baudis).

active volume in a liquid xenon detector is reduced by the outer layer, the so-called self-shielding effect.

Additionally, there are not many long-lived radioactive xenon isotopes (only ^{136}Xe radiating via double beta decay measured by EXO experiment [101], relevant only for very large scale detectors, > 1 tons), which makes xenon preferable with respect to argon for example. Most argon detectors suffer from intrinsic background from decays of ^{39}Ar isotope that is produced through cosmic activation.

As mentioned earlier, the expected signal from WIMP interactions are scintillation and ionization of the xenon atoms produced by the collisions between the WIMPs and xenon nuclei. The main background sources for these experiments are radio-impurities in the detector construction materials, neutrons from (α,n) and fission reactions, cosmic rays and their secondaries, activation of detector materials during exposure at the Earth's surface, as well as sources intrinsic to the target materials. The ultimate backgrounds might come from neutrino-induced nuclear recoils from coherent neutrino-nucleus scatters [28].

A particle can interact with xenon atoms either through coupling to the electrons (electronic recoil, ER) or the nucleons (nuclear recoil, NR). Every interaction excites the target atoms leaving a prompt scintillation response of VUV photons (178 nm). At the same time, ionization process occurs that yields free electrons. In a dual-phase (gas and liquid xenon) TPC, an electric field is applied which guides the resulting free electrons toward the liquid-gas interface, and is typically in the range of $\sim$0.5-1.0 V/cm. A stronger electric field ($\sim$10 kV/cm) is applied near the liquid-gas interface, at which the electrons get accelerated, followed by excitation of gas atoms producing secondary scintillation signal. Both signals can be read using photo-sensors which have a good quantum efficiency (QE) at this wavelength. Figure 1.7 schematically illustrates the generation of the two signals in a xenon TPC.

In general from every interaction inside a liquid xenon volume, beside the excitation and ion-
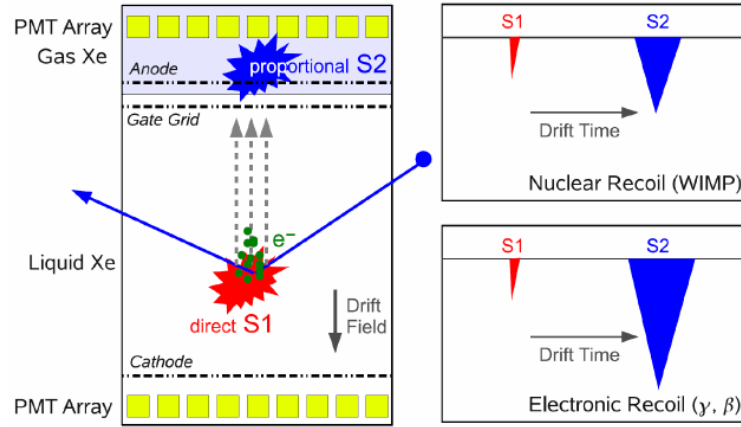
Figure 1.7: Schematics of a dual-phase xenon time projection chamber (TPC), and sketch of the waveform for electron recoils (top), and nuclear recoils (bottom). From each interaction inside the liquid xenon volume, a prompt scintillation signal (S1) is generated together with a proportional scintillation signal (S2) that is produced by ionization electrons drifting toward the liquid-gas interface by the applied drift field, where an stronger electric field is applied that accelerates the electrons and provides secondary scintillation signal through electroluminescence. Figure from [110].

ization of the xenon atoms, several processes occur simultaneously, which are listed below.

- De-excitation: Some of the released ionization electrons might survive electron-ion recombination and drift out of the interaction site to be collected. In addition, excited atoms and the recombined electron ion pairs will produce scintillation photons peaked at ($178\pm 13\,\mathrm{nm}$) [102, 103].

$$\mathrm{Xe}^* + \mathrm{Xe} \longrightarrow \mathrm{Xe}_2^*, \tag{1.12}$$

$$\mathrm{Xe}_2^* \longrightarrow 2\mathrm{Xe} + \mathrm{h}\nu(178\,\mathrm{nm}) \tag{1.13}$$

- Electron-Ion recombination: An escaping electron recombines with a Xe_2^+ ion and leaves a double exited xenon atom [104] via the following interactions

$$\mathrm{Xe}^+ + \mathrm{Xe} \longrightarrow \mathrm{Xe}_2^+, \tag{1.14}$$

$$\mathrm{Xe}_2^+ + \mathrm{e}^- \longrightarrow \mathrm{Xe}^{**} + \mathrm{Xe}, \tag{1.15}$$

$$\mathrm{Xe}^{**} \longrightarrow \mathrm{Xe}^* + \mathrm{heat}. \tag{1.16}$$

- Lindhard Quenching: If the projectile and the target material are in the same range of masses, the energy might transfer from projectile particle to target particles via elastic collisions adding heat to the target material without any detectable emission. This results in an underestimation of the energy of projectile [105].

- Bi-excitonic quenching: In the situation where the density of excitons (excited atoms) is high, the following process might happen before the particle's de-excitation [106]. This process significantly increases the ionization to scintillation signal size ratio.

$$\mathrm{Xe}^* + \mathrm{Xe}^* \longrightarrow \mathrm{Xe}^+ + \mathrm{Xe} + \mathrm{e}^-. \tag{1.17}$$
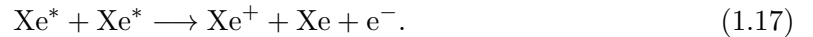
The scintillation yield, L_Y, is defined as the number of scintillation photons produced per unit energy. This parameter is dependent on the type of incoming particle as well as its energy [105, 106]. The relative scintillation efficiency ($\mathcal{L}_{eff}$) is used to quantify the quenching for nuclear recoils due to high high density of exicons. This quantity converts the scintillation signals from a particle interaction in liquid xenon into recoil energies [107].

Therefore, $\mathcal{L}_{eff}$ is defined as the light yield of nuclear recoils relative to that of 122 keV gamma rays from ^{57}Co. As mentioned above, the light yield depends on the electronic stopping power ($\frac{dE}{dx}$), which depends on the energy of the particle and its type, and therefore $\mathcal{L}_{eff}$ is an energy-dependent quantity [108]. The same argumentation is true for the ionization yield, Q_Y, defined as an absolute ionization yield of LXe.

For a given WIMP mass and cross section, the predicted differential interaction rate drops dramatically with increase of the recoil energy [109] (see figure 1.8). Hence, all experiments tend to minimize their effective threshold and background rate at lower energies in order to increase their sensitivities for WIMP interactions. In addition, it raises the importance of a precise measurement of xenon response properties (e.g. ionization and scintillation yields) at low energies with high precision. A major part of this PhD work includes an R&D project which aims to measure these parameters, and is explained in detail in chapter 4.
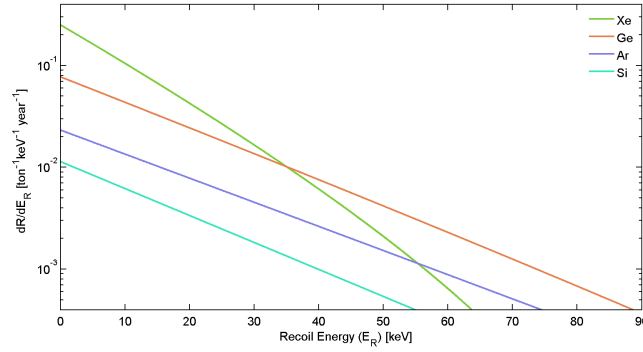
Figure 1.8: The differential interaction rate of 100 GeV WIMP and 1×10^{-47} cm^2 WIMP-nucleon cross section for xenon, germanium, argon, and silicon (figure from Prof. Laura Baudis).

The prompt and secondary scintillation signals are conventionally denoted as S1 and S2, respectively [109]. The ratio between the two observable parameters depends on the energy deposition density ($\frac{dE}{dx}$). In particular, the probability for electron-ion recombination is strongly dependent on the energy deposition density [104], and hence differs for NR and ER interactions. Hence, the S2/S1 fraction varies from the NR to ER interaction types, and can be used to discriminate the desired signal, through dark matter interactions, from the major background, due to ERs. The delay time between the S1 and S2 signals from the same event denotes the time that the electrons take to drift through the liquid xenon to reach the extraction region between the anode and gate, where the S2 signals are generated. While the drift time information is used to reconstruct the z position of the event, in case of using several photosensors distributed radially, the hit pattern can be used for (x,y) position reconstruction, and hence a 3D imaging of the event position can be achieved.

1.4   Preface

This PhD thesis includes my involvement in two major research projects described after and introduction to the XENON1T experiment that is provided in chapter 2. In chapter 3 the work on the PMT calibration system of the XENON1T experiment is addressed, whereas in chapter 4 the research efforts on using Xurich II detector for studying low energy response of xenon to nuclear recoils are described. While most content of these chapters includes my contributions to the projects, it must be noted that in both cases a collaborative effort has been conducted. Therefore, for clarification, this preface summarizes my own involvement with the two projects together with the contributions from other team members and the extent to which the work was shared. In addition, there were some minor studies that were performed during my PhD studies excluded from this dissertation that are briefly mentioned.

XENON1T PMT calibration system (hardware):   The preliminary design of the system was made by Dr. Alexander Kish who used experience earned from developing a similar system for the XENON100 experiment. Therefore, all efforts on the development of the new system were made under his supervision. I modified the design based on practical requirements foreseen for the installation of the system for the XENON1T detector. The installation was planned in several steps scheduled according to the other systems involved, such as the cryogenics, TPC, and PMT arrays (see section 3.3).

I organized the purchasing of all the required hardware including the fiber-optics while for some cases the required equipment could not be found in the market and had to be customized in communication with the companies (see section 3.1). Before purchasing the hardware required for the XENON1T system, a test setup was used at the University of Zurich to examine the performance of the whole system in a liquid xenon setup (see section 3.2). Several parts of the setup, such as the LED boxes and the LED frame, were made at the UZH mechanical workshop while engineering support from Andreas James was used for the technical design of these components.

The installation of the system was performed in four steps, as listed in table 3.2. I have managed and performed all installations steps while in several cases I received help from colleagues present on-site to overcome the practical difficulties of the handling of the fibers during the installation.

A control software for the pulse generator used to power the LEDs in the XENON1T PMT calibrations system was initially provided using C++ scripts that send commands to the device through an RS 232 port (see section 3.4). The program was later converted into the ladder diagram language used for the general XENON1T slow control software in a collaborative work with slow control working group. Therefore, a web-based platform was provided to be used by the experiments operational crew at any time to control the LED setup in order to perform calibrations of the PMTs in several modes.

In addition, in a collaborative effort with XENON1T DAQ working group the setup was commissioned and the whole data process to acquire PMT calibration data was examined and optimized. The data acquisition system was used in a different mode than usually used for the acquisition of the dark matter or calibration data. In particular a dedicated mode of the DAQ system was developed that uses a synchronized external trigger from a digital clock electronic module sending trigger signals to both the LED pulse generator and the ADC modules (see section 3.5).

XENON1T PMT calibration system (software):   The analysis software of the XENON100 PMT calibration system uses an independent package that performs the whole analysis task from

raw data processing into final measurements while, for the case of XENON1T, it was desired to provide a software which can use the data processed by the main program (PAX), similar to other analysis studies. Therefore, I made a dedicated analysis effort to study the possible bias effects on the evaluation of the PMT response which can be caused by the use of the PAX algorithm, that was not optimized for data at the very small signal levels, in the range of one to few photoelectrons. The study has pointed out that in particular the peak-finding and the pulse integration algorithms were to be improved to avoid biased estimations of the PMT response (see section 3.6.1). Therefore, the work has resulted in the development of a modified version of the PAX software that is used for the processing of data for PMT calibration purpose.

In addition, an independent analysis software was provided using Python programming language that would allow the operational crew to perform the whole analysis process of the regular PMT calibrations via a graphical user interface (GUI). The software would access the processed data and provide fits to the single photoelectron spectra from all PMTs which can be visually inspected and interactively modified by the user through the GUI platform (see sections 3.6.2 and 3.6.3). The analysis results will be transferred to a dedicated database that stores all calibration results of the experiment over time. The work on the GUI software was done in collaborative effort with Daniel Mayani who had experience in analytic characterization and testing of the XENON1T PMTs.

I commissioned the entire software package using the first PMT calibration data of the experiment after the closure of the TPC cryostat and before the filling of the xenon into the chamber. The commissioning has lead to the optimization of the LED light intensities and the DAQ settings used for the PMT calibrations.

The preliminary efforts of the PMT gain extractions using the existing fitting algorithm had revealed the presence of a noise at an amplitude comparable to the size of single photoelectron signals in most channels. Motivated by this work a noise reduction campaign was initiated that resulted into significant reduction of the noise level.

Due to the presence of the noise, the gain extraction method mentioned above could not be used for the PMT response studies and hence an alternative method was developed that was found to be less sensitive to the noise level (see section 3.7). This method was developed mostly by Dr. Shingo kazama with my support during the last few weeks of this PhD work. This method has been later used to provide gain estimations during the first science run of the XENON1T experiment. However, due to the improvements of the noise conditions, there are currently ongoing efforts to bring the fitting method back in use for the cross-checks of the extracted gain values. The compatibility of the results from the two methods are discussed in section 3.10.

Xurich II detector commissioning: As mentioned in the section 4.2, the Xurich II detector uses most infrastructure from a previous experiment used for studying the xenon response to electronic recoils. However, a new TPC was designed and optimized by testing its performance in several iterations. In addition the PMT high voltage, readout cables, connectors, and vacuum feed-throughs were modified. Other subsystems including the gas system, PMT readout boards, and DAQ electronics were also subject to changes. The work on the commissioning of the detector was almost equally shared between myself, Francesco Piastra and Dr. Alexander Kish. A master student (Hrvoje Dujmovic) was also involved into the commissioning work for the first few months. In particular the optimization of the PMT readout boards and the DAQ setup was majorly performed based on my own contributions.

In parallel to the commissioning of the detector hardware, a new data processing software was developed with several iterations of improvements based on observations of undesired features from calibration data (see section 4.3). The software was initially translated from a previously developed

software in MATLAB language that was used for the Xurich I data analysis. Later, its performance was studied in detail in several aspects such as the signal identification, and the quality of the signal property extractions (e.g. pulse width, and area). Most work on the development and optimization of the software was shared between myself, Francesco Piastra and Hrvoje Dujmovic.

The regular operations of the detector including the changes of the setup, calibration data taking, and the safety considerations were mostly shared between myself and Francesco Piastra. However, some particular operations such as the detector leveling and levelmeter calibrations were subject to my own contributions in providing the readout program for online monitoring of the liquid levels read by individual levelmeters (see section 4.4).

In addition, I provided an independent analysis program for the purpose of PMT calibrations of the Xurich II detector. The program was later modified to perform calibrations using an alternative method for gain extractions with the help from Dr. Shingo Kazama. I performed regular calibrations of the PMTs during the commissioning, calibration, and the science data taking of the Xurich II detector. The stability of the gain values are monitored and the gain estimations using both methods provides consistent results (see section 4.5).

In the last weeks of my work as a PhD student, I instructed a master student (Yanina Biondi) and a new PhD student (Chiara Capeli) to take over the operations of the Xurich II detector. In addition, I provided them with the instructions on the analysis process of the Xurich II data using the previously developed software tools.

Analysis of the Xurich II calibration data: Most signal selection cuts that are developed for the analysis of the Xurich II data are dependent on source, as well as on the detector operating conditions e.g. applied electric field, and PMT gains. Therefore, most cuts described in section 4.6 were developed on a run-based basis in shared work between the Xurich II team members. However, the development of the S2 width cut in particular was my own contribution whereas the position dependent cuts and signal corrections were established based on efforts of Francesco Piastra.

The analysis of the ^{83m}Kr data with the aim of studying the detector signal yields in response to low energy electronic recoils was performed also in a shared work between the Xurich II team members. However, I performed the analysis of the ^{137}Cs calibration data that resulted in evaluation of the quality of the discrimination power between the electronic and nuclear recoils when combined with the analysis of the data from the neutron generator. This analysis is described in details in section 4.7.2. The study includes an observation of a dependency of the discrimination power to the applied electric drift field in the TPC. Such an observation has not been reported in the existing literature until present.

Using Xurich II detector for studying the low-energy nuclear recoil response of liquid xenon: In addition to the Xurich II detector, several other devices are used to study the nuclear recoil response of liquid xenon using the neutron generator facility at UZH. Although most devices were already characterized during my studies as a Master student within the same group, after the commissioning of the detector, the entire setup had to be characterized. In particular, the time of flight measurements using a TAC (time to amplitude converter) module, and the pulse shape discrimination of the electronic and nuclear recoils using an EJ301 liquid scintillator detector and the MPD4 module had to be calibrated (see section 4.8). I performed the re-characterizations of the setup and instructed the new students for using the devices.

In addition, I modified the acquisition setup to a more advanced setup used for the nuclear recoil measurement. The new setup was designed to include online acquisition of the data from

Xurich II PMTs together with the amplitude and pulse shape discrimination parameters from the MPD4 module and the measured time of flight between the two targets. Moreover, I measured the efficiency of the hardware trigger used for the setup to evaluate the expected threshold of the setup in response to nuclear recoils.

After all the efforts on providing the prerequisites for the measurements of the low energy response of liquid xenon to nuclear recoils the acquisition of the science data was started in the last weeks of this PhD work. The new students were instructed to perform the data acquisition. However, by the end of this work, the acquired statistics of the nuclear recoil events was not sufficient to perform and actual evaluation of the light and charge yields of nuclear recoils.

The analysis of the XENON100 PMT calibration data: The analysis software of the PMT calibrations of the XENON100 experiment was developed by Dr. Alexander Kish and later modified by Dr. Annika Behrens. The analysis process required visual inspection of the automated fits to the single photoelectron spectra and possible improvements of the low quality fits through manual changes of the fit initiating parameters by the user. I performed this analysis on a weekly basis in the period from March 2013 until February 2016. The work included providing the results in a web-based database and reporting the possible problems to the experiment operational crew. This analysis work is excluded from this dissertation although the results of the analysis has been used to process the XNEON100 science data in this period. Moreover, by performing the analysis I earned the experience and skills that I later used to develop a more robust software for the XENON1T experiment.

The studies of the XENON1T detector material activation after nuclear recoil calibrations using the neutron generator: It has been foreseen to use a D-D neutron generator for the purpose of calibrations of the XENON1T detector response to nuclear recoils. The high-energy neutrons from the generator can not only interact with the xenon atoms but also with the other detector materials, resulting into activation of some stable isotopes through inelastic neutron scattering or neutron capture processes. While the activation of the short-lived isotopes with half-life in the range of less than a few days can be tolerated by the experiment, the long-lived activated isotopes can produce undesired background into the experiment. For this reason, I used the GEANT4 model provided by the Monte Carlo working group of the XENON1T experiment to simulate the activation of the detector material through neutron calibrations. The results was later reported to the collaboration. It was found that there will be no significant contribution to the existing background of the experiment from any long-lived isotopes that can be produced through activation of the material during a typical neutron calibration exposure of the XENON1T experiment using the neutron generator at the desired rates. This study is excluded from this dissertation as it has been unrelated to the two major topics of the PhD thesis.

The Monte Carlo simulations for using a ^{88}Y^{9}Be source to study the nuclear recoil response of liquid xenon: In the early stages of the commissioning of the Xurich II detector the possibility of using mono-energetic neutrons produced through (γ,n) interactions from a ^{88}Y^{9}Be source as an alternative to study the nuclear recoil response of liquid xenon was foreseen. At the time, no xenon experiment had used such a radioactive source and the study could have provided the first measurements of the nuclear recoil response of xenon using low-energy neutrons (152 keV). Therefore, I performed Monte Carlo simulations including a^{88}Y^{9}Be source into the GEANT4 model of the setup. However, as the commissioning of the detector took longer than expected, the source

was used already by other experiments, such as XENON100 for instance, and the measurements lost its initial motivation. As it was decided at the end to exclude the use of such source in the measurements using Xurich II detector, this study was also excluded from this dissertation.

Chapter 2

The XENON1T experiment

In chapter 1, the motivation for dark matter searches was addressed. In addition, several search strategies and experiments were discussed, with the focus on direct dark matter searches. As a major part of this PhD work was focused on XENON1T experiment, in this chapter, the XENON1T detector is described in detail. The experiment is located at the Laboratori Nazionali del Gran Sasso (LNGS), and aims to detect dark matter particles through their interactions with xenon atoms.

2.1   Detector overview

Figure 2.1, shows a schematic view of the XENON1T experiment. The TPC cryostat is held by a support structure inside the water tank. Next to the water tank, a building was constructed to host the experiment subsystems. On the ground floor, the xenon storage and recovery system (ReStoX), together with the krypton distillation column are installed. The DAQ and electronics are placed on the first floor, together with the control room, and the slow control system. Finally, the cryogenic and purification systems are placed on the second floor. A photograph of the experimental facility is also shown in figure 2.2.

A 7.5 m stainless steel pipe, with 350 mm outer diameter, connects the cryogenic system to the time projection chamber. Inside this pipe, several smaller pipes are installed allowing the gas xenon to flow from the ReStoX to the detector and back, also hosting the high voltage and signal cables for the photomultiplier tubes (PMTs), and the optical fibers, required for transmitting light to the TPC for calibration of the PMTs.

In addition to the PMTs installed inside the TPC to detect xenon scintillation signal, another set of PMTs is installed inside the water tank to detect and tag the incident cosmic muons that reach the experimental hall, or the particle showers induced by the muons interacting outside of the detector volume. A set of rails and carriers are provided inside the tank and around the TPC to move the external calibration sources in different directions. In the following sections, the individual detector subsystems are described in detail.
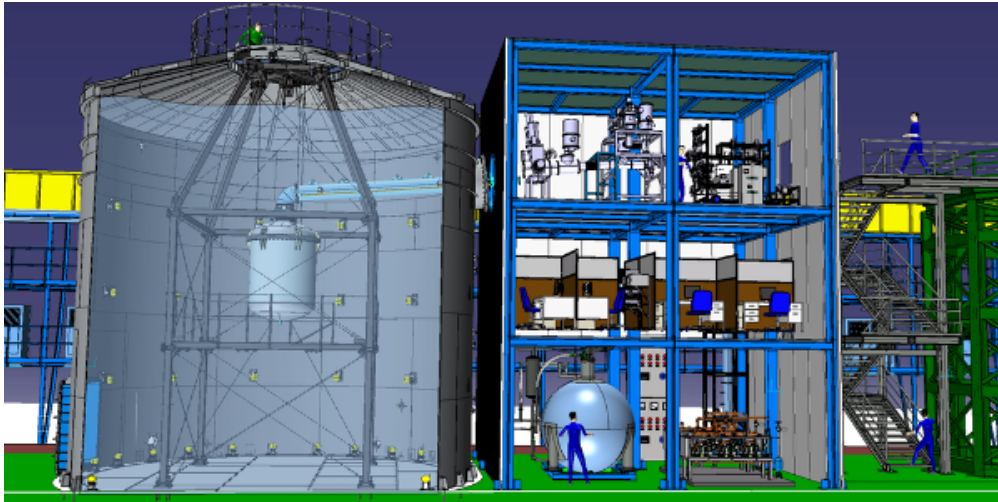
Figure 2.1: Schematic view of the XENON1T detector. Inside the water tank (left) the cryostat and its support structure are placed. A stainless-steel pipe connects the cryostat to the cryogenic system. A 3 floor service building (right) is provided next to the detector which also hosts most detector subsystems, such as the cryogenic and purification plants, DAQ and electronics.

2.2   The Time Projection Chamber

Hosted in a double-walled stainless steel cryostat, with an insulation volume that is pumped to vacuum (below 10^{-5} bar) in order to prevent temperature exchanges between the cold xenon and the water inside the tank, the XENON1T detector is filled with 3.3 tons of liquid xenon. The TPC is mechanically supported by 24 PTFE pillars, connecting a stainless-steel ring on the top with a copper ring on the bottom. Figure 2.3 shows a schematic view of the inner and outer parts of the TPC.

Between each pair of PTFE pillars, interlocking high reflectivity PTFE reflector panels are placed for maximizing the light collection efficiency (LCE) through reflecting the photons. The active volume inside the TPC is geometrically similar to a cylinder, with a height of 96 cm and a diameter of 1.0 m. It contains approximately 2 tons of liquid xenon, serving as the target for WIMP detection.

The TPC is instrumented on its top and bottom with 248 3-inch PMTs, which are fixed to PTFE holders, also to maximize the LCE. Another set of 6 1-inch PMTs are used in the outer part of the TPC (inactive xenon volume) for possible diagnostic uses such as the trigger threshold measurements, or imaging possible electrical discharges from the electrodes.

An electric (drift) field is applied between the cathode ($-$HV), and the gate (0 HV). A higher extraction field is applied across the liquid-gas interface, between the gate and anode ($+$HV). The electrodes are made out of Au-plated stainless steel and allow 90-97 % transparency.

A total number of 74 field shaping rings, made out of Oxygen-free high thermal conductivity copper (OFHC Cu), are placed between the electrodes and around the PTFE plates, connected via two chains of high value ohmic resistors. Each resistor chain has a total resitance of 197.5 GΩ. The resistances are selected based on COMSOL [171] electric field simulations, that were carried

Figure 2.2: Picture of the XENON1T experiment. The water tank on the left is made of a stainless steel cylinder with 10 m height and 10 m diameter. An artistic drawing of the internal parts is attached to the front wall of the tank. The 3 floor service building is located on the right. The xenon storage and recovery tank is visible on the ground floor, while the DAQ system and electronics can be seen on the first floor. The cryogenic and purification systems are placed on the second floor.

out in advance, in order to provide a homogeneous electric field within the TPC active volume. The choice of OFHC Cu is made to minimize the radioactivity of the TPC components, previously measured using ultra-low-background germanium detectors (same as all other components).

The LXe level is measured by 2 long (covering most of the TPC height), and 4 short (covering only the region of the liquid-gas interface) levelmeters. Measurement of the level from different positions around the TPC provides the possibility of the detector tilt estimation.

A diving bell system is placed at the top of the TPC, covering the top PMT array, in order to allow the control of the liquid level via gas flow. The inlet and outlet xenon pipes are placed on the top of the bell.

2.3 The Photomultiplier tubes

The R11410 photomultiplier is a $3''$ diameter tube produced by Hamamatsu [117] for xenon-based dark matter detectors. It operates stable at typical temperature and pressure of a LXe detector, around -100° C and 2 bar, respectively. A major advantage is its high quantum efficiency (QE) at the xenon scintillation wavelength (178 nm). A mean value of 35 % has been achieved for the tubes delivered for XENON1T, and a few tubes have a QE as high as 40 %. Along with 90 % electron collection efficiency [118], these PMTs ensure a high detection efficiency for VUV photons.

The R11410 photomultiplier has a VUV-transparent synthetic silica window, with a low temperature bialkali photocathode deposited on it. A 12 stage dynode chain electron-multiplication system provides an average signal amplification of 3.5×10^6, when operated at -1500 V. The body
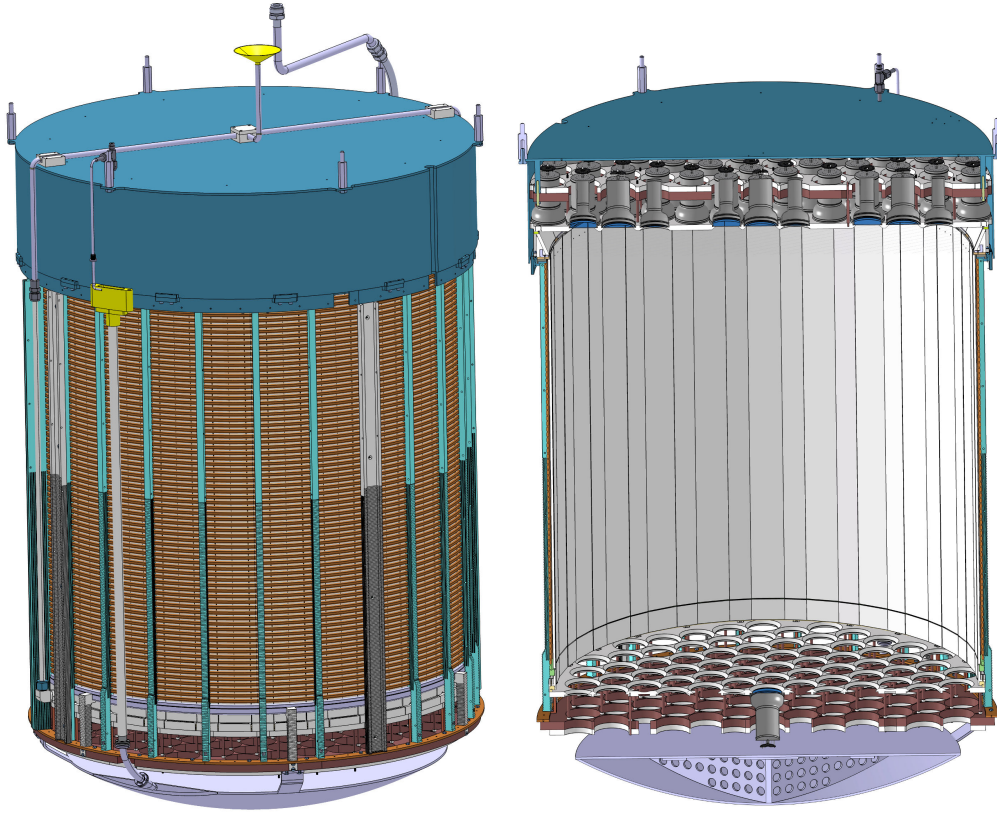
Figure 2.3: A Schematic view of the XENON1T TPC. The external view (left) shows the field shaping copper rings colored in brown. It also shows the PTFE pillars and the diving bell. The internal view (right) illustrates the top and bottom PMT arrays and the interlocking PTFE reflector panels.

of the PMT is 115 mm long, and it is made out of a Kovar alloy with a very low cobalt content. Inside the tube, the dynodes are insulated using L-shaped quartz plates. On the back side of the PMT, the stem uses ceramic material to insulate the connections to the individual dynodes. In figure 2.4, a sketch of the R11410 PMT is shown displaying its main components [119].

In several iterations of test and development collaborative work between the PMT working group of the XENON collaboration, and the Hamamatsu company, the radioactivity of the R11410 PMTs was greatly reduced [119]. This achievement was reached through measurements of the radioactive contamination in the production materials, in different versions and batches, using high-purity germanium detectors [120, 121, 122]. The resulting version of the R11410 PMTs, with lowered radioactivity, is named R1140-21. The screening results show that the activity of several different detected isotopes has been reduced significantly, causing an effective reduction of the total background expected in the XENON1T detector. For instance, the activity of ^{40}K and ^{238}U is reduced by a minimum factor of 4 and the activities of ^{226}Ra, ^{60}Co, and ^{235}U are reduced by a factor ~10, from R11410 version compared to R11410-21 [119]. Figure 2.5 illustrates the MC simulation results from contributions of different detector components to the total ER and NR backgrounds reaching the XENON1T active volume.

Before the PMTs were installed in the XENON1T TPC, their performance and operational
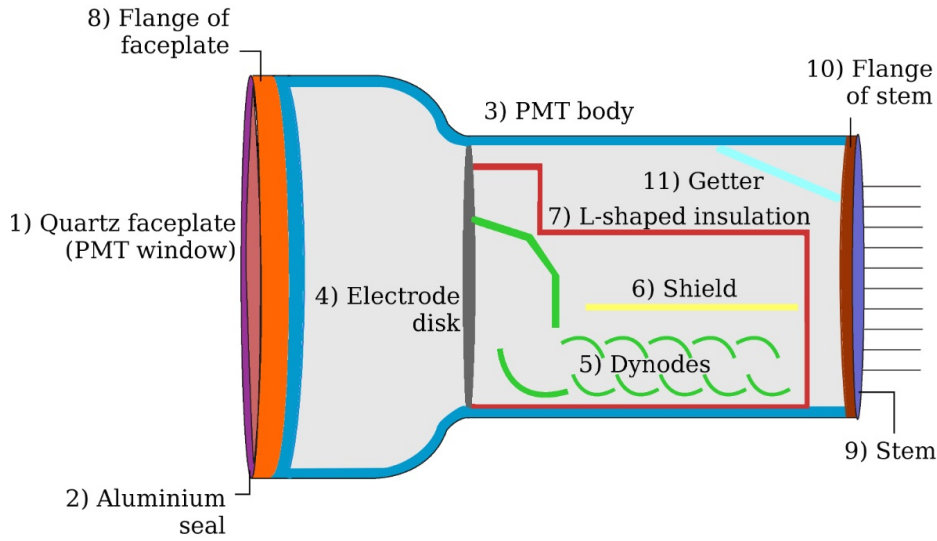
Figure 2.4: A schematic drawing of the R11410 PMT, showing its main components [119].

parameters, such as gain (photoelectron multiplication factor), afterpulse and dark count rates, were studied at room temperature as well as in LXe, using several experimental setups. For instance, the PMTs have been intensively tested to demonstrate their stable behaviour during long-term operation in LXe, and with electric field applied. At -100° C, the R11410 PMTs show a low dark count (DC) rate of ~80 Hz at -1600 V, counting peaks above 1/3 of the averaged SPE height. The corresponding resolution on the SPE peak is 35-40 %, and the peak to valley ratio for SPE spectra was measured to be at minimum 2.0 [123].

Moreover, most PMTs were tested to pass qualification requirements set for the analysis purposes of the XENON1T detector. For example, they require to havet a gain value (defined as the number of electrons read out at the anode in response to a SPE emitted from photocathode) of at least 2×10^6 in the operating voltage range. A total number of 248 tubes are currently operated inside the XENON1T TPC, selected out of 321 tested units [124]. The distribution of the SPE gain values is displayed for all tested and XENON1T selected PMTs in figure 2.6, left. The average measured gain value is larger than 5×10^6 at 1500 V, and the dark count rates are below 100 Hz at -100° C for all PMTs used for XENON1T. A similar study was performed focusing on the dark count rates at low temperature (figure 2.6, right), as well as the stability of the parameters, such as the after-pulse rate and gain during several temperature cycles [124].

Finally, the tested PMTs which met the qualification requirements were installed in the XENON1T TPC, with 127 PMTs placed on the top and 121 PMTs on the bottom arrays. Figure 2.7 shows photographs of both arrays after the installation of PMTs.

2.4 XENON1T detector infrastructure and subsystems

The XENON1T detector consists of several subsystems that are independently designed, tested and commissioned in order to serve the experiment. In this section, the subsystems of the XENON1T detector that are relevant for the topic of the next chapter are briefly described.
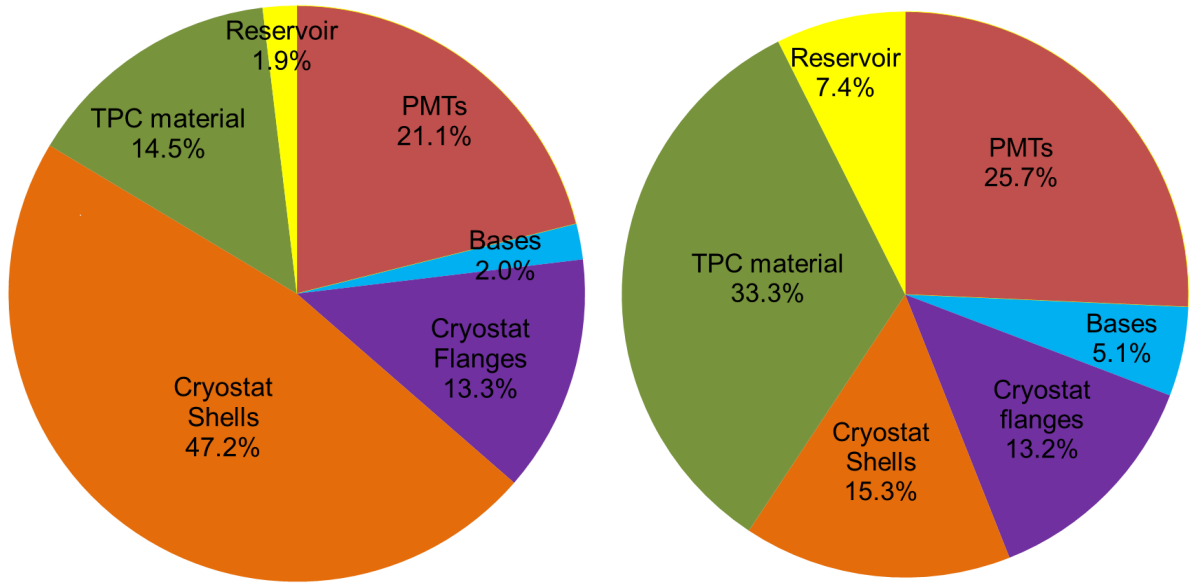
Figure 2.5: Results of the MC simulations of the contributions of different detector material on the total ER (left) and NR (right) background rates of the XENON1T detector, computed in the energy ranges of 1-12 keV and 4-50 keVnr for the electronic and nuclear recoil backgrounds, respectively, in the fiducial volume of 1 ton.

2.4.1   Shielding and muon veto

Next to the design of the detector and the selection of radiopure materials, the shielding against cosmic rays and natural radioactivity is critical to obtain the aimed sensitivity. The XENON1T detector is located in the Hall B of LNGS, where a muon flux of $(3.31 \pm 0.03) \times 10^{-8}\,\mathrm{cm}^{-2}\mathrm{s}^{-2}$ with average energy of 270 GeV has been measured [125, 126, 127].

The XENON1T water tank consists of a $\sim$10 m height and $\sim$10 m diameter cylinder, made out of stainless steel. According to MC simulations, 2 m of water as a passive shield for XENON1T detector can reduce the gamma and neutron backgrounds, produced by rock activity, by factors of 10^4 and 10^9 respectively, making the water tank an effective shield against this source of background. However, this reduction factor is less than 100 for neutrons induced by muon interactions reaching the detector [128] (see figure 2.8). A conservative estimation of the muon-induced neutron flux at LNGS cavern is approximately $7.3 \times 10^{-10}\,\mathrm{cm}^{-2}\mathrm{s}^{-2}$ for neutrons with energies higher than 10 MeV [129]. Such neutrons may constitute a dangerous background since they can cross the water shield and scatter elastically off the target nuclei, leaving a WIMP-like signal. This motivates instrumenting the water tank with PMTs to detect the Cherenkov light produced by muons or particle showers induced by muon interactions, and hence, to make it an active muon veto.

A set of 84 8-inch PMTs, model R5912ASSY from Hamamatsu, are used in the water tank to detect the Cherenkov photons. These PMTs are placed in a configuration which is optimized based on simulations to achieve maximized efficiency for detection of photons from Cherenkov radiation. The quantum efficiency of these PMTs is, in average, about 30 % at the Cherenkov radiation wavelength of water (300-600 nm).

The water tank is covered internally with a reflective foil (DF2000MA by 3M), which has >99 %
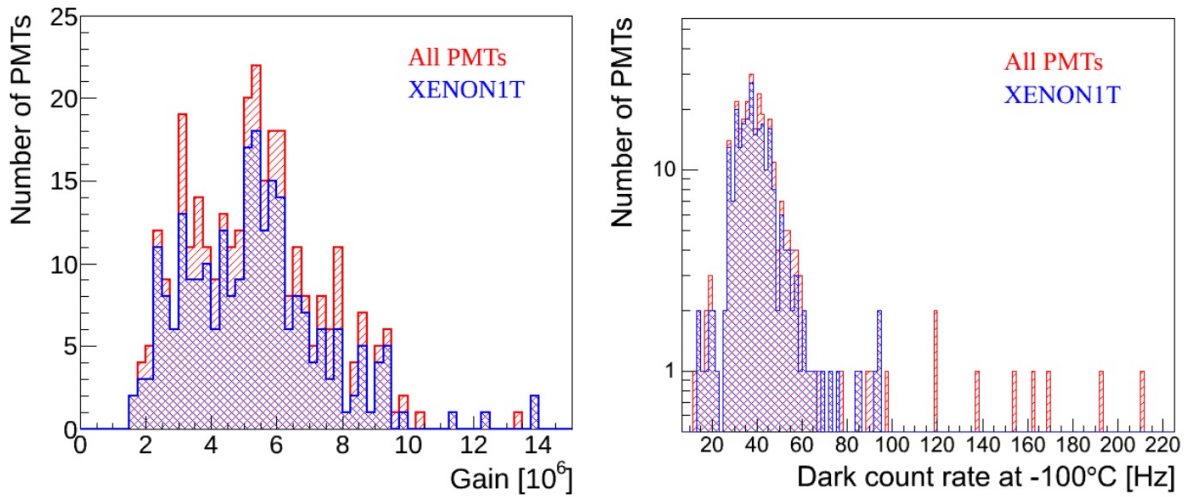
Figure 2.6: Distribution of the gain values at $1500\,\mathrm{V}$ (left) and the dark count rates at an equalized gain of 3×10^6 at -100° C (right) for all tested and XENON1T PMTs [124].

Figure 2.7: Photographs of the bottom (left) and top (right) PMT arrays after the installation of the PMTs. The PMT voltage dividing circuits and the connected signal and high-voltage cables are visible on the top array.

reflectivity for the wavelength 400-1000 nm and has a wavelength shifting property from the UV Cherenkov photons toward the blue wavelength in order to better match with the wavelength sensitivity of the PMTs [130]. Figure 2.9 shows a photograph taken from inside of the empty water tank, where the TPC cryostat and support structure can be seen, as well as the reflective foils covering the walls of the tank, and a few of the 8-inch PMTs.

According to the simulations, the efficiency of the XENON1T muon veto system is determined to be $(99.78 \pm 0.05)\,\%$ and $(71.4 \pm 0.5)\,\%$ for detection of the muons, and shower cascades generated by muons reaching the water tank, respectively. This leads to the residual neutron flux of 1.2×10^{-12} n/(cm²s) at the XENON1T cryostat surface. This is equivalent to less than 1 background event expected from muon-induced neutrons in the 5-50 keVnr recoil range of single scatter events, within the 1 ton fiducial volume after 2 years expusure [128].
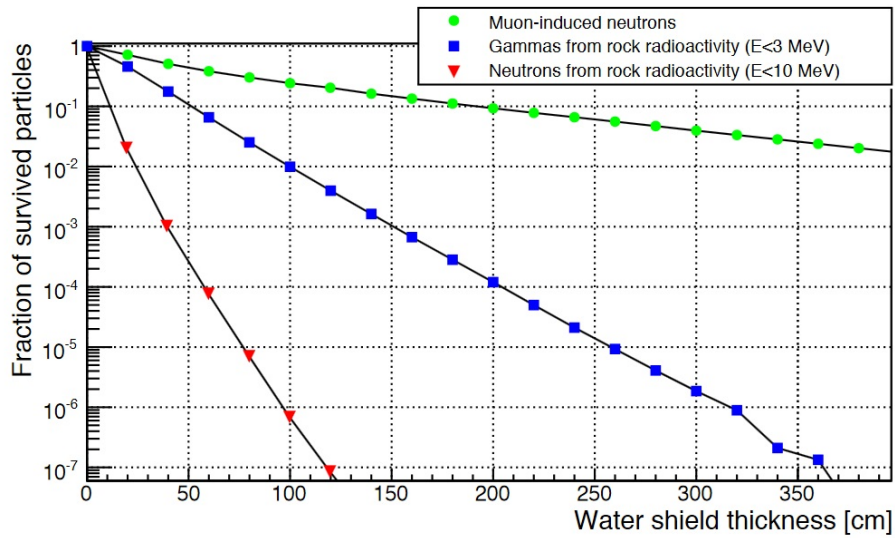
Figure 2.8: Fraction of survived particles as a function of the thickness of the water shield surrounding the detector [128]. Circular markers for the muon-induced neutrons, squared markers for the gammas from rock radioactivity and triangular markers for neutrons from rock radioactivity.

2.4.2   Cryogenics and Purification systems

In figure 2.10, a schematic drawing of the XENON1T gas system is shown together with a picture of the ReStox. The ReStox contains a stainless steel sphere of 2.1 m outer diameter, which is rated to withstand 72 bars of pressure [131], and hence can host 7.6 tons of xenon in both gas and liquid forms. In addition, the system is instrumented with an external gas filling station, from which xenon can be injected into the system, from externally connected xenon gas bottles. In case of emergency, the system is capable of recovering all xenon within a few hours.

The xenon purification system uses several high-flow heated getter pumps, enhanced with a re-circulation power of up to 100 SLPM (standard liters per minute), while an actual flow of 114 SLPM was reached in the test setup [132]. This recirculation rate corresponds to about 800 kg/day, required to presume a reasonable commissioning period of the detector, with good performance in terms of charge and light yields. The dynamics of gaseous xenon at this speed causes large pressure gradients and requires components that can handle such flow, including tubing, recirculation pump, getter and flow controller. Since the recirculation and purification are done in the gas phase, the Xe gas must be continually re-liquefied, requiring large amounts of available cooling power. To cool down xenon gas at a rate of 1 SLPM from room temperature to 175 °K, less than 2 W of power are used, out of a total of about 10.6 W that are needed to liquefy and cool at the same rate [132]. This is achieved using a set of heat exchangers between the warm and cold xenon, from inlet and outlet pipes to the detector. The heat exchange efficiency in the actual XENON1T setup is measured to reach 94 %.

In figure 2.11, the schematics of the cryogenic system can be seen. Three independent cooling sites are inline with the rest of the gas system including 2 pulse tube refrigerators (PTRs) and a liquid nitrogen tower, while at least 1 out of the 3 sites provides redundant cooling power for
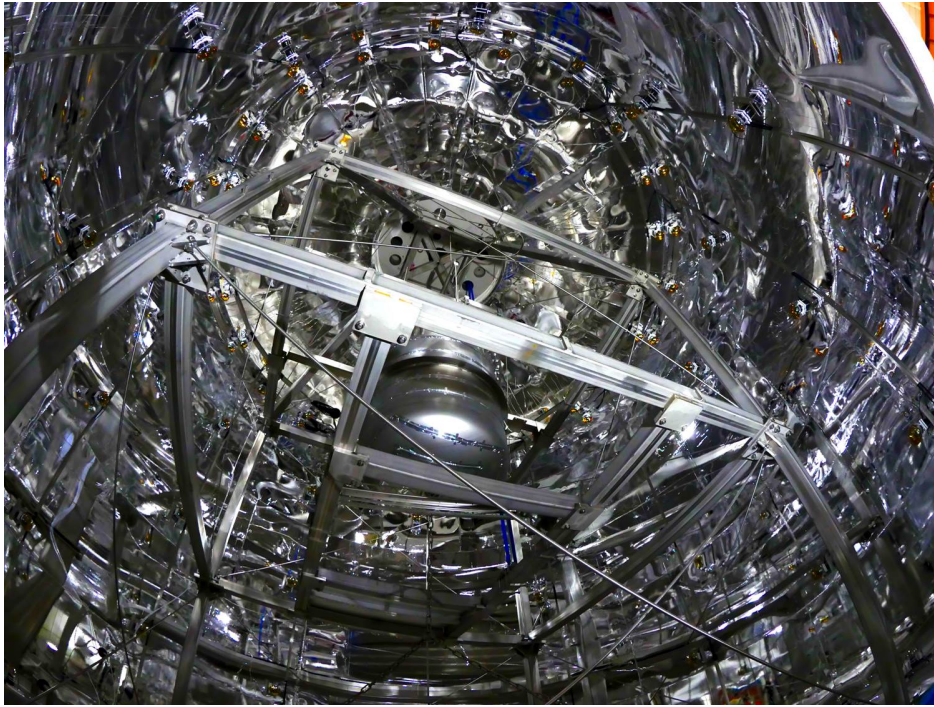
Figure 2.9: Photograph of the XENON1T water tank taken from inside before water filling. The TPC cryostat is seen in the middle with its support structure. The walls are covered with a reflective foil. The TPC support structure is viewed from the bottom and the cryostat can be seen in the center.

the case of emergency. The xenon gas flows to the cryogenic system through a vacuum insulated pipe, which hosts also "umbilical" pipe with all the cables (readout, HV, etc) and optical fibers. The schematics view of the cryogenic system is shown in figure 2.11. All cables and fibers are then connected to corresponding vacuum feed-throughs installed on a cylindrical vessel, which is called "porcupine".

A photograph of the krypton distillation column is shown in figure 2.11. Even though xenon itself has no long-lived radioactive isotopes (except for ^{136}Xe), natural xenon gas has typically (1-1000) ppb dissolved krypton atoms, which can produce intrinsic electromagnetic background through decays of its radioactive isotope, ^{85}Kr. For the XENON1T detector, to reach its goal sensitivity for WIMP searches, the krypton contamination must be reduced below 0.2 ppt, requiring purification of xenon from krypton by a factor of 10^4. The Kr distillation column has successfully been tested to accomplish this mission with over-qualifying separation factor of 1.2×10^5 [133].

2.4.3 Slow control and emergency

Safe and secure operation of a large scale experiment such as XENON1T is essential to achieve its scientific goals. Hence, all the operating parameters of the detector have to be continuously monitored and recorded. In addition, the traced parameters should be accessible remotely to the entire relevant responsible crew. The slow control system not only provides online monitoring of all parameters and access to the values at any certain time (history), but also makes possible
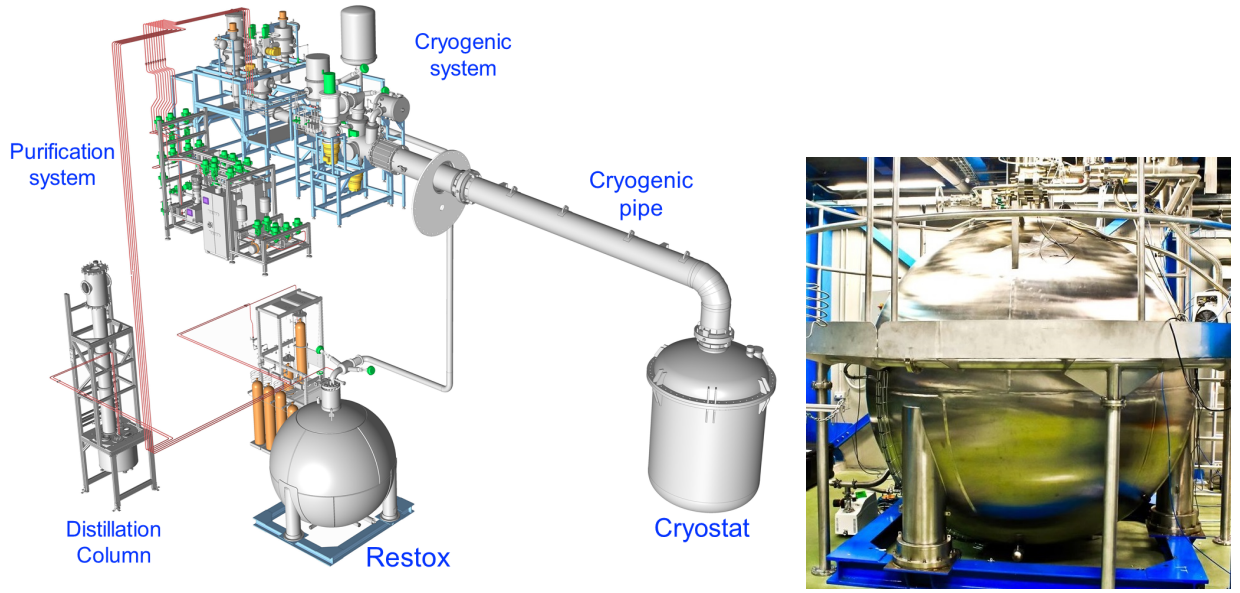
Figure 2.10: Schematics of the XENON1T gas system (left), and a photograph of xenon storage and recovery system, ReStox (right).

remote control of several parameters, through a web-based control software which is accessible to collaboration members, with several levels of authorized credentials.

The slow control system of the XENON1T experiment uses a local control station with an industrial Programmable Automation Controller (PAC), and its input/output (I/O) modules. The system is based on the General Electric (GE) [134] industry SCADA (Supervisory Control And Data Acquisition).

An example of remote access to the monitored and controlled parameters is shown in figure 2.12. The control panel for the cryogenic system is shown with several pressure, flow and temperature sensors displayed on a schematic view of the system. Similar panel is configured on a touch-screen inside the XENON1T control room, for quick and easy access of the shifters to the critical parameters.

Continuous visualization of the critical parameters (such as internal pressures, temperatures, etc.) is not necessarily required (neither practical), to guarantee a secure operation. Instead, alarm sending systems are configured, with adjustable limits on various parameters, to be sent to the responsible group in case of an emergency. Such an alarm system is also developed and integrated to the slow control. The alarm system includes dedicated platforms to send emails to the responsible crew on-site, which is on shift duty, and also to the list of experts for each subsystem.

2.4.4   Calibration systems

Various calibrations of the detector are performed for the XENON1T experiment using different sources. For instance, external γ sources are used to monitor the detector response to electronic recoils (ERs), verify the performance of the position reconstruction algorithm, and to investigate the purity of the target LXe through measurements of the electron lifetime. Two vertical belts ("I-belts", marked in blue in figure 2.13) are used, together with an additional belt, connecting two
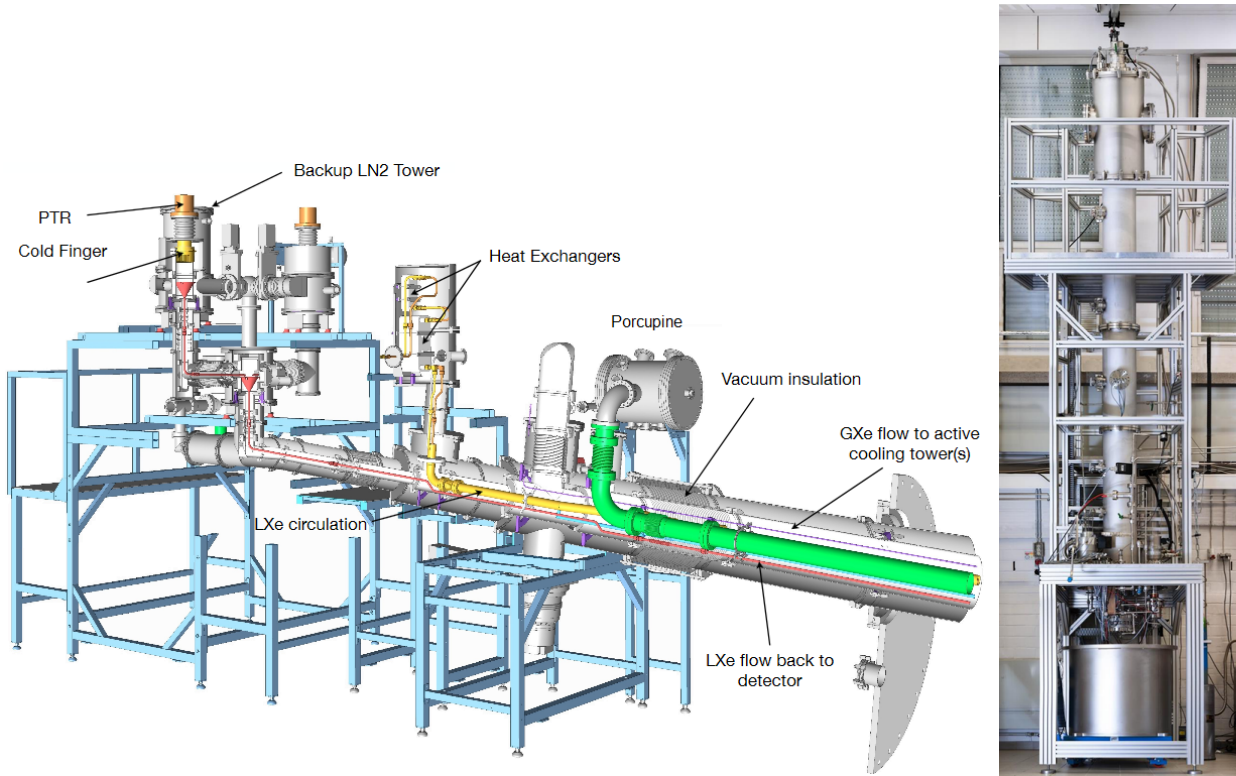
Figure 2.11: Schematics of the XENON1T cryogenic system (left), and a photograph of the krypton distillation column (right). The gas pipe is shown in yellow while the cryogenic pipe is colored green.

identical vertical belts from beneath the cryostat ("U-belt", shown in red in figure 2.13), to move the external sources placed inside collimators. The collimators are stored inside a flange above the water level, when the calibration run finishes. In particular ^{60}Co, ^{137}Cs, and ^{228}Th are used as external ER calibration sources for XENON1T.

As the mean free path for γ rays in liquid xenon is short (of the order of 1-10 cm [135]), compared to the size of the XENON1T detector, the use of external calibration sources yields a distribution of events mostly clustered close to the position of the source. Therefore, XENON1T uses also internal sources through dissolving radioactive isotopes into xenon gas itself. For example, short-lived ^{83}Rb ($\mathrm{T}_{1/2} = 86.2$ days [136]) source can be placed inside an emanation volume, instrumented within the detector gas system, which produces ^{83m}Kr isotope ($\mathrm{T}_{1/2} = 1.8$ h, see section 4.7.1). The ^{83m}Kr atoms are dissolved into xenon gas, resulting in a homogeneous distribution of ^{83m}Kr decays through the active volume after several hours of recirculation. The 9.4 keV and 32.1 keV electronic recoils from decays of the ^{83m}Kr source, can be used for low energy ER calibration of the whole volume [137]. Other sources include previously studied tritiated methane [138] (CH_3T), and ^{220}Rn ($\mathrm{T}_{1/2} = 56$ s through emanation from electrodeposited ^{228}Th [139]), which are also to be used for calibration of the XENON1T detector. Although, the long-lived isotopes need to be removed from xenon via recirculation through the heated getters at an efficient rate.

The XENON1T detector is instrumented with a platform to move a D-D neutron generator (NSD Gradel Fusion NSD-35-DD-C-W-S) around the detector for NR calibrations using mono-
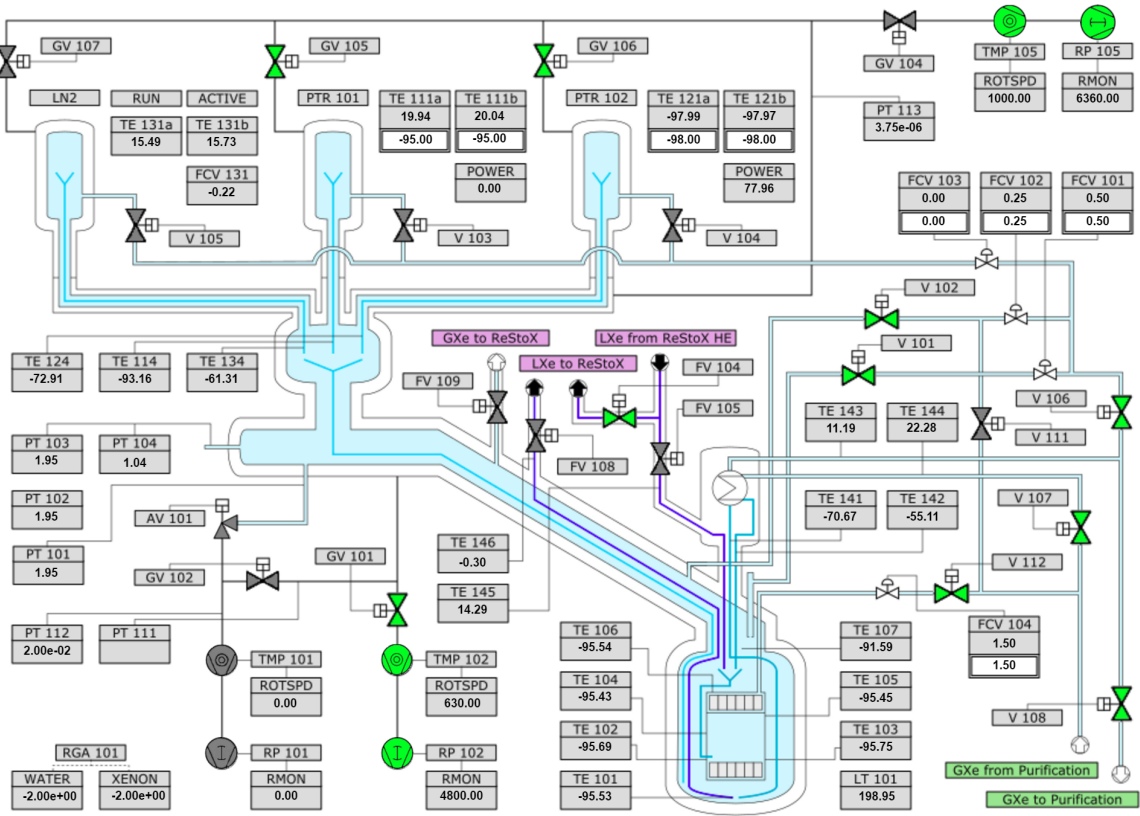
Figure 2.12: The control and monitoring panel for the cryogenic system of the XENON1T experiment. The 3 light blue volumes on the top refer to the liquid nitrogen emergency (left) and the two PTR cooling systems (middle and right), all connected through the cryogenic pipe to the TPC (bottom). The signs starting with P, F, and T on the gray boxes refer pressure, flow and temperature sensors placed at several positions.

energetic 2.45 MeV neutrons. The generator was tested at low operating voltages to achieve very low total emission rates around 10 n/s, under stable conditions, as required to reduce pile-up event rates, and also to prevent activation of the detector materials through neutron capture or inelastic scattering.

Finally, it is also required to provide a setup for regular calibration of the PMTs. For this reason a dedicated system was developed in order to guide the light from external sources towards the TPC to induce a photoelectron signal in the PMTs and calibrate their response. As this is one of the major topics of this PhD work, the system is described in detail in chapter 3.

2.4.5   Data acquisition system (DAQ)

The XENON1T DAQ system uses off-the-shelf electronics including CAEN [140] digitizers with customized firmware. Amplifier modules, model 176 with ×10 gain from Philips [141], are used inline with the signal cables, before reaching the digitizer modules.

An important upgrade of the XENON1T DAQ system compared to the previous experiment,
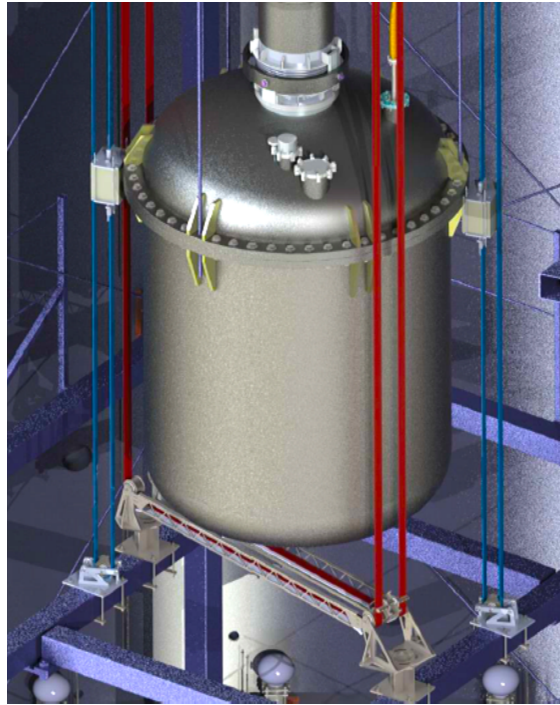
Figure 2.13: Drawing of the external calibration belts of the XENON1T experiment. The TPC cryostat and (gray) and some sections of the support structure (blue) are shown. The red belt, called U belt, can move the calibration sources around and to the bottom of the cryostat, while the other two blue belts, called I belts, can move the source in two other positions only vertically on two positions.

XENON100, is that a software trigger is used, allowing for flexible trigger algorithms to be applied independently on each readout channel. The commissioning of the system has shown the possibility of a trigger threshold at 1/3 of photo-electron on individual readout channels.

Software trigger uses a MongoDB cluster to sort and select events, at high speed data-buffering. This allows the so-called "Event Builder" software for fast trigger queries at high rates of $\sim$300 MB/s of acquisition (1 kHz event rate), expected for calibration runs. A total number of 6 "reader" computers are used to readout 32 analog-to-digital converters (ADCs) in parallel. In addition, a high-energy veto module (Skutek DDC10) is used to tag and reject high energy events online. Finally, a web frontend software for system control and online data monitoring is provided, based on Django [142] framework.

2.4.6 Raw data processor

Once the data are acquired through the DAQ system, the digitized output of each readout channel (in total 254) is recorded in the format of continuous waveform with zero-length encoded baseline, usually referred as "raw data". A software algorithm, called "Event Builder", later scans through the raw data, looking for "triggered" pulses, which is referred to places where the waveform of any readout channel exceeds a certain threshold, defined based on the gain of the PMT, used on the corresponding channel, and the noise level. This threshold is set at a very low amplitude

($\sim 1/3\,$PE), such that no useful information can be lost at this early stage. In the XENON1T terminology, such selected window of a waveform, exceeding the event builder threshold, is called a "pulse".

The triggered data contains information in raw format (waveform traces), while it is reduced to the regions where a pulse is found, in addition to several digitized samples before and after it. At this point, the raw data processor software (named PAX, standing for the Processing and Analysis for XENON1T) is used to extract useful physical information from the observed pulses.
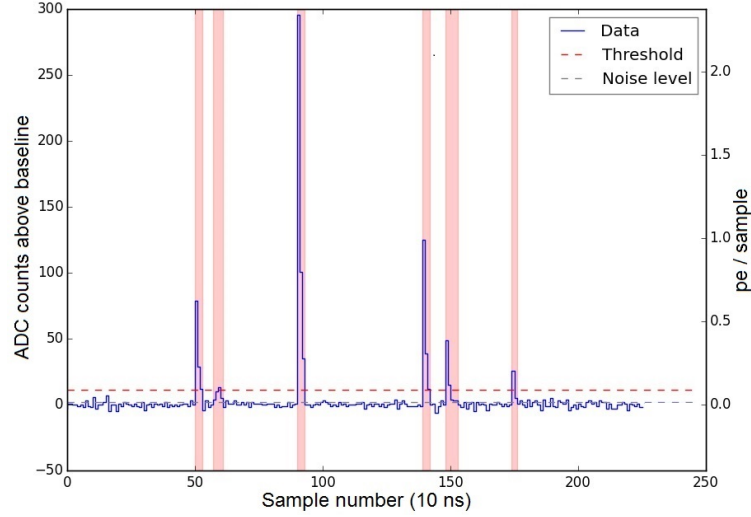
Figure 2.14: Raw digitized waveform of a single readout channel from the output of the XENON1T raw data processor (PAX). The pink regions illustrate places where the hitfinder algorithm has found a signal candidate. The dashed red and grey lines show the corresponding hitfinding, and noise level thresholds, defined for this specific trace.

At the first stage of the raw data processor, a "hitfinder" algorithm is applied, in order to identify and mark "hits". The name hit refers to another object, from a single channel waveform, selected similar to a pulse, whereas a more complex algorithm is used for its selection, rather than just a single threshold. The algorithm is developed based on calibration and simulated data, while its acceptance is well studied. Moreover, the algorithm can be modified for different analysis purposes, when a raw dataset can be reprocessed with the modified hitfinding algorithm. A hit usually contains a number of photo-electrons detected by a PMT, or possibly a noise burst. In figure 2.14, an example waveform of a single channel is shown from PAX output, while the selected hits are marked.

When the hits are identified for each channel, a clustering algorithm is used to build "peaks", another object in PAX terminology. A peak is identified when a certain number of PMTs (typically a minimum of 2-3) have a registered hit in their trace within a time window which is dependent on the size of the hits. The algorithm to select peaks is developed through a dedicated analysis which can be modified based on each channel's performance, or different purposes for various analysis (e.g. calibrations, WIMP search, etc.). Once a peak is found, its properties that contain physical information are calculated, for instance area, width, height, top array fraction.

Based on the peak properties, the peaks are classified in the next step. At this stage, S1s and S2 signals are distinguished from noise bursts. The classification algorithm is also developed based on

calibration data, with quantified uncertainties. After this stage, the S1 and S2 pairs are gathered together, creating a new object, named an "event". The properties of an event, such as drift time, and (x,y) position are calculated. Later, corrections on S1 and S2 signals, based on the electric field map and drift time, are applied. These are required as the light and charge collection efficiency parameters are not identical for all events, depending on their positions. In figure 2.15, an example event is displayed from the PAX visualization output. The identified S1 and S2 signals are zoomed at and displayed in a separate panel. In addition, the hit patterns on the top and bottom arrays are shown.
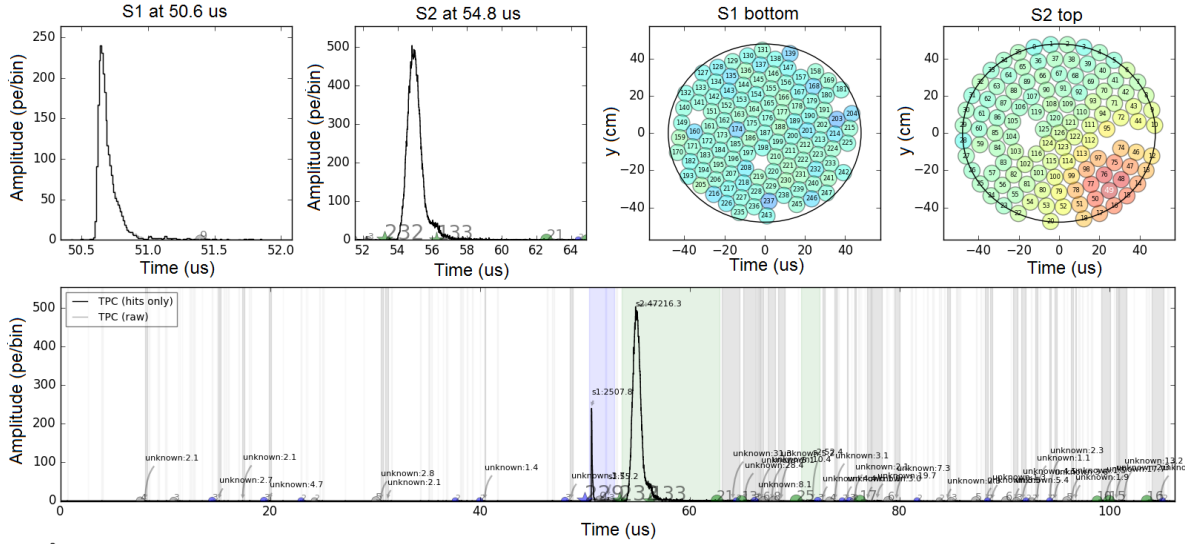
Figure 2.15: An example event from PAX output showing the raw summed waveform (bottom) together with the identified S1 and S2 (top left) pulses and top and bottom array hit patterns (top right). The colors on the PMT maps represent the relative size of the observed S2 signal.

Finally, the processed data is stored in either ROOT [143], or HDF5 (Hierarchical Data Format [144]) formats, containing all the information, as mentioned above. The processed data is later copied to the analysis computer clusters, making it accessible to the analysis task groups.

2.5   Physics reach of the experiment

In order to estimate the sensitivity of XENON1T experiment, the Profile Likelihood Ratio method is used, in the same way as the XENON100 exclusion limits were calculated [85, 145].

The observables for the analysis are the prompt scintillation signals (S1), and an idealized discrimination variable, Y that is proportional to the S2/S1 ratio. Uncertainties on the $\mathcal{L}_{eff}$ and Q_y (noted with $t_{\mathcal{L}}$ and t_Q) are taken as nuisance parameters, as well as uncertainties on the ER and NR background estimations (t_{ER} and t_{NR}), which are conservatively assumed to be 10 % and 20 %, respectively. Hence, the following equation is used as the generic definition of an un-binned, extended likelihood function for WIMP detection considering WIMP-nucleon spin-independent cross section σ [88]:

$$-2 \times L(\sigma; t_{\mathcal{L}}, t_Q, t_{ER}, t_{NR}) = 2 \times [\mu_s(\sigma; t_{\mathcal{L}}, t_Q) + \mu_{bER}(t_{ER}) + \mu_{bNR}(t_{\mathcal{L}}, t_Q, t_{NR})] -$$

$$2 \sum_{n=1}^{n_{obs}} ln\{(\mu_s(\sigma; t_{\mathcal{L}}, t_Q) \times f_s(S1_i) \times g_s(Y_i)) +$$

$$(\mu_{bER}(t_{ER}) \times f_{bER}(S1_i) \times g_{bER}(Y_i)) +$$

$$(\mu_{bNR}(t_{\mathcal{L}}, t_Q, t_{NR}) \times f_{NER}(S1_i) \times g_{NER}(Y_i))\} +$$

$$(t_{\mathcal{L}} - t_{\mathcal{L}}^0)^2 + (t_Q - t_Q^0)^2 + (t_{ER} - t_{ER}^0)^2 + (t_{Nr} - t_{NR}^0)^2$$

$$(2.1)$$

where μ denotes the expected value of a parameter, and n_{obs} is the total number of observed events within the WIMP search window, f and g are the probability distributions of the observables S1, and Y, and finally t and t^0 describe the Gaussian constraint on the nuisance parameters, and their expected values respectively.

The test statistic, q_σ, is defined as following, in order to achieve an exclusion limit:

$$q_\sigma = \begin{cases} -2ln\frac{L(\sigma; \hat{\hat{t}}_j)}{L(\sigma; \hat{t}_j)} & \text{if } \sigma \geq \hat{\sigma} \\ 0 & \text{if } \sigma < \hat{\sigma} \end{cases}, \qquad (2.2)$$

where the hat sign represents the "Maximum Likelihood estimator" (MLE), while double-hat sign shows the conditional MLE, obtained for the nuisance parameters at the fixed value of σ under test.

Monte Carlo simulations are used to obtain the test statistics for background only and signal hypothesis for all cross sections which are considered. Finally, the 90 % CL is used to set the exclusion limit.

Having the formalism clarified, a robust estimation of the background rate at the WIMP-search window is required, before a sensitivity can be obtained. The detector is modeled in GEANT4, and the screening results of all materials are used as an input for the Monte Carlo simulations. Figure 2.16 shows the energy spectra of the simulated ER background. The intrinsic background isotopes include ^{222}Rn, emanated from detector materials into the xenon gas, the fraction of the ^{85}Kr contamination that survives the distillation process, and the double-beta decay of the dominant long-lived isotope of xenon itself, ^{136}Xe. Neutrino-electron scattering from solar neutrinos also contribute to the ER background rate of the experiment as well as the radioactivity from detector components. As illustrated in figure 2.16, the ER background from the detector components is not distributed uniformly. Instead, most interactions occur at the edges of the volume, due to small mean free path of gammas in xenon. The contribution from the detector materials can be reduced through fiducialization of the detector, due to the strong self-shielding of xenon for gamma-rays.

Similar method estimates the NR background rate from the dominant sources, i.e. the radiogenic neutrons from detector components, the neutrons induced by muon interactions with detector hardware, or the rock surrounding the laboratory, and the neutrino-nucleus elastic scattering. In figure 2.17, the energy spectra of these background rates are shown, together with the spatial distribution of the simulated interactions for the radiogenic neutrons. As the mean free path of neutrons is larger than gamma particles, the fiducialization is not as efficient for NR interactions.

The ER background can be discriminated from the WIMP-like NR signal. In XENON100, a 99.75 % ER rejection could be achieved at 40 % NR acceptance [84]. The same rejection can be conservatively assumed for the XENON1T detector.

Once the background rates are calculated, the sensitivity of the detector to different WIMP masses and cross sections can be obtained, following the statistical calculations explained above.
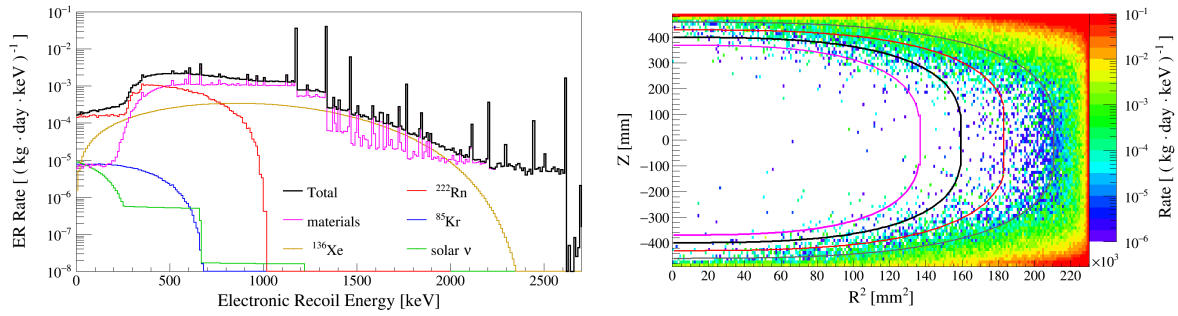
Figure 2.16: (Left); energy spectrum of the total ER background rate in the 1 ton fiducial volume. (Right); the separate contributions , and the spatial distribution of the ER background events from the detector materials inside the active LXe volume, in the (1,12) keV energy range. The purple, black, red, and brown lines represent 800, 1000, 1250, and 1530 kg super-ellipsoid fiducial volumes, respectively [88].
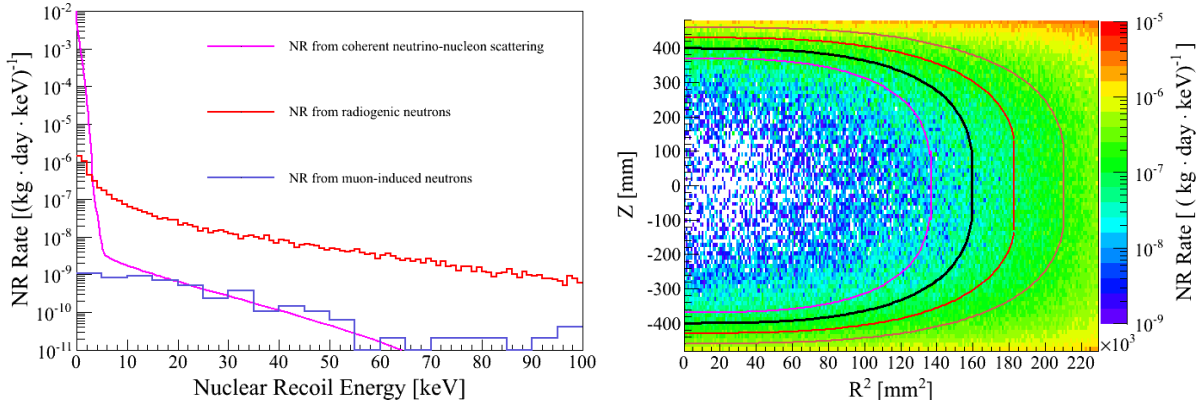
Figure 2.17: (Left); energy spectrum of the total NR background rate in the 1 ton fiducial volume, and the separate contributions. (Right); the spatial distribution of the NR background events from the detector materials inside the active LXe volume, in the (4,50) keV energy range. The purple, black, red, and brown lines represent 800, 1000, 1250, and 1530 kg super-ellipsoid fiducial volumes, respectively [88].

Figure 2.18 shows the spectra of the total background rates after discrimination, and several examples of WIMP recoil spectra for different mass and cross-section. The S1 signal range of 3-70 PE is used for the sensitivity calculations. The lower bound corresponds to XENON100 S1 threshold while the higher one marks the region where the ER background is higher than the signal rate of a 100 GeV WIMP by an order of magnitude.

The defined 3-70 PE range in S1 signal is equivalent to 4-50 keV nuclear recoil and 1-12 keV electronic recoil energy ranges. A total rate of (720 ± 60) and (0.62 ± 0.12) events /t/yr is estimated for the XENON1T experiment ER and NR backgrounds in the XENON1T experiment, respectively, within this range. After the 99.75 % discrimination is applied, these numbers are deducted to 1.62 ER/ty and 0.46 NR/ty respectively. Therefore, about 4 background events are expected after a
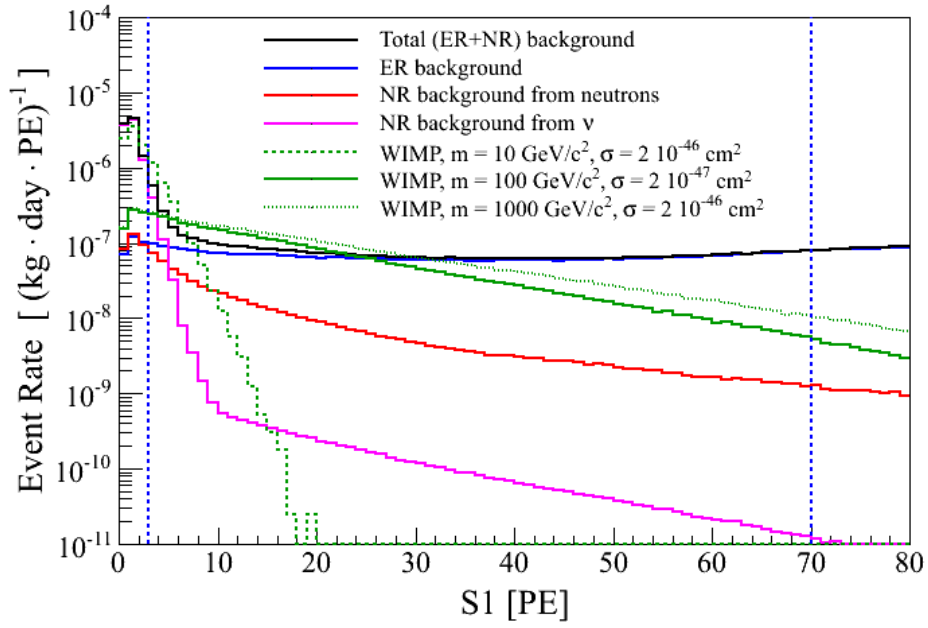
Figure 2.18: Spectra of the total background (black) and of its components together with NR spectra for three examples of WIMP signals (green) [88]. The blue curve shows the ER background spectrum while the red and magenta refer to NR backgrounds from neutrons and coherent solar neutrino scattering, respectively.

2 year exposure of a 1 ton fiducial volume for XENON1T experiment. The light collection efficiency and the resulting light yield of $7.7\,\mathrm{PE/keV}$ at zero field were also estimated using simulations of the detector geometry. These results can be projected into a exclusion limit to spin-independent WIMP-nucleon cross section shown in figure 2.19 for various WIMP masses and cross sections.

   Therefore, a minimum sensitivity of $1.6 \times 10^{-47}\,\mathrm{cm}^2$ for WIMP mass of $50\,\mathrm{GeV}$ is projected for the XENON1T experiment, which makes it the most sensitive currently running experiment aiming for direct dark matter detection.
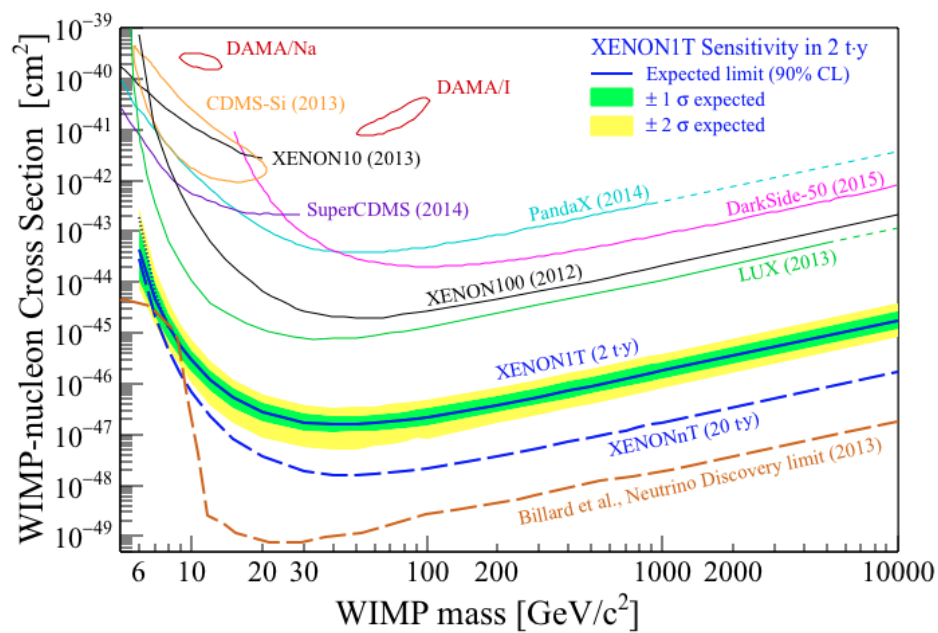
Figure 2.19: XENON1T sensitivity (90 % C.L.) to spin-independent WIMP-nucleon inter-
actions. The solid blue line represents the median value, while the $1\,\sigma$ and $2\,\sigma$ sensitivity
bands are indicated in green and yellow, respectively [88].

Chapter 3

XENON1T PMT calibration system

Using PMTs to detect xenon scintillation photons, one needs to calibrate their response prior to any further analysis. By PMT response, we refer to the number of photoelectrons that are detected by the tube in response to a deposited energy. The PMTs can be exposed to a controllable light source, which is tuned to very low light intensity, allowing for their response to single photoelectrons to be investigated. Using this knowledge it is possible to convert any signal into units of photoelectrons (PE) by dividing the total signal area by that of a single PE.

Moreover, regular calibration of all the PMTs is essential in order to keep track of the stability of their operational parameters. For example, the gain of a PMT can vary either smoothly, through aging of the device, or suddenly, through an incident. If such a change is not realized and accounted for within a short period, it can cause false interpretation of the acquired data in that period, or it similarly affects other previously optimized factors, such as the trigger settings that depend on PMT gains. Hence, monitoring the PMT gains is necessary even if the detector conditions are stable.

In addition, other parameters such as the afterpulse rate of a PMT have proven to change rapidly when a PMT is about to become faulty (due to degradation of its vacuum insulation for instance). Therefore, if all the parameters regarding PMT response are traced regularly, some incidents or false interpretation of an observed effect in the data can be avoided. Part of my PhD work includes design, development, installation and operation of the PMT calibration system of the XENON1T detector, including work on both hardware and software.

3.1   Technical design

The design of the XENON1T PMT calibration system was initiated from a similar system which was operated successfully in XENON100 over its lifetime (2007-2014) [146]. Both detectors share important factors that are crucial for the development of such calibration system. For example, both detectors are dual-phase TPCs equipped with PMT arrays on the top and bottom, and hence the optical boundary conditions are similar. In addition, the operational parameters, such as temperature and pressure are nearly identical in both systems. Therefore, the same or a similar type of optical light guides could be chosen for the new setup. However, some other factors, such as the fiber lengths, number of connecting joints, and number of light channels had to be adapted, according to the new geometry, and larger dimensions of the XENON1T detector, as compared to XENON100.

Moreover, the configuration of the fiber positions inside the TPC was optimized, based on optical simulations of the XENON1T TPC, to achieve the most homogeneous distribution of light intensity, to which the top and bottom PMTs are exposed. Other modifications, such as the LED placement, were considered based on the observed weaknesses of the previous setup. The schematic view of the system is shown in figure 3.1, and a list of all components can be found in table 3.1.
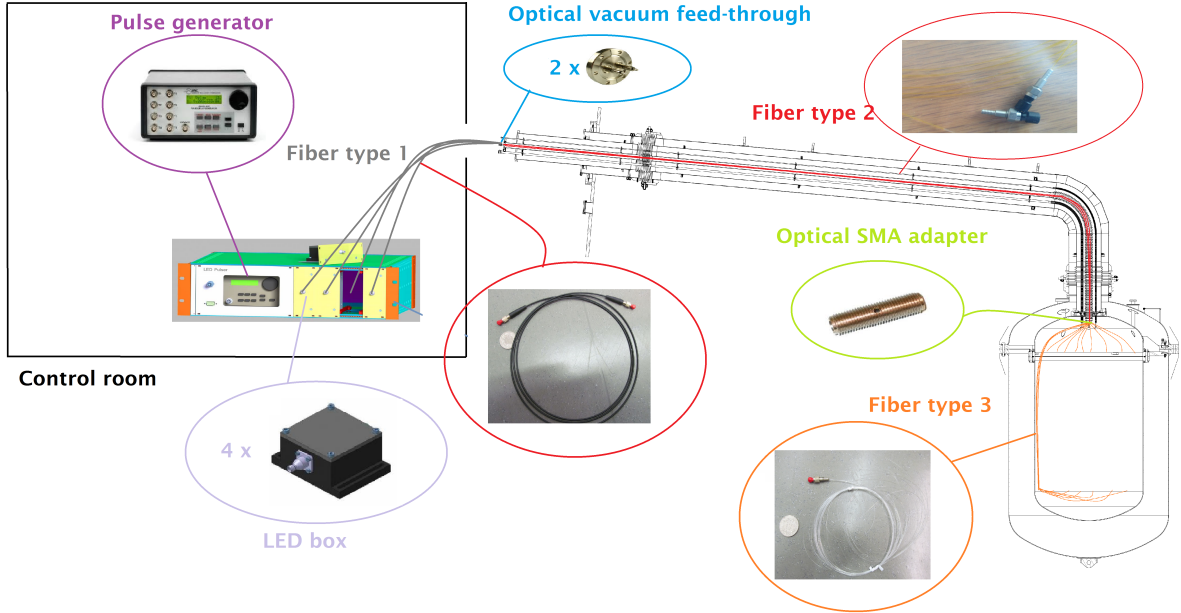
Figure 3.1: Schematics of the PMT calibration system of the XENON1T detector. The LEDs are individually placed inside black-boxes. The LED boxes and the pulse generator are placed together in a frame inside the control room. Three types of fibers are used to guide the light from the LEDs toward the PMT arrays, chosen according to operational conditions (explained in the text). SMA optical feed-throughs and connectors are used to attach the optical fibers at several positions.

An electronic pulse generator (Berkeley Nucleonics Corp. (BNC) model 505-4c [148]) is used to send synchronized pulses to LEDs (see figure 3.4). The pulse generator is configurable to be controlled either manually from its front panel, or remotely through an RS-232 communication port. A set of 4 output channels are available, each being connected to an individual LED box with a short BNC cable attached to a BNC connector on the rear side of the LED boxes. The device has an internal clock to sync all channels, however an external trigger is used in order to synchronize the light emission from LEDs with the acquisition trigger through the DAQ. Both the external input and the RS-232 ports are routed to the front panel of the LED frame for better accessibility.

A set of 4 InGaN light emitting diodes (LEDs, from Farnell Element 14 [147]) are used to emit low-intensity blue light (405 nm). The LEDs are individually installed inside a customized light-tight black box (see figure 3.2). Finally, each LED box is mechanically fixed onto an aluminum

Component	Supplier	model	Quantity (installed)
Pulse generator	Berkeley Nucleonics Corp. (BNC) [148]	505-4c	1
LED	Farnell Element 14 [147]	KINGBRIGHT L-813PBC-Z, Blue	4
Fiber type 1	Ratioplast-OptoElectronics GmbH [149]	POF1/2,2mm PE-M	4
Fiber type 2	Fiberguide industries [150]	SFS400/440/590/880Z	4
Fiber type 3	Ratioplast-OptoElectronics GmbH [149]	POF $7\times250\,\mu$m PMMA	4
SMA adapter	MDC Vacuum [151]	ADVS 1513400 -UHV	12
SMA feed-through	MDC Vacuum [151]	ZFFT-UV600-2-C40	2

Table 3.1: List of the components used for the PMT calibration system of the XENON1T experiment.

frame, that is used to place all 4 boxes inside a single frame together with a pulse generator. The frame is designed such that it can be installed inside an electronics rack in XENON1T DAQ room. A picture of the LED frame is shown in figure 3.3 together with a graphical representation of its individual parts.

A polymethyl methacrylate (PMMA) fiber (from Ratioplast-OptoElectronics GmbH [149]) is attached to each LED in order to guide the light to the vacuum feed-through. These fibers, denoted as "fiber type 1" in the setup, have 1.0 mm PMMA core, coated with 1.2 mm thick black plastic, that optically isolates the fibers from ambient light. In order to reach the feed-throughs on the second floor of the XENON1T control room from the DAQ room on the first floor, these fibers are 7 m long and have SMA connectors on both sides (see figure 3.5).

A set of 2 optical SMA feed-throughs from MDC Vacuum [151], are used to feed the light from plastic fiber ends to the vacuum side of the cryogenic system (see figure 3.6). Each flange has two SMA connectors allowing the connection of all four light channels. The feed-throughs are installed together with all other electrical feed-throughs in the "porcupine" section of the cryogenic system, as shown schematically in figure 2.11 in section 2.4.2.

The cryogenic system and the cryogenic pipe were both baked at 120 °C after closure while being vacuum-pumped in order for their surface-trapped molecules to be released through emanation, before getting exposed to xenon. During the operation of the detector, these sections are exposed to the cold xenon gas at ~ -70 °C. This large temperature gradient, that the components installed in this system will have to sustain, makes the number of qualified choices for optical fibers in this section very limited. The 660 μm silica fibers with 110 μm polyimide coating (from Fiberguide industries [150]) have an operating range of -190 to 350 °C, and were the only option found on the market, meeting such requirements (see figure 3.5). These fibers (fiber type 2) are known to be extremely fragile and inflexible. Hence, they are normally hosted in the stainless steel tubing for secure installation. As the cryogenic system is directly connected to the detector, any material in the system will produce background through emanation, hence we need to minimize the total amount of used material. Therefore, it was decided to use 7 m naked silica fibers through the
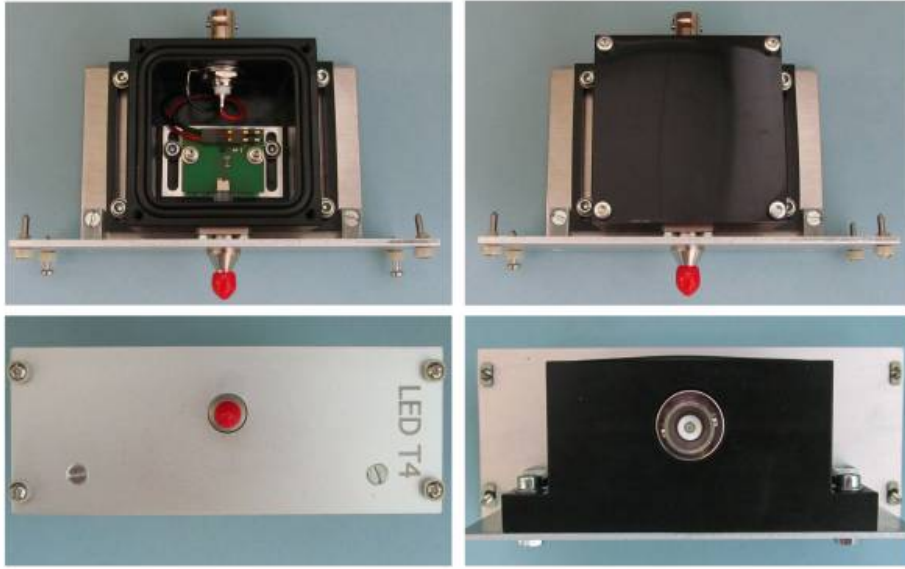
Figure 3.2: Photos of the XENON1T LED boxes from different views. The top figures show the top view of the opened (left) and closed (right) box. Optical SMA connectors are installed in the front to connect the fibers (bottom left). BNC connectors are placed on the back to power the LEDs through their connection to the pulse generator (bottom right).

cryogenic pipe, while a set of 1.5 m silica fibers with stainless steel sheeting were installed inside the cryogenic system, which is farther away from the detector, connecting each naked line to the optical feed-throughs. At each joint of fiber type 2 inside the system, a vacuum SMA adapter is used with a connector pair on both sides (see figure 3.6).

Around and inside the TPC, it is important to minimize the amount of radioactive material. Hence, very thin ($250\,\mu$m) PMMA fibers (from Ratioplast-OptoElectronics GmbH [149]) are used for this section. In order to have the most homogeneous distribution of light emitted to the PMTs, each light channel is divided into 7 channels, using 1-7 dividing SMA connectors attached to seven PMMA fibers (see figure 3.5). Using XENON100 experiment serving as a test setup, the PMMA fibers are well suited for cryogenic temperatures, and have shown long-term stability when exposed to LXe, and hence, represent an ideal candidate for light-guides at this section of the setup.

3.2   Test setup at UZH

A liquid xenon chamber (named MarmotXL) was constructed at the University of Zurich in order to be used as a test facility for various components of the XENON1T detector. Several versions of PMTs, signal and high voltage cables, connectors, PMT readout bases, and a mock-up bell system were tested, using this chamber. The xenon gas system is equipped with about 12 kg of xenon in total, a PTR system for condensation of xenon, and a vacuum cryostat. A liquid xenon chamber is installed inside the cryostat, with a holder structure that could initially host up to 5 PMTs. The chamber was later upgraded to host 10 PMTs in two arrays. At each operation of the setup, the behavior of the equipment under examination at room temperature, in vacuum, cold or

Figure 3.3: Photograph of the front side of the XENON1T LED frame with the pulse generator and the LED boxes installed (top), and a graphical model of the LED frame and its parts (bottom).

warm xenon gas, or immersed in liquid xenon can be studied.

A technical description of the setup, and the performed PMT tests using MarmotXL setup can be found in reference [124]. When all the required equipment for the XENON1T PMT calibration system, including the fibers, pulse generator, LED box, connectors, and feed-throughs were purchased and assembled, the MarmotXL setup was used for testing the PMT calibration system of XENON1T. In figure 3.7, the schematic view of the MarmotXL facility is displayed together with the schematics of the test setup for the PMT calibration system.

The test setup includes all the individual sections used in the actual XENON1T PMT calibration system, except for the fiber type 2 (silica fiber), which was previously tested for long term, during the operation of XENON100. For the XENON1T PMT calibration system fibers of the same type were purchased from the same supplier. Therefore, as it can be seen in figure 3.8, PMMA fibers (fiber type 3) were directly connected to the vacuum feed-through. A single LED box is used, connected to a single plastic fiber (fiber type 1) of the same type as in the XENON1T system. The PMMA fibers were connected to a 1-4 dividing SMA connector, whereas 1-7 dividing connectors are used in XENON1T. The fiber ends were fixed on a PTFE plate under the PMTs. The LED was driven by the same pulse generator which was later installed in the XENON1T DAQ room.

The pulse generator was connected to a computer and a set of programming scripts in C++ language were developed to send control commands to the pulse generator. The same scripts

Figure 3.4: Picture of the BNC pulse generator used for the XENON1T PMT calibration setup.
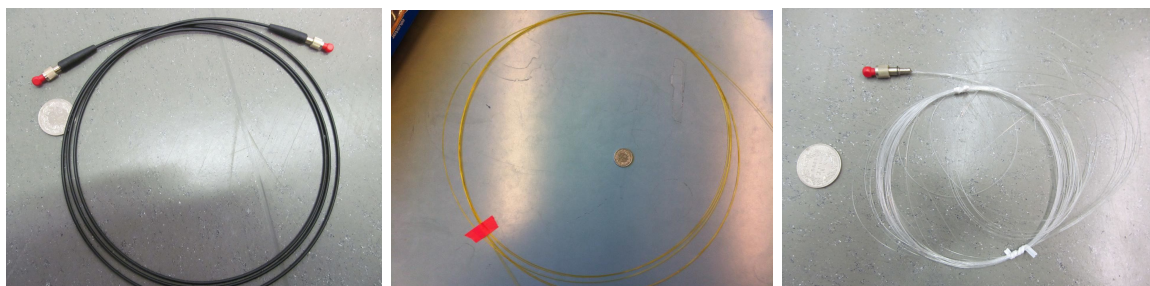
Figure 3.5: Pictures of the different optical fiber types used in the XENON1T PMT calibration setup. (Left) Plastic optical fibers, 1 mm core coated with 1.2 mm black plastic ,(middle) 770 μm Silica (quartz) fibers, and (right) 250 μm PMMA fibers are displayed.

Figure 3.6: Pictures of the optical vacuum SMA feed-through (left) and SMA connectors for air (middle) and vacuum (right) that are used for the XENON1T PMT calibration setup.

were later translated into the ladder diagram language that are used with the PAC system of the XENON1T remote control software (see section 2.4.3).

Finally, the whole setup was operated successfully using the MarmotXL chamber. The performance of the PMMA fibers inside the liquid xenon was examined, together with the light-tightness
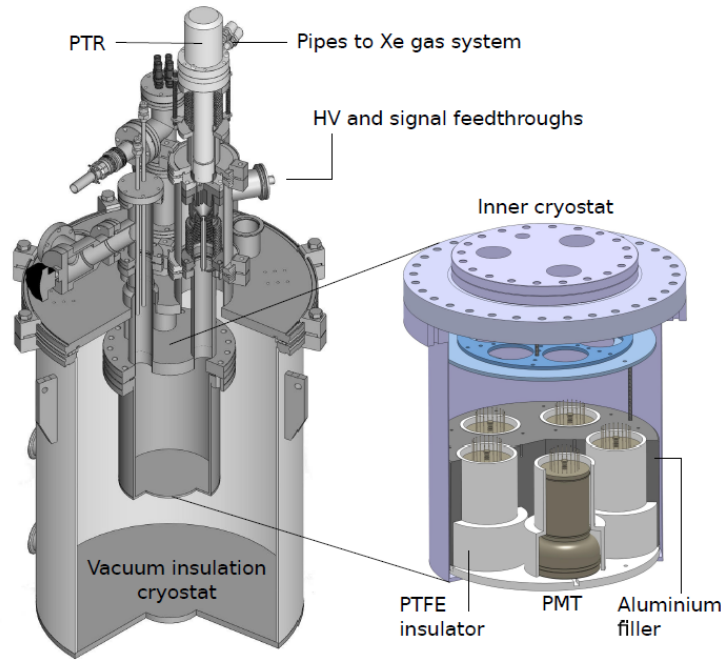
Figure 3.7: Schematics of the MarmotXL liquid xenon facility. The magnified inner cryostat illustrates the geometrical configuration of the PMT holder with 5 PMTs installed inside the chamber.

of the plastic fibers placed outside of the chamber (exposed to ambient light). In addition, the remote control of the pulse generator using the provided C++ scripts was tested. The system was later used in the MarmotXL facility for testing several batches of the XENON1T PMTs (i.e. gain, dark-count and after pulse rate measurements, as described in [124]).

3.3   Installation of the PMT calibration system at LNGS

After the examination of the setup, the installation process was planned, based on the time construction schedule of the XENON1T detector. The installation process includes all the components listed in table 3.1, and is performed in several steps. These steps are listed in the table 3.2, ordered by time. In the following, each stage is described in detail.

3.3.1   Installation of the silica fibers inside the cryogenic pipe

At the first step, the cryogenic pipe was manufactured at ALCA Technology, Schio, Italy [152]. The idea was to install all the PMT signal and high voltage (HV) cables and optical fibers into the pipe at the ALCA company, before it was closed. Later, it was considered to enclose the pipe from both ends with two stainless steel caps and pump it to vacuum, and begin the baking process and the radon emanation measurements of the pipe. Only after the pipe has passed the
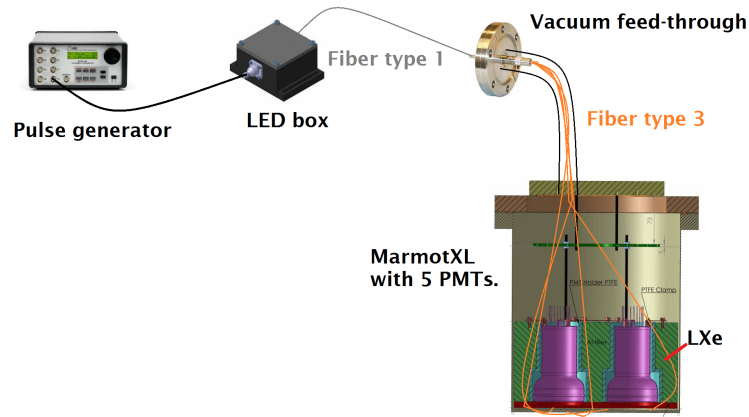
Figure 3.8: Schematics of the setup for the PMT calibration system tests at UZH with MarmotXL.

Stage	Components installed	Technical requirement	Time and Place
1	Fiber type 2	Cryogenic pipe is manufactured and is accessible on both sides.	June 2-9, 2014, Schio, Italy
2	Fiber type 2 Extension	Cryogenic pipe is installed and cryogenic system is open.	February 1-15, 2015, LNGS, Italy
3	Fiber type 3	The TPC is assembled but the PTFE plates are not inserted.	November 1-15, 2015, LNGS, Italy
4	Fiber type 1 and the LED frame	The DAQ hardware installation is complete.	February 20-March 10, 2016, LNGS, Italy

Table 3.2: The installation steps for the PMT calibration system of the XENON1T experiment, in time order. The period of the installation process at each stage is mentioned, together with the technical requirement for the corresponding process.

qualification requirements, concerning vacuum tightness and the radon emanation rate, it would have been transported to LNGS, to be installed inside the water tank, which was empty at the time, as the TPC and its cryostat were not yet manufactured. The cryogenic pipe is 7 m long, requiring a concrete plan for the insertion of flexible cables and fibers, through pulling from one side using a long pilot wire. The installation of the optical fibers was performed in June 2014.

A set of five (4 required, and 1 for redundancy) silica fibers were purchased, with the length of 7.4 m, considering 20 cm excess on each side of the pipe, to make them reachable in the next steps. The most difficult challenge at this step was handling of the very delicate silica fibers. For this reason, a long PTFE tube was provided with flexibility which is safe for the tube to hose fibers

(bending radius $\sim 15\,\text{cm}$). A large number of holes were drilled over the whole length of the tubes, to minimize the amount of material, and help the emanation process during the baking period. The tube was then enclosed using two custom-made PTFE caps in order to support the fibers from falling out (see figure 3.9). The caps were designed to be removed easily, as the working conditions at the next installation step, inside the water tank, were foreseen to be extremely difficult. All fibers were cleaned inside an ultrasonic bath with ethanol before insertion in the PTFE tube. In figure 3.9, several photos of the fibers inserted in the PTFE tube at UZH are displayed.
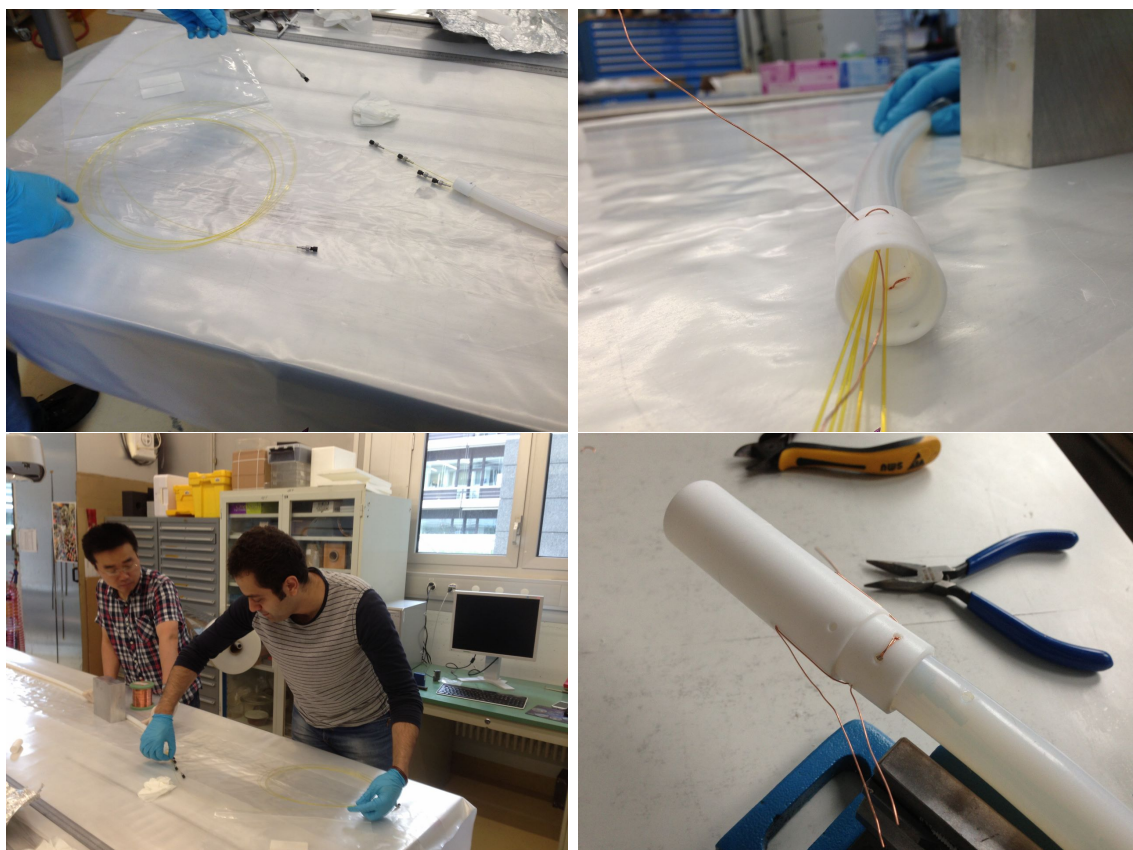
Figure 3.9: Photos from the preparations of the silica fibers at UZH before shipping to ALCA. The left figures show the process of insertion of the silica fibers inside the PTFE tube, and the right figures illustrate the process of the closure of the tube, using the designed caps.

When the PTFE tube containing the fibers was delivered to ALCA company, and after all the other signal and high voltage cables were installed, the tube was lodged with caution into the cryogenic pipe. After this was done, the pipe was closed with the stainless-steel caps, and was pumped to vacuum, getting prepared for baking and radon emanation measurements (see figure 3.10).

Once the emanation tests were finalized, the pipe was delivered to LNGS, where it could be installed at its final position. Before installation, the pipe was bent at about 90 degrees on its bellow section as it was initially designed to. At the time, the production of neither the cryogenic system, nor the TPC was complete, and hence, the pipe was not connected on neither side.
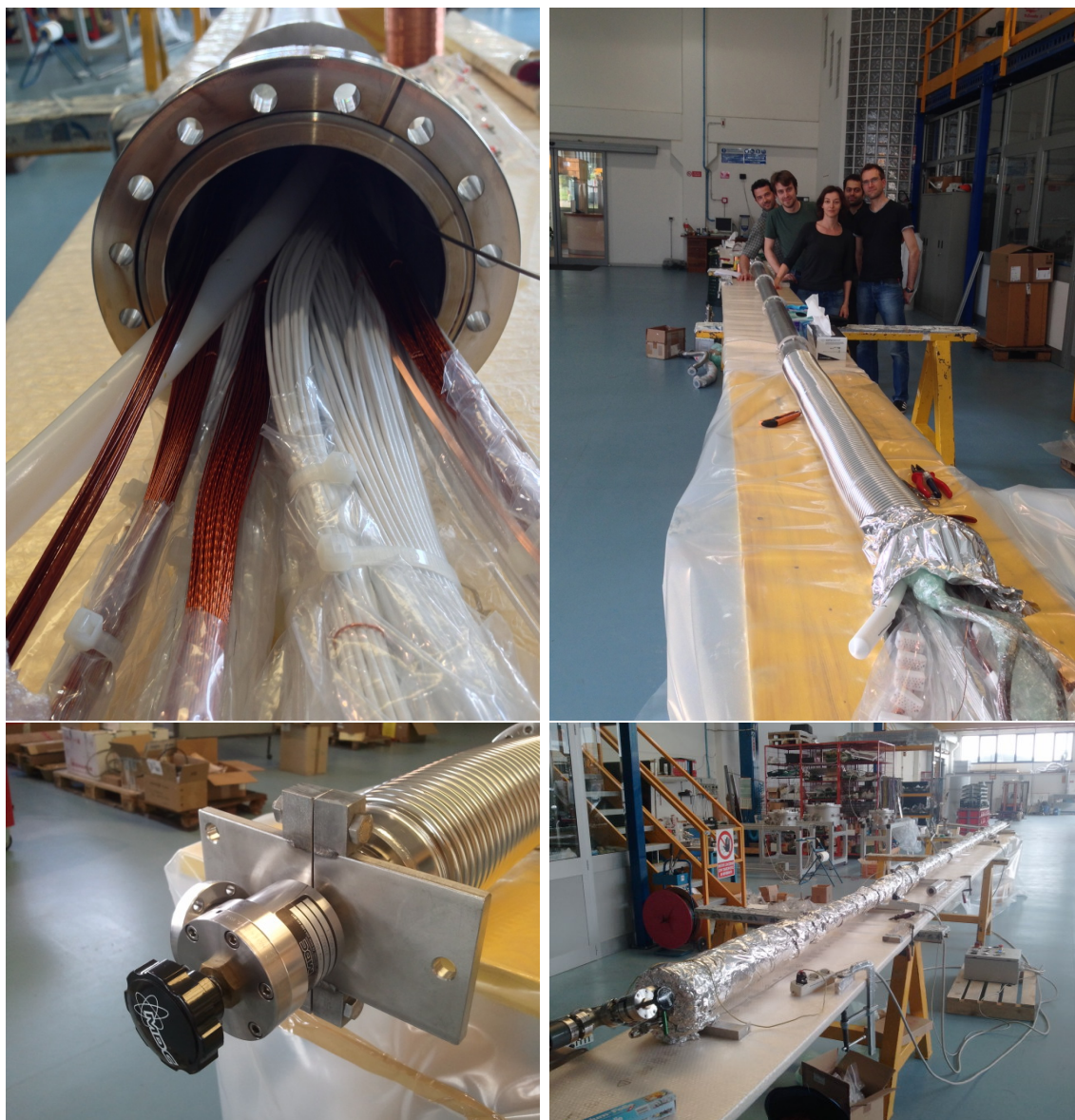
Figure 3.10: Photos from the installation of the optical fibers and cables inside the cryogenic pipe at ALCA. The top figures show the PMT signal and HV cables being installed inside the pipe, together with the PTFE tube containing the silica fibers, whereas the bottom figures show the closure of the caps and the hardware preparations for the radon emanation tests.

3.3.2   Extension of the silica fibers to the vacuum feed-throughs

In parallel to the installation process of the cryogenic system in the XENON1T building, on its second floor, the extension of the optical fibers from the cryogenic pipe to the vacuum feed-throughs had to be done. As shown earlier, the vacuum feed-throughs were installed on the porcupine. This section had to be installed at the last step, after all the cables and optical fibers are extended to their final length, out of the cryogenic pipe. Therefore, in February 2015, the top cap of the

cryogenic pipe was re-opened inside a clean room, that was provided in advance, and the cables were pulled out of the pipe to their final position. To each silica fiber, another 1.9 m long silica fiber was attached using SMA connectors, while the new extension fibers were coated by stainless steel, as mentioned earlier. The fibers were guided through the 90° knee structure of the cryogenic system, upwards into the porcupine. In the final step, the porcupine was moved to its position, and fixed after all the cables and fibers were mechanically connected inside. Figure 3.11 shows several photos from this process.

Figure 3.11: Photos from the extension of the optical fibers and cables to the vacuum feed-throughs inside the clean room built on the second floor of the XENON1T service building at LNGS.

3.3.3   Installation of the PMMA fibers

By the end of October 2015, the XENON1T TPC had been assembled in a clean room environment provided at the above ground laboratory at LNGS. After the TPC pillars and copper field shaping rings were installed, and before the PTFE reflective panels were connected, the PMMA fibers should have been fixed into the reflector panels.

As the final position of the fibers has a direct impact on the light distribution pattern on the PMT arrays, a set of Monte Carlo simulations were performed to study the uniformity of the light collection efficiency (LCE) in the TPC, for various geometrical configurations of the fiber end positions inside the TPC. The full geometry modeled with GEANT4 was used to simulate photons isotropically emitted (ideally assumed) from the fiber ends.

Similar simulations that were carried out for XENON100 experiment resulted in a light distribution which was in agreement with the LCE pattern observed from LED data. In order to achieve maximum uniformity, the fiber ends were positioned symmetrically around the TPC in two sets of 12 fibers (30 degree distances), situated at two different heights of the TPC. The final results of the simulations indicate that the configuration with fiber ends at the two heights $Z_1 = 1/3$ and $Z_2 = 2/3$ from the bottom of the TPC provides the most uniform LCE between the top and bottom PMT arrays. Figure 3.12 shows the simulation results of the LCE mean value and standard deviation over the top and bottom array PMTs for different Z positions of the fibers. In the same figure the LCE value at each PMT position is shown for fiber ends placed at -602 mm (= 1/3 height of the TPC) respective to the position of the gate electrode.
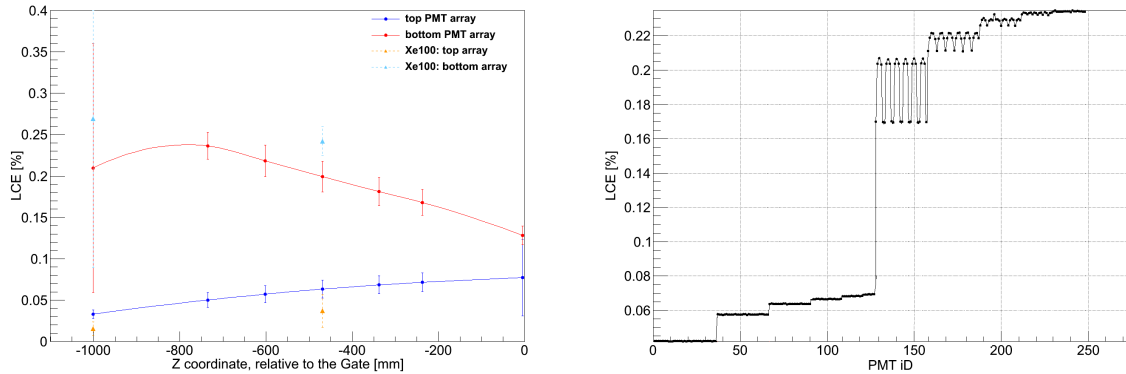
Figure 3.12: The mean and standard deviation of the light collection efficiency (LCE) over the top and bottom PMT arrays of XENON1T from simulations of symmetric fiber positions around the TPC (left), and the LCE value for each PMT resulting from illumination from fiber ends placed at -602 mm from the gate height (right). Plots from Dr. Alexander Kish.

While the uniformity within each PMT array varies by ∼20 %, the rather large difference in illumination level between the two arrays was inevitable (similar to XENON100). This difference is caused mainly by the difference of the reflective indexes of the gaseous and liquid xenon, considering all the light sources are inside the liquid phase while the top array is in the gas phase. The PMTs 1-36 are placed at the last ring on the top PMT array such that about half of their photocathode window area is covered by the PTFE reflective panels, hence their LCE values are lower than all the other PMTs.

As an outcome of the simulation results, out of 24 PTFE panels, manufactured to be installed at XENON1T TPC, two $250\,\mu m$ holes were drilled on 12 reflective PTFE panels at heights of 359.5 and 606.5 mm. Even though it was initially planned to place the 12 panels symmetrically around the TPC, such that each drilled panel has two neighboring solid panels, two of neighboring panels that were dedicated to cover the resistor chains had to be skipped. Thus, the final configuration is not completely symmetric. This was because the panels that cover the resistor chain were likely to experience several removal/reinsertion cycles, which is a dangerous operation for the fibers as they may be easily pulled out of the holes. Therefore, a final radial configuration as shown in figure 3.13 was achieved.

A total number of 28 PMMA fibers were available from the 4 available light channels, after the 1-7 splitting SMA connectors. Out of those, 4 channels were reserved to be fixed on the outside of the TPC volume for calibration of the 1-inch diagnostic PMTs. The other 24 were divided into 4 sets of 6 fibers splitting from each light source. As the possibility of the damage of the light channels was foreseen, a configuration was favored at which, in case of any loss of light channels, the maximum uniformity of the illumination is presumed. Therefore, each fiber set was distributed symmetrically around the TPC at a certain height. Consequently, two light channels contribute to the 12 fibers on the top, and the other 2 light channels make the bottom 12 light sources, as shown in figure 3.13 (projected to the bottom array). In this configuration, a redundancy for the number of light channels is considered and a uniform illumination could be practically possible only with two light source channels. This was because the possibility of loosing 1-2 light channels during the installation process was foreseen. The positions of the fiber ends through the reflector panels after the installation are also marked on a photograph of the TPC before the installation of the electrodes in figure 3.13.
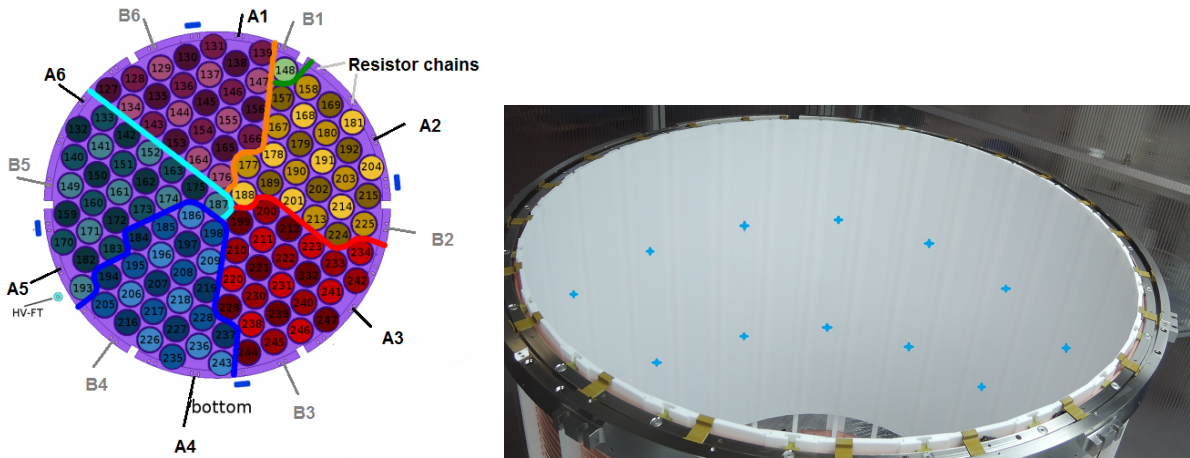
Figure 3.13: The final configuration of the installation of PMMA fiber ends at each height of the XENON1T TPC projected on the bottom PMT array (left) and a photo of the TPC after insertion of the PTFE panels with positions of the fiber ends marked in blue (right). "A" and "B" refer to the groups of 6 fibers split from the same light source.

The installation of the PMMA fibers into the reflective PTFE panels was performed through the following procedure. First, each fiber group was unrolled, and each of the individual fibers was wrapped around a custom-made plastic spool. Two sets of the wrapped fibers were unrolled at a time, while from each set one was installed at the bottom, and the other at the top of each PTFE

Figure 3.14: Photos from the installation of the PMMA fibers in the XENON1T TPC. The PMMA fibers used for the XENON1T PMT calibration system are 250 μm thick and therefore, cannot be viewed easily from the photos.

panel. A length of 1-2 m was retained from each fiber end, respective to its distance from the top of the bell, in order to reach the SMA connectors on the silica fibers under the cryogenic pipe. Before insertion of the fibers, they were passed between the copper rings and behind the top ring at the planned position of the respective PTFE reflector panel. This process makes the installation of the panels feasible after insertion of the fibers. While the fibers are being pulled out from the hole inwards into the TPC, the PTFE panels were slid down to their dedicated positions. After all panels were installed, the fibers were cut at a length of 3-5 mm inside the TPC, with an imperfect cut, made intentionally to presume maximum light dispersion. In figure 3.14, several photos of this

installation process are displayed.

3.3.4   Installation of the plastic fibers and the LED frame

After the assembled TPC was relocated to the underground laboratory, and before the cryostat was closed, the PMMA and silica fibers were connected at the top of the diving bell and under the cryogenic pipe, thus guiding the light all the way from the vacuum feed-throughs to the TPC.

In March 2016, when the DAQ room was prepared with all the cabling, the hardware work for the installation of the XENON1T PMT calibration system was finalized. The LED frame was installed into the corresponding electronics rack, and the plastic fibers (fiber type 1) were guided through a hole from the cryogenic (second) to the DAQ (first) floor. The fibers were later attached to the LED boxes, using the SMA connectors on the front panel. After an initial test, it was found that out of 4 installed light channels, one had lost optical connection, and hence was excluded from the setup. The other 3 light channels are used for the calibrations of the PMTs.

3.4   Pulse generator remote control system

For several reasons, regarding different purposes of the PMT calibration data, one might need to change the LED settings. For instance, a high illumination of LEDs in the range of 5-10 PE per trigger is needed for the afterpulse data acquisition, while for the gain calibrations a lower intensity of 0.5-2 PE per trigger is preferred. In addition, the detector conditions might vary over time, requiring readjustment of the settings. Moreover, for every use of the LEDs, they should be switched on/off, and the trigger input, pulse amplitude, pulse width and other parameters might require resetting after every reboot of the device.

Therefore, it is essential to develop a robust, safe and reproducible method for controlling the pulse generator output. Even though the device can be operated through manual control using its front panel, an operation that can be performed only through presence of the personnel on-site, it is required to check or modify some setting remotely.

As mentioned earlier, the device can be controlled remotely through a RS 232 communication port, connected to a computer. Within the test phase, a set of C++ programming scripts were provided, and used to send the commands listed in an ASCII file to the device. All the operating parameters of the device can be controlled by sending commands provided in the operation manual. For instance, the trigger settings, pulse width, amplitude, frequency, etc., could be altered or inquired from the device, using specified commands in the syntax of "Standard Commands for Programmable Instruments" (SCPI). As an example, sending the command:

:pulse1:width 0.0000001 < cr >< lf >

changes the width of the first channel signal to 100 ns. Or similarly:

:pulse2:width? < cr >< lf >

inquires the device about the width of the pulses on the second channel, returning a value in units of seconds.

For a large experiment, at the scale of XENON1T, it is desirable to have all control programs within a single platform. In this way, all users can follow a single training unit, provided by the experts, and required to achieve sufficient skills for secure handling of the control systems, rather than having every individual subsystem attributed to its stand-alone control program. Therefore, the control software of the pulse generator was translated from the previously tested scripts (in C++) into the ladder diagram language, that is used for the general slow control system.

As mentioned in the previous chapter, the XENON1T slow control system uses a SCADA based web platform as the interface for the users. The web system is accessible remotely, either from a user within the local network, or similarly, by using a VPN connection, for security considerations. Shifters (referred to the periodic responsible operators of the experiment) are given "basic access" to every individual control software with a limited user-power, that is considered safe, having only the general knowledge, learned through taking training lessons. However, for various subsystems such as the TPC, the PMTs, and the Cryogenics, there exists a list of "experts", with authorized access to the full control program.

In case of the control program for the PMT calibration system, the most risky operations include any situation at which the LEDs are illuminated at high level (either large voltage amplitude or very long pulses) that can increase the internal current of the PMTs. In order to avoid such situation, only a list of predefined "calibration modes" are provided by the experts respective to common use-cases of the system (e.g. gain calibration, afterpulse measurements, etc.), that can be loaded and run by the shifters. Figure 3.15 shows the SCADA webpage for the PMT calibration system with an example calibration script that is sent to the device.
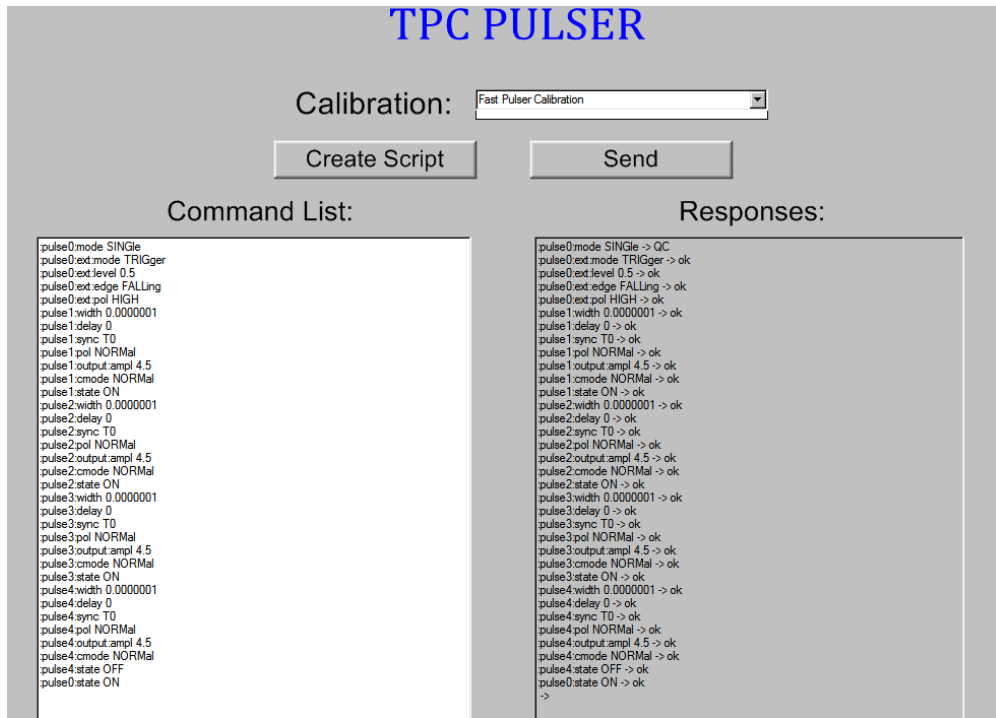
Figure 3.15: An image of the SCADA panel from the XENON1T slow control remote access webpage, dedicated to remote control of the pulse generator used for the PMT calibrations.

Several scripts were provided for such typical use-cases, as listed in table 3.3. When a "calibration mode" is loaded, all the commands that the software sends to the device are listed on a screen panel (white panel in figure 3.15). These commands are accessible only by the experts. Once the list of commands are verified by the user, they can be sent to the device by clicking on the "Send" button. To every command that is sent, the device replies with a set of characters that either include the answer to a query, or only confirmation that a certain command is received. These replies are also printed in a separate panel.

Script	Function
Switch on	Switches on the device and arms the external trigger system. All LEDs are set to 1.0 V. This voltage is not enough to switch on LEDs and generate photons. However, it is used for consistency of the experimental conditions for the noise and LED runs, used for the model-independent PMT calibration (see section 3.7). The LED pulse width is set to 100 ns (minimum) on all channels.
Low illumination	Sets the amplitude of the LED channels to a low illumination level, such that all PMTs receive less than 0.1 PE per trigger (desired for gain calibration by the fitting method (see section 3.6.2).
High illumination	Increases the amplitude such that all PMTs receive an average of 0.5-2.0 PE per trigger, desired by the model-independent method (see section 3.7).
LED off	Lowers the amplitude of the LEDs back to 1.0 V without switching off the device or disarming the trigger, for the purpose of a noise measurement after LED data.
Afterpulse	Increases the amplitude of all LEDs to illuminate all PMTs with 5-10 PE per trigger, desired for afterpulse measurements.
Switch off	Secures the device by first switching off the LEDs followed by disarming the external trigger.

Table 3.3: The list of provided calibration modes for the users of the XENON1T slow control software to run the PMT calibrations.

3.5   Data acquisition

Despite the normal data acquisition mode of the XENON1T DAQ system, which includes a software trigger with a very low threshold, the PMT calibration data aims to study the response to the smallest signals, i.e. single photo-electrons (SPEs). Therefore, even a low trigger threshold (of approximately $\sim 1/3$ of PE) implies non-negligible effects on the acceptance of such pulses, and consecutively the interpretation of the response. For instance, if the analysis method expects, by a first order approximation, a Gaussian distribution of observed signals around the SPE peak, the results will be biased towards higher gain values, due to the trigger acceptance being higher for larger SPE peaks. In order to avoid such complications, one usually uses data with much lower trigger thresholds. In this case, especially since the noise bursts and ADC baseline fluctuations occur at amplitudes comparable to SPEs, any applied trigger or peak-finding threshold becomes an issue. To prevent this, one can constrain the search areas of each waveform to a small range where the SPE pulses are expected to appear, and avoid implementing any threshold requirement. Such trigger algorithm is usually referred as "time-triggered", or "externally triggered" system. Figure 3.16 shows the distribution of the noise rate and the calculated single PE acceptance for different trigger thresholds applied on the XENON1T data.
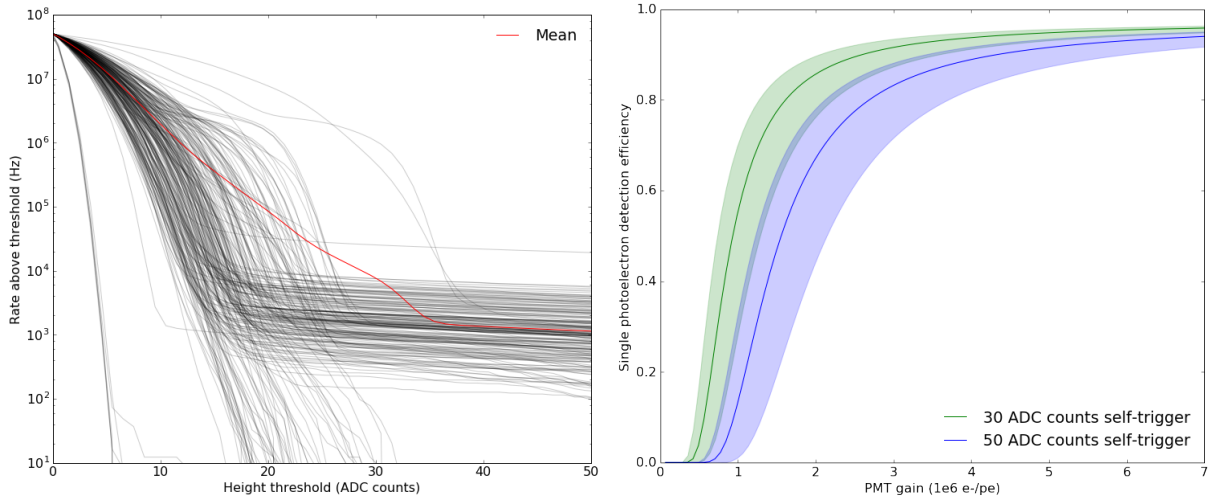
Figure 3.16: Distribution of the noise rate (left) and the calculated single photo-electron acceptance (right) for different software triggers applied on XENON1T data. Plots from Jelle Aalbers.

This can be achieved by sending the same trigger pulse to both the LEDs and the acquisition system. For instance, one may configure the ADC to record $10\,\mu$s pulses after each trigger received at time t_0. At the same time, the user may send an LED pulse at the time $t_1 = t_0 + \Delta t$ with $0 < \Delta t < 10\,\mu$s. In this way, in every waveform, the PMTs are illuminated around the time t_1, where an SPE response is expected. Figure 3.17 shows several superimposed waveforms of a single PMT channel, and the distribution of the pulse maximum position for all PMTs, using the LED data acquired by this method. Such DAQ configuration constrains the search window for signals to a very small section. Whereas, in the normal acquisition mode, if the threshold is reduced to such low values, the acquired data will include all fluctuations of each trace, resulting into very high acquisition rates that require a huge amount of disk space and processing power to store and process the data.

Figure 3.18 shows the schematic representation of the XENON1T PMT calibration data acquisition setup. A digital clock module is used to send timed trigger signals in "Nuclear Instrumentation Module" (NIM) standard at a given frequency (typically 100-500 Hz). The pulses are first sent to the ADCs, as hardware trigger. However, they are also fanned into a level adapter, that converts them to "Transistor-Transistor-Logic" (TTL) standard, as required by the BNC pulse generator. As the BNC module is configured to use external trigger, when a TTL pulse is received, it will send four synchronized pulses with the set amplitude and width to each LED. The light from the LEDs illuminates the PMT arrays through the optical fibers, and the ADC modules record the PMT signals when each trigger is received.

After the LEDs were tested and their time delay with respect to the trigger signal was tuned, the illumination amplitude on every PMT was studied in detail, and was adjusted accordingly. The LED voltages must be set such that all PMTs receive a rather uniform exposure, under which every PMT receives a small fraction (e.g. $5\,\%$) of the triggers with an observed photon from the LEDs. In this case, the probability of detecting a double PE by a PMT is negligible (¡0.01 %) assuming the Poisson distribution of detection probabilities. As shown in figure 3.12, even though we expect
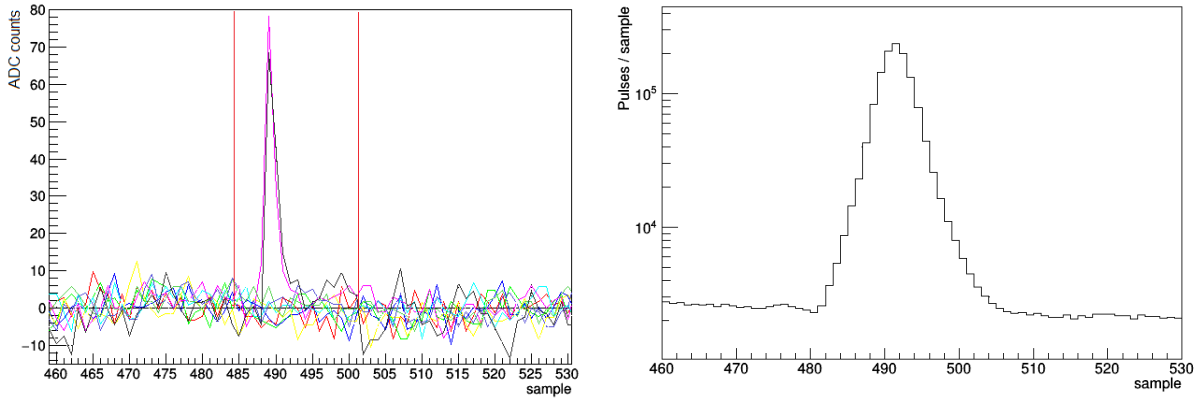
Figure 3.17: (Left); the superimposed waveforms from the PMT calibration data of a single PMT channel, zoomed around the LED time window indicated by the vertical red lines. (Right); the distribution of pulse maximum sample position for all PMTs. Each sample corresponds to 10 ns, given by the 10^8 Hz sampling frequency of the XENON1T ADC modules.

to be capable of adjusting the system in a way that all PMTs within either top or bottom receive rather uniform illumination, the main challenge is to overcome the large difference in light collection efficiency between the top and bottom arrays. Hence, we define the parameter $\lambda = -ln(\frac{N_0}{N})$, where N_0 denotes the number of traces with no signal observed, and N is the total number of triggers in a LED dataset, and tune the LEDs to reach a uniform distribution of this parameter for all PMTs. Figure 3.19 shows the distribution of this parameter versus PMT channels after the LED light tuning was performed.

The results are compatible with the expected distribution of the parameter λ from simulations, as shown in figure 3.12. The relative illumination ratio between the PMTs in the brightest (center of the bottom PMT array) and the darkest (edge of the top PMT array) regions is about 4-5 (see figure 3.12), consistent with the expectations from the difference in light collection efficiency. The outer most ring of the PMTs on the top array have about half of their photo-cathode window covered by the PTFE reflective panels, and hence are exposed to lower illumination.

3.6   Analysis software

This section describes the analysis software framework which was developed by a collaborative work between PMT, analysis and calibration working groups of the XENON1T experiment. The goal of this work was to provide an analysis software that is capable of performing the following tasks:

- Process the raw PMT calibration data into information required to extract individual PMT gains and other operational parameters e.g. noise, dark rate, etc.

- Plot single PE spectra for all PMTs and perform systematic fits.

- Extract the gain values and corresponding systematic uncertainties for every channel, and store the information in a dedicated database.
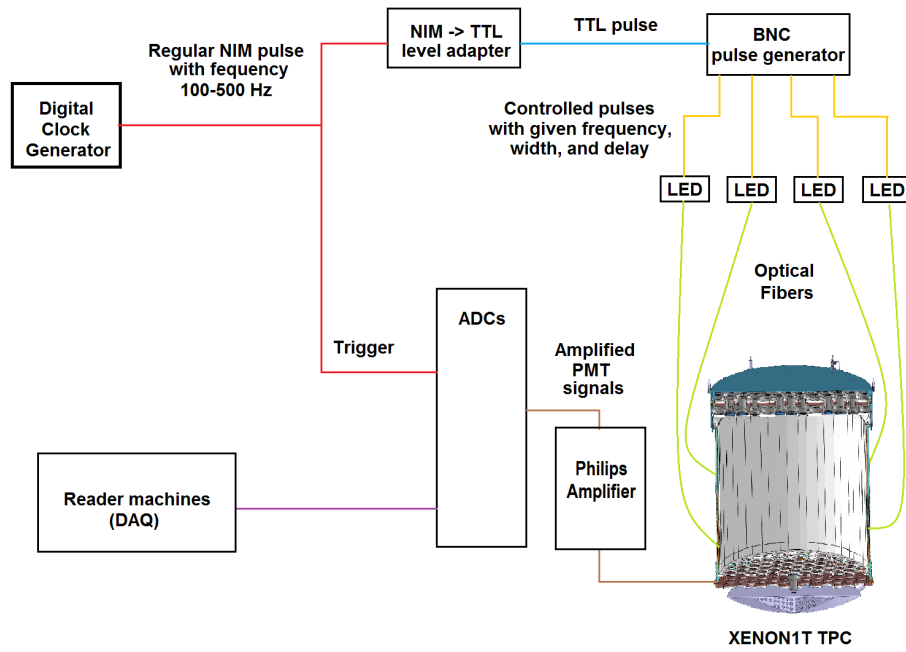
Figure 3.18: Schematic view of the XENON1T PMT calibration data acquisition system.
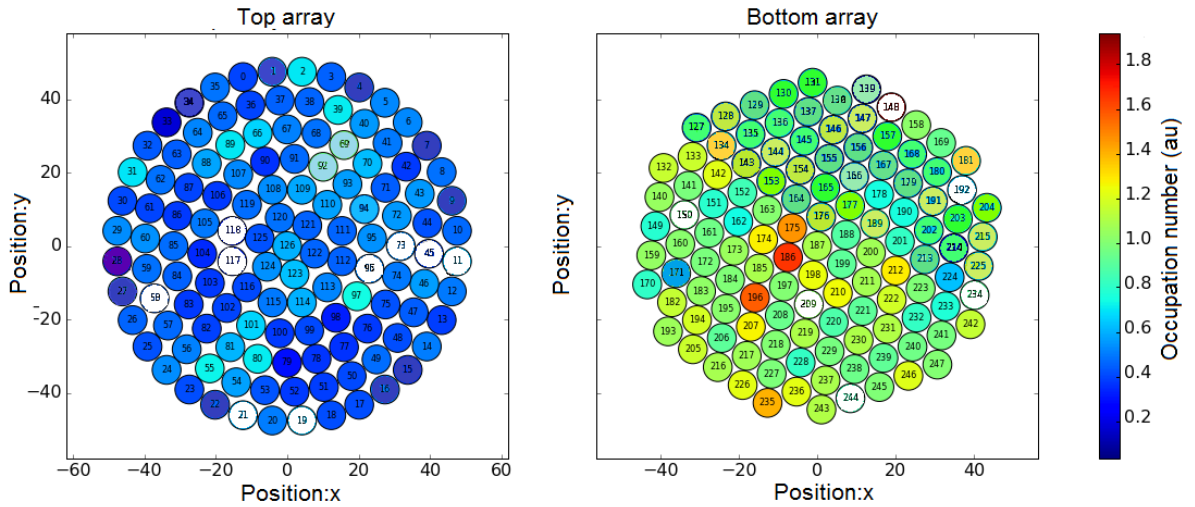
Figure 3.19: Measured values of the illumination parameter λ (occupation number) for the top (left) and bottom (right) PMT arrays projected on the corresponding maps. The PMTs colored white are physically powered off for technical reasons. For all other PMTs the color-bar shows the occupancy.

In addition, it was considered that the whole process above had to be performed on a regular basis, by corresponding shifters of the experiment. As visual inspection of the goodness of fits and

manual modifications for the process may be required, and considering that the work has to be done by shifters, which do not necessarily have experience in studying the PMT response, it was decided to provide a graphical user interface (GUI) to simplify handling of the analysis process.

3.6.1   Raw data processing

The XENON1T experiment uses a general raw data processing package named PAX, explained in the previous chapter. The software includes several plugins for handling the input/output formats, peak finding algorithm, and signal processing. Unlike the XENON100 raw data processor that was able to perform analysis only on the summed waveform of all PMTs, PAX is capable of processing the waveform of every channel separately. After the peak finding and signal processing are performed on single channels, secondary processing including the clustering of signals, their classification, position reconstruction, and corrections is applied on the summed PMT traces, all through the same software package.

Considering the PAX capability of processing data from single PMT channels, it might serve as a viable software to be used for the PMT calibration data processing. However, PAX has been developed and optimized for processing the acquired data, in particular, the dark matter and calibration data. Even though the software has a reasonable (quantified) acceptance for the smallest quanta of physical observables (single PE, see figure 3.16) from detector response, most of the features are optimized for larger S1 and S2 pulses. For instance, 9.4 keV line (lowest energy line used for calibrations) from krypton calibration includes S1 signals, which are, on average, about 55 PE, considering the measured light yield of 6-7 PE/keV, and the corresponding S2 signals are more than 100 times larger. The SPE signals expected from LED data however, are not the prior point of interest to be considered for such studies. In particular, the peak finding algorithm, and the integration algorithm (that calculates the area of pulses, which is proportional to the number of observed PEs), are not as precise for small signals, at the SPE level. Since for the PMT calibration purposes only single or double PE pulses are acquired, it is very important that the efficiency of such algorithms is studied with more caution, and possibly improved for this special purpose.

Hence, even though for simplicity and consistency reasons, it was preferred that the raw data processor for the PMT calibrations is not different from the standard one, a modified version of PAX was provided after detailed studies of its performance on single PE pulses. However, most features are preserved, and only the peak finding algorithm and integration process are modified. In the following, the motivation for such revisions is described, together with a detailed illustration of the plugins.

Peak finding algorithm: In PAX, a peak is found when the signal amplitude at a sample within the waveform exceeds a set threshold. The threshold is adjustable, and is set equal to a constant factor multiplied by the root mean square (RMS) of the noise spectrum. This factor is typically set between 6-8 times the baseline RMS, as lower values result in a large number of found "peak" candidates due to electronic noise, which significantly increases the required computing power and data processing time (see figure 3.20).

The average height of a single PE is 50-120 ADC counts depending on the PMT gain, and the different channels have a baseline fluctuation RMS in the range of 4-10 ADC counts. The distribution of the baseline RMS is plotted in figure 3.21, for the top and bottom PMT arrays. The mentioned numbers refer to the period before the first XENON1T calibration campaign (April-May 2016), when this analysis was executed. Motivated by this work, a noise reduction campaign
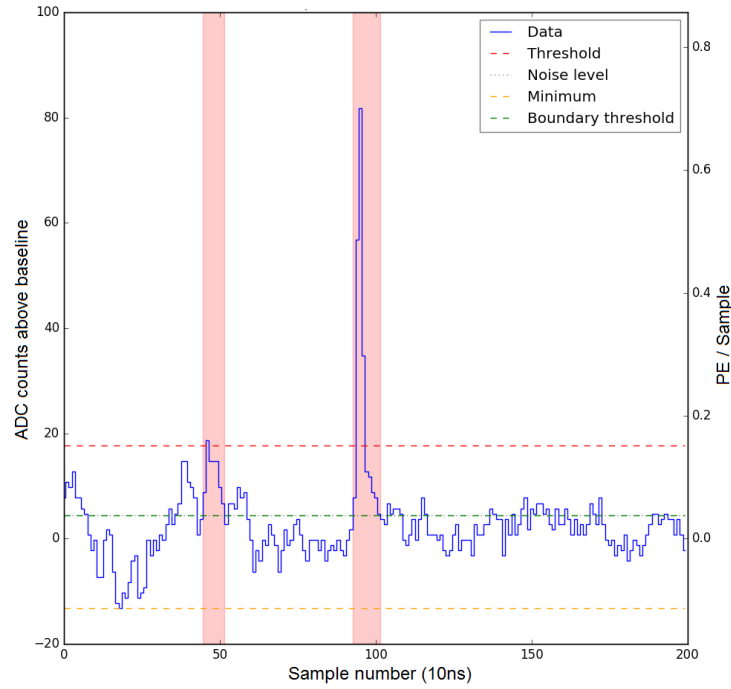
Figure 3.20: An example waveform of a single PMT channel processed by PAX. The green dashed line shows the baseline (noise) RMS level and the red dashed line shows the peak finding threshold, set to 4 times the noise RMS. The selected peak candidates are shown in shaded pink regions.

was initiated. Figure 3.22 shows the same distribution in September 2016, representing a notable reduction in the baseline fluctuations amplitude.

The choice of the peak finding threshold at 6-8 times the noise RMS was found to be very inefficient for the PMT calibration purpose. Fortunately, regarding the hardware trigger system used for the PMT calibration data acquisition, and using short LED pulses (100 ns), the search window for the data processor could be significantly constrained, causing a remarkable reduction of required time and computing power. For instance, figure 3.23 shows the pulse area versus the peak positions from all traces of a single PMT in a calibration dataset. The SPE events, induced by the LED pulses, are well restricted within the 150-200 ns time window. The acquisition window was arranged to be $2\,\mu$s long with a $1\,\mu$s pre-trigger with respect to 100 ns LED pulses synchronized with the trigger at the middle of the waveform. Using such short pulse search windows permitted the lowering of the peak finding threshold to values around 3-4 times the noise RMS.

Integration algorithm: As mentioned, the structure of the algorithm that calculates the area of single PE pulses is very important for calibration of the PMT response. Considering the very short rise and fall time (3 ns and 10 ns, respectively) of the SPE signals from R11410 PMTs, the length of the SPE pulses extends only up to 30-40 ns in total (3-4 samples at 10^8 Hz sampling rate). Hence, even if the integration algorithm ignores only 1 sample when integrating the SPE pulses, it already creates a significant bias towards lower gain values when used. In contrast, having too long integration window, not only can possibly bias the response (if the noise is not ideally bipolar
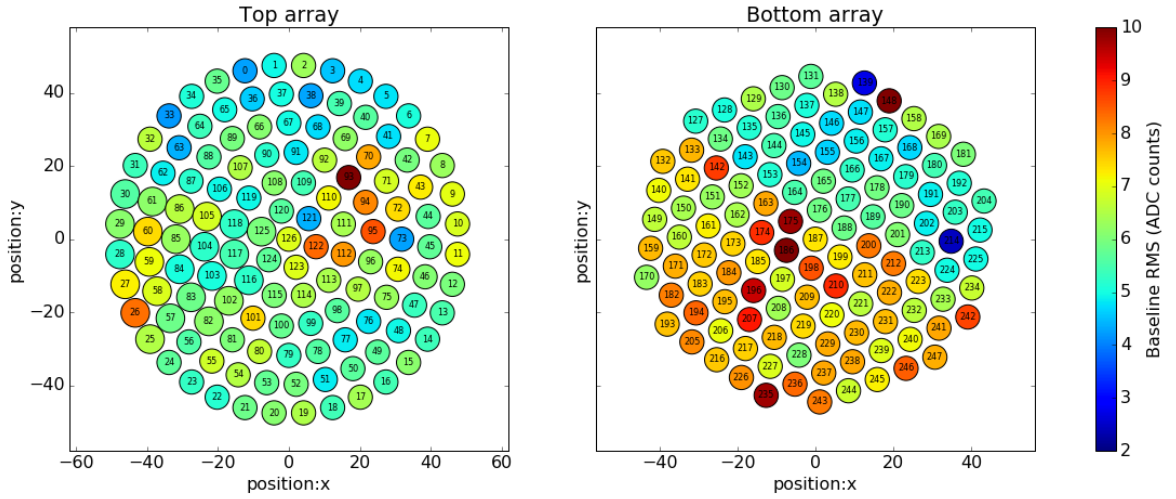
Figure 3.21: Map of the baseline RMS measured for all PMT channels of the XENON1T experiment for the data acquired in May 2016, before the start of the XENON1T first calibration campaign.
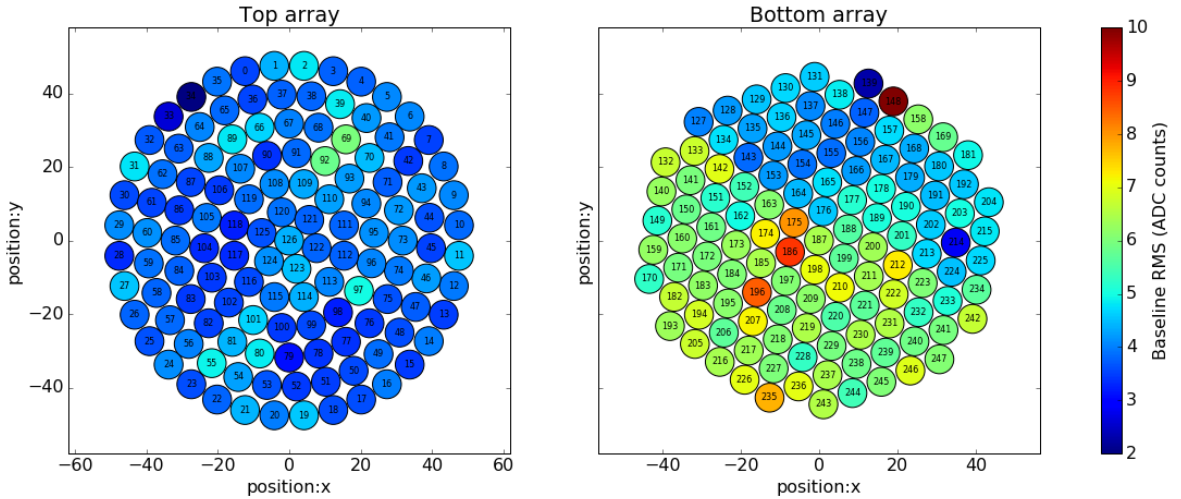
Figure 3.22: Map of the baseline RMS measured for all PMT channels of the XENON1T experiment for the data acquired in September 2016, after the noise reduction campaign. Figures from Dr. Richard Saldanha.

around zero, such that the biases cancel when summed), but it will also widen the distribution of single PE area, making the fitting of the spectra and evaluation of the gain more difficult. By adding every sample which does not belong originally to the single PE pulse, the standard deviation of its distribution increases in quadratic form, i.e:

$$\sigma_{tot} = \sqrt{\sigma_{1pe}^2 + n \times \sigma_{noise}^2}, \tag{3.1}$$
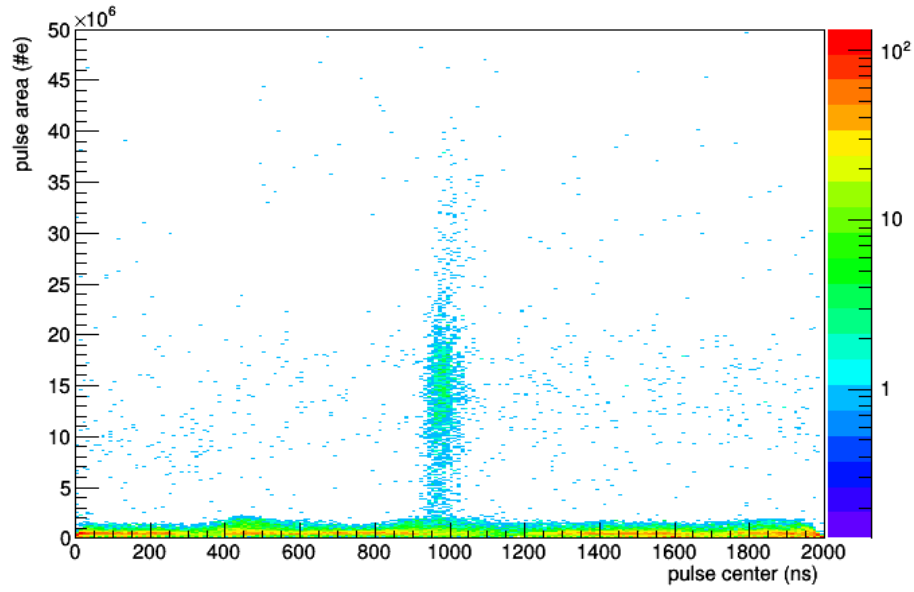
Figure 3.23: Pulse area versus the peak position from all traces of a single PMT in a XENON1T PMT calibration dataset.

with n being the number of samples which do not belong to the single PE pulse.

The integration algorithm of PAX works such that when a peak is found, starting from the maximum position, a window extends in both directions until the sample value falls below a threshold. This threshold is smaller than the peak-finding threshold and is normally fixed at $(1\times)$ the noise RMS level. This process, for large signals, yields a consistent estimate for the actual length of the pulse, but the method is not as precise when used for pulses in the range of SPE signal. It is observed that the integration algorithm can miscalculate the pulse area by 10-20 % deviations from the correct value when applied to SPE pulses.

An assumption is usually made on the distribution of the sample values around the baseline, to be symmetric around zero (equivalently, to have null expectation value). In presence of a noise source, which does not obey this regularity assumption (has positive expectation value for instance), the method has a bias in estimation of the pulse area. For XENON1T this was found to be the case. A regular periodic noise with 2 MHz frequency and 10-15 ADC counts amplitude was identified in more than half of the channels. When such noise comes in phase with single PE pulses, the PAX method extends the integration window until the noise vanishes, causing a significant overestimation of the pulse width (typically 150-200 ns) for single PE pulses and a positive bias in the calculated area.

In figure 3.24, an example single PE pulse is displayed, in phase with a 2 MHz noise bump. Also, in the same figure the area that PAX calculates for the pulses versus a fixed integration window (from 2 samples before the maximum until 4 samples after) is plotted, while the width ratios (PAX to fixed window method) are visualized by the color bar. It is clear that the area that PAX calculates for pulses, which are 2.5-3 times wider than the 60 ns fixed window, is on average 15-20 % larger than the one determined by the other method. For the events not affected by noise, the two methods produce consistent results for both calculation of the area and the width.
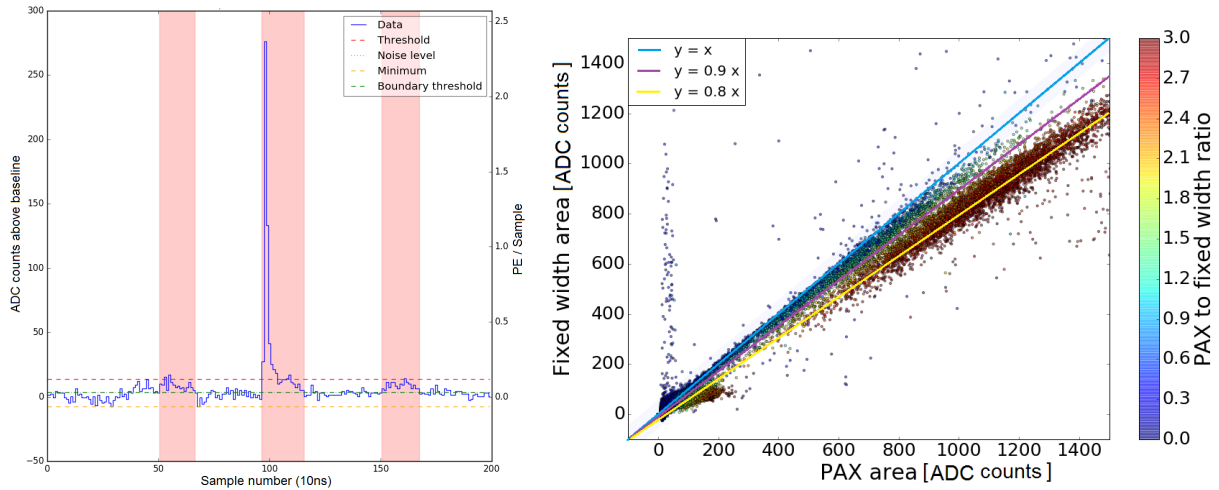
Figure 3.24: An example waveform representing the PAX integration algorithm applied on a found single PE pulse in presence of noise (left), and pulse area calculated by the PAX algorithm versus the area determined by a fixed integration window (2 samples before the maximum until 4 samples after). The pulse width ratio is indicated by the color bar (right).

Hence, it was motivated to introduce an independent integration algorithm for PAX, before it could be used for processing the PMT calibration data. Since the expected variations for different PMT channels in rise and fall time are negligible, considering the sampling frequency, an obvious proposal can be a fixed integration window, to be used for all PMTs at a range which is just enough to contain all the (largest) single PE pulses. As an example to illustrate this point, figure 3.25 shows the spectra of several samples before and after the maximum from all events for a single PMT.

In order to quantify such effects, for each sample around the maximum, the mean value was calculated, together with the positive and negative deviations from the mean. Positive deviations can be generated through contributions from single PE pulses on a sample, while negative deviations purely belong to statistical fluctuations of the ADC baseline and bipolar noise. Hence, the "significance" of a sample could be defined in the following ways:

- by the mean value of that sample being compared to the noise RMS;

- by the positive deviation of that sample compared to the noise RMS;

- by the ratio between positive and negative deviations of the sample.

Figure 3.26 displays these values calculated for a single PMT as an example. Consequently, these quality parameters were calculated for all PMTs, and it was found that for majority of the PMTs, only 1 sample before the maximum and either 2 or 3 samples after the maximum are "significant", compared to the other samples considering all the 3 definitions of significance, mentioned above. Since in general, adding samples to the integration is less dangerous than not including samples that potentially belong to single PE pulses, conservatively, integration window of 70 ns wide, starting from 2 samples before and ending at 4 samples after the maximum was proposed for all PMTs. In a most sophisticated necessity, this can be evaluated from the same method separately for each PMT, while this was not considered crucial, since all PMT channels showed similar significance, as expected.
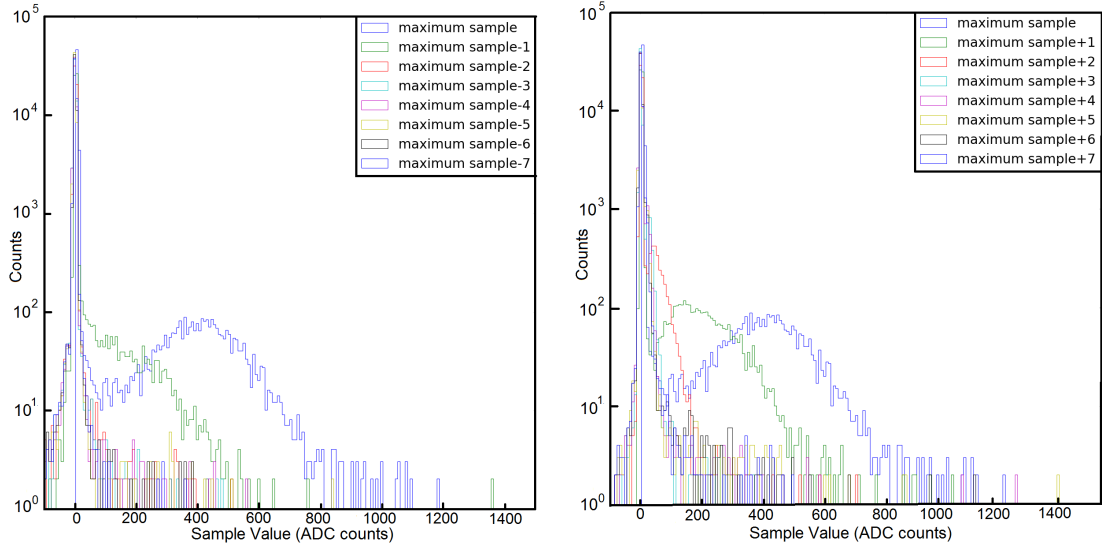
Figure 3.25: Spectra for several samples before (left) and after (right) the maximum sample in the trace from all the peaks found in the calibration data for one channel of the XENON1T PMT system.

3.6.2   Spectrum fitting and gain extraction

The gain of a PMT, defined as the number of electrons at the readout, produced by a single photoelectron released from the photocathode, can be estimated by a minimized χ^2 fit to the distribution of the PMT response to SPE signals. However, it is technically not trivial to expose the PMTs to a pure sample (beam) of single photons within a liquid xenon TPC. Even in the case when a single photon hits the PMT photocathode, there is a probability (dependent on the photon wavelength) that two photoelectrons are produced [153]. In addition, the photon might escape the photoelectric effect on the photo-cathode window, and produces a photo-electron by hitting the first dynode directly [154], resulting ai under-amplified output (because 1 multiplication step has been skipped). The under-amplification of the output signal can also occur through skipping another dynode stage [155], or inelastic back-scattering off the first dynode [154, 156].

Hence, attempting to study the PMT response, the appearance of noise pulses, under-amplified and double photoelectron signals is inevitable. Therefore, these terms need to be accounted for when the single PE spectrum is to be described. For XENON1T PMT calibration system, the incident photons are emitted with 405 nm wavelength at which the probability of double PE emission is negligible [153]. This condition is favored when the response of PMTs to single PE is the subject of interest while for studying the response to single photons, using a light source which emits photons with wavelength close to 178 nm from xenon scintillation photons is suggested, such that this process is naturally accounted for.

The probability that the light source exposes a PMT to 0,1,2, or more photons naturally follows a discrete Poisson statistics. Therefore, when tuning the light settings, one usually attempts to fix the number of triggers at which a single PE pulse is observed, around 5 %, in the case of which the probability of 2 or more photons reaching the PMT window at the same time is insignificant (< 0.1 %).

Finally, the exact charge distribution of properly amplified single PE signals is also not known.
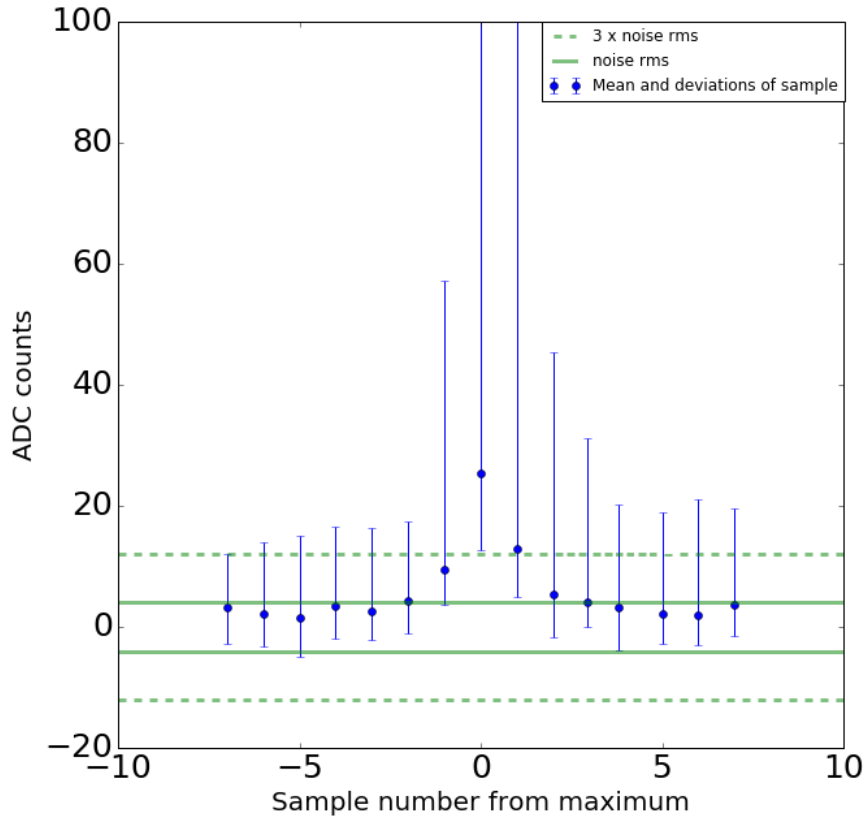
Figure 3.26: The mean value of samples around the pulse maximum positions plotted together with the calculated positive and negative statistical deviations. The solid green lines shows noise RMS and the dashed green lines illustrate 3 times noise RMS values.

In principle, one can assume the multiplication factor from every dynode stage is described by a binomial distribution. Having several dynodes with different multiplication factors (set by the voltage divider circuit on the PMT base), and considering the quantum efficiency as an extra parameter, some sophisticated studies were done to simulate the final distribution using Monte Carlo techniques [157, 158] or complicated statistical approximations [159]. Some other references suggest estimation of this output distribtuion simply by Gaussian distribution [160]. For the XENON1T PMT calibration software, the latter was found to provide good fits to the observed spectra.

Hence, the XENON1T PMT calibration software uses the following function to fit the single PE spectrum.

$$f = A_0 \times exp(-\frac{(x - x_0)^2}{2\sigma_0^2}) + A_{UA} \times exp(-\frac{(x - x_{UA})^2}{2\sigma_{UA}^2}) + \sum_{n=1}^{N} A_n \times exp(-\frac{(x - x_n)^2}{2\sigma_n^2}) \qquad (3.2)$$

$$x_n = nx_1, \ \sigma_n = \sqrt{n}\sigma_1, \ \frac{A_n}{A_{n-1}} = \mu_n \qquad (3.3)$$

The first term, denoted with index 0, refers to the noise distribution. The noise and baseline fluctuations are assumed to be Gaussian distributed around the baseline. It often occurs that the noise consists of several components. In such case, the software automatically neglects the components with smaller amplitude and fits only the largest component of noise, which has the most significant impact on the single PE part of the spectrum (see figure 3.27).

The second term in equation 3.2 refers to the under-amplified (UA) signals which are also assumed to be Gaussian-distributed. The range for x_{UA} parameter is restricted between 0 to 0.5 times the mean position of a single PE pulse, x_1.

The last term in equation 3.2 is a sum over Normal distributed terms from 1,2,3 or more photo-electrons. The number N is usually 2-3 depending on the light settings. The amplitudes, A_i, are normalized by Poisson nature of the number of observed photo-electrons. The position of the peak that corresponds to n PE, is forced to be equal to n times the position of 1 PE expectation value, and the variance of the n PE distribution with respect to 1 PE is fixed as well.

The software consists of several plugins that are used in series to perform an automated fit to the spectrum. First, the processed data, from the output of the modified version of PAX, is accessed, and the area of pulses are used to plot the single PE spectra for all PMTs. Then, a plugin is used to scan the spectra, and look for the features representing a typical single PE spectrum, for other plugins that use this information as a prior:

- Noise top: Maximum of the noise peak.

- Plateau: Point where the noise peak reaches the SPE distribution. This may indicate the valley, or an additional noise component.

- Valley: Minimum between the noise and the single PE peak. Some spectra may not have a valley, but will have the plateau instead.

- SPE top: Indicating the top of the single PE peak.

The spectra can appear in various shapes, depending on the light settings, noise conditions, PMT HV settings, etc. Hence, a plugin is programmed such that it can classify the spectra for several types, regarding the presence or absence of the mentioned features. Figure 3.27 illustrates two examples of the SPE spectra, over which this plugin is applied.

Next, another plugin fits the spectrum in the reasonable range, that is expected to belong to SPE or noise pulses, based on the points derived from the scanning plugin. Gaussian functions are used for such fits. The values from these fits are used as initial search values, when the software attempts to fit the full spectrum with the sum function. This process increases the success (merge) rate (meaning to minimize the number of fits that fail to converge), and the computing power efficiency of the fitting process. Examples of spectra which are fit by initiating functions, and the sum function, are shown in figure 3.28

The results of the final fit are converted to physical units following equation 3.4, and are saved in a file that is transferred to a database where all PMT calibration results are stored. These values are used for analysis and diagnostic purposes throughout the operation of the detector.

$$\text{Gain} = \frac{R\ \mu}{A\ f\ Z\ e}[\text{ADCcounts}], \tag{3.4}$$

where μ is the mean of the SPE peak from the fit, A is the amplification factor from amplifiers on PMT signals ($\times 10$ in this case), f is the sampling frequency of the ADC modules (10^8 Hz), Z is the impedance of the readout ($50\,\Omega$), and e the electron charge (1.60218×10^{-19} C). ·
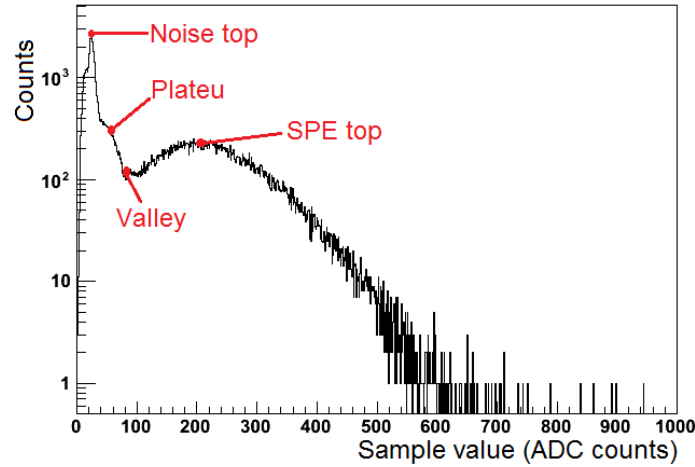
Figure 3.27: Example of the single PE spectra from the XENON1T PMTs. The PMT calibration software first scans the spectra and looks for the typical features that can be used for the fitting routines.
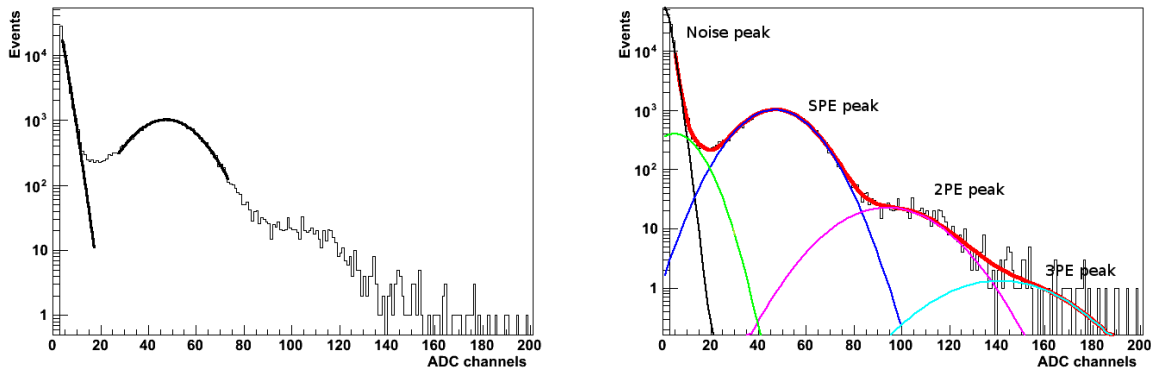
Figure 3.28: Examples of the single PE spectra from two of the XENON1T PMTs after initialization fits (left) and final fit (right) are carried out by the PMT calibration software.

3.6.3   Graphical User Interface (GUI)

As mentioned earlier, the automated fitting which is implemented through the PMT calibration software may fail to properly fit all the spectra for every calibration run. This might occur due to changes of the response of a certain PMT, change of noise conditions, or faulty behavior of some electronic module (e.g. amplifier, ADC, cables, connectors, etc.). Therefore, it is foreseen that the user can visually check the fits and their quality factors for every run. A GUI plugin is provided using Python graphical library, "TkInter".

The GUI allows the user to perform the PMT calibration data processing, analysis and input/output handling through a single platform. Figure 3.29 shows an example PMT single PE spectrum displayed through the GUI.
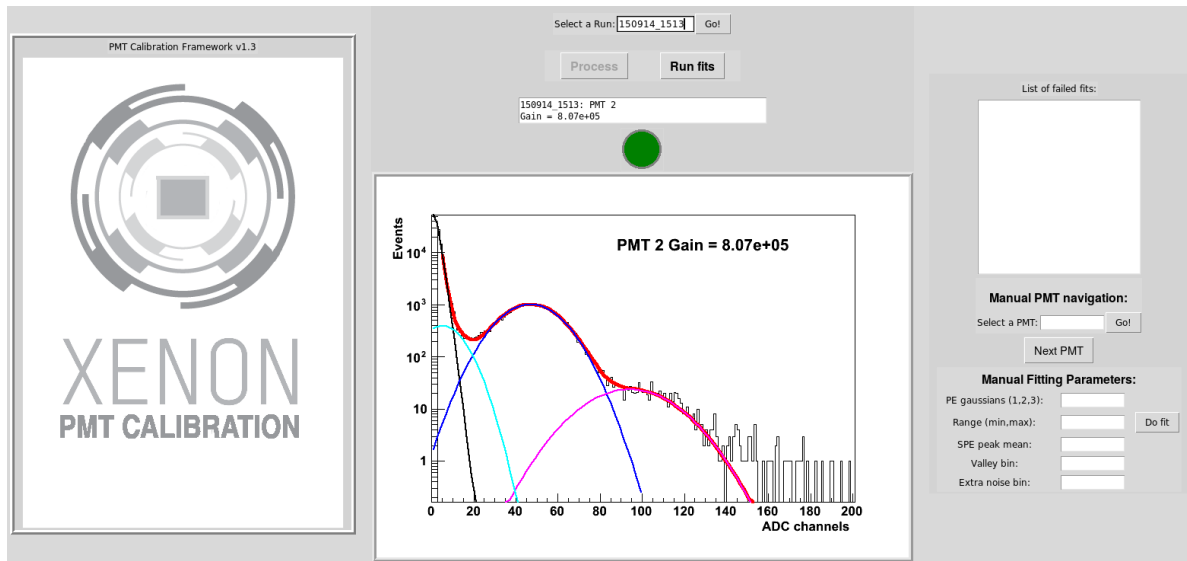
Figure 3.29: An image of the PMT calibration GUI with a PMT single PE spectrum being displayed.

The user needs to provide the date and time corresponding to the acquired data which is to be analyzed. By clicking the "process" button, the raw data processor will find and process the specified dataset, and will store the output in a dedicated folder within the analysis machine. Then, by clicking on "Run Fits", the GUI operates the analysis software, that accesses the processed data automatically. The fits will be displayed on the GUI platform, and a list of fits with low quality parameters (e.g. χ^2 and resolution) will be displayed over the panel on the top right. Once the user has visually verified that the all fits are properly applied, he can select all PMTs within the low quality fit list and manually supervise the fitting algorithm, until a reasonable fit is achieved. In other case, when the fitting algorithm fails, the PMT channel(s) with low quality fits can be excluded from the output. This manual interpretation can be manipulated through a list of "support" parameters, that the user can allocate on the left bottom of the GUI platform and reapply the fitting process. The support parameters that can be manually adjusted include adding or reducing the number of Gaussian functions in the fit, the mean value and estimated range of the SPE peak, and the sample where the "valley" has appeared. A list of common issues that occur will be provided for the users, together with the procedure to manually procure the fits throughout the platform.

Once all the fits are verified both through visual inspection and automatic scanning of the quality parameters, the results will be stored as a list of output parameters in a separate file for every calibration. A web-based database is also provided for PMT specifications based on MySQL. All the information about PMTs installed in the detector, including producer datasheet, previous incidents, connected electronics, results of previous qualification tests, and the radioactive screening results are included in the database. In addition, all the weekly calibration results can be accessed through the database within a interactive map of the PMT arrays. The analysis working group can inquire all the calibration results from the database and process this into information useful for higher level analysis.

3.7   Alternative gain extraction method

The gain estimation method described in previous section is based on some approximations on the type of the distributions of single, double and several PE responses. A new method is recently developed [161], that makes no assumption on such distribution, and extracts the gain values statistically. As mentioned earlier, since the rather high level of noise amplitude raised the level of systematic uncertainties on the estimation of PMT gains using fitting method, the new method was actually used to calibrate the PMTs, as it was found to be less sensitive to such effects. Hence, the method is briefly described in this section.

The method requires acquisition of two consecutive datasets. In the first dataset, the LEDs are not pulsed (or actually, pulsed with small voltages, below the voltage required to overcome the photo emission work function), while the second dataset sends LED pulses. All other electronic settings are shared between the two datasets. In this way, two separate distributions can be achieved, one with all pulses, including noise and dark-counts of the PMTs with no response of PMTs to low-intensity light from the LEDs. The mean value of the single PE distribution ($E[\psi]$) can be estimated using the following statistical expression:

$$E[\psi] = \frac{E[T] - E[B]}{\lambda}, \tag{3.5}$$

where λ is the mean number of photoelectrons induced by LED pulses, and $E[T]$ and $E[B]$ are the mean values of "LED-on" distribution and "LED-off" distribution, respectively. The values of $E[T]$ and $E[B]$ can be obtained through calculating the mean value of each distribution numerically. Figure 3.30 displays an example distribution of such acquired LED data for one of the XENON1T PMTs.

It is still assumed that the distribution of the number of photoelectrons produced by a strongly attenuated light source is to a very good approximation Poissonian, hence:

$$V[\psi] = \frac{V[T] - V[B]}{E[L]} - E^2[\psi] = E[\psi], \tag{3.6}$$

where parameter V denotes the variance of the distributions. Following the assumption above, the distribution of number of photoelectrons produced can be expressed in the following way:

$$L(p) == \frac{\lambda^p e^{-\lambda}}{p!}, \tag{3.7}$$

where $L(p)$ denotes the number of events including p photoelectrons. Hence, the parameter λ can be estimated:

$$\lambda = -ln((L(0)) \simeq -ln(N_0/N), \tag{3.8}$$

where N is the total number of triggers and N_0 is equal to the number of triggers with zero LED-induced PEs, calculated using the following equation:

$$N_0 = A_S \frac{N}{A_B}, \tag{3.9}$$

where A_B and A_S are fixed threshold cuts used to estimate the number of triggers with zero LED-induced photoelectrons in the "LED-off", and "LED-on" data respectively.
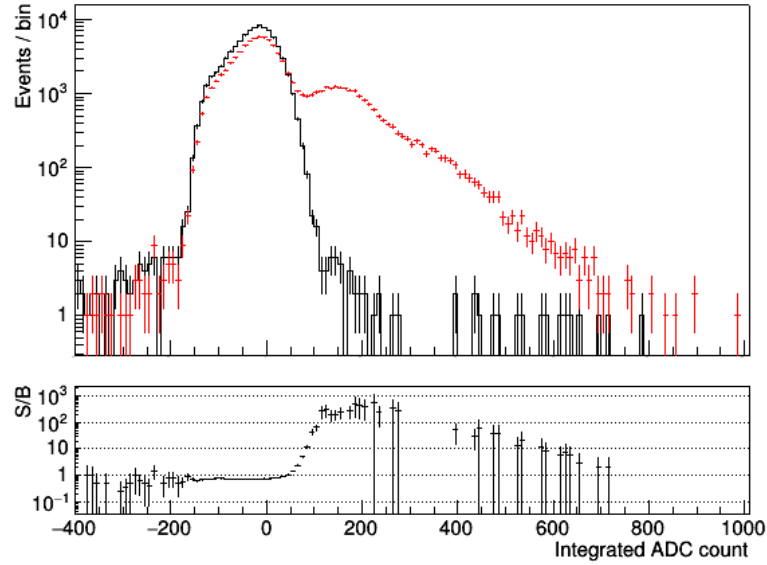
Figure 3.30: The signal area spectra from the two consecutive LED data acquired for one of the XENON1T PMTs in "LED-off" (black) and "LED-on" (red) modes. The bottom panel shows the residual differences.

Figure 3.31 illustrates the threshold values A_B and A_S for the "LED-off" and "LED-on" data. In the real analysis, these parameters are estimated through studying the variations of the estimated parameter λ, as a function of the threshold. The threshold is fixed at the maximum sample position, after which the estimated value of the parameter λ starts to decrease. The effects of the errors from evaluation of the threshold positions on the derived gain values are accounted for in the estimations of systematic uncertainties.

As another alternative method to calculate PMT gains, the response of PMTs to SPEs from PMT dark count and after pulses can be studied. In order to perform such a measurement, the single PMT hits are selected from events of a calibration data. The selection requirement passes only events in which only a single PMT has observed a hit. Since these hits are observed by only a single PMT, they mostly include the PMT dark count or afterpulses. Figure 3.32 shows an spectrum of the lone hits area observed by a PMT in a Rn calibration data of the XENON1T experiment.

Since such data is not acquired through the use of an external trigger with restricted search window for light signals due to short pulses sent to the light source, a peak-finding algorithm needs to be applied with a low threshold to select SPE signals from the noise and baseline fluctuations. This is done by applying an small threshold, set to a fraction of a SPE signal, for peak-finding through the raw data processor. As expected, the resulting measured response values are observed to be strongly dependent to the applied threshold.

In addition, the probability of detecting two or more PEs generated by the afterpulse signals varies for each PMT. This is because the rate of afterpulses is different for each PMT. Hence the unlike for the case of fitting SPE spectra from LED data that presumes distributions of single, double or more PEs with following a know (Poisson) statistics, for the fitting of the spectra using this method the ratio of the peaks referring to different distributions cannot be fixed. This effect
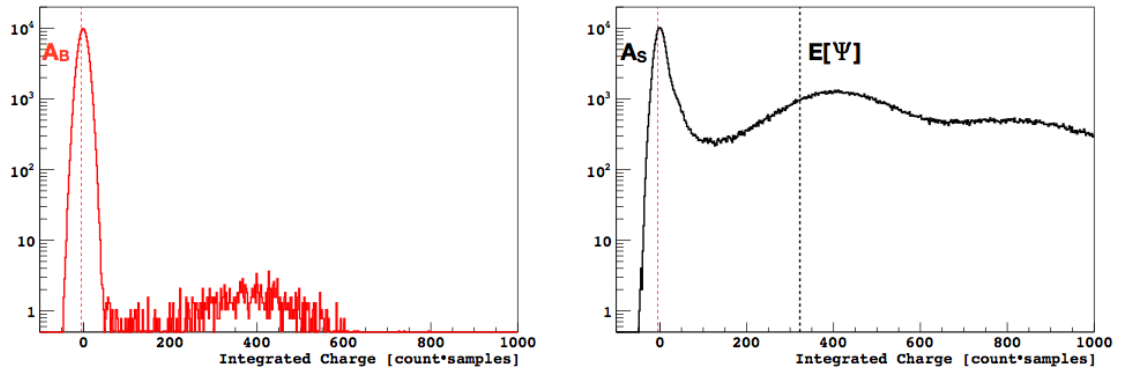
Figure 3.31: Example of the measured distribution of the PMT output charge for an "LED-on" (left) and a background run (right). The dashed red vertical line indicates the threshold cut used to estimate the parameter λ. The number of 0-PE triggers is calculated from the number of events that fall below the threshold cut, A_B and A_S. The solid black line in the right spectrum indicates the estimated single PE mean [161].
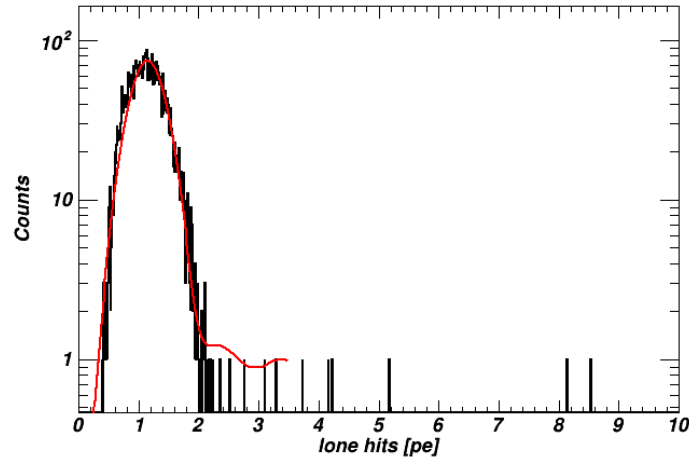
Figure 3.32: Example of a spectrum of the hit area from the events selected through a requirement of a single hit being observed by a single PMT from a Rn calibration data of XENON1T. The spectrum if fitted with several Gaussian functions to account for the distribution from single, double or more PEs observed by the PMT. The horizontal axis shows the hit area calibrated by LED data using the model-independent method.

introduces additional systematic errors on the evaluation of the PMT gains that need to be considered. Therefore, for the evaluation of the PMT response to SPE signals, only the LED method is used in the analysis of the XENON1T data.

3.8   PMT response to xenon scintillation photons

The main goal of the PMT calibration system described in this chapter is to measure the response of XENON1T PMT to single PEs detected by PMTs from photons generated by the blue LED light source. However, it is known that the response of PMTs is dependent also on the wavelength of the incident photons. The difference between the two raises by possible chances that a single photon detected by a PMT can produce either an under-amplified signal in the output through skipping one of the charge multiplication sections, or even a double photoelectron (DPE) signal. The chances for producing the DPE signal depend specially on the wavelength of the incident photon. While the probability of a DPE signal from a xenon scintillation photon with 175 nm wavelength is measured to be 18-24 %, such probability are expected to be negligible for a photon from a blue LED light source with 405 nm wavelength [153].

Once either of the two response parameters mentioned above are measured for a PMT, the other parameter can be estimated by accounting for the under-amplified or DPE production fraction. However, despite the measurements in reference [153], there is a lack of systematic evaluations of the precise values for DPE and under-amplified signal fractions. Different experiments either measure one of the two parameters regarding the relevancy for the analysis purposes or both.

The methodology that is described in the previous sections of this chapter suits the evaluation of the PMT response to SPEs. This is because due to negligible chances of DPE production using low-energy photons from an LED, one can statistically account for other deviations from observing SPE signals such as the under-amplified signals. For instance, using the fitting method, the under-amplified signals are fitted with a separate function and are excluded from the estimations of the SPE response. Also the probabilities of two or more photons reaching a PMT from an LED are well known to be Poission distributed, helping to reduce the degrees of freedom in the fitting function that might increase the systematic errors of the measurement.

However, for the XENON1T analysis, the response of PMTs to scintillation photons is also studied. The events with small S1 signals ($<$100 PE) are selected. The spectrum of the registered hit area for individual PMTs contains majorly single PE signals. Two example spectra of such distribution are shown in figure 3.33.

Such spectra can be fitted with Gaussian functions for the SPE peak and the under-amplified signals or DPEs. The mean value of the fit to the SPE peak is considered as the PMT response to scintillation photons. The method is expected to contain systematic bias to larger gain values due to the applied peak-finding threshold. It is also observed that the resulting gain values are correlated with the light collection efficiency at the position of each PMT.

3.9   Results

The commissioning of the XENON1T PMT calibration system, described in detail in this chapter, was successfully carried out by April 2016. Since then the system is being regularly used during the operation of the XENON1T experiment. The flow-chart shown in figure 3.34 shows the interactive process required for a particular PMT calibration run of the experiment together with the actions required by the user and the interfaces with other detector subsystems such as DAQ, slow control.

An approximated time required for a single PMT gain calibration run, using the fitting method or the model-independent method is 15 minutes or 1 hour, respectively. In addition, the processing of the raw data is expected to take as long as 1-2 hours. Once the processed data is accessible,
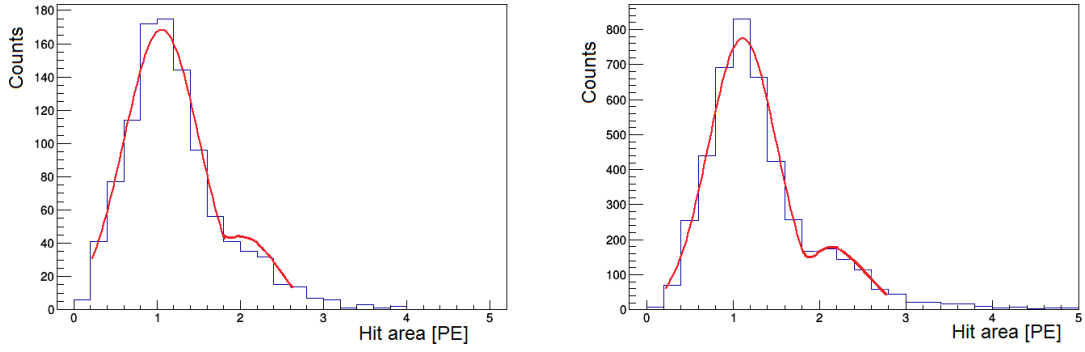
Figure 3.33: Examples of the fitted spectra of the hit area from the events selected through a list of events with small S1 signals from XENON1T background data. The spectrum if fitted with several Gaussian functions to account for the distribution from single, double or more PEs observed by the PMT. The horizontal axis shows the hit area calibrated by LED data using the model-independent method.
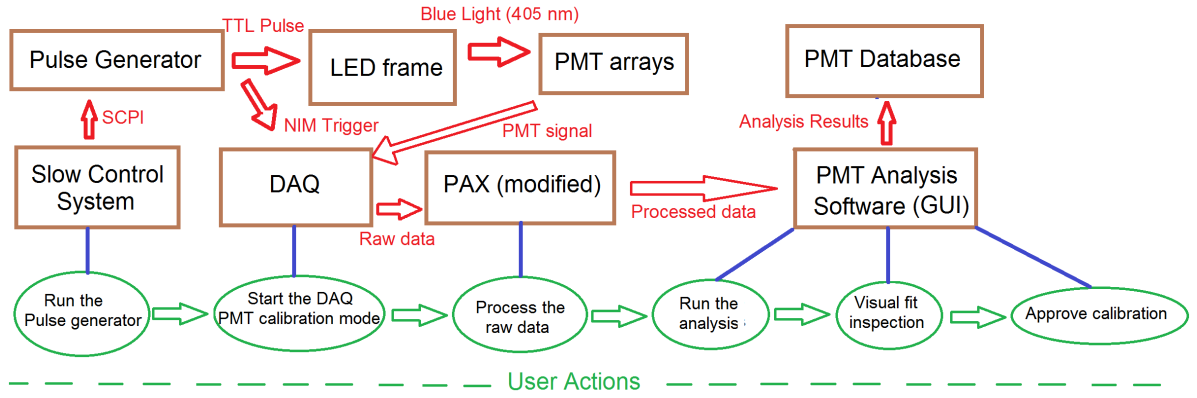
Figure 3.34: The process of a particular PMT calibration run of the XENON1T experiment displayed schematically. In addition, the interfaces of the PMT calibration system with other detector subsystems, such as DAQ and slow control are shown. The green flow-chart on the bottom illustrates the actions required from the user.

additional 20-30 minutes are required to perform a full analysis of the gain calibration data. Thus, a total of 4-5 hours are required to accomplish a full gain calibration of all PMTs. It is scheduled to perform the PMT calibrations at least once per week and before and after any change of experimental conditions (e.g. HV settings) or calibrations using sources.

The results of several month of continuous operation of the XENON1T experiment (11.2016 - 03.2017) shows that under steady conditions, the light intensity output of the PMT calibration system is very stable. Figure 3.35 shows the measured value of the occupancy number (λ, refer to section 3.5) for 4 PMTs versus time. The measured values of the PMT response are consistent within the expected systematic errors of the measurement. Figure 3.36 shows the measured gain

values for the same PMTs versus time. The measured occupancy is stable for all PMTs within a maximum deviation of 7-8 %.
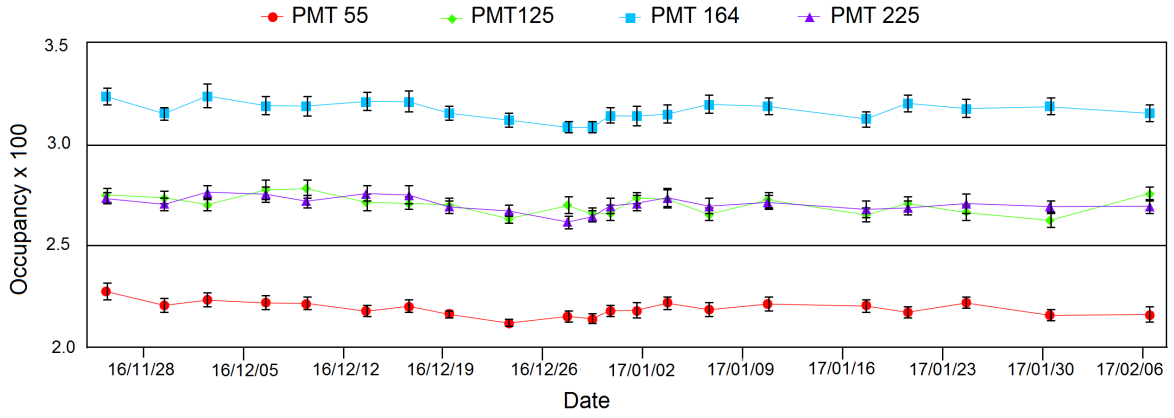
Figure 3.35: The measured value of occupancy number, λ, versus time displayed for 4 PMTs. The corresponding PMTs are chosen from the edge (55) and center (125) of the bottom PMT array and the edge (225) and center (164) of the top PMT array.
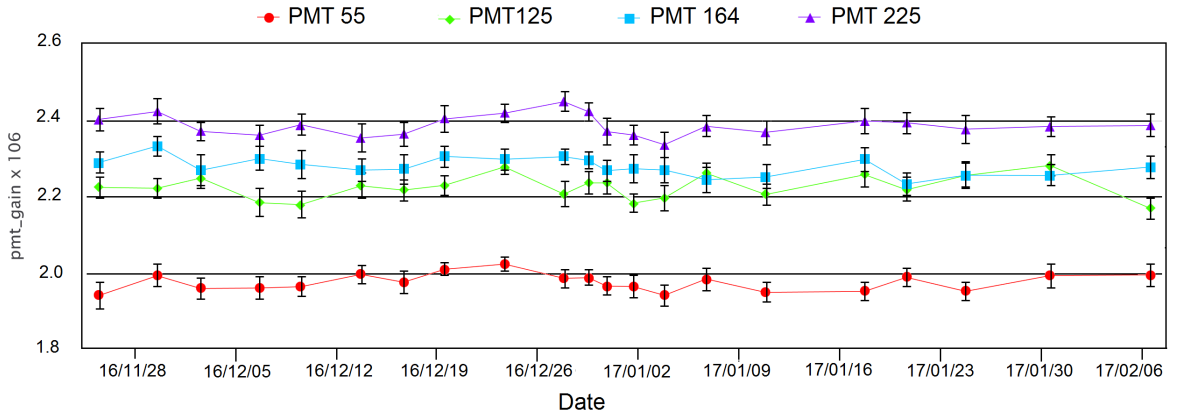
Figure 3.36: The measured PMT single PE gain value versus time, displayed for 4 PMTs. The corresponding PMTs are chosen from the edge (55) and center (125) of the bottom PMT array and the edge (225) and center (164) of the top PMT array.

3.10   Summary and discussions

The PMT calibration system of the XENON1T experiment was designed, developed and tested at UZH using MarmotXL chamber. The choice of components was made based on the previous experience from the XENON100 detector, and considering the technical challenges foreseen during the construction of the XENON1T experiment. The installation of all components was performed

in several steps in parallel to the manufacturing and construction of other XENON1T subsystems such the TPC, cryogenic system.

A set of C++ scripts were provided to communicate with the pulse generator that is used for the PMT calibration system of the XENON1T detector. The resulting software was tested within the test setup at UZH. Later, the same software was translated into the ladder diagram scripts that are used for the general remote control software of the experiment. These new software was developed and commissioned in collaboration with the slow control working group.

After the installation of the XENON1T TPC and DAQ systems, the PMT calibration system was commissioned in collaboration with the DAQ, PMT, and slow control working groups. The LED light intensities were tuned to the desired level for PMT calibrations and after-pulse measurements. Dedicated calibration modes were provided through the remote control software of the pulse generator, to be accessed and used by the responsible personnel. The system is currently in use since summer 2016, with no major problems reported until present.

The capabilities of the XENON1T raw data processing algorithm, included in PAX software, were investigated for the purpose of the PMT calibrations. The peak finding and pulse integration algorithms of PAX were noted to represent undesired bias effects on the evaluation of the PMT response to single PE signals, and hence, the corresponding plugins were modified within PAX in order to meet the requirements for this analysis.

A GUI software was developed, based on Python programming scripts, that provides interactive platform for the users to analyze the PMT calibration data. In addition, the GUI provides possibility for visual inspection of the fits on SPE spectra, that are used to extract PMT gain values. Moreover, a possibility for an interactive improvement of the fits is provided within the platform.

Due to presence of a periodic noise on most XENON1T PMT signal channels at the time this PhD work, the mentioned analysis software failed to obtain results from the PMT calibration data with expected quality, as the noise amplitude was for most channels at the same range as of the SPE signals. This study had provided a motivation for a noise reduction campaign, that later resulted in significant improvement of the noise conditions. In the meanwhile, an alternative method was provided that was less sensitive to noise, and thus was used for the calibration of the PMTs.

Currently, with the improved noise conditions, both methods are used to calibrate the PMT signals, providing independent references for evaluation of PMT response that can be used for systematic cross-checking. Figure 3.37 shows the measured gain values from both methods for all PMTs.

As shown in figure 3.37, the gain values calculated by the fitting method are in most cases higher than those measured by the model-independent method by an average difference of 13.4 %. This is attributed to the improper evaluation of the under-amplified signals in the SPE spectra by the fitting method and is currently under investigation. This might lead to a biased evaluation of the gain toward larger values. As it is seen in figure 3.38, the relative differences are constant within the measurements errors for most PMTs.

Similarly, comparing the gain values using PMT dark count pulses, explained in section 3.7 with the values of the model-independent method is performed. In figure 3.39 the PMT gains calculated by the this method are plotted for all PMTs in the units of PEs calibrated by the LED data using model-independent method. The resulting gains are also larger and the median ration is 11.2 % respective to the gains from model-independent method. This is attributed to the systematic bias expected for this method caused by the applied peak-finding threshold and the afterpulse signals. The calculated gain values are observed to be correlated with the relative afterpulse rate of the PMTs.

Finally, as mentioned in section 3.8, the response of the XENON1T PMTs to scintillation pho-
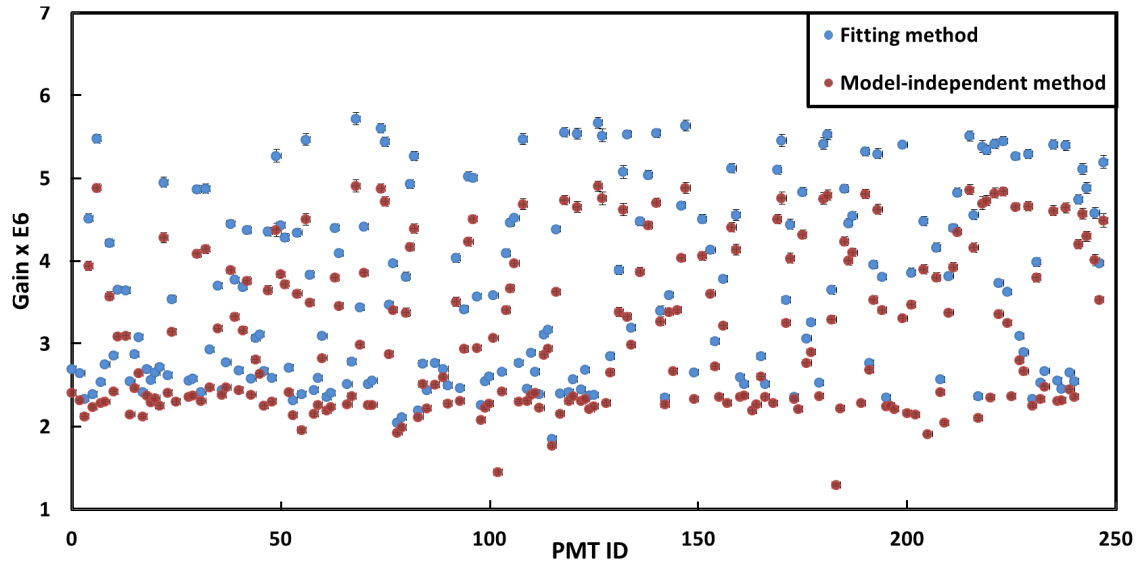
Figure 3.37: The gain values evaluated by the fitting (blue) and model-independent (red) methods of gain extraction for the PMTs in the XENON1T detector.

tons has been also studied. In figure 3.40 the delivered gain values are shown in the units of number of observed PEs according to the PMT gain values using LED data. The median gain ratio compared to the values from model-independent method are 1.05 and 1.07 for the top and the bottom PMT arrays respectively. The deviations are attributed to the expected bias from the applied peak-finding threshold as well as from the fit to the spectra since the DPE fraction can be not completely accounted for. The calculated gain values are correlated also with the light collection efficiency at the position of each PMT.
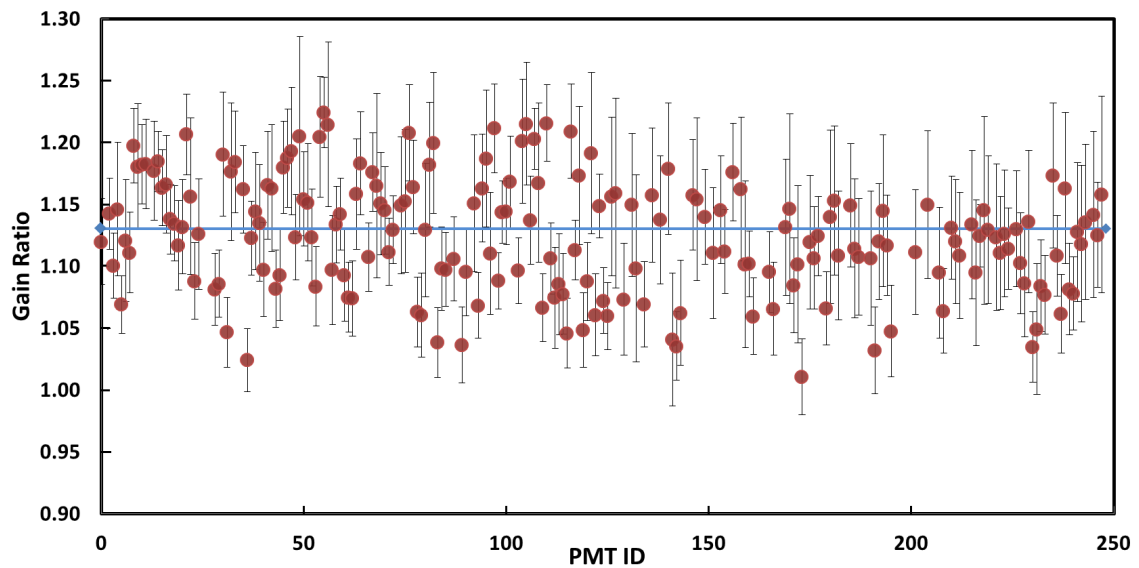
Figure 3.38: The ratio between the PMT gain values measured by the fitting and the model-independent methods for all XENON1T PMTs. The solid blue line shows the average ratio for all PMTs.
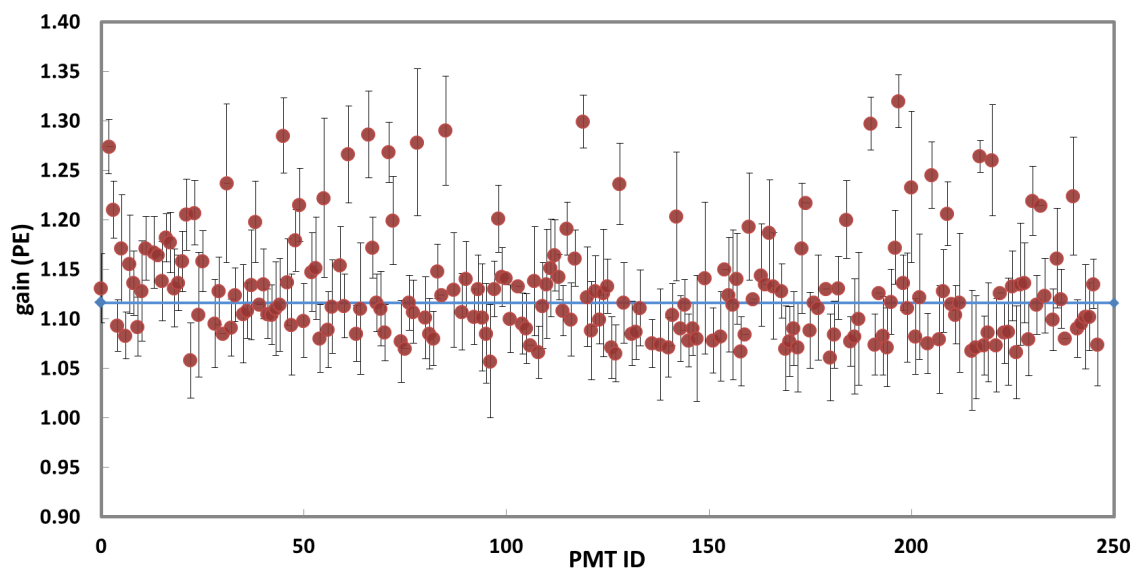
Figure 3.39: The gain values measured for all XENON1T PMTs using single hits registered on individual PMTs from Rn calibration data. The gains are reported in units of PEs from PMT calibrations using LED data. The blue line shows the median gain for all PMTs.
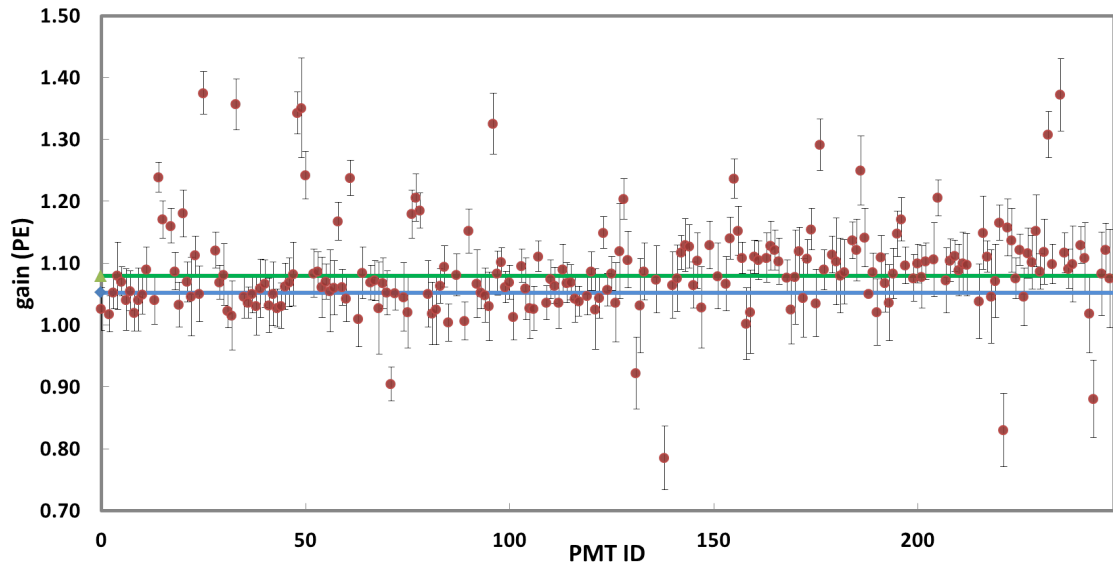
Figure 3.40: The gain values measured for all XENON1T PMTs using small S1 signals from XENON1T background data. The gains are reported in units of PEs from PMT calibrations using LED data. The blue and green lines denote the median gain for the PMTs from the top and bottom arrays, respectively.

Chapter 4

Measurements of the low energy response of liquid xenon with the Xurich II detector

4.1 Motivation

The energy deposited in a xenon target can be calculated from the S1 and S2 signals using the following equations:

$$E_{nr} = \frac{S1 \times S_{er}}{L_Y \times \mathcal{L}_{eff} \times S_{nr}} = \frac{S1 \times S_{er}}{L_{Ynr}(E_{nr}) \times S_{nr}}; \tag{4.1}$$

$$E_{nr} = \frac{S2}{Q_Y(E_{nr}) \times \epsilon}, \tag{4.2}$$

where L_Y[PE/keVnr] is the light yield for electronic recoils at $122\,\mathrm{keV}$, S_{er} and S_{nr} are the suppression factors of the photon production due to quenching effect in presence of an electric field for ERs and NRs respectively, and ϵ denotes the detected photo-electrons (PE) per extracted electron. $\mathcal{L}_{eff}$ is the relative scintillation yield of NR to ER, normalized relative to the value measured for the $122\,\mathrm{keV}$ gammas from $^{57}\mathrm{Co}$ radioactive source, and $Q_Y[e^-/\mathrm{keVnr}]$ and $L_{Ynr}[\gamma/\mathrm{keVnr}]$ are the absolute ionization and scintillation yield for NRs,respectively.

Figures 4.1 and 4.2 show the results of all existing measurements of $\mathcal{L}_{eff}$ and Q_Y, respectively [162]. None of the experiments have measured the xenon response to NRs for energies below $3\,\mathrm{keVnr}$, except for the very recent measurements in reference [116].

The uncertainties on the measured values for the ionization and scintillation yield of xenon in response to nuclear recoils are relatively large below $5\,\mathrm{keVnr}$. The expected WIMP interaction rate is the highest at lower energies (see figure 1.8). Moreover, there is a discrepancy between the theoretical models that provide estimations of these parameters (e.g. NEST [162]) and the measurements from experimental data. Hence any possible measurement that can reduce the uncertainties of these parameters can lead to a significant improvement on uncertainties of the current and future large scale WIMP search xenon detectors.

The Xurich I liquid xenon TPC was built and used at the University of Zurich (UZH) to measure the response of liquid xenon to low-energy Compton electrons [113]. The detector was later upgraded (Xurich II, shown in figure 4.3) by minimizing the amount of inactive materials in order
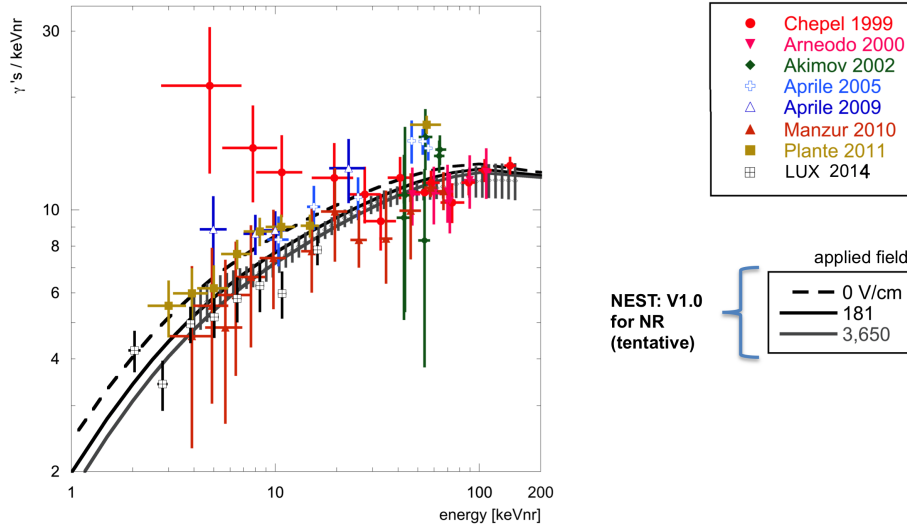
Figure 4.1: Results of the measurements of the absolute scintillation yield for nuclear recoils as a function of the nuclear recoil energy [162]. The lines represent the model from NEST (Noble Element Simulation Technique [162] for different applied electric fields.

to reduce the uncertainties due to multiple scattering. If the particle scatters within the inactive material before it reaches the active volume, its energy differs from the expected initial energy from the source, resulting in systematic errors on the measurements of the recoil energy.

A small active volume (3.1 cm height and 3.1 cm diameter) is used in order to reduce the systematic uncertainties in determination of the scattering angles. This is important as there are only two photomultiplier tubes (PMTs), used one at the top, and one at the bottom of the TPC, and hence reconstruction of the radial position is not possible. The upgraded detector is designed to be used in a setup which is shown in figure 4.3, together with a D-D neutron generator, and a liquid scintillator detector (EJ301 [114]) for tagging the scattered neutrons. The setup aims to measure the response of liquid xenon to NRs down to 0.5-0.6 keVnr.

As shown schematically in figure 4.4, by exposing a xenon target to mono-energetic neutrons, using a second detector for tagging scattered neutrons at a known angle, the xenon response to NRs at different energies can be studied, varying the scattering angle. If a neutron with initial energy E_n scatters off an atom with mass number A, at an angle θ, the energy transferred to the nucleus (E_{nr}) can be determined using the following relation, which is derived directly from the kinematics of the interaction:

$$E_{nr} = \frac{2E_n}{(1+A)^2}[1 + A - \cos^2(\theta) - \cos(\theta)\sqrt{A^2 + \cos^2(\theta) - 1}]. \qquad (4.3)$$

In order to measure this parameter with high precision, the systematic errors of the experiment on the measured values of E_n and θ have to be minimized. For the neutron measurement setup at UZH, as shown in figure 4.5, 14.5 % resolution (sigma over mean value) was measured on the initial energy of neutrons around 2.45 MeV peak [163]. While the distribution that is observed in figure 4.5 refers to a measurement using two liquid scintillator detectors serving as both scattering and tagging targets, the expected width of the recoil energy observed by the xenon target is of the
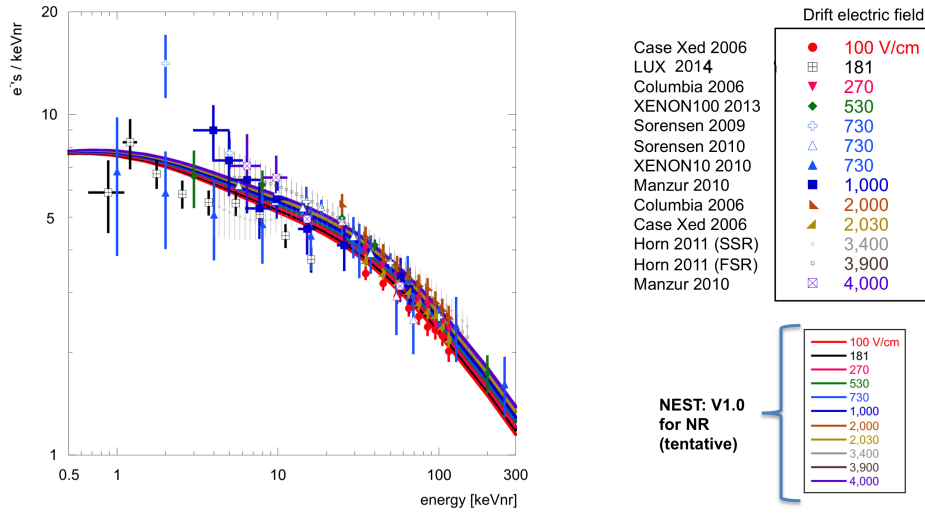
Figure 4.2: Results of the measurements of the Q_Y parameter as a function of the nuclear recoil energy [162]. The lines represent the model from NEST (Noble Element Simulation Technique [162] for different applied electric fields.

same range ($\sim 15\,\%$), according to MC simulations [172].

There is a single PMT installed in the EJ301 liquid scintillator detector and 2 PMTs on the top and bottom of the Xurich II TPC. Hence no radial position reconstruction is possible and the diameters of the EJ301 ($7.0\,\mathrm{cm}$) and Xurich II TPC ($3.1\,\mathrm{cm}$) will introduce a systematic uncertainty on the evaluation of the scattering angle θ. This can however be controlled only by increasing the distance between the scattering and the tagging targets, sacrificing the coincidence event rate. As an example, at the distance of $1\,\mathrm{m}$ between the two targets, the estimated geometrical uncertainties are $6\,\%$ [163] from MC simulations.

If the detector dimentions are large enough, with respect to the $13\,\mathrm{cm}$ total mean free path for $2.45\,\mathrm{MeV}$ neutrons [164, 165], instead of two separate scattering and tagging targets, double scatters within the same xenon volume can be used, in a similar method, for measuring xenon response to NRs (see reference [116] for instance). The advantage is that, since a resolution below $1\,\mathrm{cm}$ can be achieved on the position of the two interactions, the calculated value for θ is more certain (except for larger detectors where the position reconstruction resolution is worse). However, it is more complicated to evaluate the distribution of the initial energy of neutrons before the first scattering in this case, due to the possible inelastic scattering of neutrons off the atoms of other materials on its way (e.g. water inside the Cherenkov veto, cryostat, etc.). This requires a more sophisticated study of the energy distribution of incident neutrons to be carried out (see reference [166] as an example). Moreover, it is practically easier to use a small scale R&D detector for such measurements if the effect of varying other parameters such as liquid level, purity, or applied electric field is the subject of study. Besides, using separated scattering and tagging target has the advantage of easing the tagging of the coincidence events, through reduction of the accidental background event rate.
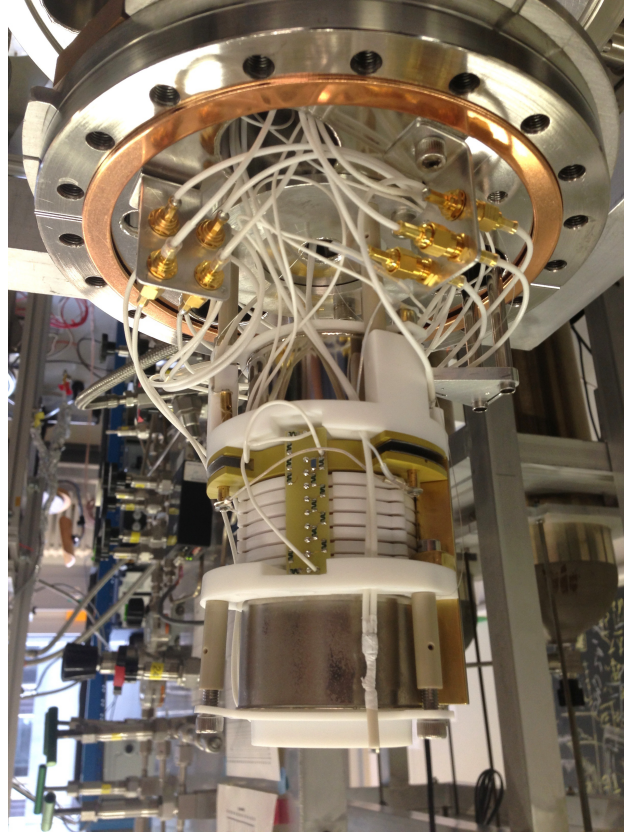
Figure 4.3: A photograph of the Xurich II detector. The TPC is seen with the top and bottom PMTs installed together with the filed cage and the voltage divider circuit. Also, the readout cables of the PMTs and the levelmeters are visible.

4.2   The Xurich II detector

The detailed description of the Xurich I detector can be found in reference [167]. However, since the Xurich II detector inherits most of the subsystems designed for Xurich I (e.g. gas system, cryogenic vessel, PMTs, and etc), those systems are also concisely described in this section. A rendered CAD model of the detector can be seen in figure 4.6.

4.2.1   Cryogenics and gas system

A vacuum-insulated cryostat is used to provide insulation from heat exchange with the environment, as shown in figure 4.7. A copper cold finger, also vacuum insulated, is immersed in a liquid nitrogen (LN) bath, at $77\,^{\circ}$K. The cold finger attaches to the bottom of an aluminum can, that in turn attaches at the top to the stainless steel vessel containing the TPC. The path of heat flow is thus from the stainless steel vessel to the aluminum radiation shield, from there to the copper cold finger, and finally to the liquid nitrogen bath.

Resistive heaters are located on the top flange of the cryostat, and are powered by a Cryocon model 34 temperature controller [168]. This allows for controlling the temperature, and hence the
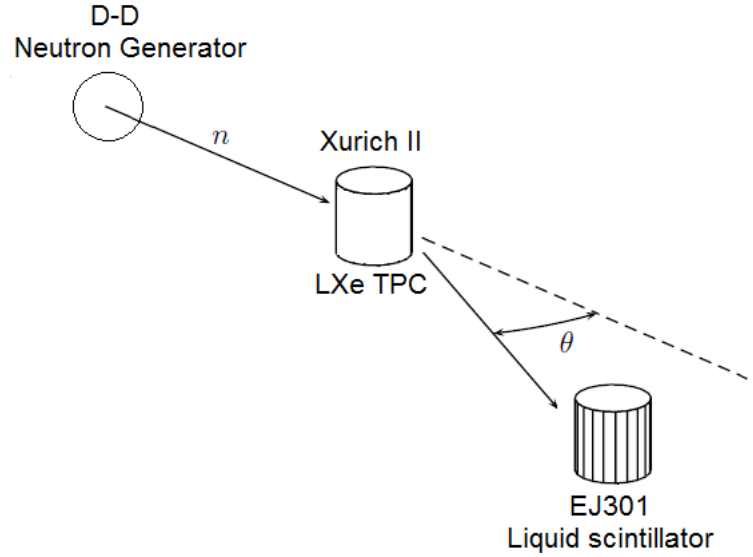
Figure 4.4: Schematic of the setup for measuring nuclear recoil response of xenon at UZH. The neutrons from the D-D neutron generator scatter off the xenon atoms within the Xurich II TPC at an angle θ, and are tagged using a liquid scintillator detector.

pressure, within the TPC, with a long-term stability. Two temperature sensors are placed in the system, located on the bottom of the TPC (LXe), and on the top flange of the inner cryostat vessel. Figure 4.8 shows the measured temperature from both sensors during the cool-down process and filling of xenon. A pressure sensor monitors the GXe pressure in the system.

An automated LN filling system is instrumented with a solenoid valve connected to a LN dewar. The valve is controlled by a readout device, that is connected to 2 temperature sensors. The sensors are placed inside the LN can at two different heights. The device starts the filling when the LN level is below both sensors (due to evaporation), and the process stops once LN covers both sensors.

A dedicated gas system was designed and constructed for the Xurich experiment, that allows for safe filling, recovery, and recirculation of the xenon gas within the detector. The system is mostly plumbed with $1/4''$ Swagelok connections [169]. A heated zirconium getter is used to purify the xenon through continuous recirculation and absorb the electronegative impurities and water molecules. The system is schematically shown in figure 4.9. It was upgraded for Xurich II project with the following main modifications.

- A ^{83}Rb emanation volume was appended together with a bypass line. When calibration of the detector using ^{83m}Kr radioactive source is required, the emanation volume is exposed and the bypass line is closed. Otherwise, the emanation volume is fully isolated from the system (see figure 4.9).

- The connections to the getter and recirculation pumps were reorganized, to allow monitoring of the xenon gas flow during recovery process. This facilitates continuous monitoring of the flow, during both filling and recovery. By integrating the gas flow over time, a measurement of the amount of gas, which is transferred can be performed online.
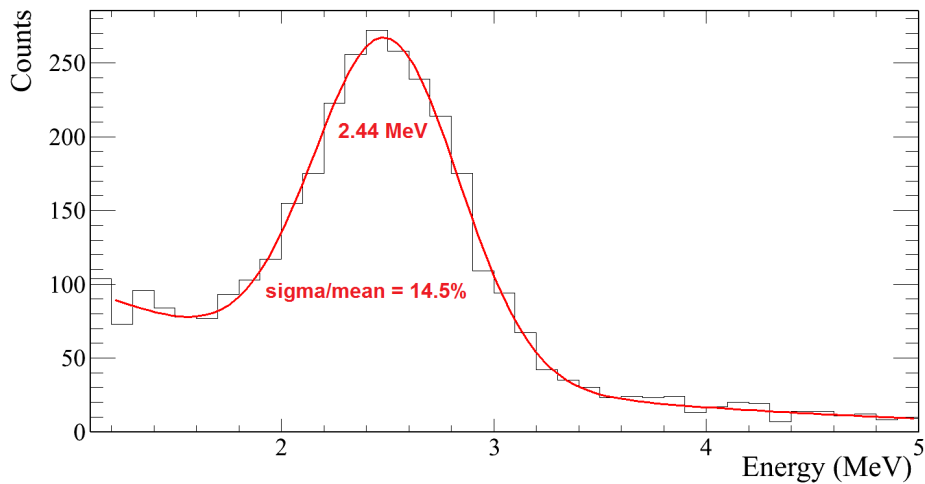
Figure 4.5: Measured energy distribution of neutrons from the D-D generator at UZH reaching the experimental hall, measured by two liquid scintillator detectors used as both scattering and tagging targets.

- An emergency bottle was added to the system, instrumented with a 1-direction differential pressure valve, which is calibrated to open when the pressure difference on the two sides exceeds 0.5 bar (only in one direction, from the detector toward the bottle). Hence once the pressure inside the chamber increases to dangerous regime (2.5 bar), the valve permits the gas to safely evacuate into the emergency bottle.

Figure 4.9 shows the schematics of the gas system, indicating the flow lines for the recirculation and recovery processes. Once the xenon filling is completed, the recirculation pump is turned on and the Xe is directed along the path indicated by the arrows. The flow rate of the xenon gas is controlled by a metering valve, indicated on the diagram in figure 4.9 as the valve icon with a diagonal arrow through it (number 10). The nominal gas recirculation flow for the Xurich II detector is 075-0.80 SLPM.

4.2.2   Data acquisition system (DAQ)

The schematics of the Xurich II data acquisition system are shown in figure 4.10 when it is operated in "general" data acquisition mode (e.g. detector calibrations, etc). However, for the final goal of this experiment, a different setup is used, which is described in the following. The latter is set in order to acquire data in coincidence with an additional liquid scintillator detector, serving as the tagging target. This coincidence setup is displayed schematically in figure 4.14.

The signals are digitised by a CAEN V1724 [140] flash analog-to-digital converter (ADC) module, with 10 ns sampling period, 2.25 V full scale, 14 bit resolution and 40 MHz bandwidth. The digitized signals are transferred to a computer through an optical fiber. The computer receives and stores the acquired data on a RAID storage, which is continuously being synchronized with a dedicated hard drive on the CPU cluster at the UZH Department of Physics.

Considering the rather high S2 yield of the detector (see section 4.7.1), and the PMT gains of 2-3 $\times 10^6$, large S2 signals (> 40 keV) exceed the 2.25 V range of the ADC module. Hence, while
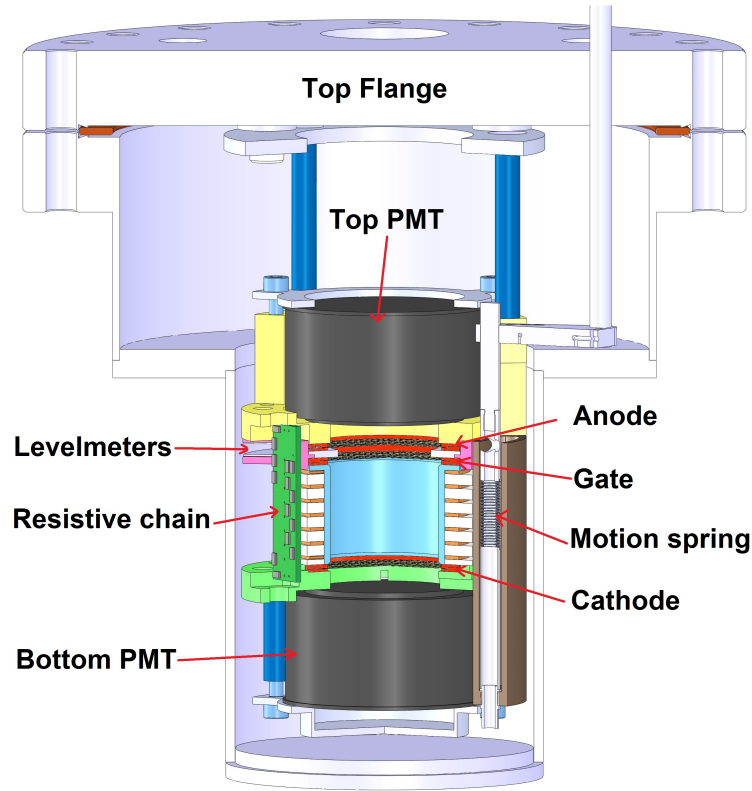
Figure 4.6: Rendered CAD model of the Xurich II detector. The PMTs are shown in black. The TPC consists of a reflective PTFE cylinder, colored in light blue and 3 electrodes, cathode, anode, and gate. It also includes copper field shaping rings, connected to a voltage dividing circuit.

taking calibration data, the signals are attenuated by a factor 10, to avoid saturation of the ADC module. In addition, as there was no protection provided for the ADC module internally, both PMT signals are initially connected to a fan-in-fan-out module (CAEN N625 [140]), that cuts off the signals at 2 V, before the maximum range of the ADC module is reached.

The trigger is generated by a CAEN N840 discriminator module [140], using the signals from the bottom PMT as input. This is because we aim to trigger on S1 signals for events at low energy, and bottom PMT receives (on average) larger S1 signals, due to both the higher quantum efficiency (PMT property) and light collection efficiency (detector property, due to reflection of photons at the liquid gas interface) of the bottom PMT, compared to the top one.

The discriminator level (threshold) can be adjusted manually. In our setup, as the maximum trigger acceptance at low energy regime is aimed, this parameter is set to its minimum level, above the noise and baseline fluctuation amplitude. This is achieved through studying the trigger rate by increasing the threshold from smallest values, as shown in figure 4.11. Hence, considering the noise level from the Xurich II electronics, that is limited to 5-6 mv in amplitude, the trigger threshold of 8 mV was used.

Having the threshold value set at 8 mV, one must verify the effective trigger acceptance for S1 and S2 signals at different energies. Therefore, a dedicated measurement was carried out, using two
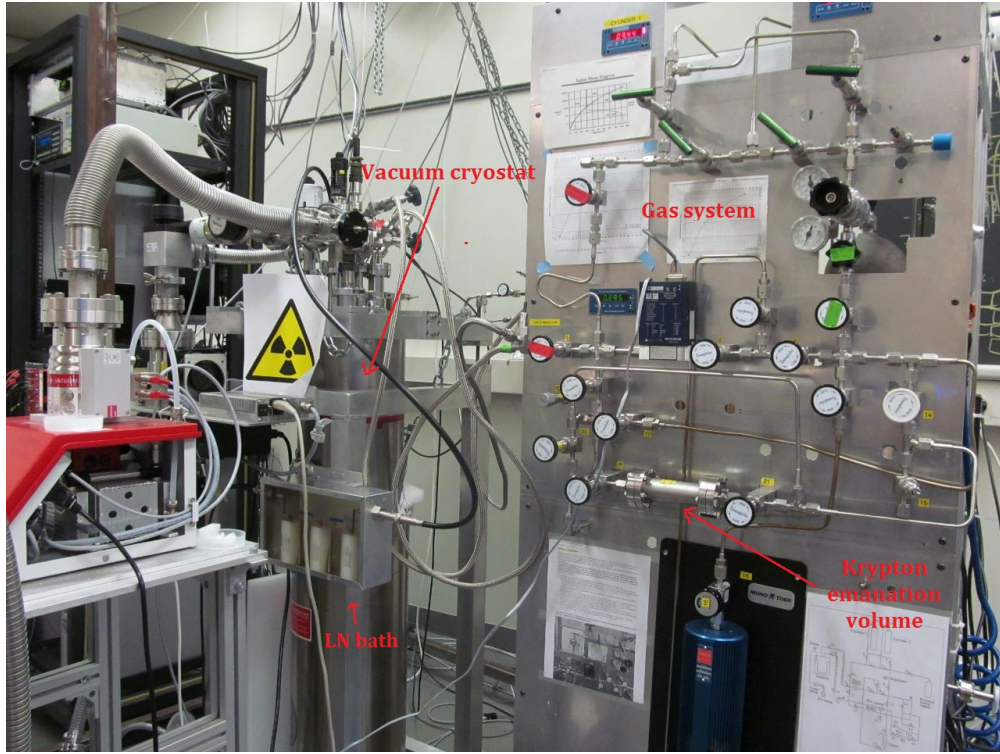
Figure 4.7: Photograph of the Xurich II detector and gas system. The outer cryostat is seen, which is continuously pumped to vacuum during operation. The container beneath the cryostat includes a liquid nitrogen bath which is used for the cooling of the system. The front view of the gas system is also shown, where the krypton emanation volume and the getter can be seen.

scalar modules, to monitor the number of generated and accepted triggers, while pulses of different amplitude were sent to the discriminator module using a digital pulse generator. The acceptance, defined by the ratio of the accepted to all generated triggers, was calculated for ∼10000 events at several amplitudes around the 8 mV threshold, and the results are shown in figure 4.12. However, as illustrated in the same figure, the acceptance was found to be also a function of the pulse width. For the measurements of acceptance the pulse width was fixed at $1\,\mu$s, comparable to the width of an average S2 signal (which is expected to generate the trigger at low energies). Therefore, we might need to take into account that the error bars on these measurements are under-estimated, due to ignorance of the trigger acceptance dependency on the pulse width.

Even though the error bars on measurements of the trigger acceptance are under-estimated for amplitude values close to the actual trigger threshold (8-8.5 mV), this is indeed not the case if the pulse amplitude is increased sufficiently higher than this value. It was observed that >8.6 mV, the measurements of trigger acceptance provide reproducible results of nearly 100 % acceptance, regardless of the set pulse width.

In order to convert the results on the estimated trigger threshold to S1 and S2 signal sizes, in figure 4.13, the S1 and S2 pulse area as a function of height are displayed for 32.1 and 9.4 keV signals from ^{83m}Kr calibration data (chosen in a range close to the pulse heights near the 8 mV
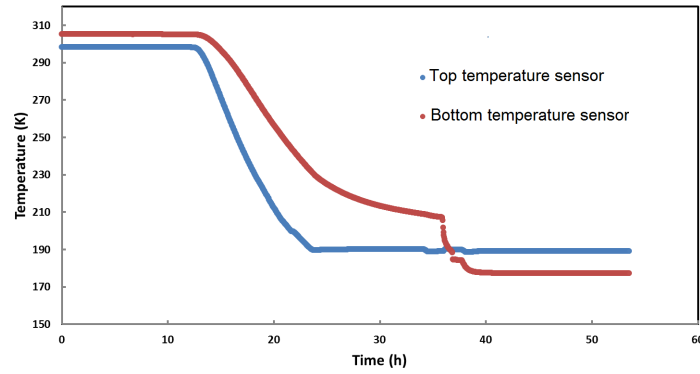
Figure 4.8: The monitored temperature within the Xurich II TPC fro the two sensors during cooling of the detector and filling liquid xenon.
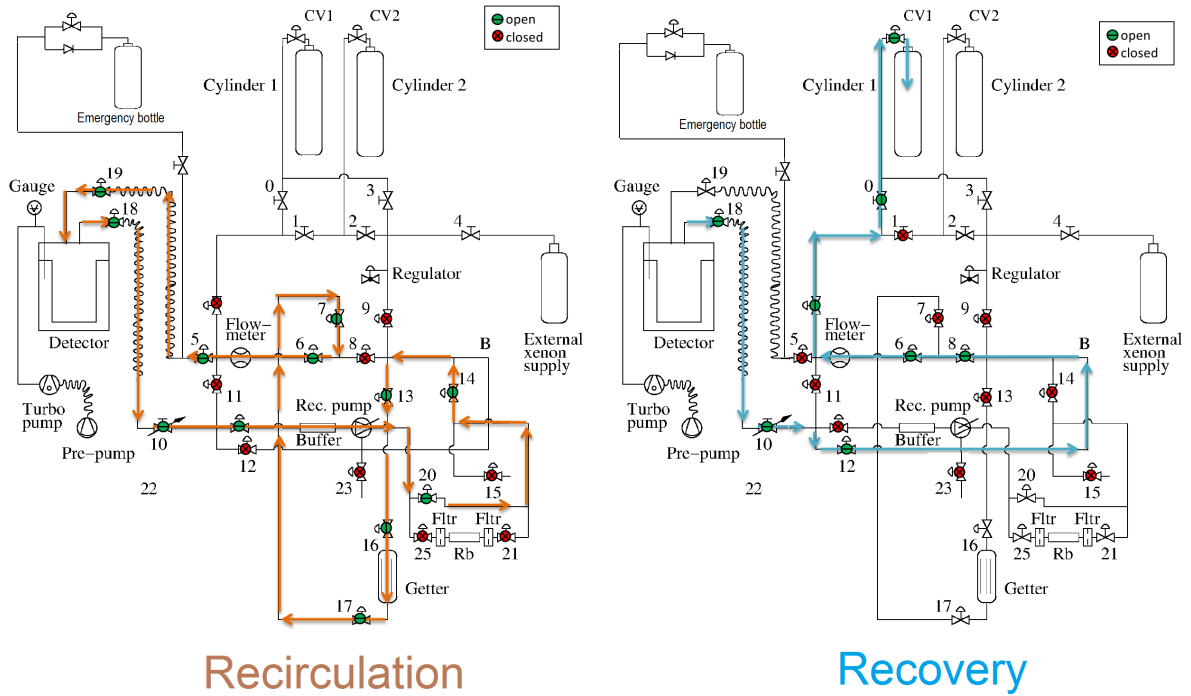
Figure 4.9: A schematic view of the Xurich II gas system. The GXe flow line is also displayed for recovery (left) and recirculation (right) modes.

trigger threshold). A linear fit to the event density profiles, within these parameter space, allows a conversion of event energy (area) to pulse amplitude, considering thats $1\,\mathrm{mV} = 7.28\,\mathrm{ADC}$ counts. Equations 4.4 and 4.5 show the resulting conversion factors for S1 and S2 pulses, respectively. As shown in the figure 4.13, the main population of $9.4\,\mathrm{keV}$ S2s is mostly distributed around $165\,\mathrm{ADC}$ counts, considerably far from the threshold at $\sim$60-70 ADC. Note that $\times 10$ attenuators are used for top and bottom PMT signals, which are removed for neutron coincidence measurements. From these
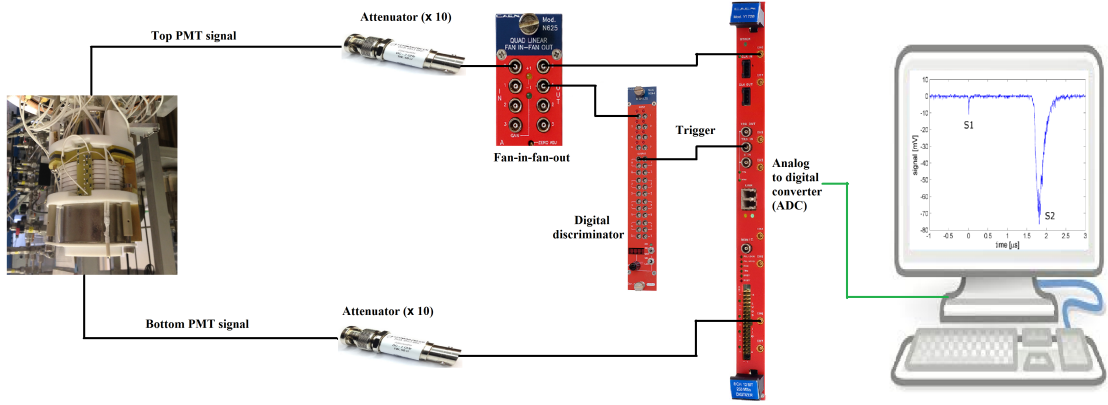
Figure 4.10: The schematics of the Xurich II data acquisition system described in the text.
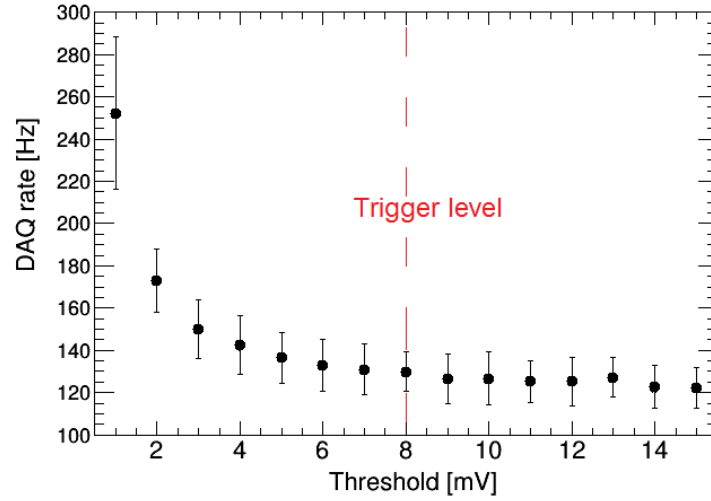
Figure 4.11: Total acquisition rates derived varying threshold values set on the discriminator module of the Xurich II electronics setup.

results, it is estimated that the setup exhibits 100 % trigger efficiency for ERs above 0.5-0.6 keV energy range. This can be further improved, if necessary for very low energy measurements, using an amplifier on the PMT signals.

$$S1[PE] \equiv 3.41(S1 \text{ Pulse Height}[ADC]) \equiv 0.47(S1 \text{ Pulse Height}[mV]) \tag{4.4}$$

$$S2[PE] \equiv 53.50(S2 \text{ Pulse Height}[ADC]) \equiv 7.35(S2 \text{ Pulse Height}[mV]) \tag{4.5}$$

In order to estimate the trigger threshold level for signals from nuclear recoil interactions, which are relevant for the aim of the experiment, the following approximations are made:

- The expected S1 and S2 sizes at the trigger threshold of 8 mV ($\simeq$60 ADC) are $\sim$11 PE and
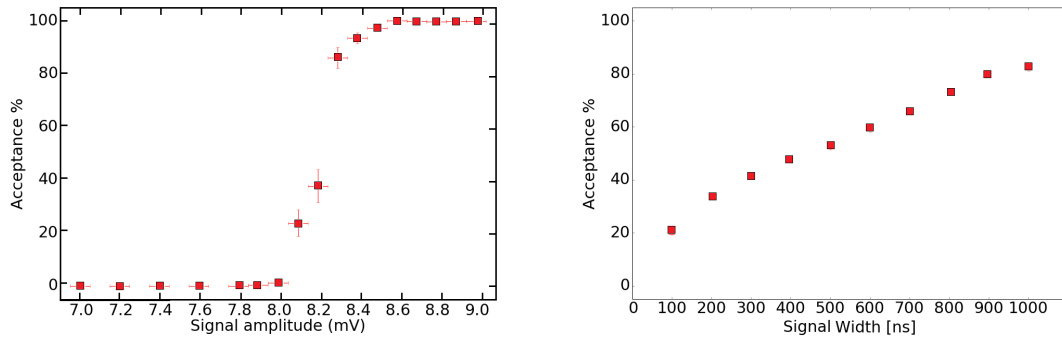
Figure 4.12: (Left); the measured trigger acceptance for various input pulse heights for fixed width at $1\,\mu$s. (Right); the acceptance varying the pulse width for pulses with fixed height at $8.3\,$mV.

$\sim 60\,$PE, respectively. This estimation is made based on conversion of S1 and S2 pulse height to area from equations 4.4 and 4.5;

- The measured S1 and S2 yields at low energies on bottom PMT (used for trigger), using $9.4\,$keV energy line from ^{83m}Kr calibration data (refer to section 4.7.1) are $10.6\,$PE/keV and $650\,$PE/keV, respectively;

- And the ratio of the S1 and S2 signal yields for ER to NR interactions at low energies (below $10\,$keV) are approximately 6.0 and 6.5, respectively. This is estimated by the comparison of the current measurement results of xenon scitillation and ionization yields for ER and NR interactions.

Therefore, it is estimated that the trigger threshold for the Xurich II DAQ for measurements of the nuclear recoil response corresponds to $\sim 0.6\,$keV and $\sim 6.1\,$keV considering S2, or S1 signals to generate the trigger, respectively. This can be easily improved, if necessary, using an amplifier on the signal cable reaching the input of the discriminator module (after fan-in-fan-out).

A different electronics setup is used for the neutron scattering measurements (see figure 4.14). In this case, the aim is to select events that correspond to a registered pair of interactions in the xenon TPC and in the tagging liquid scintillator (EJ301). Such events should mostly belong to elastic scattering of gammas or neutrons off the xenon and the atoms in the liquid scintillator detector.

As shown in the figure, the top and bottom PMTs are similarly read through the ADC module, and the trigger setup is the same as the "normal" data acquisition mode, except for removal of the attenuators. Following equation 4.3, the range of expected recoil energy through $2.45\,$MeV neutrons scattering off the xenon atoms is 0-30 keVnr. Hence, such interaction are not generally expected to produce large S2 signals, that saturate the electronic modules (i.e. fan-in-fan-out, or the ADC module).

The signal from EJ301 organic liquid scintalltor is fed into a dedicated pulse shape discrimination module, MPD4 from Mesytec [174]. This module is optimized for neutron-gamma discrimination (signal and background in this case). The "Amp" output of the module corresponds to the height of the input signal and hence is proportional to the energy of the interaction. The "PSD" output
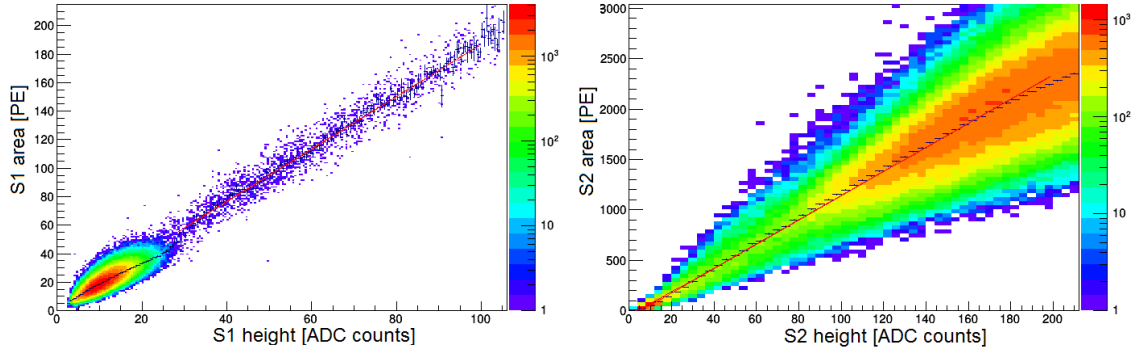
Figure 4.13: The S1 pulse area as a function of the pulse height for 32.1 keV population of events from ^{83m}Kr calibration data (left), and S2 area as a function of height for 9.4 keV events. The red line shows a linear fit to the evaluated event density profile, used to derive a conversion factor between the parameters.
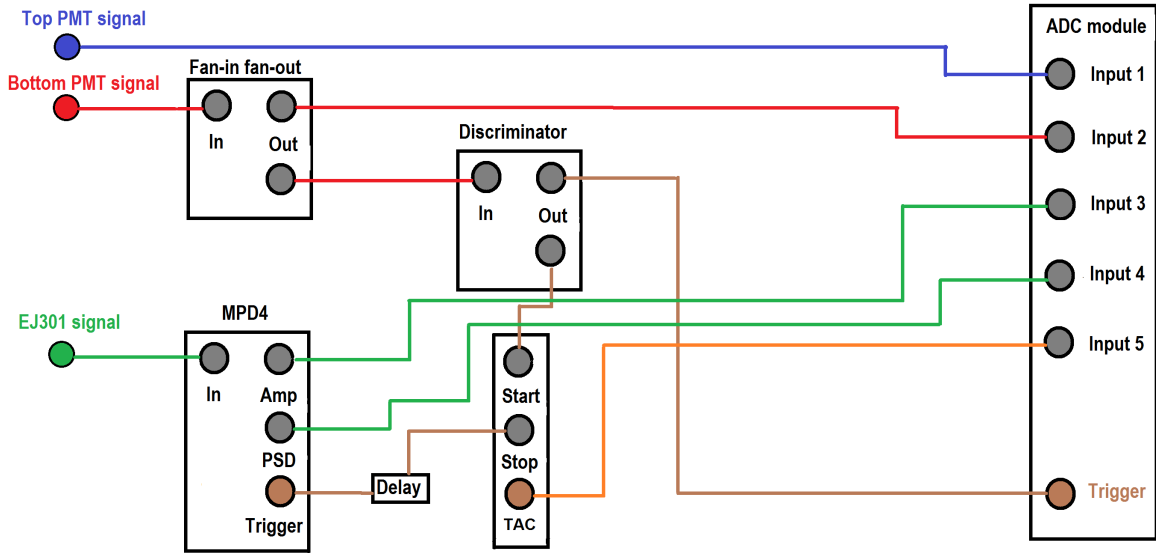
Figure 4.14: Schematics of the Xurich II data acquisition system when operated in coincidence mode.

denotes calculated pulse shape discrimination parameter. It is proportional to the fraction of the pulse tail to total area, as the pulses differ in their tail for NR to ER interactions (because the ratio of the triplet to singlet excited states differ). Moreover, there is a trigger output that produces a NIM signal from every input event. Both the "Amp" and "PSD" outputs of the MPD4 are also read by the ADC module. The characterization and calibration of these parameters are described in section 4.8.

Another very important parameter to be determined, along with the xenon TPC and scintillator

signals, is the time of flight (TOF), that takes for the scattered neutron (gamma) to travel between the Xurich II TPC, and the scintillator. This parameter can be used to calculate the recoil energy by subtraction of the kinetic energy from the initial energy of the neutrons (gammas). In addition, it can be used as an independent measure of the particle type (considering "fast" gammas and rather "slow" neutrons). Hence, a time to amplitude converter (TAC) module from ORTEC [175] is used to read the TOF. A separate output of the discriminator module is used as the "start" point of the TAC module. The trigger output from MPD4 is delayed by a value which is used to calibrate all the respective delays of the electronics system (e.g. cable lengths, internal delays of the other modules), to coincide the timing between the start and stop signals. And finally, the output of the TAC module is also read by the ADC module. Coincidence events are, in this case, selected through the analysis process, by picking events that have non-zero TOF value registered. The calibration of the TOF, for its conversion to physical units, is described in section 4.8.

4.2.3 Time Projection Chamber

The Xurich II dual-phase TPC contains a cylindrical active volume of 3.1 cm diameter and 3.1 cm height. The active volume hosts about ∼80 g of xenon. The TPC is made of polytetrafluoroethylene (PTFE), Torlon and polyetheretherketone (PEEK) (see figure 4.6).

An electric field is applied by a set of three electrodes, two of which are fixed on a Torlon spacer (anode and gate), and cathode. The electrodes are hexagonal etched stainless steel meshes (2.7 mm pitch), made of thin (0.1 mm thickness) plates. The optical transparency for the meshes is 93 %. The drift field, applied in the LXe volume is controlled by the cathode voltage and can be set up to 2 kV/cm. The extraction field, applied between the gate and the anode in the GXe volume, is above 10 kV/cm. This extraction field results in 100 % extraction efficiency for electrons that reach the liquid-gas interface [170]. The uniformity of the drift field is ensured by seven copper field shaping rings, separated by PTFE spacers. All the rings and the electrodes are connected through a dedicated voltage-divider circuit with a total resistance of 1.05 GΩ.

The electric field design was optimized based on simulations, using COMSOL [171, 172] and the KEMfield software, developed for the KATRIN experiment [173]. Figure 4.15 illustrates the electric field derived from KEMfield simulations. The mean deviation from uniformity in the target volume is 2.8 %. The nominal fiducial volume cut used for analysis removes 3 mm from the top and bottom, reducing the mean field deviation from uniformity to 0.9 %.
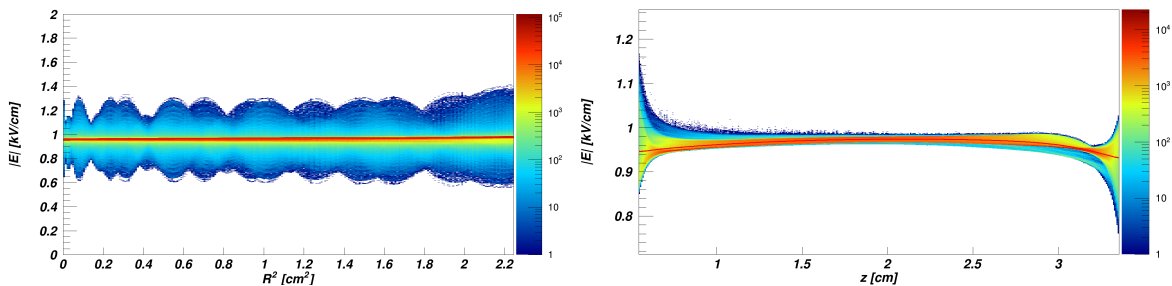
Figure 4.15: The simulated electric field as a function of radius (left) and height (right) of the Xurich II TPC for the optimized configuration. Plots from Julien Wulf.

Two 2-inch PMTs, model R9869 from Hamamatsu [117], are placed on the top and the bottom

of the active xenon volume, to readout the scintillation and ionization signals. These PMTs are equipped with synthetic silica (SiO_2) windows and 12 amplification stages (dynodes). The quantum efficiency of their photocathode is at least 175 nm is 35 % according to the producer.

The PMT voltage divider circuits that were developed for the Xurich I project, were initially used for the Xurich II experiment. In this version of the voltage dividing circuits, positive high voltage source was considered in order to allow for measurements of the xenon response parameters at zero field. This is because under this condition, the PMT body will be at ground (HV= 0) and hence, there will be no field in the TPC volume, in contrary to the configuration with a negative high voltage source, where the PMT body will also be at the negative high voltage. However, it was found that in response to large S2 signals (>1 V amplitude range), the waveform from both PMTs contain an overshoot and ringing features (see figure 4.16).

A dedicated study was performed to modify the electronic layout in order to prevent such behavior. For instance, in figure 4.16, an average waveform of 1000 events is plotted for two different configurations of the readout circuit, when the PMTs are exposed to artificial large signals ($\sim$1 V $\simeq$ 8000 ADC counts), sent from a pulse generator, and their response is studied. Finally, it was found that when the circuit is altered from positive high voltage source to negative, the mentioned features vanish. The modification of the circuit has the advantage of placing the dynode resistor chain (with high impedance) between the high voltage and signal sections, that prevents the mentioned overshoot and ringing to occur (see figure 4.17). Therefore, it was decided to use the negative high voltage source configuration in the setup.

In addition, a dedicated measurement was performed to study the linearity of the bases, varying the resistor chain total impedance, while keeping the ratios as optimized values provided by the producer, and also varying the values of the 5 capacitors, which are used to increase the linearity of the PMT response. The linearity is defined as the uniformity of the PMT response (gain) for very small and very large signals. The best configuration of the positive high voltage (with minimized ringing and overshoot in amplitude), and the negative configuration of the readout circuit are shown in figure 4.17.

4.3   Raw data processor

In this section, the raw data processing algorithm, developed for the Xurich II experiment is described. The development of the software was initiated based on a previous software that was used for the Xurich I data processing (described in detail in reference [167]). However, for several reasons, a new software was required to be developed. In particular, the DAQ system was modified, resulting in generation of data in a completely different format than the one used for Xurich I. In addition, the old software was written in MATLAB programming language, while the ROOT programming language was desired to be used for the new software. Finally, the algorithm performance was improved (especially regarding the signal identification algorithm).

The algorithm begins processing raw PMT traces (from the top and bottom PMTs) through analyzing the first and the last 50 samples (each sample corresponds to 10 ns data acquisition period from ADC). In general, the traces are acquired in longer windows than twice the drift length ($\simeq$ 19 μs at 1 kV/cm nominal drift field), meaning that no matter whether the S1 or S2 pulses have generated the trigger (placed at the center of the waveform), the first and last 0.5 μs of each trace do not generally include physical signals. Of course, the possibility of pile-up events exists, whereas the acquisition rate usually does not exceed 100 Hz, keeping the pile-up probability below 0.5 %. The information that is extracted from these samples consists of the average baseline value, and
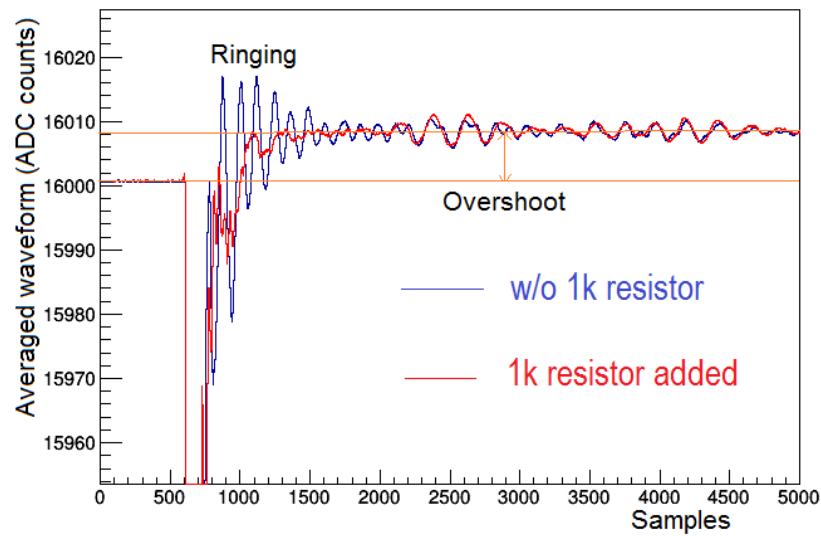
Figure 4.16: The averaged waveform of 1000 events for the two different configurations of positive high voltage networks tested for the Xurich II PMTs. A significant improvement on the ringing amplitude is observed (red trace) after a $1\,\mathrm{k\Omega}$ resistor is added to decouple the high voltage input from the rest of the circuit (R21 in figure 4.17).
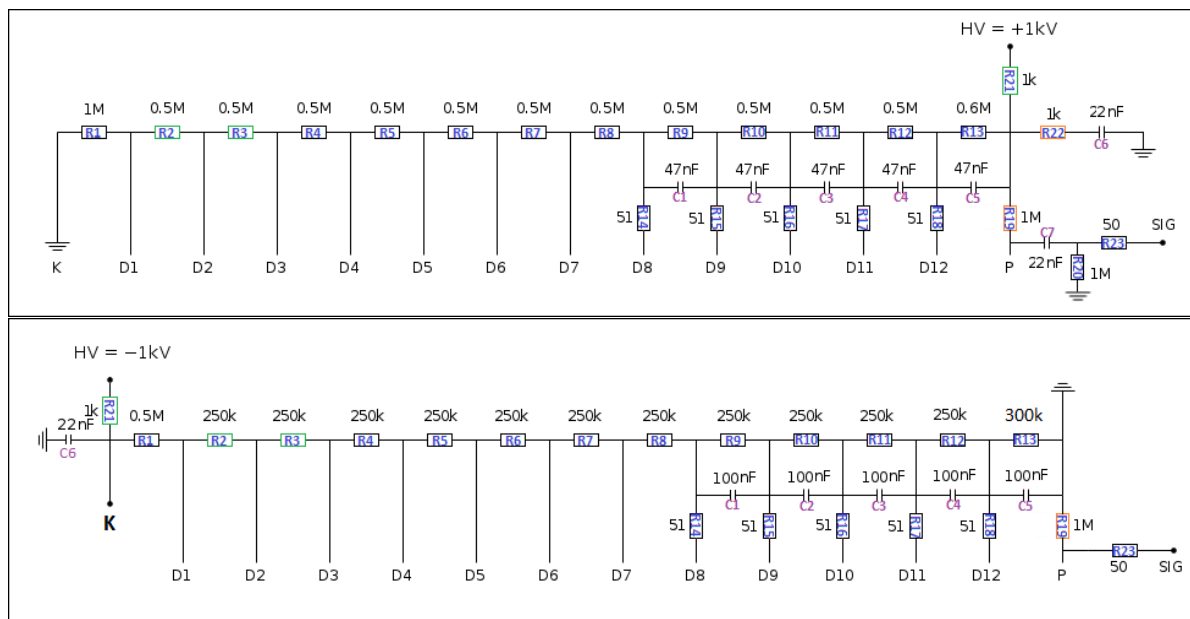
Figure 4.17: The optimized configuration of the voltage divider circuit using positive high voltage source (top), and the final layout using negative high voltage and optimized capacitor-impedance values to achieve best linearity, as defined in the text.

root mean square (RMS) in the units of ADC counts, that is calculated and compared on both sides of each event.

In case if the baseline mean value within the first and last samples differ by more than 3 times the calculated RMS, the event is discarded for analysis. Finally, the whole trace is subtracted from the baseline mean value, in order to both inverse the negative traces, and to project the pulses to zero baseline, for later calculation of the pulse properties (e.g. height, area, and etc).

Once the baseline subtraction is performed, the algorithm finds candidates for possible S1 and S2 signals through the PMT traces. The candidate regions are initially selected by finding regions of the waveform where the sample values exceed 3 times the noise RMS of the same trace. The regions of the waveform where no signal candidates are found, will be flattened (meaning to project their sample values to zero), for the sake of the required computing power. Next, for the sections of the waveform that survive flattening, the following 3 parameters are calculated. Among these parameters, the S1 and S2 filters (width based filters) were formerly introduced in the literature [167, 176], while the χ^2 filter was developed within a collaborative work dedicated for processing Xurich II data [172].

- S1 Filter: The S1 filter (formulated below) is a width based property of the pulses that is calculated for every sample (noted with "s"). The property is found to be strongly efficient in identifying S1 pulses and their discrimination from noise and baseline fluctuations. The parameter calculates for every sample (that is not flattened), the sum of the sample values (W), in a symmetric window around it, that is comparable to the size of largest S1s. Due to the short decay constant of the xenon scintillation light (4.3 ns and 22 ns for the singlet and triplet components, respectively [177]), and a fast transit time of the PMTs employed in the experiment (20 ns according to the producer), the time window of 80 ns is chosen to be sufficient for deriving S1 filter, and hence, the width of the window is fixed at (w_1=) 8 samples.

$$F1_s = \sum_{i=s-\frac{w_1}{2}}^{s+\frac{w_1}{2}} W_i \tag{4.6}$$

- S2 filter: Similar to the S1 filter, the S2 filter is also calculated for every sample in the trace that survives flattening. However, the length of the sample summation window (w_2) is increased to the approximate width of the largest S2s (fixed at 1.1 μs equal to 110 samples), while the maximum value of the S1 filter within the window is subtracted (see equation 4.7). Since the S2 pulses are on average about 10 times wider than S1 pulses, the value calculated for the S2 filter is significantly larger for S2s compared to S1s (see figure 4.19). This allows discrimination of the two pulse types.

$$F2_s = \sum_{i=s-\frac{w_2}{2}}^{s+\frac{w_2}{2}} W_i - Max(F1_i) \left(s - \frac{w_2}{2} < i < s + \frac{w_2}{2} \right) \tag{4.7}$$

- χ^2 filter: The χ^2 filter corresponds to the actual S1 likelihood as it would be defined in statistics terminology. Even though it is practically difficult to manually select a subset of signals which only contain S2s, it is rather easy to operate the detector in a condition where production of S2 signals is naturally prohibited (simply, through halting the extraction field).

In this way, it is easy to select some statistics of pure S1 pulses. One can normalize these signals with respect to their height and demonstrate an averaged S1 pulse. The shape of such signal depends however, on the applied drift field through quenching effects [113, 178]. The quenching effect becomes more significant with increasing the electric field amplitude and thus the average signals get smaller in size (see figure 4.18), resulting in smaller S1 signals both in height and width. Therefore, the parameter is defined separately for all nominal drift fields, that are used for the experiment for the calibration and the neutron data acquisition. The equation below shows how the filter is calculated for sample s. The summation is limited to the range restricted to the "left" (-2) and "right" ($+15$) samples, found to belong to the normalized S1 signal, relative to the 0 sample, which points to its maximum, and T denotes the S1 template sample value. Figure 4.18 shows the χ^2 template for different applied cathode voltages.

$$\chi_s^2 = \sum_{i=-l}^{r} \left(\frac{W_{s+i}}{\sum_{j=-l}^{r} W_{s+i}} - T_i \right)^2 \tag{4.8}$$
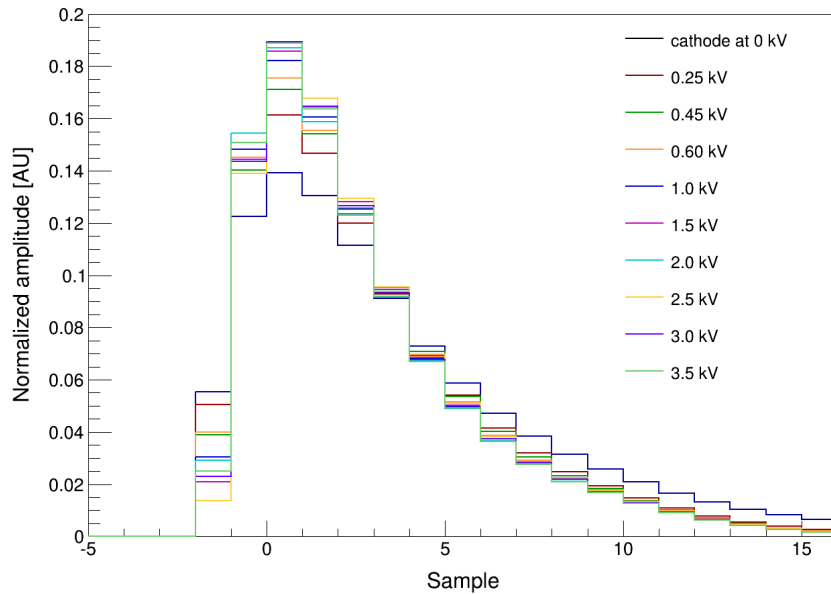
Figure 4.18: The S1 signal templates derived for the bottom PMT using calibration data acquired with the grounded anode mesh. For each electric field setting, ranging from $0\,\mathrm{kV/cm}$ (cathode at ground) to $1.16\,\mathrm{kV/cm}$ (cathode at $3.5\,\mathrm{kV}$), an S1 template is built and shown in this figure in a different color.

The S2 filter is very sensitive to tiny fluctuations above the baseline, and it also identifies most noise bursts as S2 candidates. The filter is also sensitive to S1 pulses, and this is the reason why the maximum of the S1 filter is subtracted in equation 4.6. Consequently, for S1 identification, one needs to require S1 filter providing a more significant value for S1 likelihood, than the S2 filter

($F1 > F2$ through the investigated signal trace). An example waveform that consists of normal S1 and S2s which are identified by the filters is illustrated in figure 4.19.
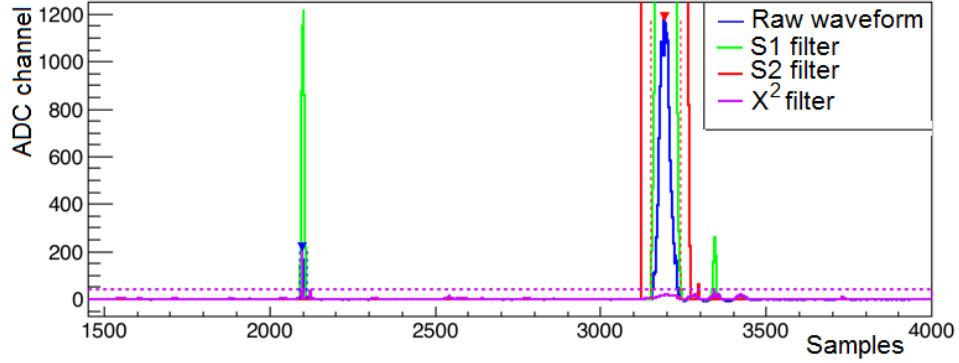
Figure 4.19: An example waveform analyzed by the Xurich II raw data processing algorithm. The blue color illustrates the raw waveform, while the red, green, and magenta display S2, S1 and the inverted χ^2 filters respectively, as described in the text.

It was observed that the S1 filter fails in particular situations to identify S1 pulses properly, in particular when the S1 pulse is too close to an S2 signal ($<1\,\mu$s corresponding to events in the top 2 mm of the TPC below the gate), or when it is surrounded by noise bursts, or when two S1 signals are close to one another (pile-up). In such cases, the S2 filter extends to the S1 pulse region, and qualifies the selection requirement. An example of such issue is shown in the trace displayed in figure 4.20.
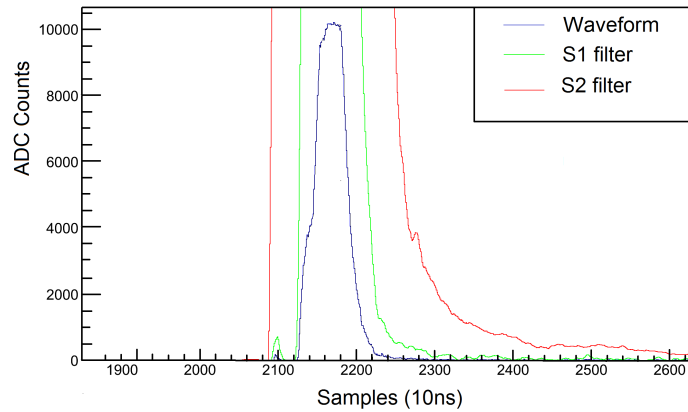
Figure 4.20: An example waveform analyzed by the Xurich II raw data processing algorithm. The blue color illustrates the raw waveform while the red and green colors display S2, S1 filters respectively. The small S1 centered at sample 2100 would be missed by the algorithm in the absence of the χ^2 tagging method, as the S2 filter in that region is far stronger than S1 filter near this region.

The χ^2 filter serves as an independent measure of the S1 likelihood that does not rely on the comparison between two filters. This makes it capable of identifying S1s, even when they are very close to S2 pulses. For instance, one can see in figure 4.21, that the small afterpulse S1, which is very close, in time, to the large S2, can be identified by this filter. A threshold is set for the inverse χ^2 filter value, for S1 signals to be identified. This threshold is derived through systematic analysis of all signal candidates versus their measured χ^2 filter value (see figure 4.21).
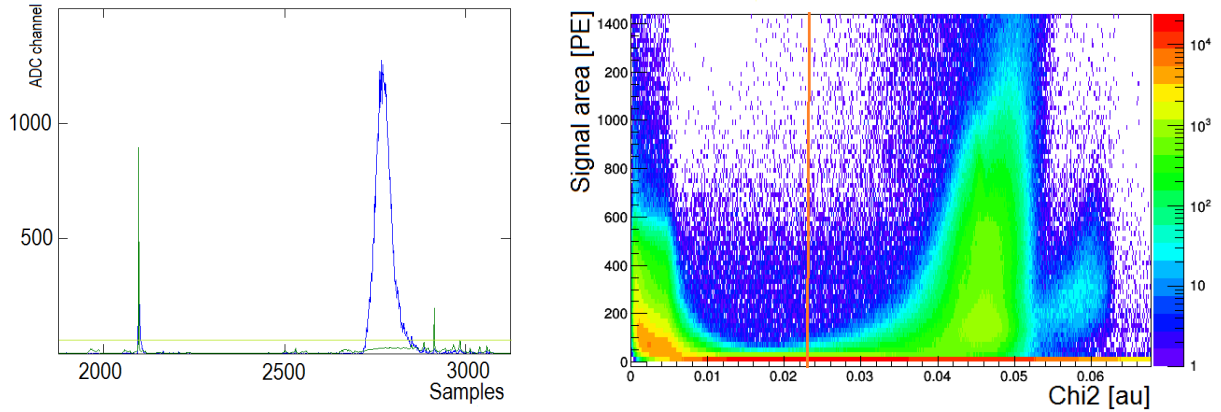
Figure 4.21: (Left,) an example waveform from the Xurich II data with χ^2 filter (green) calculated over the trace (blue) and the threshold for S1 identification. (Right,) signal area converted to photo-electrons versus calculated χ^2 for all S1 or S2 candidates found in a dataset.

Finally, based on the pros and cons discussed above, for each method, the following algorithm was found to be the most efficient for signal identification. First, S1 and S2 search regions are appointed, where $F2 > 0$ or $F1 > 0$. Then, the S2 search regions are scanned to find S2 candidates where $F2 > F1$ condition is presumed, for every sample within the region. If the condition is met, the region will be removed from both search lists. Otherwise, it will be removed from S2 search regions only. If the S2 candidate cannot be identified based on S1 and S2 filters, it is verified by the χ^2 test. If the calculated χ^2 value exceeds the threshold, the signal is selected as an S2, and vice versa. Finally, after the S2 scanning is finished, over the remained S1 candidate regions, similar control tests are applied. Either if the $F1 > F2$ through the whole region, or if χ^2 test is passed, the candidate will be identified as an S1. At this point, that region will be removed from the search region list, until there are no more regions left to be scanned. The classification algorithm is also illustrated in figure 4.22.

Once a S1 or a S2 signal is identified, its properties will be calculated in a window restricted by the end points where the $F2$ filter reaches either zero or a local minimum. Such properties include pulse width (full width at half maximum (FWHM) or at 10 % (FWtM)), height, area, center of mass position, and etc, for both S1 and S2 signals. The S1 pulses are similarly limited between the regions where the S1 filter is zero or reaches its local minimum. The software finally collects all the information about the events including the number of S1s and S2s, and their respective properties, and stores them in a dedicated ROOT file for each dataset, for analysis usage. A list of extracted parameters from each identified S1 and S2 signals is provided in table 4.1.
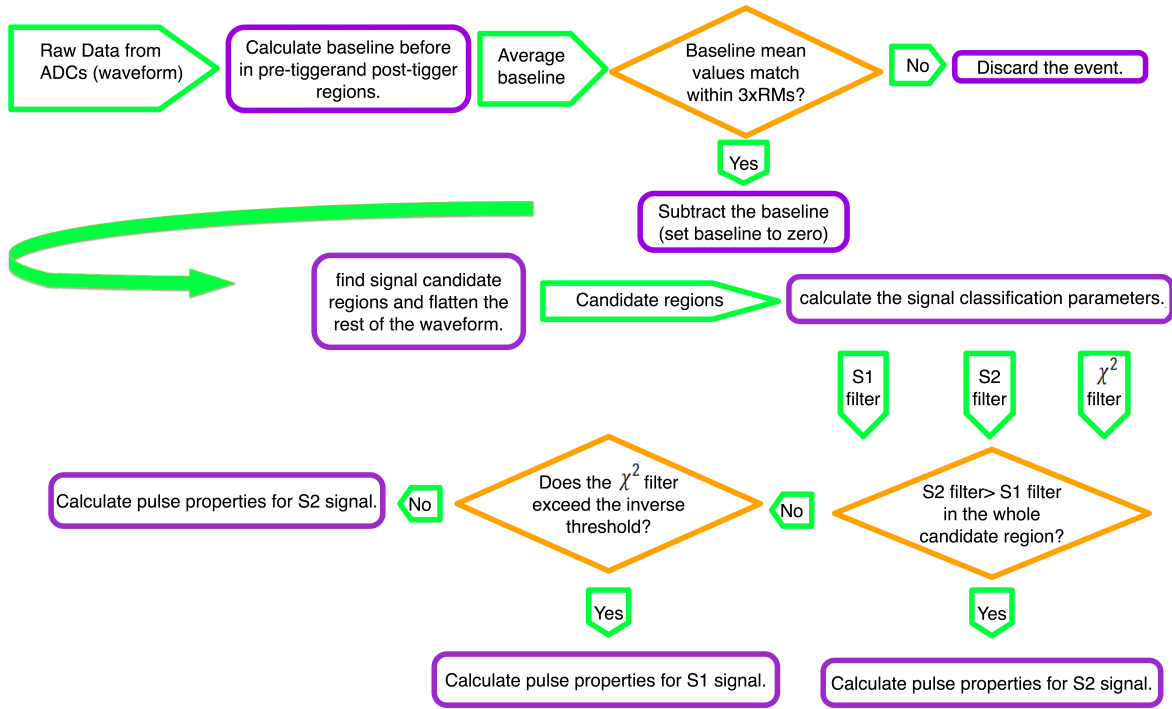
Figure 4.22: Flow-chart of the Xurich II pulse classification algorithm. The detailed description can be found in the text.

In addition to the information listed in table 4.1, which is saved for every signal found in an event, more information is also stored in the output ROOT file. For instance, the number of found S1 and S2 pulses, the maximum trace value in the whole waveform, event number, drift time (calculated between the largest identified S1 and S2 pulses), etc are stored for analysis uses.

4.4   Detector leveling

The operation of a xenon TPC requires precise control of the liquid level inside the volume. In most detectors, including Xurich II, parallel plate capacitors are used as level-meters (LVMs). Xenon dielectric constant is different in gas (1.00 at 293 °K [179]) and liquid (1.87 at 165 °K [180]) phases. Hence, when the liquid level between the capacitor plates changes, the total capacitance alters accordingly. Therefore, online readout of such capacitors, placed inside the xenon volume, can be used for determination of the liquid level.

The Xurich II detector uses a total of 4 capacitor LVMs, one of which is placed outside of the active volume and is 5 cm long. This LVM is used to monitor the LXe level during filling and recovery processes. Another set of 3 capacitors are placed symmetrically inside the TPC (see figure 4.6). These LVMs measure the liquid level in the critical region, between the anode and the gate where the electroluminescence occurs, and are only 3 mm long. They are used for both precise measurement of the liquid level, and the leveling of the TPC. The detector might get tilted due to mechanical pressure, or thermal expansion/contraction, which may be not uniform in all directions.

Parameter	Description
Area	The integral of the sample values, saved in both units of ADC counts and photo-electrons (divided by the PMT gain value).
Height	The maximum amplitude in the identified signal in ADC counts.
FWHM	(Full Width Half Maximum); The width of the pulse restricted by the two samples where the trace value reaches 1/2 the maximum in both directions, in number of samples (10 ns).
FWtM	(Full Width 10 % Maximum); The width of the pulse restricted by the two samples where the trace value reaches 1/10 the maximum on both directions, in number of samples (10 ns).
Position	The sample position of the maximum point of the signal.
Rise time	Number of samples that takes to reach the signal maximum position from zero.
Maximum S1 filter	The maximum value of the S1 filter within the signal time window.
Maximum S2 filter	The maximum value of the S2 filter within the signal time window.
Maximum χ^2 filter	The maximum value of the χ^2 filter within the signal time window.

Table 4.1: Short list of parameters extracted by the Xurich II raw data processor from every identified signal (S1 or S2). All parameters are calculated for the individual top and bottom PMT waveform.

Any small difference in the size of the gas gap in the TPC results in a non-uniform electric field, that introduces position dependency for the S2 signals, both in size and width.

Each of the four LVMs are connected by two cables attached to each plate. On one side, named as "common", the cables from all LVMs are electrically in contact, while on the other side, each LVM is individually read, through a dedicated cable. All these cables are connected to a vacuum feed-through, which contains a 10-pin Amphenol [181] connector, with the remaining (5) pins being not used. The feed-through is connected externally to a universal transducer interface (UTI) board, that measures the capacitance values. The data from the UTI board are transferred to a computer. A LabView [182] program communicates with the UTI board, and stores the capacitance values. The program is also instrumented with several visual features, that plot the raw capacitance, and the actual (calibrated) liquid levels, from each LVM online, during acquisition. Such features allow online diagnostics of the problems with liquid level adjustments and detector leveling.

The liquid level inside the TPC can be raised or lowered externally, by the use of a motion feed-through, which moves a section inside the condensation weir, including a circular hole that connects the weir and the TPC volumes (see figure 4.6). Since the weir is always colder than the TPC, the liquid level inside the TPC never exceeds the bottom of the hole. The motion feed-through allows adjustment of the liquid level with an instrumental precision of 0.025 mm. It is also used to calibrate the LVMs, by manual variation of the liquid level at several steps, while the LVMs are being monitored. The raw data from the UTI that are proportional to capacitance values

by arbitrary units (since the impedance of the readout section is unknown), are acquired for the calibration of the 3 LVMs, as shown in figure 4.23. The long levelmeter is only used to provide a rough estimation of the liquid level during the xenon filling process and is hence, excluded from the precise calibration process.
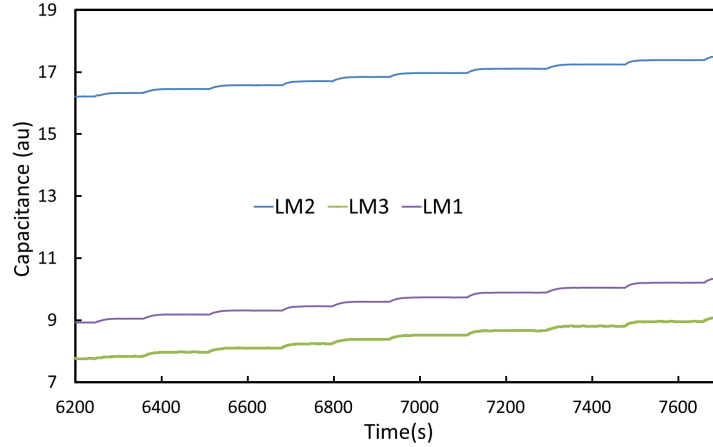
Figure 4.23: The capacitance values read out from the UTI board plotted as a function of time. For calibration of the LVMs, the liquid level inside the TPC increased in small steps (0.125 mm) while data from the 3 short LVMs are being acquired.

For every run of the experiment (that is denoted as the period between two consequent filling and recovery of LXe to the detector), the LVMs are calibrated, using a minimum value and the slope of each LVM that are derived from the best linear fit to the calibration data, as illustrated in figure 4.24. The calibration results are then transferred to the LabVIEW program, to allow online monitoring of the actual levels calculated from each LVM, needed for the leveling of the TPC.
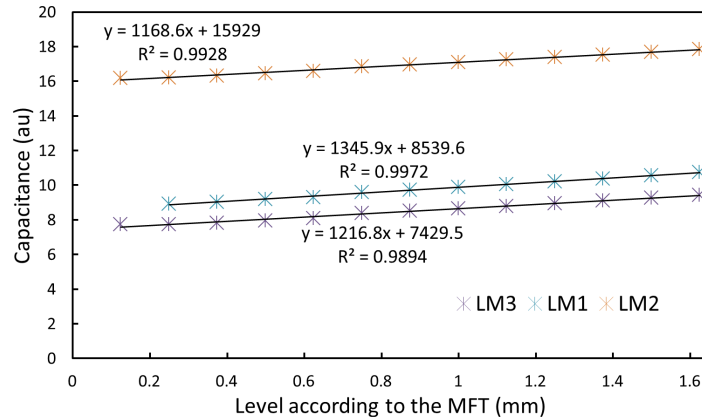
Figure 4.24: Linear fit to the acquired calibration data from the 3 short LVMs in the Xurich II detector. The slope from the fit allows conversion of the capacitance values in arbitrary units to actual liquid level (in mm) from the bottom plate of each LVM.

Once the calibration of the LVMs is obtained, the tilt inside the TPC can be determined, based on the difference between the liquid levels sensed by each short LVM. The stand unit that mechanically holds the Xurich II cryostat includes 3 screws that can be used to tilt the cryostat externally. This feature permits compensation of the tilt inside the TPC. Figure 4.25 shows the data from 3 short LVMs acquired when the detector was being leveled. The precision of the LVMs is approximatly $10\,\mu$m, as derived from the RMS of the fluctuations of the readout capacitance values. Once the 3 LVMs read equal values within this precision, the leveling process is finished.

Finally, after the leveling of the detector, the actual liquid level is set based on a dedicated analysis to optimize the S2 quality parameters (uniformity, resolution, and size). It was found that the best quality is achieved when the liquid level is raised to 2.00 mm above the bottom LVM plates of the Xurich II TPC. The short LVMs present a nonlinear behavior, when the liquid level exceeds the bottom 2/3 of their height. This is a known effect of capacitor LVMs, that is caused by the so-called "capillary effect" of fluids [183, 184]. Hence, the LVM readout values are not trusted at this range. Therefore, the liquid level is lowered, at a last step, back to the region where the LVMs can be read.
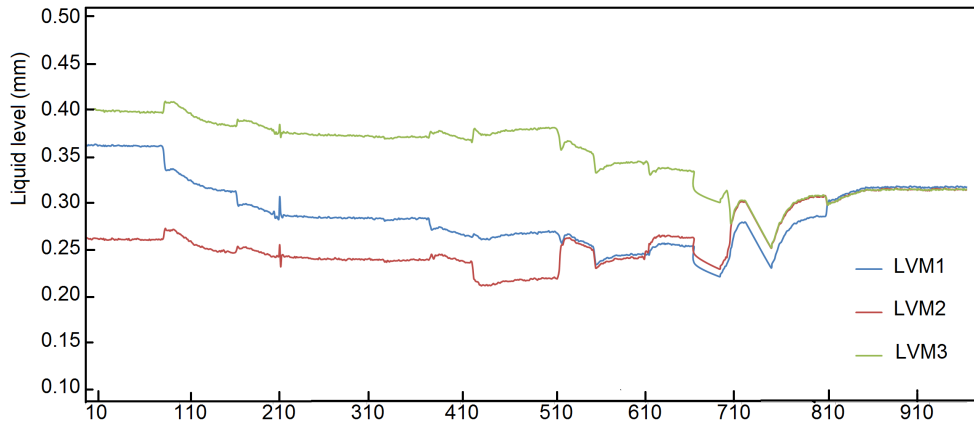
Figure 4.25: Data from the 3 short LVMs of the Xurich II TPC during the leveling process. The rather sudden fluctuations correspond to the external tilting of the TPC, that are promptly sensed by the LVMs.

4.5   Calibration of the PMTs

A simplified version of the PMT calibration system of the XENON1T experiment, described in section 3, is also implemented for the Xurich II detector. An optical vacuum feed-through with a single SMA connector is used, attached to a plastic fiber (2.2 mm outer diameter), that connects the feed-through to an small LED box. Another SMA connector, which divides the light input between 4 identical PMMA fibers, is attached to the vacuum side of the feed-through, inside the cryostat. However, only two of the PMMA fibers are actually used, inserted to the TPC, and placed below the top and above the bottom PMTs. A pulse generator is used to send short (60 ns) pulses to the LED, and trigger signals to the data acquisition system. Short traces of 2 μs are recorded for PMT

calibrations and the PMT signals are amplified using a ×10 amplifier, before they are connected to the ADC module.

An independent raw data processor script is used for PMT calibrations as it requires much simpler analysis than the one used for other data, as several features of the raw data processor, such as signal classification and etc, are not needed for PMT calibrations. This script looks for pulses within a very short window, where the LED is pulsed. Figure 4.26 shows several super-imposed waveforms of a typical dataset of the Xurich II PMT calibrations. Another script plots the spectra of pulse area for both PMTs, and fits the results using several Gaussian functions distributed according to Poisson statistics, respective to the distributions of single, double and triple photo-electrons. Figure 4.27 shows an example of the fitted spectrum of the bottom PMT, and the measured gain values for different high voltages. The PMT voltages were fixed at minimum values (to prevent saturation of the electronics e.g. ADC modules) where the gain calibration had sufficient quality (considering the resolution, signal and noise separation and peak-to-valley ratio).
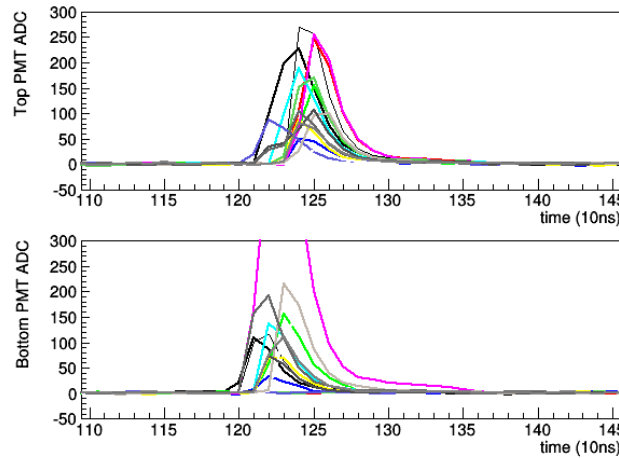
Figure 4.26: Several super-imposed PMT traces from the Xurich II PMT calibration data. The figure illustrates that using short 60 ns pulses to power the LEDs for each trigger nicely constrains the single photo-electron signals within a short (100-150 ns) window, calculated through evaluation of the sample significance for samples near the window.

This method for PMT calibrations is reproducible and provides consistent results until the last run of the experiment where most calibrations and characterization studies were performed (March-December 2016). In this period, the adjustment of the LED voltage was practically not possible, to achieve spectra with only 1 and 2 photo-electron peaks being statistically significant. The variations of the LED voltage had resulted either in too weak light intensity where the single PE peak could not be distinguished from noise distribution, or too strong where a large fraction of events had deposited more than 3 PE in the PMTs. Such behavior is attributed to the the optical PMMA fibers, being moved from their ideal positions, and hence, the issue could not be fixed without recovery and opening of the detector, which was not a desired operation.

Hence, it was decided to modify the PMT calibration procedure from the fitting method mentioned above, to the model-independent method, described in section 3.7, which is proven to be less sensitive to the light intensity. However, the fitting method was also used in parallel, after
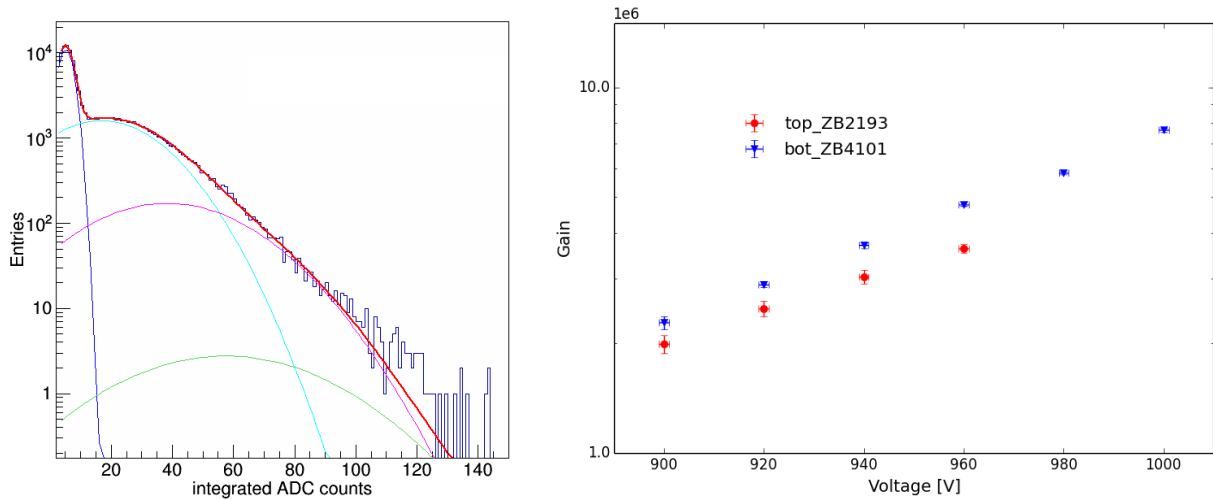
Figure 4.27: (Left); an example single photo-electron spectrum for the Xurich II bottom PMT fitted with 3 Gaussian functions corresponding to single, double and triple photo-electron distributions and (right), the gain versus high voltage curve of both PMTs. According to the producer, the gain value varies as a function of applied high-voltage by a power function, $Gain = A \times HV^{kn}$ with n being the number of dynode stages and k and A being constant.

adding more Gaussian functions to the fit, for cross-check. The results from both methods have been consistent within the expected errors. In figure 4.28, the long-term stability of the PMT gains is shown, using gain values determined from both methods. The deviation of the mean values are 0.6 % and 0.9 % from the two methods for bottom and top PMTs, respectively, in the period where both methods were used.

Finally, the average gain values calculated using the model-independent method were respectively $(2.90 \pm 0.04) \times 10^6$ for the top PMT, at $870\,V$, and $(3.73 \pm 0.09) \times 10^6$ for the bottom PMT, at $940\,V$. These values are used to convert information from raw PMT traces into number of photo-electrons observed in each PMT, during the data processing.

4.6   Data analysis

After the detector operation has reached optimized conditions, and the processing of the raw data is established, using provided average PMT gain values, the detector has to be calibrated to study its response in several aspects (e.g. energy calibration, response to NR and ERs, and etc). However, prior to the detector calibration, the data quality needs to be verified, in order not to include systematic errors due to unknown effects, or undesired physical effects such as field distortions, and etc. For instance, not all acquired events might include proper physical interactions, with S1-S2 pairs registered. Instead, some noise burst might have reached the trigger threshold, and be classified as an S2 candidate whose properties are calculated, and stored like other S2 signals.

Hence, in order to prevent such events to enter the final analysis, the distribution of events is studied with respect to the position dependency of parameters, correlations between S1 ans S2 signals and electric field and signal quality cuts are defined based on such studies. A list of cuts
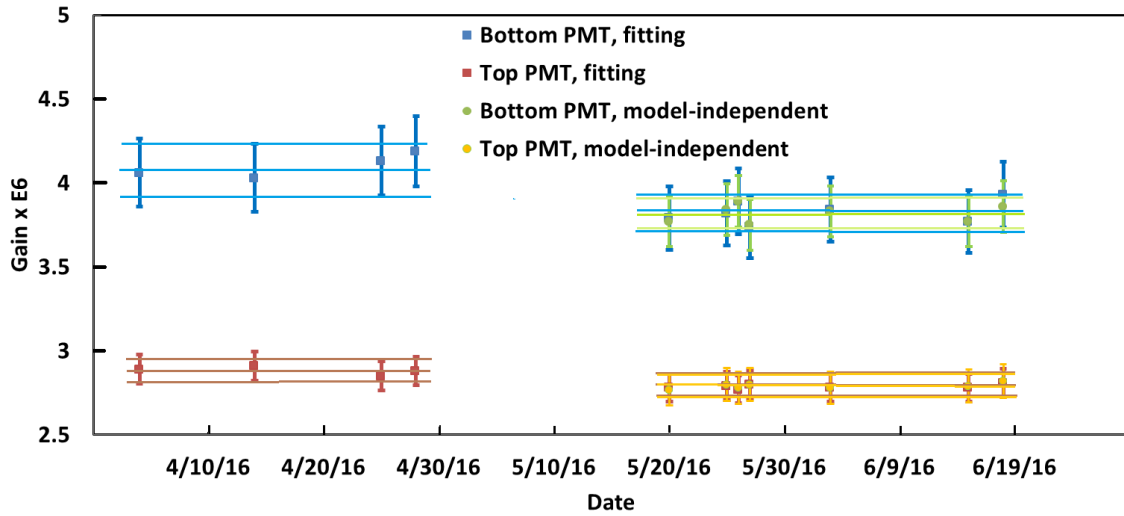
Figure 4.28: The long-term stability of the gain values for the Xurich II PMTs determined by the fitting and the model-independent methods. Both methods provide consistent results within the errors. The fitting method was performed for a longer period of time as the light intensity was not sufficient at this period for the model-independent method to be used. The gap in the middle of the plot with no data points correspond to a forced change of thermodynamics of the system (temperature, recirculation flow and pressure). The lines show the mean and RMS values, calculated for each measurement.

that are developed to be applied on Xurich II data are mentioned in the following with a short description of the purpose and application of each cut, among which there is a so-called "S2 width cut" that has been a topic of this PhD work, and is described in more details. The efficiency (or acceptance) of the cuts depend on several factors such the source that is used, the electric field that is applied, DAQ rate and etc. Hence, the acceptances are calculated for individual physics analysis, separately.

Basic requirements: The following list of cuts are used to select only events which correspond to physical interactions inside the xenon volume. If an event does not pass these requirements, it is excluded from the analysis.

- There is at least one S1 signal from both PMTs.

- There is at least one S2 signal from both PMTs.

- The largest S2 signal occurs after the largest S1, or equivalently the determined drift time should be positive for signals from both PMTs.

Waveform quality cuts: The following cuts are based on requirements that are raised by the constrains from the electronic setup and signal processing. Many physical events may not survive the following cuts, resulting in a reduction of our statistics (even though by maximum a few percent). Large systematic errors are expected to enter the analysis if such selection is avoided.

- It is required that the S1s and S2 signals in both PMTs do not occur in the first and the last 100 samples of each trace. As mentioned in section 4.2.2, the total trace length has been fixed in a time window more than twice larger than the drift length of the TPC, measured at the electric field that is applied for the corresponding data. For instance, the maximum drift time of events is measured to be 18 μs when a drift field of 1 kV/cm is applied. This means that normally, the respective S1 and S2 pairs should not appear at the beginning, and at the end of the traces, where the baseline properties are calculated, regardless of whether the S1 or the S2 signal has triggered the event. However, in exceptional cases, such as multiple-scattered, or pile-up events, this might occur, resulting in a wrong evaluation of the baseline which effects all the signal property calculations. Hence, such events are discarded by this cut.

- The events should not saturate the ADC or the fan-out modules. As mentioned in section 4.2.2, both PMT signal cables are fed into the fan-out, that filters out signals above 2 V amplitude, before they reach the ADC module (which has a range of 2.25 V). In figure 4.29, the maximum trace values from both PMT signals are plotted, where the saturation effect is clearly visible near 14000 ADC counts. The requirement for this cut has been set conservatively, as illustrated by the dashed lines in the figure, to minimize the number of possible saturated events that survive the cut. The saturation occurs for S2 signals from ER interactions larger than 40 keV when no attenuators are use. This corresponds to approximately 250 keVnr energy for NR events, considering the lower expected S2 yield. This is far above the energy range of interest (0-100 keVnr) for the nuclear recoil measurements.
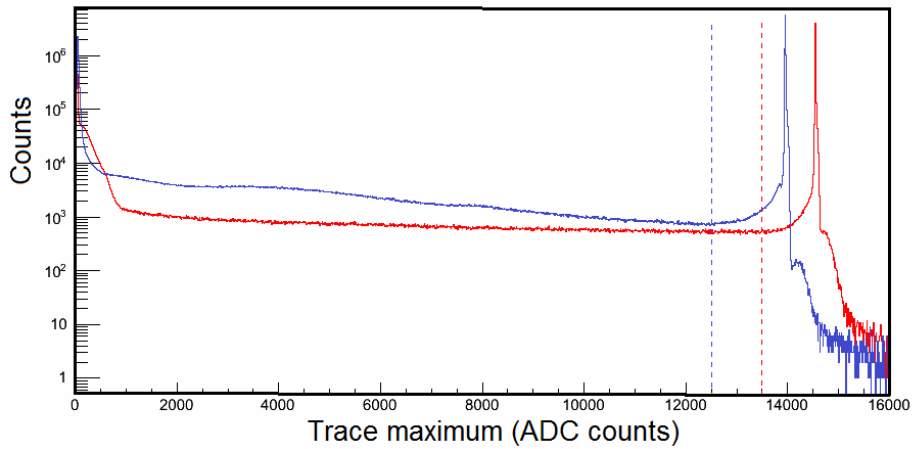
Figure 4.29: The spectrum of waveform maximum values from an acquired dataset for the top (red) and bottom (blue) PMT traces. The dashed lines denote the maximum allowed range, required by the saturation cut.

Coincidence cuts: A physical interaction, resulting in a S1 and S2 pair of signals, should have registered both signals in coincidence between the two PMTs. Therefore, one can require this in practice for selection of desired events, hence rejecting events due to noise or dark counts in a single PMT. Hence, the time difference between the top and bottom PMTs for both S1 ans S2 pulses

has been studied, to derive the coincidence requirement conditions. It was found that the S2 time difference widens for events with larger drift time (from the bottom of the TPC, due to diffusion of the electron cloud). Events within small intervals of drift time are selected and the distribution of their S1 and S2 time differences are fitted with a Gaussian function (assuming normal distribution). The 2 and 3 sigma bands are declared at each slice and the resulting points are fitted by a linear function of the drift time. This work is illustrated in figures 4.30 and 4.31. Based on the degree of quality required for the analysis, either of the bands can be used.
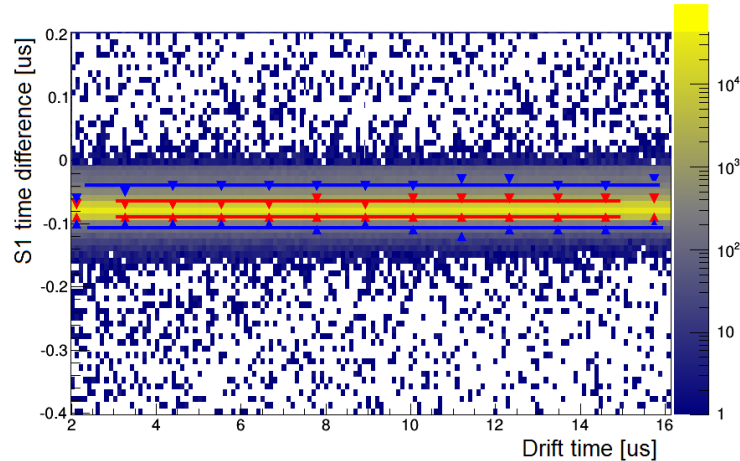
Figure 4.30: The 2 (red) and 3 (blue) sigma bands from the Gaussian fits to the distribution of S1 time difference for events selected from slices in drift time from a ^{83m}Kr dataset, fitted with a linear function. The resulting band corresponds to a temporal requirement on the S1 coincidence.

Position-dependent cuts: Since only 1 PMT is used on the top and bottom of the Xurich II TPC, no (x,y) position reconstruction is possible, unlike the Z position which can be calculated from the delay time between the S1 and S2 signals. Interactions can occur in the liquid xenon region above the gate, as well as in the gas xenon, also generating S1 and S2 signals. While, due to large electric field distortions at these regions (see figure 4.15), such event should be discarded from the analysis. In addition, some events appear in the data from interactions below the cathode. The drift time, as well as the S2 asymmetry parameter (defined below) are used to estimate the Z position of an interaction.

$$S2 \ asymmetry = \frac{S2_{top} - S2_{bot}}{S2_{top} + S2_{bot}} \tag{4.9}$$

In figure 4.32, the S2 asymmetry of the 9.4 keV energy line from ^{83m}Kr calibration (see section 4.7.1) is shown versus the size of the S2 signals, in the units of detected photo-electrons. Beside the main population of events, there are two other distributions observed with very small or very large asymmetries. Selecting events based on S2 asymmetry yields rejection of such events. These events are mostly attributed to afterpulses or misidentified S1 signals.

In figure 4.33, the size of S2 signals from the bottom PMT are plotted as a function of the drift time. A cut on drift time can select events only which correspond to physical interactions between
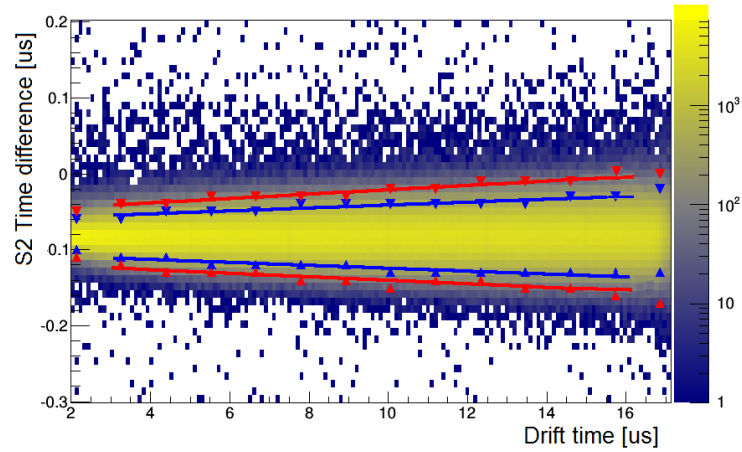
Figure 4.31: The 2 (blue) and 3 (red) sigma bands from the Gaussian fits to distribution of the S2 time difference for events selected from slices in drift time from a ^{83m}Kr dataset, fitted with a linear function. The resulting band corresponds to a temporal requirement on the S2 coincidence.
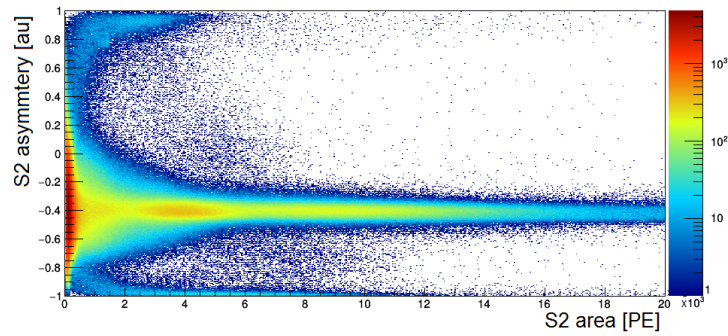
Figure 4.32: The S2 asymmetry for the 9.4 keV line from ^{83m}Kr calibration, as a function of the size of S2 signals.

the cathode and the gate, far from the regions where electric field distortions are expected from simulations.

S2 width cut: A necessary step toward the analysis of NR response of a xenon TPC is to develop an efficient and reproducible method to avoid multiple scattering events, referred to events where an incident particle scatter more than once in the active volume. The corresponding S2 signals of a multiple scattering event are usually too close to each other to be distinguished by the processing algorithm. In such case, the properties of the respective S1 and S2 pairs would be miscalculated. This can yield biased estimation of the detector response to NRs.

However, such events can also be removed through a selection of S2 signals based on their width. The S2 width not only depends on the size of the S2 signals, but also varies based on the Z position
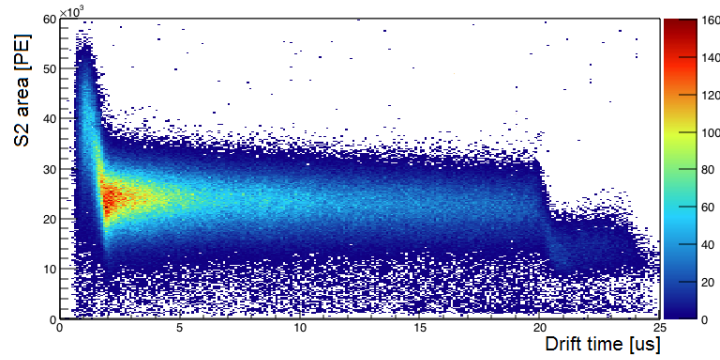
Figure 4.33: The S2 signal size in photo-electrons versus the drift time of events measured by the bottom PMT.

of the event, as the electron could experiences diffusion effect while traveling in the liquid xenon toward S2 extraction region. Hence, for event that occur deeped in liquid xenon, the diffusion effect is more significant resulting in S2 signals which are wider in shape. A dedicated analysis work was performed to define a cut on S2 width, as a function of both S2 size and drift time of events, which is described below.

The calibration data acquired with ^{137}Cs radioactive source are used. The events are divided into slices of 1000 PE in S2 size from the top and bottom PMTs, between 0-14000 PE, where the dependencies are found to be smooth. This range corresponds to 0-20 keVee and 0-100 keVnr estimated interval for electronic and nuclear recoils respectively. For each slice, the S2 width is plotted versus the drift time and is sliced for the drift length of interest (3-16 μs), into 50 slices. The distribution of events projected on S2 width parameter is considered at each slice, and the mean values together with the 2 % and 95 % quantiles are marked. These quantile limits are set based on the maximum cut acceptance, where the dependency of the S2 width against drift time stays smooth (as judged by the fit quality). The derived "upper" and "lower" quantile bands are then fitted with the following function:

$$f = p_0 \, dt + \sqrt{p_1 + p_2 \, dt}, \tag{4.10}$$

where dt denotes the drift time and p_0, p_1, p_2 are the free parameters of the fit function. This process is illustrated in figure 4.34 for an instance slice of S2 size from the bottom PMT. The function in equation 4.10 is used since the dependency is theoretically expected to be proportional to a linear term based on the recombination probability, and a squared root term due to the geometrical dispersion of the electrons. The recombination occurs between electrons and ions in liquid xenon, whereas the dispersion effect happens due to the repulsive force between the electrons.

The procedure above is repeated for all slices in S2 size for both PMTs, and the resulting fit parameters (sets of the 3 parameters p_0, p_1, p_2) are recorded. Next, the variations of each parameter are separately investigated versus the S2 size. It is observed that the most significant parameter is p_1 for all curves (from the upper and lower bands of the top and bottom PMTs), and the respective recombination and dispersion factors are small, which is expected, considering the small height of the active volume (3 cm). Therefore, in order to avoid the analytic complications from fitting 3 correlated parameters for the upper and lower bands of both PMT signals, only p_1 parameter is fitted, and the other two are averaged over the S2 size. Figure 4.35 shows the fits to the parameter
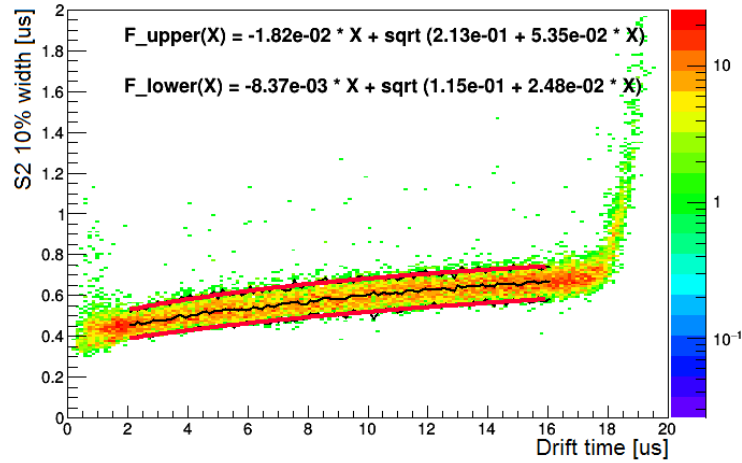
Figure 4.34: The distribution of S2 width versus drift time for an example slice in S2 size, between 5000 to 6000 PEs, measured by the bottom PMT signals for the ^{137}Cs calibration data of the Xurich II detector. The black curve represents the connected points of the 2, 50, and 95 % quantiles derived for each slice in drift time. The red curves show the fits to the upper and lower bands of the S2 width with the function that is described in the text. The X axis title refers to the drift time measured from the bottom PMT. In most cases, the drift time is equally measured for both PMTs, except if either of S1 or S2 signals are not identified for one channel. Such events are removed by the coincidence requirement.

p_1 in each case. Note that a function is used for the fit with large number of degrees of freedom, as expressed in equation 4.11, since the dependency of the parameter is theoretically unknown.

$$F(S2) = p_0 + p_1 \, log(S2) + p_2 \, \sqrt{S2} + p_3 \, S2 \qquad (4.11)$$

Therefore, the S2 width cut is defined based on its dependency on drift time and S2 size. Figure 4.36 shows the S2 width versus drift time plotted for all events seen by the bottom PMT from calibration data, and the respective accepted and rejected events resulted from application of the S2 width cut.

Finally, the cut has been studied for its main purpose, removal of the multiple scattering events, using ^{83m}Kr calibration data. The advantage is that the ^{83m}Kr metastable state follows two consecutive decays with 154.4±1.1 ns half-life [186]. Such interactions yield a large statistics of double S2 signals which are mostly not distinguished by the processing algorithm, and hence, their behavior is similar to those of the multiple scattering events.

In the left plot of the figure 4.37, the S2 width of events is plotted versus the time difference between the first and second largest S1s on the bottom PMT, from a ^{83m}Kr calibration data. It can be seen that in the range of 0.1 to 0.6 μs of the S1 time difference, the S2 width (width of the largest S2) is increasing, suggesting that the corresponding S2 signals are not distinguished by the processing software. In contrast, for the event with larger time difference, the two S2s are well separated by the processor, and consequently, the width of the largest S2 is distributed uniformly, with respect to the S1 time difference. The right plot illustrates the same population, after the S2 width cut is implemented. It is evident that the efficiency of the cut to remove events with
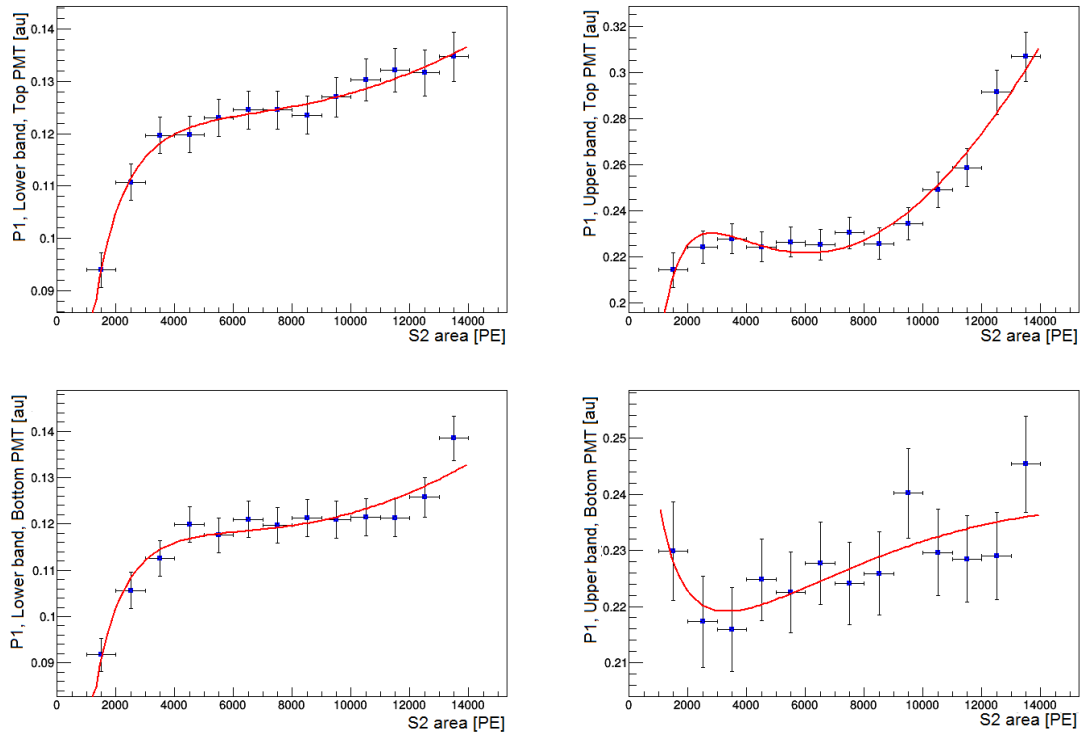
Figure 4.35: The variations of the fit parameter p_1 described in the text versus the S2 size from the top PMT lower (top left) and upper bands (top right) and the bottom PMT lower (bottom left) and upper bands (bottom right). The graph is fitted with a function, and the resulting fit function is used for the declaration of the S2 width cut as a function of drift time and S2 size.

two consecutive S2s which correspond to interaction with >300 ns time difference, is near unity. In conclusion, the S2 width cut can be used to remove majority of the multiple scattering events even in the case when the two S2 signals are not separated by the processing algorithm.

Signal size corrections: The light collection efficiency in the TPC volume is expected to be non-uniform, as followed from the non-uniformity of the optical boundary conditions within the TPC geometry, considering that the scintillation photons experience multiple reflections before they are detected by the PMTs. Such effects can be compensated in the analysis, to obtain position corrected S1 areas. As the S2 signals would appear above the liquid-gas interface independently of the Z position of interaction, such dependencies are neglected for S2 signals. Figure 4.38 shows the variation of the S1 size as a function of drift time (or, equivalently the Z position of interaction) while the correction function is also illustrated. In the same figure the variations of the corrected S1 size are shown, that are limited to maximum 2 %, after the correction is applied.

As a summary, all the cuts that are described above are listed in the table 4.2 with their short description and functionality.
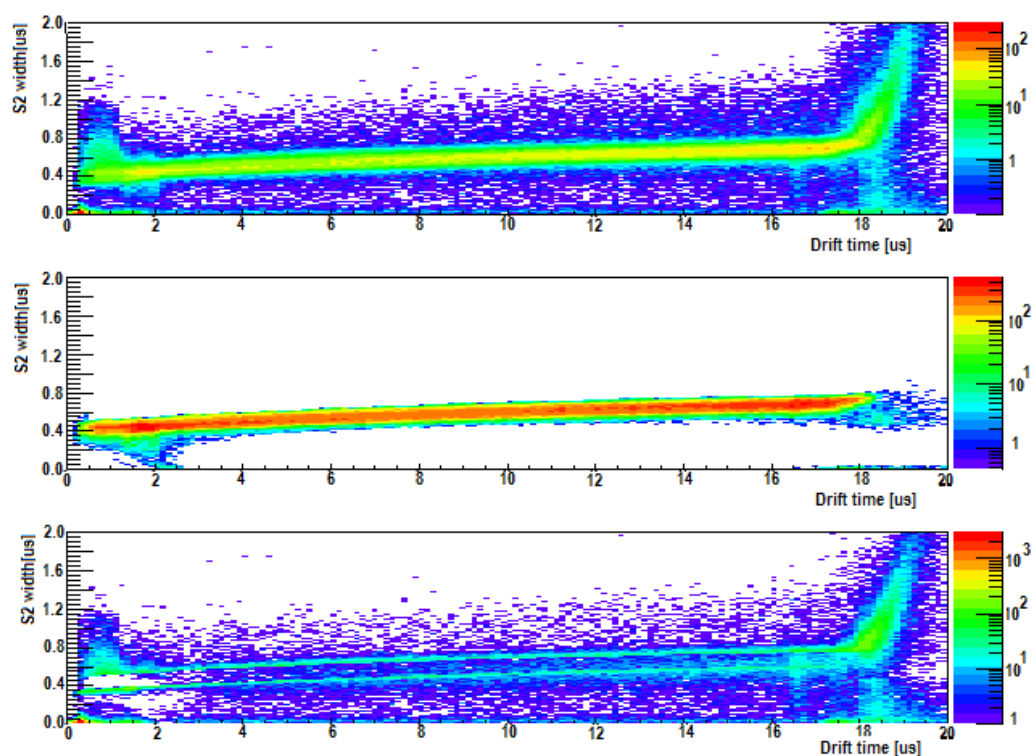
Figure 4.36: The S2 width versus drift time for all events (top) seen by the bottom PMT in the ^{137}Cs calibration data of the Xurich II detector, and the respective accepted (middle) and rejected (bottom) events resulted from the S2 width cut.
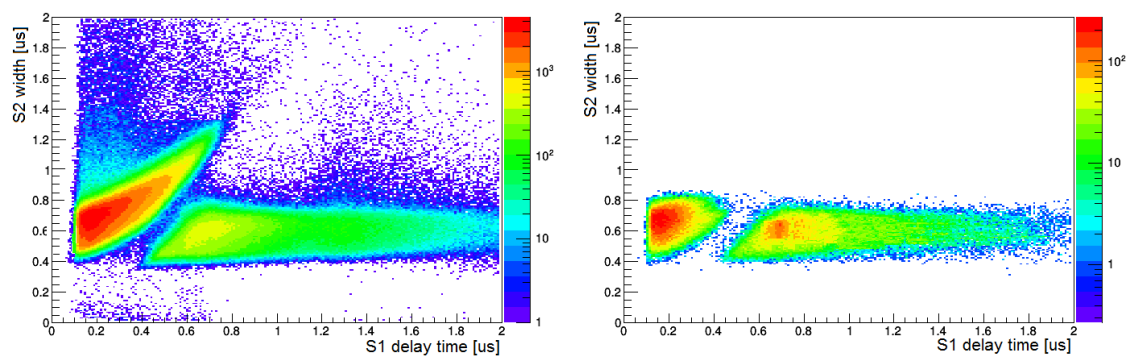
Figure 4.37: The width of the largest S2 pulses versus the time difference between the largest and the second largest S1s for the bottom PMT from a ^{83m}Kr calibration data of the Xurich II detector for all events (left) and those which survive the width cut (right).
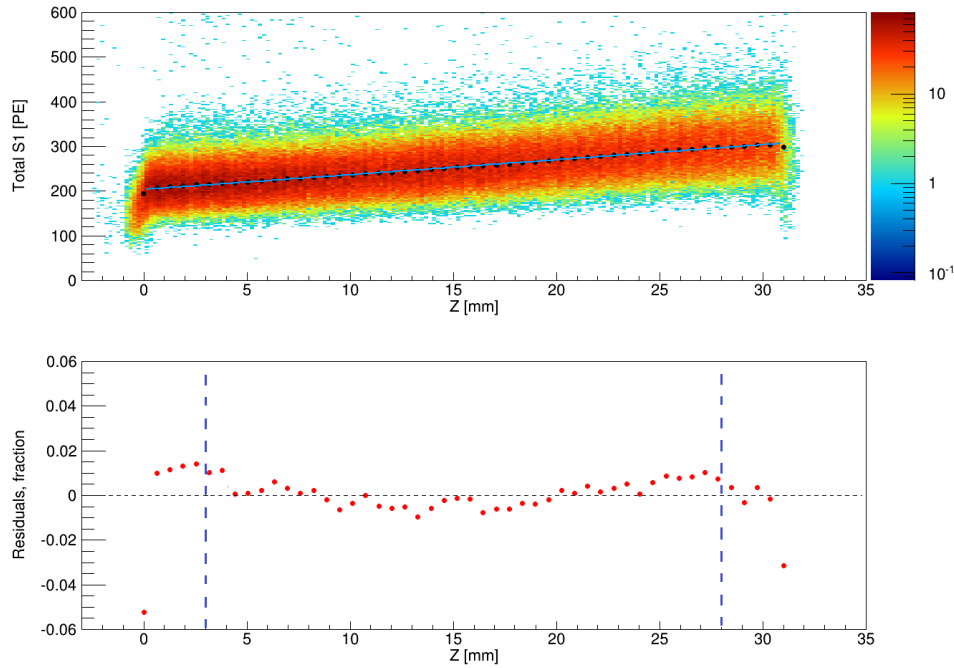
Figure 4.38: The dependency of the S1 signals on the drift time of events, corresponding to the Z position of interaction. The fit function to the black points is used to calculate the inverse correction function. The bottom plot illustrates the residual deviations of the S1 size after the correction is applied. The projection of fiducialization cut on the drift time is illustrated by the dashed blue lines.

4.7 Calibrations

Prior to the neutron scattering measurements, calibration using different sources to measure Xurich II detector parameters such as light and charge yield are performed. In addition the ER and NR bands are characterized. In this section, the analysis for different calibration data is described with focus on the ^{137}Cs calibration which aims to study the discrimination between ER and NR interactions.

4.7.1 Energy calibrations with a ^{83m}Kr source

As it can be seen in the schematic of the Xurich II detector's gas system, displayed in figure 4.9, an emanation volume is instrumented in the gas system, which can expose the xenon gas to a ^{83}Rb source. ^{83}Rb decays into ^{83}Kr, with a half-life of 82.6 days through electron capture [185]. The krypton atoms can easily get mixed and carried by the xenon gas to the active volume. The excited krypton de-excites leaving an isomer metastable state ^{83m}Kr. The de-excitation of this isomer state with a half-life of 1.86 h, follows by a secondary de-excitation with a half-life of (154.4±1.1) ns [186]. This process is illustrated in the decay scheme, shown in figure 4.39.

The interactions from the ^{83m}Kr source inside the active volume produce two consecutive S1 and S2 pairs which can be either resolved or not, based on the decay time of the excited state,

Cut	Description	Usage
Number of S1s	There is at least one S1 seen by both PMTs.	Removes noise events.
Number of S2s	There is at least one S2 seen by both PMTs.	Removes noise events.
Positive drift time	Requires that the largest S2 signal appears after the largest S1, for both PMT channels.	Removes non-physical events and gas events.
Saturation cut	Discards events with maximum trace values above the saturation limit.	Removes events saturating the electronic modules.
Early and late signal cut	Discards events with S1 or S2 signals in the first or the last 100 ns time window of waveform (where baseline is evaluated).	Avoids miscalculation of the signal properties caused by wrong evaluation of the baseline.
Coincidence	Requires the largest S1 and S2 signals on the two PMT channels to occur in coincidence.	Discards non-physical events and events with large afterpulses.
Asymmetry cuts	Requires a range for accepting S1 and S2 asymmetry parameters.	Discards gas events and events from below the cathode.
S2 width cut	Requires S2 signals from both PMT channels to have a width within a range based on their size and the drift time of an event.	Discards multiple scattering events and events with low S2 signal quality (not fully extracted).

Table 4.2: Short list of all cuts developed for the Xurich II data analysis with short description and functionality.

resulting in the populations of 41.5, 32.1, and 9.4 keV ER interactions. Indeed, using the Xurich II detector, a large statistic of events with both resolved S1 and S2 pairs was achieved. Figure 4.40 shows the population of the first and the second largest S1 and S2 pairs from a [83m]Kr calibration data of the detector, selected by a requirement on equality of the S1 and S2 delays (time difference between first and second largest signals).

Since the Xurich II experiment aims to study the low energy response of liquid xenon, the 3 energy lines from [83m]Kr calibration are useful for energy calibration of the detector (in response to ERs), considering the region of interest. Such calibrations include the determination of the anti-correlation between the charge and light signals, which is dependent on the applied electric field in the TPC. For instance, figure 4.41 shows the 2D Gaussian fit to the anti-correlated S1 and S2 signals from both 9.4 and 32.1 keV energy lines, from which the light and charge yields at the respective electric field can be evaluated.

The signal generation mechanism in liquid xenon, described in section 1.3, can be expressed in terms of deposited energy ϵ and the number of emitted photons N_γ and electrons N_e in the following form [100]:
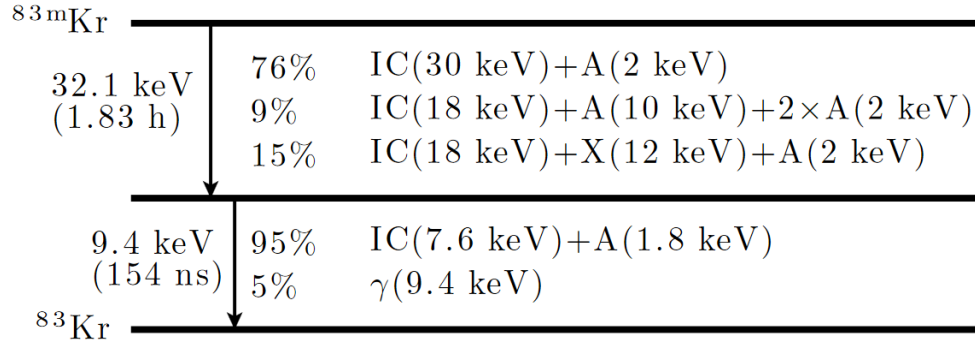
Figure 4.39: The decay scheme and branching ratios of ^{83m}Kr. The decay always passes through two transitions, giving mostly internal conversion (IC) and Auger (A) electrons. A small amount of the energy is carried by gamma (γ) and X-rays (X) [187].
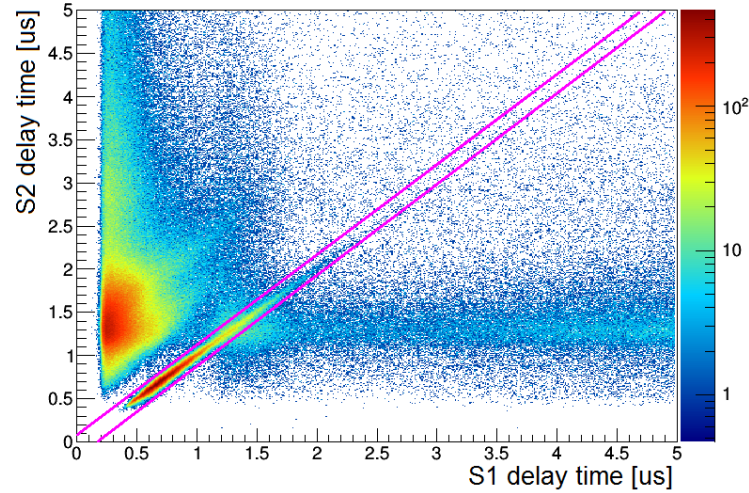
Figure 4.40: The time difference between the first and second largest S2s versus S1s plotted for all events from a ^{83m}Kr calibration data. The magenta lines show the limits used to select separated S1 and S2 pairs corresponding to 9.4 and 32.1 keV energy lines.

$$\epsilon = W_q(N_\gamma + N_e), \tag{4.12}$$

$$N_\gamma = N_{ex} + rN_i, \tag{4.13}$$

$$N_e = N_i(1 - r), \tag{4.14}$$

where N_i and N_{ex} are the number of generated ions and excitons, while W_q is the average energy required to produce a quanta (electrons or photons), and r refers to the fraction of generated
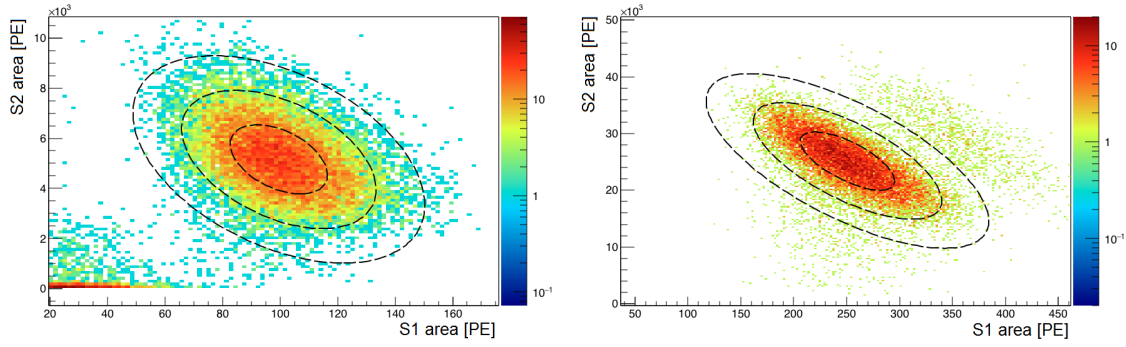
Figure 4.41: The distribution of S2 versus S1 size from selected 9.4 (left) and 32.1 keV (right) interactions. The dashed ellipses represent the 2D fit to the data at 1,2, and 3 sigma contours.

charged quanta which experience recombination process.

W_q is measured to be $(13.7\pm0.2)\,\text{eV}$, independent of drift field and deposited energy [188] whereas r is expected to be strongly correlated with the applied electric field. For instance, the most recent model used in NEST to express the dependency of r as a function of applied electric field is of the form:

$$r = 1 - kE\left(1 + \frac{1}{kE}\right),\tag{4.15}$$

$$k = \frac{4a^2\mu}{\alpha N_i}\tag{4.16}$$

where E denotes the applied electric field. μ denotes the mobility in xenon and α and a are the recombination coefficient and the box volume size, respectively. This expression for the parameter r follows a theoretical model, named as Thomas-Imel box model for electron-ion recombination in xenon [189]. This model was used to fit the ER calibration data using Xurich I detector acquired at different electric fields [187].

The ^{83m}Kr calibration data are acquired at various drift fields (0.22, 0.26, 0.38, 0.53, 0.67, 0.82, 0.96, and 1.26 kV/cm), and the resulting S1 and S2 yields are calculated in the units of PE/keV. Figure 4.42 shows the measured values of the S1 and S2 yield calculated for the 32.1 keV line versus the applied electric field. The results of this work are plotted in S2 versus S1 yield plane as shown in figure 4.43. The obtained values for the zero field light yields are 10.27, 12.52, and 10.25 PE/keV respective to 9.4, 32.1, and 41.5 keV energy lines. There is a $\sim$(50-70) % improvement on the zero field light yields observed compared to the what was measured using Xurich I detector (6.74 PE/keV, and 6.43 PE/keV for 9.4 keV and 32.1 keV lines, respectively [187]).

At this stage, the quenching of the signals from applied electric field can be evaluated. In order to compare our results with the measurements using the Xurich I detector, figure 4.44 shows the measured values for the S1 and S2 yield, normalized by the S1 yield at zero field (S_0) and the the theoretical total amount of initial charge produced prior to electron-ion recombination (Q_0). The value S_0 is measured using data with cathode electrode set to ground. In addition, through fixing the ratio N_{ex}/N_i, Q_0 to 0.06 [190], can be evaluated at 94.3 % the value of the S2 intercept, derived from the point where the fitted lines in figure 4.43 cross the vertical axis.
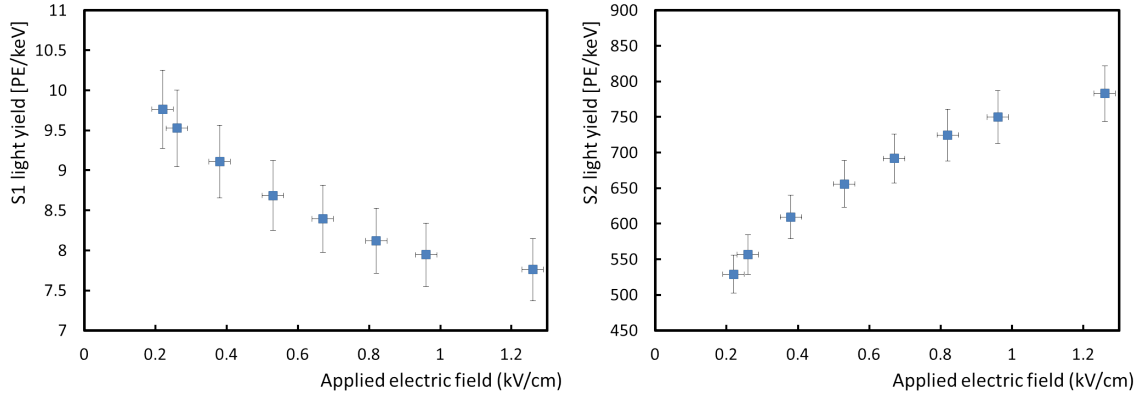
Figure 4.42: The S1 (left) and S2 (right) yield values calculated for the 32.1 keV line out of ^{83m}Kr calibration data, plotted versus the applied electric field through the drift volume.

The Field quenching parameters $S(E)/S(0)$ and $Q(E)/Q(0)$ can be expressed according to the Thomas-Imel model:

$$\frac{S(E)}{S(0)}, \frac{Q(E)}{Q(0)} = a_1 a_2 E \; ln \left(1 + \frac{1}{a_2 E} \right) + a_3, \tag{4.17}$$

where the parameters a_1, a_2, a_3 can be derived by a fit to the acquired data points versus applied electric field. For the case of S1 light yield, the parameter a_3 is fixed to unity and the function therefore contains only 2 free parameters. The fit functions are also shown in figure 4.44 whereas the resulting parameters are listed in table 4.3. For the measurements in reference [187] the normalized charge yields are calculated only for the summed energy line 41.5 keV. This is because the two transitions could not be resolved for their S2 signals. However, with the data from Xurich II detector, we observe sufficient statistics of fully resolved S1 and S2 pair signals from 32.1 and 9.4 keV transitions and hence for each energy line both charge and scintillation signals yields could be calculated versus field (see table 4.3).

E (keV)	a_{1S}	a_{2S}(cm/kV)	a_{3S}	a_{1Q}	a_{2Q}(cm/kV)	a_{3Q}
9.4	-0.33 ± 0.08	0.71 ± 0.07	1.0	0.29 ± 0.08	2.0 ± 0.6	0.084 ± 0.014
32.1	-0.52 ± 0.05	1.01 ± 0.13	1.0	0.34 ± 0.06	1.8 ± 0.5	0.078 ± 0.012
41.5	-0.49 ± 0.02	0.98 ± 0.13	1.0	0.33 ± 0.06	1.7 ± 0.5	0.082 ± 0.014

Table 4.3: Results of the quenching factor measurements from the fit to the data from ^{83m}Kr calibration at different electric field. The index S or Q refers to the evaluation of the parameters using fits to the S1 or S2 quenching values, respectively.

Finally, it is observed that the resulting a_i parameters from the fits to the data points of normalized charge and light yields using the Thomas-Imel box model are compatible with the measurements using Xurich I detector within the systematic errors.
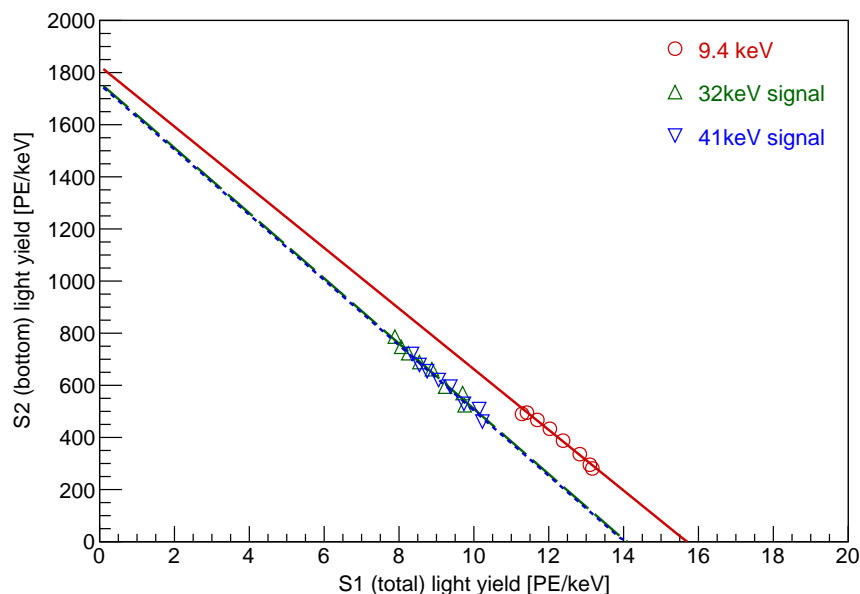
Figure 4.43: Anti-correlation between the scintillation and ionization signals measured in the Xurich II detector. The S1 and S2 light yields for 32.1 keV and 41.5 keV are the same while they are slightly higher for the 9.4 keV line. The different slope for the latter can be attributed to the systematics introduced by the analysis cuts. Figure from Francesco Piastra.
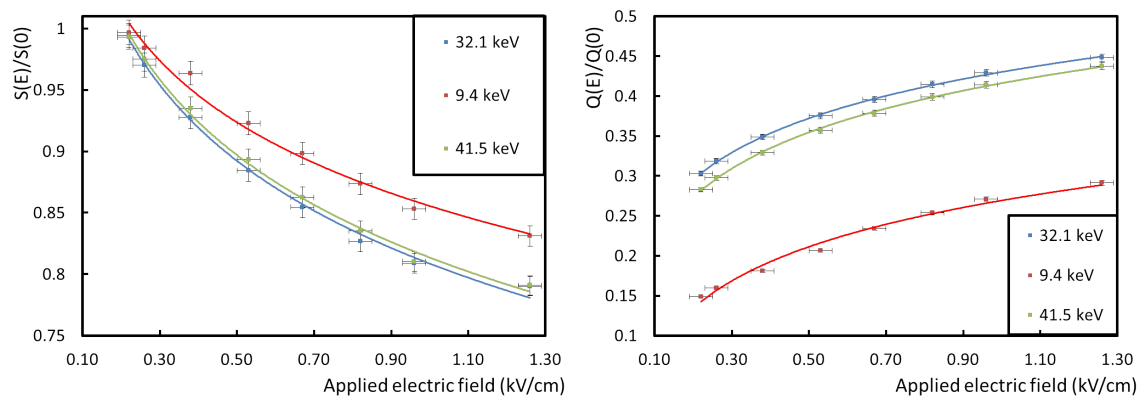
Figure 4.44: Field quenching measured by the S1 (left) and S2 (right) signals yields using 3 energy lines from ^{83m}Kr calibration data as a function of the applied electric field. The solid lines show a fit to the data using a function expressed in the text.

4.7.2 ^{137}Cs calibration and measurements of electronic/nuclear recoil discrimination

The ^{137}Cs radioactive isotope decays via beta emission, into an excited state of ^{137}Ba, which de-excites into the ground state through emission of a 662 keV gamma with 85.1 % branching ratio [191]:

$$^{137}\mathrm{Cs} \longrightarrow\ ^{137}\mathrm{Ba}^* + e^- \tag{4.18}$$

$$^{137}\mathrm{Ba}^* \longrightarrow\ ^{137}\mathrm{Ba} + \gamma\ (662\ keV). \tag{4.19}$$

Although the full absorption peak for 662 keV gammas cannot be observed within the Xurich II TPC (mean free path $\simeq 4.0$ cm in LXe [135]), the wide spectrum of the Compton scattered gammas can be used for calibration of the ER band.

For every coincidence interaction between the Xurich II TPC and the liquid scintillator, the type of the incident particle can be determined from the PSD output of the MPD4 module, which is optimized for neutron and gamma discrimination. However, as mentioned earlier, one can also use the S2/S1 ratio from interactions in liquid xenon to discriminate ER from NR interactions. But, at low energies, which is the region of interest for neutron scattering measurements, the two bands are not well separated. For the purpose of Xurich II analysis, a combination of the MPD4 PSD parameter and the time of flight (which also differs significantly for neutrons compared to gammas) is used for particle discrimination, and the bands from the xenon TPC are only used as a cross-check.

The discrimination of ER and NR interactions using S2/S1 ratio is commonly used for xenon TPC detectors. For each experiment, the discrimination bands are defined based on the data from neutron and gamma calibrations. The discrimination quality, usually quoted by the NR acceptance calculated from Monte Carlo simulations at a given ER rejecting power, differs for each system. Since it is known that the S2 and S1 yields of the xenon detectors significantly depend on the applied electric field, a natural question is whether the discrimination quality can depend on the field as well. However, there has been no measurements found on literature that systematically confirms or excludes such dependency, except for the measurements described in [192, 193] that observed no dependency of the discrimination power by varying applied electric field in liquid xenon.

Therefore, we aim to measure the dependency of xenon discrimination power for ER and NR interactions on the applied electric drift field using Xurich II detector. In order to compare the discrimination power quantitatively, data are acquired at different fields using both ^{137}Cs and the neutron generator. The cathode voltage was set to 1.5, 2.0, 2.5, and 3.0 kV corresponding to 0.53, 0.67, 0.82, and 0.96 kV/cm drift field, respectively.

For each ^{137}Cs dataset, the following procedure is performed to define the ER band. The range of 0-200 PE is used for the analysis, corresponding to $\sim$0-130 keVnr assuming an average light yield of 10.1 PE/keV (refer to section 4.7.1) and average $\mathcal{L}_{eff}$ value of 0.15 (see equation 4.1).

Figure 4.45 shows the discrimination parameter, defined as the logarithm of the S2/S1 ratio, versus the interaction energy, read by the size of the summed (total) S1 signal in number of photo-electrons for events from ^{137}Cs calibration data. Note that all the signal quality cuts, defined in the previous section are applied to the data. The list of all the cuts applied to the data for this analysis and the corresponding cut acceptances are listed in table 4.4. The discrimination parameter distribution is profiled, and the mean values are fitted with a fifth degree polynomial. This is also illustrated in the same figure.
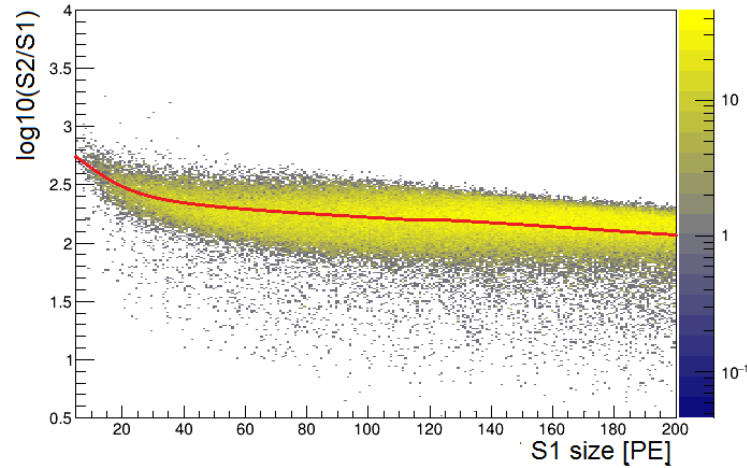
Figure 4.45: The discrimination parameter versus the total corrected S1 size for the ^{137}Cs calibration data after the signal quality cuts are applied. The distribution is profiled over the horizontal axis and the mean values at each bin are fitted with a fifth order polynomial (red line).

Cut	Low energy acceptance (%)	N−1 acceptance (%)	Cumulative acceptance (%)	Deviation (%)
Number of S1s	100.0	100.0	100.0	0.3
Number of S2s	52.8	100.0	52.8	0.9
Saturation	83.4	92.0	36.2	1.5
Early and late signal	49.8	100.0	34.0	1.1
Positive drift time	15.8	90.0	12.7	0.8
Coincidence	14.2	90.0	6.6	2.0
Asymmetry	11.4	68.1	4.5	1.8
S2 width cut	23.4	89.7	4.2	2.4

Table 4.4: The list of cuts applied to the data prior to the discrimination analysis with the corresponding acceptances. The low energy acceptance refers to the acceptance of the cuts for events at the energy range of interest (requiring S1 size <200 PE). Whereas the n−1 acceptance refers to the acceptance of the cut after all other cuts applied to the data. The Cumulative acceptance refers to the acceptance of the the cuts being applied in order from top to bottom. And the deviation is the calculated standard deviation of the cut (N−1) acceptance on data acquired on different electric fields. The total fraction of survived events are 0.042 of the total events.

A change of parameters is performed, over which the shape of the ER band is uniform (flat). The new parameter is derived from subtraction of the fit function, shown on figure 4.45, from the discrimination parameter. The distribution of events using the new (flattened) discrimination

parameter is displayed in figure 4.46 for two datasets. In each slice, the distribution of events is projected over the flattened discrimination parameter and the median value and lower quantiles at $\pm 1.0\,\sigma$ and $\pm 1.5\,\sigma$ are calculated. An eighth order polynomial function is used to fit the $-1.5\,\sigma$ quantile points (corresponding to 93.3 % quantiles), defining the ER band.
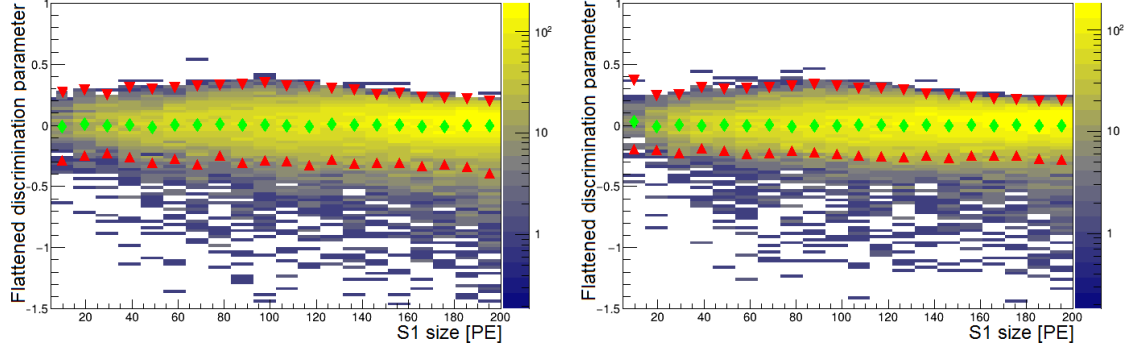
Figure 4.46: The flattened discrimination parameter versus the total corrected S1 size from a ^{137}Cs calibration data at nominal drift field of 0.53 kV/cm (left) and 0.67 kV/cm (right). The green markers display the median while the markers show the $+1.5\sigma$ and -1.5σ quantiles calculated for each slice of S1 size.

Using the defined quantile band, the NR band can be defined by removing events above the ER curve. Figure 4.47 shows the distribution of events from the neutron generator data with the fits to the $-1.5\,\sigma$ quantile points from ^{137}Cs data, for different electric fields, as examples.

In order to quantify the discrimination power the following parameters are used:

- The width of the ER band at -1.5σ and $+3\sigma$ interval from ^{137}Cs calibration data.

- The sample purity of the NR events after rejecting ERs, defined as :

$$\text{Purity} = 1 - \frac{N_{above}}{N_{tot}}, \tag{4.20}$$

  where the N_{above} is the number of events above the ER band and N_{tot} is the total number of events in the data acquired using the neutron generator.

- The separation significance of the bands, in units of ER band standard deviation, defined as:

$$\text{Separation} = \frac{M_\gamma - M_{below}}{\sigma_\gamma}, \tag{4.21}$$

  where M_γ is the median of the gamma band from ^{137}Cs data and M_{below} is the median of the band attributed to NR events after rejection of event above the ER band using neutron generator data, and the σ_γ denotes the -1.0σ width of the ER distribution also derived from the ^{137}Cs data.

Figure 4.48 shows the comparison of the width of both ER band and the separation parameter for each slice in S1 signal size at different fields. For the estimation of errors, the following were considered:
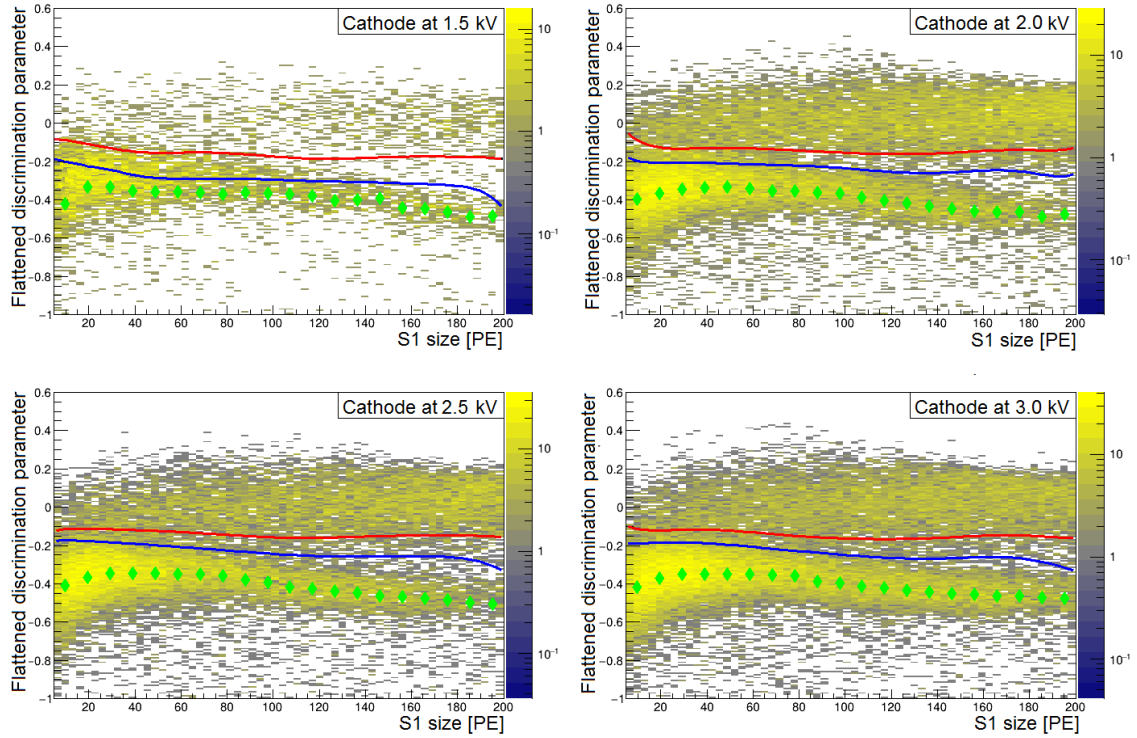
Figure 4.47: The flattened discrimination parameter versus S1 size for data from neutron generator with the cathode voltage set to 1.5, 2.0, 2.5 and 3.0 kV. The red and blue lines show the fits to -1.0σ and -1.5σ quantile bands, respectively, which are calculated from the same distribution of events using ^{137}Cs data radioactive source. The green markers illustrate the median of the NR band, after rejecting the events above -1.5σ ER band.

- The propagated errors from fit to the ER band quantiles.

- The propagated errors from the dependency of the applied cuts on S1 signal size.

- The statistical error calculated for each slice made on S1 area.

In most cases, the errors from the width cut dependency on the S1 size was dominant, where the observed deviations from mean value were 2.5-3.0 % within the range of interest, except for the data acquired with cathode voltage set to 1.5 kV, where the statistical errors dominate.

In figure 4.49 the average value of the ER band width, the separation significance, and the sample purity are plotted versus applied electric field. As it can be seen, there is no significant dependency of the discrimination power on the electric field observed by the sample purity, whereas the ER band width is significantly larger and the separation significance is smaller for the data with the lowest field (0.53 kV/cm).

To summarize, all the measured values for the mentioned parameters are also listed in table 4.5. We conclude that while no significant dependency of the discrimination quality on the applied electron drift filed is observed in the range of 0.67-0.96,kV/cm, our analysis indicates the discrimination is worse at a lower field of 0.53 kV/cm. In particular, it is measured that the width of the ER
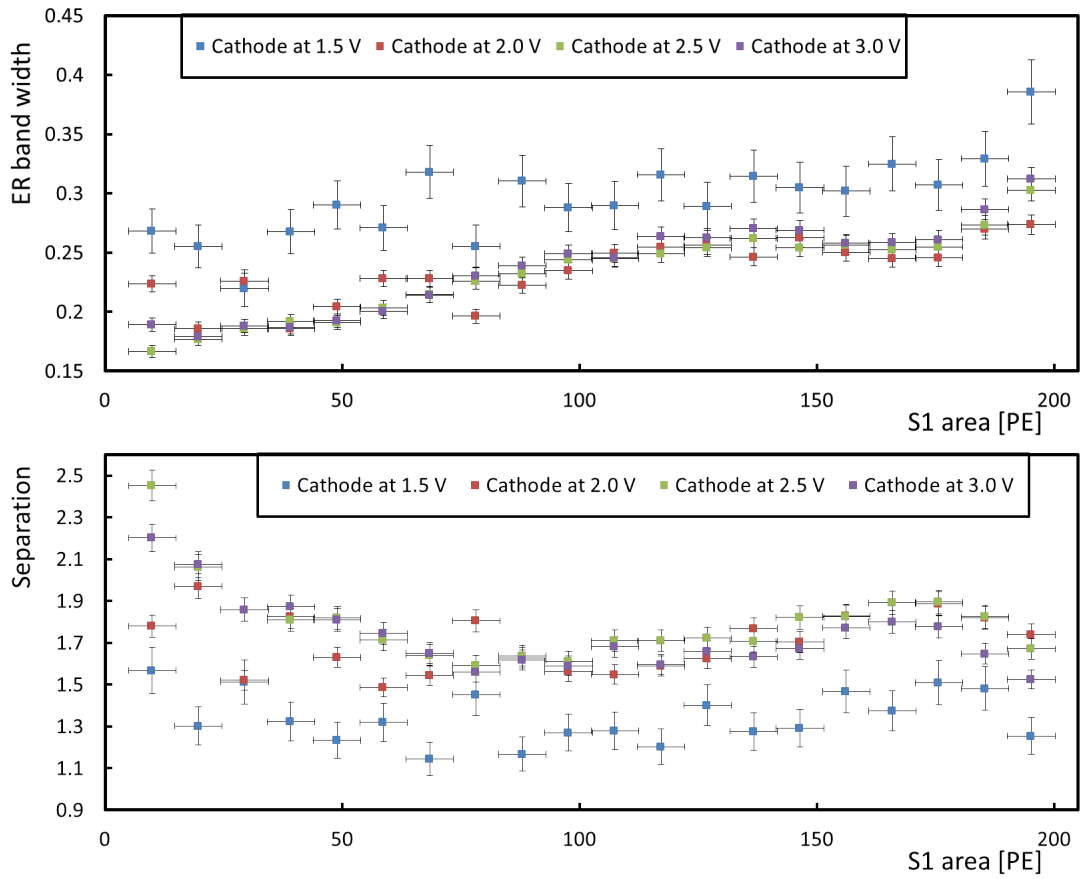
Figure 4.48: Comparison of the width of the ER band (top) and the separation significance (bottom) versus S1 area for various drift fields. The errors on the evaluation of electric field (horizontal error bars) are calculated by propagation of the uncertainties from electric field simulations.
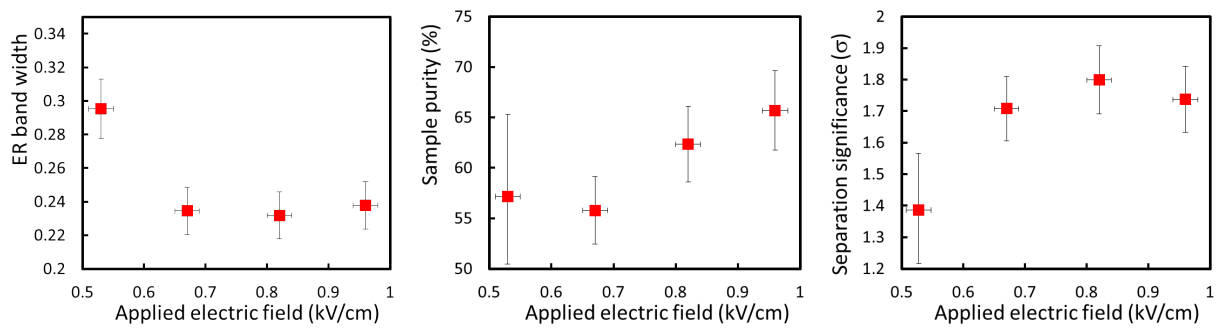
Figure 4.49: Comparison of the average ER band width (left), sample purity (middle), and the separation significance (right) versus applied electric field.

band is larger at this field with $2.6\,\sigma$ level of significance and the separation significance is smaller

by $1.9\,\sigma$. These results disfavor the use of xenon TPC detectors operated at lower electric fields near $0.5\,\mathrm{kV/cm}$. In particular, it predicts that XENON100 experiment, operated at $0.53\,\mathrm{kV/cm}$ could have improved discrimination quality at higher applied electric fields. The measurements are ongoing to increase the number of data points and the statistics of events acquired at each field in order to study such dependencies in a more systematic manner.

Electric field (kV/cm)	ER band width	Sample purity (%)	Separation significance (σ)
0.53±0.03	0.30±0.03	57.2±7.9	1.39±0.19
0.67±0.03	0.23±0.02	55.8±3.5	1.71±0.12
0.82±0.02	0.23±0.02	62.3±3.7	1.80±0.13
0.96±0.02	0.24±0.02	65.7±3.9	1.74±0.12

Table 4.5: The averaged values of discrimination quality parameters at different electric fields.

4.8 Characterization studies of the setup for the neutron scattering measurements

Prior to the commissioning of the Xurich II TPC, the other components of the setup for coincidence measurements, including the liquid scintillators, neutron generator, MPD4 module, and measurements of the time of flight were characterized, and the work is described with details in my MSc thesis (reference [163]). However, some characterizations had to be repeated, considering the technical modifications of the actual setup that effect the analysis.

For instance, the measurements of the time of flight using the TAC module strongly depend on the length of cables and connectors that are used. Hence, the time of flight calibration had to be repeated for the final configuration, where the coincidence measurements are performed.

Similar to the method that was described in [163], a ^{22}Na radioactive source is used for calibration of the time of flight. As illustrated in figure 4.14, the TAC module converts the time difference between the trigger signal from the discriminator, taking the signal from the bottom PMT as input, and the trigger output of the MPD4 module, using the input from EJ301 scintillator, into pulse height. The total length of cables used for each of the mentioned trigger signals to reach the TAC module is about $12\,\mathrm{m}$, meaning that it takes about $40\,\mathrm{ns}$ for the signal to travel this distance. This is comparable to the range of expected time of flight for $2.45\,\mathrm{MeV}$ neutrons to travel a distance of about $1\,\mathrm{m}$.

Hence, the systematic errors on the signal delays need to be excluded from the measurements of the time of flight through a proper calibration in the actual setup. The ^{22}Na radioactive source is placed in the middle between the Xurich II TPC and the liquid scintillator. This isotope follows a β^+ decay into a ^{22}Ne excited state. While the de-excitation of the ^{22}Ne emits a gamma with $1.275\,\mathrm{MeV}$, the annihilation of the $e^+\,e^-$ pairs also produces a pair of gamma particles with $511\,\mathrm{keV}$ energy that are kinematically forced to travel in opposite directions [194].

$$^{22}\mathrm{Na} \;\longrightarrow\; ^{22}\mathrm{Ne}^* \;+\; e^+ \;+\; \nu_e^- \qquad (4.22)$$

$$^{22}\text{Ne}^{*} \ \longrightarrow \ ^{22}\text{Ne} \ + \ \gamma \ (1.275 \ MeV) \tag{4.23}$$

$$e^{+} \ + \ e^{-} \ \longrightarrow \ 2 \ \gamma \ (511 \ keV) \tag{4.24}$$
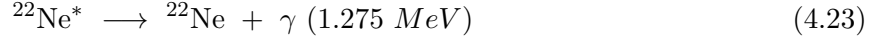
Therefore, the two $511\,\text{keV}$ gammas are expected to arrive at both targets in coincidence. Using such coinciding events, the time of flight readout can be calibrated. First, the TOF value corresponding to zero time difference needs to be evaluated and second, the conversion of the output (in arbitrary units) into physical units has to be determined. These requirements can be both fulfilled through taking several calibration data using ^{22}Na source varying delays from an electronic module, applied to one of the trigger signals (see figure 4.14). Figure 4.50 shows the distribution of TOF spectrum acquired for several calibrations using ^{22}Na source and the resulting linear fit to the data points from which the zero value and the conversion factor can be extracted.
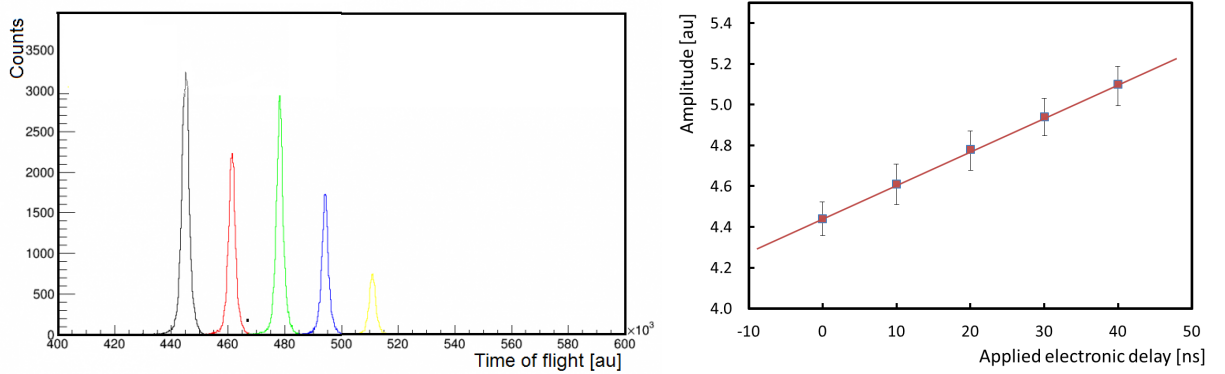
Figure 4.50: (Left); the time of flight spectra for several coincidence measurements using ^{22}Na radioactive source with applied electronic delay to the "stop" trigger. (Right); a linear fit to the time of flight calibration data. The slope of the fit function is used to convert time of flight output into units of seconds.

In addition, the optimization of the MPD4 module settings, also described in [163], needed to be verified and the pulse shape discrimination capabilities should be quantified. The optimization of the internal configuring parameters was done to achieve the most flat distribution of ER band. In order to study the discrimination quality, ^{22}Na and AmBe radioactive sources are used to achieve pure ER and NR + ER bands respectively. ^{241}Am emits alpha particles that with some probability interact with ^{9}Be atoms, producing neutrons through (α,n) reactions [195].

$$^{241}\text{Am} \ \longrightarrow \ ^{237}\text{Np} \ + \ ^{4}_{2}\alpha \ + \ \gamma \tag{4.25}$$

$$^{4}_{2}\alpha \ + \ ^{9}\text{Be} \ \longrightarrow \ ^{12}\text{C} \ + \ n \ + \ \gamma \tag{4.26}$$

Figure 4.51 shows the distribution of PSD versus AMP parameters from MPD4 module output. The ER band is distributed around the PSD values of $\sim$1400 units while the NR band shows deviations to higher PSD values with a good separation from ER events at for events with higher energies (higher AMP). The ER band can be defined on the pure sample of ERs in the ^{22}Na data.

The neutrons can be selected in the regions outside the ER band and with a selection above a minimum value of AMP, as shown in the figure.

Applying this procedure to the ^{22}Na and AmBe data yields a sample purity (refer to section 4.7.2) of 32 % derived at 95 % quantile bands for gamma rejection. Note that, since a pure sample of NR recoils cannot be used. The quality of discrimination will be improved in the final analysis, using the combination of the PSD and TOF parameters, as described in the following section.
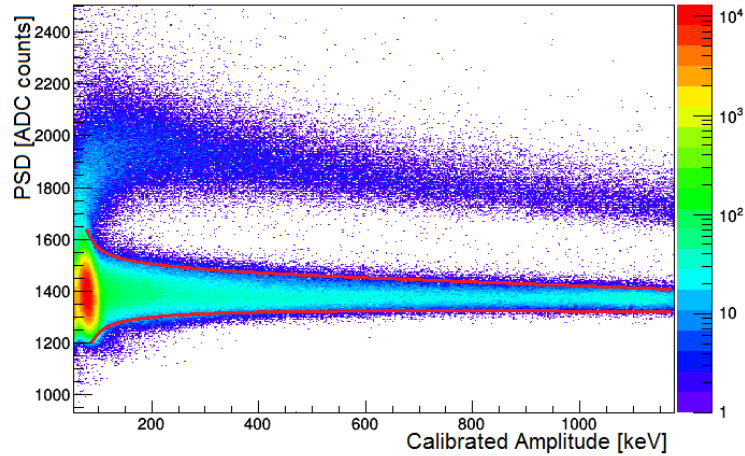
Figure 4.51: The PSD versus AMP distribution of events from AmBe calibration data using MPD4 module and the EJ301 scintillator inline. The red lines show the 95 % quantiles defined on the ER sample using ^{22}Na radioactive source.

4.9   Measurements of the nuclear recoil response

Using all the work described in the previous sections to provide optimal and stable operating conditions and development of the preliminary analysis steps including the raw data processing and signal quality selections, as of the start of August 2016, the Xurich II detector is taking data in coincidence mode, as described in section 4.2.2.

By the end of December 2016, the data have been acquired at five different configurations of the angle and distance of the liquid scintillator detector with respect to the LXe target. Table 4.6 provides the list of configurations. The expected recoil energy is determined through insertion of the geometrical parameters into equation 4.3 (assuming A = 131.293 amu for xenon). The expected time of flight is calculated with the following equations.

First, the kinetic energy of neutrons after scattering is calculated, using the assumption on the initial energy distributed around $E_n \simeq 2.45$ MeV , and E_{nr} from equation 4.3.

$$E_k = E_n - E_{nr}, \tag{4.27}$$

Then, the speed of neutrons after scattering can be estimated, knowing the rest mass of neutrons, $m_n = 1.0086654$ amu.

$$E_k = \frac{1}{2} m_n \left(\frac{v}{c} \right)^2 \implies v = c \sqrt{\frac{E_k}{m_n}}, \tag{4.28}$$

And finally, the time of flight is derived, using the distance ΔX between the primary and tagging detectors.

$$\Delta t = \frac{\Delta X}{v} \tag{4.29}$$

Item	Distance ±0.5 [cm]	angle ±0.25 [deg]	Recoil energy [keVnr]	Time of flight [ns]
1	71.5	26.5	3.9±0.3	33.1±2.2
2	68.0	27.5	4.2±0.3	31.5±2.3
3	80.5	35.0	6.7±0.4	37.2±2.5
4	93.5	50.0	13.3±0.7	43.2±2.9
5	95.0	59.5	18.3±0.9	43.9±2.9

Table 4.6: The table of coincidence data acquired with the Xurich II detector by the end of December 2016. Each configuration includes a measured distance of the tagging (scintillator) detector with respect to the xenon TPC. The expected recoil energy and the time of flight are calculated using (non-relativistic) scattering kinematics (see the text). The systematic errors include propagation of the instrumental errors on measurements of distance and angle as well as the expected distribution of the initial neutron energy.

Due to technical reasons, the operation of the neutron generator has not been very stable and the data acquisition took longer than expected. It is found that even under stable operation of the neutron generator, the rate of coincidence nuclear recoil events is of the order of 1 event per hour, resulting low statistics of such events. In order to illustrate this, figure 4.52 shows the distribution of the PSD parameter from MPD4 module versus the time of flight of all coincidence events passing the basic quality cuts.

Once the recoil energy distribution is obtained, comparison of such spectrum with the one produced by Monte-Carlo simulations follows evaluation of the parameters $\mathcal{L}_{eff}$ and Q_y for the given recoil energy, the final goal of the Xurich II project once sufficient statistics of coincidence events are recorded. The expected major sources of systematic uncertainties of such measurements are listed below.

- Uncertainties on the measurements of the angle and distance between the two interactions. The dimensions of the both Xurich II TPC and the EJ301 scintillator, divided by their distance raises an error in evaluation of the distance and the scattering angle. Because of the lack of position reconstruction capabilities of the two detectors, such uncertainties cannot be avoided. For instance, the expected relative uncertainties at a distance of 1 m between the two detectors is 6 % [163] from MC simulations.

- The statistical distribution of the initial neutron energy is rather wide near the mean value (2.45 MeV). As shown in figure 4.5, the measured distribution represents a sigma over mean value of 14.5 %. These uncertainties should be projected to the calculation of the recoil energy to obtain the systematic errors.
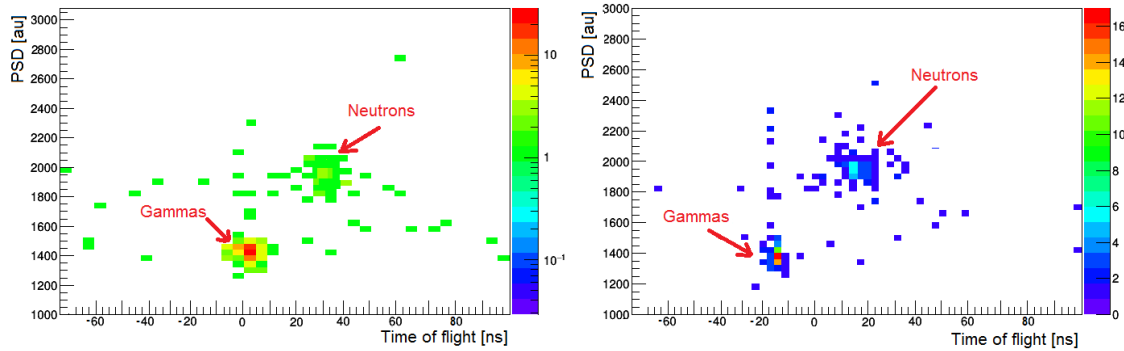
Figure 4.52: The PSD versus time of flight for all coincidence events after the signal quality cuts for the data acquired at 26.5 (left) and 35 (right) scattering angles. The population of events with zero TOF value denote coincidence gamma scatterings while the neutron cluster is populated at higher TOF and larger PSD values. Note that logarithmic colorbar is used for the left figure whereas normal scale is used for the right plot for better visualization of the low statistics.

- As mentioned in section 4.2.2, the trigger efficiency is estimated to be near unity for electronic recoil events above 0.5 keV. However, at low energies close to this threshold, the actual efficiency needs to be determined using the pulse height distribution of the S1 and S2 signals from nuclear recoils. Hence, at low scattering angles, the expected errors on the evaluation of the trigger efficiency will introduce additional systematic uncertainties to the final results.

Hence, the most prominent expected systematic uncertainties of the mentioned measurements of the xenon response to low energy nuclear reocils, using the Xurich(II) experiment, is attributed to the absence of radial position reconstruction capabilities in neither the Xurich(II) TPC, nor the scintillator target. Hence, the geometrical uncertainties of the position of interaction inside each target, will be directly propagated in the interpretation of the final results. The corresponding diameters are 3.1 and 7.0 cm for the scattering and tagging targets, respectively. Such dimensions, are not negligible compared to the distance between the two targets being practically limited to 0.5-1.0 m. Therefore, it is suggested that for an upgrade of the setup, in order to improve the precision of the measurements, several photo-sensors are instrumented for both targets, permitting radial position reconstruction.

4.10   Summary and discussions

The Xurich II dual phase xenon detector was constructed with the aim of measuring the low energy response of liquid xenon to nuclear recoil. Although the detector inherits most subsystems (e.g. gas system, cryogenics, some feed-throughs, pressure and temperature sensors, etc), during the commissioning of the detector several components were upgraded or modified. For instance, one of the PMTs, the PMT voltage dividing circuit, the TPC parts, several of the cables, connectors and feed-throughs, few sections of the gas system, DAQ and electronics were modified. In particular, the TPC design was modified based on electric field simulation.

All detector subsystems were commissioned individually during this PhD work. For instance, the gas system was upgraded by adding a ^{83}Rb emanation volume, used for calibrations with ^{83m}Kr intrinsic radioactive source together with a bypass pipeline. In addition, an emergency xenon bottle was added to the system and the connections to getter and recirculation pumps were reorganized to allow continuous monitoring of the xenon gas flow during recovery process.

The data acquisition system was also upgraded using ADC modules of newer technology, with better resolution. All electronic modules were tested including signal amplifiers, attenuators, pulse shape discrimination trigger generator, and etc. The trigger efficiency was measured and nearly 100 % acceptance is estimated for electronic recoils with energies higher than 0.6 keVnr. For the measurements of nuclear recoil response acquired at small angels where the expected recoil energy is very low (3-4 keVnr), this threshold can be further lowered by using and amplifier.

Beside the DAQ system dedicated for calibration of the detector, an advanced system was designed for acquisition of data in coincidence with an EJ301 liquid scintillator detector, used for tagging scattered neutrons. The individual electronic modules of this system were also characterized including a time -to-amplitude converter (TAC) module for measurement of time of flight, and a pulse shape discriminator module for neutron and gamma discrimination. The additional modules were also individually characterized during this work.

A raw data processing software was developed for the Xurich II detector. The software was commissioned using the calibration data. In particular, several signal classification algorithms were examined and as a result a combined algorithm was developed using three independent methods.

The capacitor levelmeters used for the Xurich II TPC are read by a Labview program through a serial connection to a UTI board. The program was upgraded for online monitoring of the actual liquid level being read by the three capacitors, after importing calibration results of each levelmeter. The program was then used for leveling of the TPC using external tilting screws attached to the vacuum cryostat.

Moreover, a PMT calibration system was installed using PMMA optical fibers to guide the light from an LED into the vacuum cryostat and to the PMTs. In addition, an analysis script was provided to process the PMT calibration data into evaluation of the PMT gains. The resulting gain values have been monitored regularly during the operation of the detector. The gain values delivered by two different methods are consistent and were stable within the systematic errors of the measurement for an operation of several months. The PMT readout base were studied in details for their response to signals from Xurich detector and a new version of the bases was developed after observation of several issues, such as ringing, and overshoot.

The analysis of the calibration data of the experiment was carried out to develop signal quality cuts to be used for the selection of events for the nuclear recoil response study. In addition, the response of the detector to the low energy electronic recoils from ^{83m}Kr data was studied in detail, resulting into evaluation of S1 and S2 signal yields, measured at different applied electric drift fields. The S1 and S2 yields measured for the 9.4 keV energy line are ranged between 10.5-12.5 PE/keV and 270-550 PE/keV, whereas the measured ranges for 32.1 keV line are 7.8-9.8 PE/keV and 480-790 PE/keV, respectively, for the electric fields ranged between 0.22-1.26 kV/cm.

In addition, the measurements of the quenching of the S1 and S2 signals as a function of the applied electric field are performed using a fit to the obtained yields from ^{83m}Kr calibration data using Thomas-Imel box model. The observed values of the fit parameters are consistent within the systematic error bars with the ones measured in reference [187] using the Xurich I detector. In addition, we observe an improvement of the zero field light yield compared to Xurich I detector by ~50 % and ~70 % considering the 9.4 keV and 32.1 keV energy lines, respectively. Furthermore, since sufficient statistics of events with resolved S1 and S2 pairs from ^{83m}Kr calibration data are

observed, the normalized charge yield could be studied for all the 3 lines while it was evaluated only for the summed 41.5 keV energy line in reference [187]. This is attributed to the improvements in the DAQ setup and analysis capabilities used for the Xurich II detector.

Furthermore, the discrimination power of xenon was studied at different electric fields using the analytic comparison of the data from a ^{137}Cs radioactive source and the neutron generator. The discrimination power measured by several other xenon experiments are shown in table 4.7.

Experiment	Field [kV/cm]	ROI [keVnr]	NR acceptance [%]	ER rejection [%]
ZEPLIN-II [196]	1.0	14-58	∼50	98.5
XENON10 [197]	0.73	4.5-26.9	∼45	99.9
ZEPLIN-III [198]	3.4	7-35	∼50	99.987
XENON100 [85]	0.53	6.6-43.3	20-60	99.75
LUX [199]	0.18	3-27	∼50	99.9
Lin et al. [192]	0.2, 0.7, 1.0	5.5-11	∼50	99.999

Table 4.7: The discrimination power reported by several xenon detectors.

As it can be seen in table 4.7, XENON100 and LUX experiments, which set the current best sensitivities among direct WIMP search experiments, have fixed their ER rejection band at limits where about 50 % NR acceptance (20-60 % value quoted for XENON100 is calculated for the whole range of interest in energy) is reached. The corresponding reported ER rejection powers are 99.75 % and 99.9 % for the XENON100 and LUX experiments, respectively [85, 199]. Among the large scale detectors, ZEPLIN-III has reached the best discrimination power with ∼50 % NR acceptance at ER rejection power of 1 over 7800 events [198]. However, the reported value in reference [192] which is measured using a R&D scale xenon TPC is the best discrimination power claimed for xenon detectors in the literature with ∼50 % NR acceptance calculated after ER rejection power of 1 in 10^5 events.

Our analysis of the Cs calibration data and the ER bands shows that the width of the band is relatively larger for the Xurich II detector compared to other experiments. This is attributed to the presence of the events that occur near the edges of the TPC which cannot be excluded from the analysis due to absence of (x,y) position reconstruction capabilities. The regions near the edge of the TPC are expected to have lower charge collection efficiency compared to the center since part of the electron cloud drifting toward the gas phase can get trapped or slowed down in the surface of the PTFE reflector. This will cause such events to have lower S2/S1 ratio and populate as a leakage of the ER band toward the NR region. Hence, it motivates the upgrade of the detector through installation of several photosensors instead of either the current top or the bottom PMTs to allow for (x,y) position reconstruction of events within the TPC volume.

Due to the presence of observed leakage of events from the ER band toward the NR region from ^{137}Cs calibration data of the Xurich II detector, an NR acceptance of ∼60 % is derived using an ER rejecting band of 97.7 %. Increasing the ER rejection power through lowering the ER band further than this limit results in sharp reduction of the estimated NR acceptance. Therefore, it is not expected that the current version of the detector can set comparable discrimination power limits to the current best detectors listed above. The NR acceptances are estimated through a Gaussian fit to the NR band distribution over the flattened discrimination parameter. In order to provide more precise estimations, Monte Carlo simulations are required to reproduce the distribution of the NRs within the Xurich II detector. However, concerning the measurement of comparing the

discrimination power as a function of drift field, the low discrimination power of the detector is not an considered as an issue hence all the experimental conditions similar for the measurements at different fields except for the applied electric field, which is the parameter under study.

The discrimination power was compared using 3 different quantities: electronic recoil band width, separation significance of the ER and NR bands, and sample purity at given electronic recoil rejection power. It has been observed that the comparison of the sample purity parameter provides no significant difference between the electric fields, while comparing both the ER band width and the separation significance indicates that the discrimination quality is worse for the data acquired with the lowest field (0.53 kV/cm) compared to the other data (at 0.67, 0.82, and 0.96 kV/cm).

Our measurements show that the operation of the xenon TPC detectors at low applied electric drift fields near 0.5 kV/cm can result in lower discrimination capabilities than higher fields. These results are in disagreement with a previous measurement reported in references [192, 193] at which no dependency of the discrimination quality is observed through varying the electric field. We expect that regarding its high S1 and S2 signal yields, the Xurich II detector is more sensitive to such variations of parameters and hence we attribute the discrepancy of our results with previous measurements to the higher sensitivity of the detector. The detector is currently being used to acquire data at more electric fields and with higher statistics in order to validate this hypothesis.

Finally, after characterization of all the components used in the setup for coincidence nuclear recoil measurements, data was acquired at 5 scattering angles corresponding to nuclear recoil energy mean expectation values of 3.9, 4.2, 6.7, 13.3, and 18.3 keVnr. The observed rate for coincidence neutron scatterings is approximately 1 event per hour, requiring long data acquisition periods at each configuration to achieve sufficient statistics, considering the technical difficulties of operating the neutron generator stably for long-term. The coincidence nuclear recoil data acquisition is currently ongoing. Once the recoil energy distribution is obtained for each angle, comparison of such spectrum with the one produced by Monte-Carlo simulations yields evaluation of the xenon scintillation and ionization yields ($\mathcal{L}_{eff}$ and Q_y) for the corresponding recoil energy.

Chapter 5

Conclusions and Outlook

The nature of the dark matter has remained a mystery for physicists. Motivated by several independent observational evidences and following suggestions provided by physics theories, several experiments have been constructed trying to detect dark matter, in particular in the form of WIMPs. Using the modern advanced technology and past experience, the current generation of experiments will reach unprecedented sensitivities.

The XENON1T experiment is predicted to reach the world-leading sensitivity for WIMP-nucleon spin-independent cross-sections after about 20 days of exposure, and to improve this limit by more than a order of magnitude, by 2 year exposure. During this thesis work, I was involved, in the construction, commissioning, and data analysis of the XENON1T experiment.

In particular, the XENON1T PMT calibration has been designed, tested, installed, and commissioned, resulting in successful calibration of all PMTs, regularly performed until present. In addition, a dedicated analysis work was carried out to determine the PMT response to single photo-electrons. A software package is provided, equipped with a graphical user interface (GUI) that can be used by the collaboration members. The package is capable of performing the entire analysis process, from raw PMT data, into extraction of the response parameters, such as gain, single photo-electron resolution.

The PMT calibration system has been in use of the operation crew of the experiment as of May 2016 and by now experiences more than half a year of stable operation. The results of the weekly gain calibrations indicate an stable gain value for all PMTs within maximum 3.5 % variations over 3 month operation after the final gain equalization. These variations are compatible with the expected systematic errors of the measurements. Similarly a deviation of maximum 4.0 % is observed for the occupancy parameter from all PMTs which quantifies the light illumination intensity for each PMT. The current gain values of all the functional PMTs ranges $(1.92\text{-}4.64)\times10^6$.

The next generation XENONnT experiment aims to improve these limits even further, through utilizing the existing infrastructure of the XENON1T experiment. The new detector consists of a new TPC with double the liquid xenon mass, and approximately 35 % better photosensor coverage, than the XENON1T detector. A major part of the currently installed and commissioned PMT calibration system of XENON1T can be reconfigured and used for the XENONnT experiment. In particular, only the PMMA fibers installed inside the cryostat can be replaced by new branches while the rest of the system including the silica fibers, plastic fibbers, vacuum feed-throughs, LED frame, and pulse generator can be reused.

The existing Xurich I detector at university of Zurich, that was used to study the xenon response to low energy electronic recoils, was upgraded to study the xenon response to nuclear recoils. The

new (Xurich II) detector was successfully commissioned, with various calibration carried out to study and optimize the detector performance at various operational conditions. A major topic of this thesis includes the commissioning of the Xurich II detector, and all its subsystems (such as the gas system, DAQ, and raw data processing algorithm), that was successfully achieved.

Through a preliminary study of the trigger efficiency for the DAQ system configured for the neutron measurements using Xurich II and a liquid scintillator tagging detector an effective energy threshold of 0.6 keVnr is estimated for nuclear recoils. This can be further improved via using an amplifier on the signal from the bottom PMT that generates the trigger through a discriminator module, if needed.

In addition, the response of the detector to the low energy electronic recoils from ^{83m}Kr data was studied, with the S1 and S2 signal yields measured for different electric drift fields. The S1 and S2 yields measured for the 9.4 keV energy line are ranged between (10.5-12.5) PE/keV and (270-550) PE/keV, whereas the measured ranges for 32.1 keV line are (7.8-9.8) PE/keV and (480-790) PE/keV, respectively, for the electron fields ranged between (0.22-1.26) kV/cm.

The liquid xenon discrimination power for electronic and nuclear recoils was studied using three different quantities: electronic recoil band width, separation significance of the two bands, and sample purity at given electronic recoil rejection power, and at four different applied electric fields (0.53, 0.67, 0.82, and 0.96 kV/cm). The measured values for the sample purity at different fields are consistent within the systematic errors. The average sample purity measured by the ER rejection using -1.5σ (93.3 %) band provides a sample purity of 60.5 % in average. However, the ER band width measured for the data at 0.53 kV/cm electric field is larger compared to the average of the other fields by 2.6 σ level of significance. In addition, the separation significance was observed to be smaller at the lower field by 1.9 σ. Hence, we conclude that the discrimination quality is worse this field compared to the range of 0.67-0.96 kV/cm.

Moreover, several other components were characterized to provide a dedicated setup for measurements of nuclear recoil response, using a D-D fusion neutron generator facility at UZH. The setup includes an additional organic liquid scintillator detector, served as the tagging target, and a pulse shape discrimination module for the signal/background separation. Having all the components fully characterized, neutron measurements are already ongoing, aiming to collect sufficient statistics from scattered neutrons at various angles. Comparing such data with Monte Carlo simulations using detailed GEANT4 model of the experimental setup will result in a measurement of the liquid xenon response to nuclear recoils down to sub-keV energies.

The measurements of the low energy response of liquid xenon will limit the current uncertainties in the scintillation and ionization yields. The future larger scale experiments, such as DARWIN can take advantage of the measured response parameters with high precision to reach the ultimate sensitivities for WIMP search experiments.

DARWIN will be an experiment using a multi-ton liquid xenon TPC, with the primary goal to explore the experimentally accessible parameter space for WIMPs. In case the dark matter particles are discovered by existing or future experiments prior to DARWIN, it will measure WIMP-induced nuclear recoil spectra with high statistics and constrain the mass and the scattering cross sections with maximum precision.

Acknowledgments

First I thank my PhD advisor, Prof. Laura Baudis, for admitting my entrance to the group, first as a Master student, and later as a PhD student. Only under her vise supervision I could have managed to reach this level. Her kind support has helped feel strong and confident while taking my first "baby steps" into the world of science.

I thank Dr. Alexander Kish, who has directly supervised me for all the science projects I was involved at during this PhD work. Using his suggestions and guidance, I could solve the problems I encountered through my work.

Over the years in XENON group at UZH, I have used help and support of several Postdoctoral researchers, Aaron Manalaysay, Teresa Marrodan, Marc Schumann, Michelle Galloway, Domenico Franceo, Yuehuan Wei, Shingo Kazama, Martin Auger, and fellow graduate student, Gaudenz Kessler, Francesco Piastra, Daniel Mayani, Peter Barrow, and Julien Wulf. Often you helped me reach a higher level of understanding both physics and life related subjects. To all of you I am thankful for helping me pass this stage.

I thank especially Francesco Piastra with whom I shared the work on the work on the Xurich II detector. The most exciting moments I experienced on physics related topics happened during the discussions we had.

Furthermore, I thank Daniel Mayani for our close collaborative work on the XENON1T PMT calibration software. It has been very nice experiencing working together with you beside our all-time close friendship that I hope will continue.

None of the hardware work that I managed to carry out during this PhD would have been possible without the kind support of Andreas James. His professional engineering view of the problems has helped our group and the XENON collaboration to excel at hardware challenges.

Many thanks to Regina Schmid, Carmelina Genovese, Ruth Halter, and Monika Röllin who helped me feel safe and comfortable about the large amount of required bureaucratic work during this PhD.

I also thank Giovanni Benato and Francesco Piastra for helping me improving my programming skills. Without your support, I would have been even a worse programmer than I am! In addition, I will always miss the Italian coffee breaks we used to have every now and then after lunch. Thanks for introducing me to the true concept of the "real coffee", which has helped me avoid the midday nap in front of my computer during these years.

Moreover, I need to mention that I enjoyed the very nice coffee breaks that I shared mostly with Daniel Mayani and Peter Barrow complaining about the length of weekly group meetings.

Finally, I thank my lovely wife, Saghar, for her supportive attitude during the past years. Even after the hard time I had to managing the distance between the pressure and stress from work and my personal life, with her kind view into our relationship, the bonds between us have become stronger during this period. I will be forever grateful for your patience.

Bibliography

[1] R. Durrer, and R. Maartens, "Dark energy and dark gravity: theory overview", Gen. Rel. Gravit. , 40:301–328, (2008).

[2] J. Kapteyn, "First attempt at a theory of the arrangement and motion of the sidereal system", APJ 55 302 (1922).

[3] F. Zwicky, "Die Rotverschiebung von extragalaktischen Nebeln", Helvetica Physica Acta 6 110 (1933).

[4] V. C. Rubin, N. Thonnard, and J. Ford, W. K., "Extended rotation curves of high-luminosity spiral galaxies", Astrophys J225 L107 (1978).

[5] H. Babcock, "The rotation of the Andromeda Nebula", Lick Observatory bulletin no. 498 (1939).

[6] Peter R. Hague, Mark I. Wilkinson, "The degeneracy of M33 mass modelling and its physical implications", arXiv:1408.4452 [astro-ph.GA] (2015).

[7] E. E. Richards, et al. , "Baryonic distributions in the dark matter halo of NGC 5005", Mon. Not. Roy. Astron. Soc. 449 no. 4 3981,(2015).

[8] M. Pato, F. Iocco, and G. Bertone, " Dynamical constraints on the dark matter distribution in the Milky Way", JCAP 12 001, (2015).

[9] B. Fuchs, " The Amount of Dark Matter in Spiral Galaxies", arXiv:astro-ph/0010358v2 [astro-ph] (2000).

[10] A. Einstein, "Lens-Like Action of a Star by the Deviation of Light in the Gravitational Field", Science 84 506 (1936).

[11] F. Zwicky, "Nebulae as gravitational lenses", Phys. Rev. 51 290 (1937).

[12] D. Clowe, et al. , "A direct empirical proof of the existence of dark matter", Astrophys. J. 648 L109 (2006).

[13] M. Bradac, et al., "Revealing the properties of dark matter in the merging cluster MACSJ0025.4-1222", Astrophys. J.687 959 (2008).

[14] W. A. Dawson, et al. , "Discovery of a Dissociative Galaxy Cluster Merger with Large Physical Separation", Astrophys. J. 747 L42 (2012).

[15] D. Harvey, R. Massey, T. Kitching, A. Taylor, and E. Tittley, "The non-gravitational interactions of dark matter in colliding galaxy clusters", arXiv:1503.07675 [astro-ph.CO] (2015).

[16] F. Kahlhoefer, K. Schmidt-Hoberg, M. T. Frandsen, and S. Sarkar, "Colliding clusters and dark matter self-interactions", Mon. Not. Roy. Astron. Soc. 437 no. 3 2865, (2014).

[17] Maxim Markevitch, "Chandra observation of the most interesting cluster in the Universe", arXiv:astro-ph/0511345 [astro-ph], (2005).

[18] S. M. Faber, R. E. Jackson, "Velocity dispersions and mass-to-light ratios for elliptical galaxies", APJ. 204: 668F–683, (1976).

[19] G. W. Collins, "The Virial Theorem in Stellar Astrophysics", Pachart Press,(1978)

[20] R. Ciardullo, G. H. Jacoby, H. B. Dejonghe, "The radial velocities of planetary nebulae in NGC 3379", APJ. 414: 454C–462,(1993).

[21] R. Minchin, et al, "A Dark Hydrogen Cloud in the Virgo Cluster", APJ 622L: L21–L24, (2005).

[22] Planck Collaboration, "Planck 2015 results. XIII. Cosmological parameters", A&A 594, A13, (2016).

[23] WMAP Collaboration, "Nine-Year Wilkinson Microwave Anisotropy Probe (WMAP) Observations: Cosmological Parameter Results", Astrophys. J. Suppl. 208, (2013).

[24] P. J. E. Peebles, "The Large-Scale Structure of the Universe", Princeton University Press. ISBN 0-691-08240-5, (1980).

[25] V. Springel et al, "Simulating the joint evolution of quasars, galaxies and their large-scale distribution", Nature 435:629-636, (2005).

[26] B. Paczynski, "Gravitational microlensing by the galactic halo", Astrophys. J. 304, (1986).

[27] Macho collaboration, " MACHO Project Limits on Black Hole Dark Matter in the 1-30 Solar Mass Range", Astrophys. J. 542 281, (2000).

[28] L. Baudis, "Dark matter detection", J. Phys. G: Nucl. Part. Phys. 43 044001, (2016).

[29] T. M. Undagoitia and L. Rauch, "Dark matter direct-detection experiments", arXiv:1509.08767 [physics.ins-det], (2015).

[30] S. Tremaine and J. E. Gunn, "Dynamical role of light neutral leptons in cosmology", Phys. Rev. Lett. 42 407, (1979).

[31] C. S. Frenk, S. D. M. White, "Dark matter and cosmic structure", Annalen Phys. 524 507–34, (2012).

[32] L. Canetti, M. Drewes, T. Frossard and M. Shaposhnikov, " Dark Matter, Baryogenesis and Neutrino Oscillations from Right Handed Neutrinos", Phys. Rev. D 87, 093006, (2013).

[33] K. N. Abazajian et al, "Light Sterile Neutrinos: A White Paper", arXiv:1204.5379 [hep-ph], (2012).

[34] A. Kusenko, "Sterile neutrinos: The Dark side of the light fermions", Phys. Rept. 481, (2009).

[35] S. Weinberg, "A New Light Boson?", Phys. Rev. Lett. 40 223, (1978).

[36] R. Peccei and H. R. Quinn, "CP Conservation in the Presence of Instantons", Phys. Rev. Lett. 38 1440, (1977).

[37] E. W. Kolb and M. S. Turner, "The early universe", Addison-Wesley 1 1–547,(1994).

[38] G. G. Raffelt, "Astrophysical axion bounds", Lect. Notes Phys. 741 51, (2008).

[39] K. Olive et al (Particle Data Group), "Review of Particle Physics", Chin. Phys. C 38 090001, (2014).

[40] J. Preskill, M. B. Wise, and F. Wilczek, "Cosmology of the invisible axion", Phys. Lett. B 120 127–32, (1983).

[41] M. Dine, W. Fischler, and M. Srednicki, "A Simple Solution to the Strong CP Problem with a Harmless Axion", Phys. Lett. B104 199, (1981).

[42] J. E. Kim, "Weak Interaction Singlet and Strong CP Invariance", Phys. Rev. Lett. 43 103, (1979).

[43] P. W. Graham, I. G. Irastorza, S. K. Lamoreaux, A. Lindner, and K. A. van Bibber, "Experimental Searches for the Axion and Axion-like Particles", Annual Review of Nuclear and Particle Science, Vol. 65: 485-514, (2015).

[44] J. Jaeckel, and A. Ringwald, "The Low-Energy Frontier of Particle Physics", Annual Review of Nuclear and Particle Science, Vol.60:405-437, (2010).

[45] P. Arias, et. al., "WISPy cold dark matter", JCAP 1206:013, (2012).

[46] A. Ringwald, " Exploring the Role of Axions and Other WISPs in the Dark Universe", Phys. Dark Univ. 1:116, (2012).

[47] P. Brun, "Axion-like particles: possible hints and constraints from the high-energy Universe", Journal of Physics: Conference Series 460 012015, (2013).

[48] L. Ackerman, M. R. Buckley, S. M. Carroll, and M. Kamionkowski , "Dark Matter and Dark Radiation", arXiv:0810.5126 [hep-ph], (2008).

[49] N. Borodatchenkova , D. Choudhury , and M. Drees, "Probing MeV Dark Matter at Low–Energy e^+ e^- Colliders", Phys.Rev.Lett.96:141802, (2006).

[50] M.Krawczyk, D. Sokolowska, and B. Swiezewska, "2HDM with Z_2 symmetry in light of new LHC data", J. Phys.: Conf. Ser. 447 012050, (2013).

[51] The BABAR Collaboration, "Search for a dark photon in e^+ e^- collisions at BABAR ", Phys. Rev. Lett. 113, 201801, (2014).

[52] K. Greisen, "End to the cosmic ray spectrum?", Phys. Rev. Lett. 16 748, (1966).

[53] D. J. Chung, E. W. Kolb, and A. Riotto, "Superheavy dark matter", Phys. Rev. D59 023501, (1999).

[54] V. Berezinsky, M. Kachelriess, and A.Vilenkin, " Ultra-high energy cosmic rays without GZK cutoff", Phys.Rev.Lett.79:4302-4305, (1997).

[55] P. Blasi, R. Dick, and E. W. Kolb, " Ultra-high energy cosmic rays from annihilation of superheavy dark matter", Astropart.Phys.18:57-66, (2002).

[56] A. Ibarra, R. Toldra, " Neutralino spectrum in top-down models of UHECR", JHEP 0206:006, (2002).

[57] Murayama, Hitoshi, "Supersymmetry phenomenology". arXiv:hep-ph/0002232, (2000).

[58] S. P. Martin, "A Supersymmetry Primer", arXiv:hep-ph/9709356, (1997).

[59] M. Dine "Supersymmetry and String Theory: Beyond the Standard Model", p. 169 (2007).

[60] H. Baer, X. Tata , " The Minimal Supersymmetric Standard Model", Cambridge University Press. p. 127. ISBN 9780511617270, (2006).

[61] G. Giudice, M. Luty, H. Murayama, and R. Rattazzi, "Gaugino mass without singlets", Journal of High Energy Physics. 9812 (12), (1998).

[62] T. Appelquist, H. Cheng, B. A. Dobrescu, "Bounds on universal extra dimensions", Physical Review D. 64 (3): 035002, (2001).

[63] T. Kaluza, "Zum Unitatsproblem in der Physik", Sitzungsber. Preuss. Akad. Wiss. Berlin. (Math. Phys.) 966, (1921).

[64] O. Klein, "Quantum Theory and Five-Dimensional Theory of Relativity", Z. Phys. 37 895, (1926).

[65] M. Schmaltz and D. Tucker-Smith, "Little Higgs Review", Annu. Rev. Nucl. Part. Sci. 55:229-270, (2005).

[66] H. Cheng, I. Low, "Little Hierarchy, Little Higgses, and a Little Symmetry", JHEP 0408:061, (2004).

[67] S. Arrenberg et al, "Dark Matter in the Coming Decade: Complementary Paths to Discovery and Beyond", arXiv:1310.8621 [hep-ph], (2013).

[68] M. Cahill-Rowley et al, "Complementarity of dark matter searches in the phenomenological MSSM", Phys. Rev. D 91, 055011, (2015).

[69] R. J. J. Grand et al, "The Auriga Project: the properties and formation mechanisms of disc galaxies across cosmic time",arXiv:1610.01159 [astro-ph.GA], (2016).

[70] L. Bergstrom, "Dark matter evidence, particle physics candidates and detection methods", Annalen Phys. 524 479–96, (2012).

[71] O. Adrian et al, "An anomalous positron abundance in cosmic rays with energies 1.5–100 GeV", Nature 458, 607-609, (2009).

[72] K. N. Abazajian, N. Canac, S. Horiuchi, and M. Kaplinghat, "Astrophysical and dark matter interpretations of extended gamma-ray emission from the Galactic Center", Phys. Rev. D 90, 023526 , (2014).

[73] C. Ming-Yang, Y. Qiang, S. T. Yue-Lin, F. Yi-Zhong, " A possible dark matter annihilation signal in the AMS-02 antiproton data", arXiv:1610.03840 [astro-ph.HE], (2016).

[74] A. Boyarsky, O. Ruchayskiy, D. Iakubovskyi, and J. Franse, "Unidentified Line in X-Ray Spectra of the Andromeda Galaxy and Perseus Galaxy Cluster", Phys. Rev. Lett. 113, 251301, (2014).

[75] M. Cirelli, " Status of Indirect (and Direct) Dark Matter searches", arXiv:1511.02031 [astro-ph.HE], (2015).

[76] H.E.S.S. Collaboration, " Search for a Dark Matter annihilation signal from the Galactic Center halo with H.E.S.S", Phys.Rev.Lett.106:161301, (2011).

[77] J. Goodman, M. Ibe, et al.,"Constraints on Dark Matter from Colliders", Phys.Rev. D82 , 116010 1008.178, (2010).

[78] A. Askew, S. Chauhan, B. Penning, W. Shepherd, and M. Tripathi, "Searching for Dark Matter at Hadron Colliders", International Journal of Modern Physics A, Vol. 29 1430041, (2014).

[79] ATLAS Collaboration,"A measurement of the ratio of the W and Z cross sections with exactly one associated jet in pp collisions at $\sqrt{s}$=7 TeV with ATLAS", JHEP 1304, 075 1210.4491,(2013).

[80] ATLAS Collaboration,"Search for dark matter in events with a Z boson and missing transverse momentum in pp collisions at $\sqrt{s}=$8 TeV with the ATLAS detectorS", Phys. Rev. D 90, 012004,(2014).

[81] CMS Collaboration),"Search for dark matter, extra dimensions, and unparticles in monojet events in proton–proton collisions at $\sqrt{s}=$8 TeV", Eur.Phys.J. C75 no.5, 235, (2015).

[82] CMS Collaboration), "Search for New Physics with a Mono-Jet and Missing Transverse Energy in pp Collisions at $\sqrt{s}=$7 TeV", Phys.Rev.Lett. 107, (2011).

[83] M. Schuman,"Dark Matter 2014", EPJ Web Conf. 96 01027, [1501.01200],(2015).

[84] XENON100 collaboration, "The XENON100 Dark Matter Experiment", Astropart. Phys.35 573, [1107.2155], (2012).

[85] XENON100 collaboration, "Dark Matter Results from 225 Live Days of XENON100 Data", Phys. Rev. Lett. 109, 181301, (2012).

[86] LUX collaboration, "Improved Limits on Scattering of Weakly Interacting Massive Particles from Re-analysis of 2013 LUX data", Phys. Rev. Lett. 116, 161301, (2016).

[87] PandaX-II Collaboration, "Dark Matter Results from First 98.7-day Data of PandaX-II Experiment", arXiv:1607.07400 [hep-ex], (2016).

[88] XENON collaboration, "Physics reach of the XENON1T dark matter experiment", JCAP04. 027,(2016).

[89] LUX-ZEPLIN (LZ) collaboration, "LUX-ZEPLIN (LZ) Conceptual Design Report", LBNL-190005, [1509.02910], (2015).

[90] DARWIN collaboration, "DARWIN: towards the ultimate dark matter detector", arXiv:1606.07001 [astro-ph.IM], (2016).

[91] M. Schumann, L. Baudis, L. Buetikofer, A. Kish and M. Selvi, "Dark matter sensitivity of multi-ton liquid xenon detectors", JCAP 1510 016, [1506.08309], (2015).

[92] DarkSide Collaboration, " Results from the first use of low radioactivity argon in a dark matter search", Phys. Rev. D 93, 081101, (2016).

[93] B. Henning, Darkside-20k Collaboration, "Darkside-20k: A 20 ton Liquid Argon Dark Matter Experiment", APS April Meeting 2016, abstract #H16.004, (2016).

[94] J Schieck et al., "Direct Dark Matter Search with the CRESST II Experiment", arXiv:1611.02113 [astro-ph.CO], (2016).

[95] SuperCDMS Collaboration, "New Results from the Search for Low-Mass Weakly Interacting Massive Particles with the CDMS Low Ionization Threshold Experiment", PRL 116, 071301, (2016).

[96] R. Agnese, et al., "Projected Sensitivity of the SuperCDMS SNOLAB experiment", arXiv:1610.00006 [physics.ins-det], (2016).

[97] J. Lewin, and P. Smith, "Review of mathematics, numerical factors, and corrections for dark matter experiments based on elastic nuclear recoil", Astropart. Phys., 6, pp. [87–112], (1996).

[98] Laura Baudis, "WIMP dark matter direct-detection searches in noble gases", Physics of the Dark Universe 4 50, (2014).

[99] M.C. Smith, et al., "The RAVE Survey: Constraining the Local Galactic Escape Speed", Mon.Not.Roy.Astron.Soc.379:755-772,2007, (2007).

[100] E. Aprile, T. Doke, "Liquid Xenon Detectors for Particle Physics and Astrophysics", Rev.Mod.Phys.82:2053-2097, (2010).

[101] M. Auger et al, "Search for Neutrinoless Double-Beta Decay in 136Xe with EXO-200, Phys. Rev. Lett. 109, 032505, (2012).

[102] O. Cheshnovsky, B. Raz, and J. Jortner, "Temperature dependence of rare gas molecular emission in the vacuum ultraviolet", Chem. Phys. Lett. 15, 475, (1972).

[103] J. Jortner, L. Meyer, S. A. Rice, and E. G. Wilson, "Localized excitations in condensed ne, ar, kr, and xe", J. Chem. Phys. 42, 4250, (1965).

[104] M. Tanaka et al., "LET dependence of scintillation yields in liquid xenon", Nucl. Instrum. Meth. A457. 454, (2001).

[105] J. Lindhard and M Scharff, "Energy dissipation by ions in the keV region", Phys. Rev. 124, 128- 30, (1961).

[106] A. Hitachi, "Properties of liquid xenon scintillation for dark matter searches", Astropart. Phys. 24, 247, (2005).

[107] G. Plante et al., "New Measurement of the Scintillation Efficiency of Low-Energy Nuclear Recoils in Liquid Xenon", arXiv:1104.2587v1 [nucl-ex], (2011).

[108] A. Manalaysay, "Towards an improved understanding of the relative scintillation efficiency of nuclear recoils in liquid xenon", arXiv:1007.3746v1 [astro-ph.IM], (2010).

[109] V. Chepel, and H. Araujo, "Liquid noble gas detectors for low energy particle physics", Phys. Rev. D 88, 012006, (2013).

[110] E Aprile, "The search for particle dark matter with the XENON imaging time projection chambers", Journal of Instrumentation, Volume 8 , (2013).

[111] P. Sorensen, and C. E. Dahl, "Nuclear recoil energy scale in liquid xenon with application to the direct detection of dark matter", Phys.Rev. D83 063501, (2011).

[112] XENON100 collaboration, "Response of the XENON100 dark matter detector to nuclear recoils", JINST 8 R040016, (2013).

[113] Laura Baudis, et al. , "Response of liquid xenon to Compton electrons down to 1.5 keV", Phys. Rev. D87 115015, (2013).

[114] http://www.eljentechnology.com/index.php/joomla-overview/this-is-newest/71-ej-301.

[115] J. Mock, et al. , "Modeling pulse characteristics in Xenon with NEST", J. Inst. 9, T04002-T04002, (2014).

[116] LUX Collaboration, "Response of liquid xenon to Compton electrons down to 1.5 keV", arXiv:1608.05381 [physics.ins-det], (2016).

[117] http://www.hamamatsu.com

[118] K. Lung et al. ,"Characterization of the Hamamatsu R11410-10 3-Inch Photomultiplier Tube for Liquid Xenon Dark Matter Direct Detection Experiments", arXiv:1202.2628 [physics.ins-det], (2012).

[119] The XENON Collaboration, "Lowering the radioactivity of the photomultiplier tubes for the XENON1T dark matter experiment", arXiv:1503.07698 [astro-ph.IM], (2015).

[120] L. Baudis et al. ,"Gator: a low-background counting facility at the Gran Sasso Underground Laboratory", JINST, 6:P08010, (2011).

[121] D. Budjas et al. " Highly Sensitive Gamma-Spectrometers of GERDA for Material Screening: Part 2", arXiv:0812.0768 [physics.ins-det], (2008).

[122] G. Heusser, M. Laubenstein, and N. Neder, "Low-level germanium gamma-ray spectrometry at the μBq/kg level and future developments towards higher sensitivity", Appl. Rad. Isot. , (2004).

[123] L. Baudis et al. , " Performance of the Hamamatsu R11410 Photomultiplier Tube in cryogenic Xenon Environments", JINST 8 P04026, (2013).

[124] P. Barrow et al. , " Qualification Tests of the R11410-21 Photomultiplier Tubes for the XENON1T Detector", arXiv:1609.01654 [astro-ph.IM], (2016).

[125] LVD Collaboration, " Muon 'Depth – Intensity' Relation Measured by LVD Underground Experiment and Cosmic-Ray Muon Spectrum at Sea Level", Phys.Rev. D58 092005, (1998).

[126] The MACRO Collaboration, "Measurement of the residual energy of muons in the Gran Sasso underground Laboratories", Astropart.Phys.19:313-328, (2003).

[127] V.A. Kudryavtsev, L. Pandola, and V. Tomasello, " Neutron- and muon-induced background in underground physics experiments", Eur.Phys.J.A36:171-180, (2008).

[128] The XENON Collaboration, "Conceptual design and simulation of a water Cherenkov muon veto for the XENON1T experiment", JINST 9, P11006, (2014).

[129] D.-M. Mei, and A. Hime, "Muon-Induced Background Study for Underground Laboratories", Phys.Rev.D73:053004, (2006).

[130] C. W. Geis, "Untersuchung der DF2000MA Reflektorfolie in Hinsicht auf ihre Verwendung im XENON1T MuonVeto" , Research thesis, Johannes Gutenberg University Mainz, (2012).

[131] E. Aprile et al., "Facility and method for supplying liquid xenon", patent FR2986061 (A1), (2013).

[132] E. Aprile et al., "Performance of a cryogenic system prototype for the XENON1T Detector", arXiv:1208.2001 [physics.ins-det], (2012).

[133] S. Rosendahl et al., "A novel ^{83m}Kr tracer method for characterizing xenon gas and cryogenic distillation systems", JINST 9 P10010, (2014).

[134] General Electrics, http://www.ge.com/

[135] K. Ozone, "Liquid Xenon Scintillation Detector for the New $\mu \to e\gamma$ Search Experiment", Ph.D. Thesis, Department of Physics, University of Tokyo, Japan, (2005).

[136] National Nuclear Data Center, Brookhaven National Laboratory, http://www.nndc.bnl.gov/nudat2/.

[137] L. W. Kastens, S. B. Cahn, A. Manzur, and D. N. McKinsey, "Calibration of a Liquid Xenon Detector with Kr-83m", Phys.Rev.C80:045809, (2009).

[138] LUX Collaboration, "Tritium calibration of the LUX dark matter experiment", Phys. Rev. D 93, 072009 , (2016).

[139] R.F. Lang et al., "A ^{220}Rn source for the calibration of low-background experiments", JINST 11, P04004, (2016).

[140] CAEN, http://www.caen.it/csite

[141] Philips, www.usa.philips.com

[142] Django, web framework, https://www.djangoproject.com/.

[143] ROOT, Data analysis framework, CERN, https://root.cern.ch/.

[144] Hierarchical Data Format, https://support.hdfgroup.org/HDF5/.

[145] XENON100 Collaboration, "Likelihood Approach to the First Dark Matter Results from XENON100", Phys. Rev. D 84, 052003, (2011).

[146] A. Kish, "Dark Matter Search with the XENON100 Experiment", PhD thesis, University of Zurich, (2011).

[147] Farnell   Element 14,   http://uk.farnell.com/kingbright/l-813pbc-z/led-10mm-x-bright-blue-7cd-465nm/dp/2335786.

[148] http://www.berkeleynucleonics.com/model-505

[149] http://www.ratioplast.com

[150] http://www.fiberguide.com/wp-content/uploads/2013/03/All_Silica_Fiber_0301131.pdf, page 5.

[151] http://www.mdcvacuum.eu/sites/default/files/pdfs/CAT60311.pdf

[152] http://www.alcatechnology.com/

[153] C.H. Faham et al., "Measurements of wavelength-dependent double photoelectron emission from single photons in VUV-sensitive photomultiplier tubes", Journal of Instrumentation 10 P09010, (2015).

[154] F. Kaether, C. Langbrandtner, "Transit time and charge 655 correlations of single photoelectron events in R7081 photomultiplier tubes", Journal of Instrumentation 7 (09) P09002, (2012).

[155] D. Carter, "Photomultiplier Handbook: Theory, Design, Application, Lancaster, Pennsylvania", Burle Industries, Inc., (1980).

[156] S. O. Flyckt, C. Marmonier, "Photomultiplier tubes: principles and applications, Photonis", Brive, France (2002).

[157] F. J. Lombard, F. Martin, "Statistics of electron multiplication", Review of Scientific Instruments 32 (2) 200–201, (1961).

[158] J. Prescott, "A statistical model for photomultiplier single-electron statistics", Nuclear Instruments and Methods 39 (1) 173 – 179, (1966).

[159] A.G. Wright, "The statistics of multi-photoelectron pulse-height distributions", Nuclear Instruments and Methods V579, I3, 11, 967–972, (2007).

[160] E. Bellamy et al., "Absolute calibration and monitoring of a spectrometric channel using a photomultiplier", Nuclear Instruments and Methods 339 (3) 468 – 476, (1994).

[161] R. Saldanha, L. Grandi, Y. Guardincerri, and T. Wester, "Model Independent Approach to the Single Photoelectron Calibration of Photomultiplier Tubes", arXiv:1602.03150 [physics.ins-det] , (2016)

[162] NEST (Noble Element Simulation Technique), http://nest.physics.ucdavis.edu/site/.

[163] P. Pakarha, "Preparations for measurements of the low energy response of liquid xenon" , Master thesis, Ecole polytechnique federale de lausanne (EPFL), (2012).

[164] I. Israelashvili, et al., " A Comprehensive Simulation Study of a Liquid-Xe Detector for Contraband Detection", arXiv:1501.00150 [physics.ins-det], (2015).

[165] ENDF nuclear data, http://www.nndc.bnl.gov/exfor/endf00.jsp .

[166] J. R. Verbus et al., "Proposed low-energy absolute calibration of nuclear recoils in a dual-phase noble element TPC using D-D neutron scattering kinematics", arXiv:1608.05309 [physics.ins-det], (2016).

[167] A. Manalaysay, "Response of liquid xenon to low-energy ionizing radiation and its use in the XENON10 Dark Matter search" , PhD thesis, University of Zurich, (2009).

[168] Cryogenic Control Systems Inc., http://www.cryocon.com/.

[169] Swagelok Fluid System Technologies, http://www.swagelok.com/.

[170] E. Aprile, K. Giboni, P. Majewski, K. Ni and M. Yamashita, "Proportional Light in a Dual-phase Xenon Chamber", IEEE Transactions on Nuclear Science 51, (2004).

[171] COMSOL, https://www.comsol.com/.

[172] H. Dujmovic, "Characterization and Calibration of a Liquid Xenon Time-Projection Chamber", M.Sc. thesis , (2014).

[173] D. Furse, "A Modern, Extensible C++ Particle Tracking Package" , (2014).

[174] Mesytec, pulse shape discrimination module (MPD4), http://www.mesytec.com/products/nuclear-physics/MPD-4.html .

[175] ORTEC, advanced measurement technology, http://www.ortec-online.com/ .

[176] G. Plante, "The XENON100 Dark Matter Experiment: Design, Construction, Calibration and 2010 Search Results with Improved Measurement of the Scintillation Response of Liquid Xenon to Low-Energy Nuclear recoils", PhD thesis, University of Columbia, (2012).

[177] T. Doke, K. Masuda, "Present status of liquid rare gas scintillation detectors and their new application to gamma-ray calorimeters", Nuclear Instruments and Methods in Physics, V. 420 A 62, (1999).

[178] E. Aprile, et al., "Simultaneous Measurement of Ionization and Scintillation from Nuclear Recoils in Liquid Xenon for a Dark Matter Experiment", Phys. Rev. Lett. 97, 081302, (2006).

[179] D. R. Lide, "CRC Handbook of Chemistry and Physics", Boca Raton (FL), CRC Press, (1990).

[180] R.L. Amey, "Dielectric Constants of Liquefied Noble Gases and Methane", Journal of Chemical Physics V40 I1 10.1063, (2004).

[181] Amphenol, https://www.amphenol.com/.

[182] LabVIEW System Design Software, National Instruments, http://www.ni.com/labview/ .

[183] A. J. Leadbetter and H. E. Thomas, "Density and surface tension of liquid xenon and theory of corresponding states for the inert gases" , Trans. Faraday Soc., 61, 10-19, (1965).

[184] J. A. Campbell and J. H. Hildebrand, "The Structure of Liquid Xenon", The Journal of Chemical Physics, V11, I 7 10.1063/1.1723852, (2004).

[185] I. Dostrovsky, S. Katcoff, A. W. Stoenner, "Decay Scheme of ^{83}Rb", Physical Review, vol. 136, I 1B, pp. 44-49, (1964).

[186] S.-C. WU, "Nuclear Data Sheets for A = 83", Nuc. Data Sheets, 92, 893, (2001).

[187] A. Manalaysay, et al., "Spatially uniform calibration of a liquid xenon detector at low energies using 83m-Kr", Rev.Sci.Instrum.81:073303, (2010).

[188] M. Szydagis, A. Fyhrie, D. Thorngren, and M. Tripathi, "Enhancement of NEST Capabilities for Simulating Low-Energy Recoils in Liquid Xenon", arXiv:1307.6601 [physics.ins-det], (2013).

[189] J. Thomas and D. A. Imel, "Recombination of electron-ion pairs in liquid argon and liquid xenon", Phys. Rev. A36, 614, (1987).

[190] T. Takahashi, et. al., "Average energy expended per ion pair in liquid xenon", Phys. Rev. A12, 1771 (1975).

[191] G.Audi, "The NUBASE Evaluation of Nuclear and Decay Properties", Nuclear Physics 729:3-128. Bibcode 2003NuPhA.729, (2003).

[192] Xaixuan Ni, "Probing the intrinsic electron recoil rejection power in liquid xenon for DM searches", Joint TeVPA/IDM Conference, Astroparticle physics, (2014).

[193] Qing Lin, "Response and Discrimination of Low-Energy Electronic and Nuclear Recoils in Liquid Xenon", Workshop on Calibration of Low Energy Detectors, KICP, University of Chicago, (2015).

[194] R.E. Lapp and H.L. Andrews, "Nuclear Radiation Physics", Prentice-Hall, Englewood Cliffs, NJ, (1972).

[195] D. Charles, D. Ferguson, T. Kazi, "Commercial radioactive sources", Monterey Institute of International Studies, (2003).

[196] G. J. Alner et al., "First limits on WIMP nuclear recoil signals in ZEPLIN-II: a two phase xenon detector for dark matter detection", Astropart.Phys.28:287-302, (2007).

[197] XENON Collaboration, "First Results from the XENON10 Dark Matter Experiment at the Gran Sasso National Laboratory", Phys. Rev. Lett. 100, 02130, (2008).

[198] D. Yu. Akimov et al., "WIMP-nucleon cross-section results from the second science run of ZEPLIN-III", arXiv:1110.4769 [astro-ph.CO] (2011).

[199] LUX Collaboration, "First Results from the LUX Dark Matter Experiment at the Sanford Underground Research Facility", Phys. Rev. Lett. 112, 091303, (2014).